



**HAL**  
open science

# Contribution to the mathematical and numerical study of certain problems of biological membrane, magnetorheological fluid and image processing

Houda Fahim

► **To cite this version:**

Houda Fahim. Contribution to the mathematical and numerical study of certain problems of biological membrane, magnetorheological fluid and image processing. Analysis of PDEs [math.AP]. Université de Picardie Jules Verne; Université Cadi Ayyad (Marrakech, Maroc), 2021. English. NNT : 2021AMIE0019 . tel-03707102

**HAL Id: tel-03707102**

**<https://theses.hal.science/tel-03707102>**

Submitted on 28 Jun 2022

**HAL** is a multi-disciplinary open access archive for the deposit and dissemination of scientific research documents, whether they are published or not. The documents may come from teaching and research institutions in France or abroad, or from public or private research centers.

L'archive ouverte pluridisciplinaire **HAL**, est destinée au dépôt et à la diffusion de documents scientifiques de niveau recherche, publiés ou non, émanant des établissements d'enseignement et de recherche français ou étrangers, des laboratoires publics ou privés.

## Thèse de Doctorat en Cotutelle

*Mention Mathématiques*

présentée à *l'Ecole Doctorale en Sciences Technologie et Santé (ED 585)* de  
**l'Université de Picardie Jules Verne**

*et*

à *l'Ecole Doctorale en Science de L'ingénieur de la Faculté des Sciences et  
Techniques* de  
**l'Université Cadi Ayyad - Marrakech**

par

**Houda Fahim**

pour obtenir le grade de Docteur de l'Université de Picardie Jules Verne

***Contribution to the mathematical and numerical  
study of certain problems of biological membrane,  
magnetorheological fluid and image processing***

Soutenue le 20 février, après avis des rapporteurs, devant le jury d'examen :

<b>M. A. H Bentbib, Professeur, Université Cadi Ayyad</b>	<b>Président</b>
<b>M. M. Bendahmane, MCF HDR, Université de Bordeaux</b>	<b>Rapporteur</b>
<b>M<sup>me</sup> V. G Bognar, Professeur, Université de Miskolc</b>	<b>Rapporteur</b>
<b>M. F. Karami, Professeur, Université Cadi Ayyad</b>	<b>Rapporteur</b>
<b>M. Y. Mammeri, MCF HDR, Université de Picardie Jules Verne</b>	<b>Examineur</b>
<b>M. C. Misbah, Directeur de Recherche, CNRS Grenoble</b>	<b>Examineur</b>
<b>M. M. Guedda, Professeur, Université de Picardie Jules Verne</b>	<b>Directeur de thèse</b>
<b>M. N. Alaa, Professeur, Université Cadi Ayyad</b>	<b>Co-directeur</b>

# Acknowledgments

Throughout the four years of this dissertation I have received a great deal of support and assistance.

I would first like to thank my supervisors, Professor Alaa Nour Eddine and Professor Guedda Mohammed, whose expertise was invaluable in formulating the research questions and methodology. Thank you for welcoming me to the laboratory, for allowing me to get involved in many projects, and for giving me all your trust. Thank you for giving me a place as a collaborator in your own right. Your insightful feedback pushed me to brought my work to a higher level. You make me choose the right direction and successfully complete my dissertation by providing me with the needed tools.

My gratitude extends to the rest of my thesis committee members, who were involved in the validation survey for this manuscript: the president Pr. Abdeslam Hafid Bentbib; thesis reporters Pr. Mostafa Bendahmane, Pr. Gabriella Bogнар and Pr. Fahd Karami, and thesis examiners Pr. Chaouqi Misbah and Pr. Youcef Mammeri, for generously offering there time, support and goodwill throughout the presentation and the rapport of my dissertation document.

I would like also to express my sincere appreciation to the International Affairs Department(DAI) of Picardie Jules Verne University of Amiens for making my stay at the laboratory of Fundamental and Applied mathematics (LAMFA) in good conditions (as part of my cotutelle thesis between Marrakech and Amiens in France). This experience helped me a lot to improve my skills on the scientific and even on the personal level.

During my research studies, i was able to benefit from the financial support of the German-French-Maroccan graduate school living fluids (grant CFDA-Q1-14), mannaged by Pr. Chaouqi Misbah, and Pr. Christian Wagner. Thank you for making me a member of the CFDA and for your financial support during my research internships abroad. Exchanges and meetings in other countries were and well always be a pleasure.

I would particularly like to thank Pr. Misbah Chaouqi for welcoming me at the Interdisciplinary laboratory of physics (Liphy) in Grenoble. I really enjoyed my stay in Grenoble and my visit to this laboratory where i met an amazing and available team. As a member of my thesis committee, thank you for your valuable guidance and for all the opportunities you gave me to further my research.

I also had the opportunity to work with Pr. Gabriella Bognar and Pr. Robert Kersner, during my stay in France as a part of the French-Hungarian Scientific Cooperation Project PHC-Balaton (grant 41897UF), managed by Pr. Guedda and Pr. Bognar. Thank you for this amazing opportunity.

I would like to acknowledge my colleagues from my laboratory either in Morocco or in France, for creating and maintaining such a good atmosphere of the office. Working with you has been a pleasure. I would have made some very good friends there.

Finally, I would like to thank my parents for their wise counsel and sympathetic ear. You were always there for me. I could not have completed this dissertation without your support. A big thank to my friends, who provided stimulating discussions as well as happy distractions to rest my mind outside of my research.

# Contents

<b>List of Figures</b>	<b>5</b>
0.1 Résumé Substantiel . . . . .	6
<b>1 On the equilibrium shape of red blood cells</b>	<b>26</b>
1.1 Description of the mathematical model of red blood cells and vesicles . . . . .	27
1.1.1 The biological structure of vesicles and Red blood cells . . . . .	27
1.1.2 Construction of the physical model . . . . .	30
1.1.3 A constrained optimization problem . . . . .	36
1.2 The biconcave character of red blood cells in 2D and 3D axis-symmetric domain . . . . .	37
1.2.1 Canham-Helfrich problem in two-dimensional axis-symmetric domain . . . . .	37
1.2.2 The problem formulation in the two-dimensional axis-symmetric case . . . . .	40
1.2.3 Variable change . . . . .	43
1.2.4 Numerical simulations . . . . .	54
1.2.5 Canham-Helfrich problem in three-dimensional axi-symmetric Domain . . . . .	61
1.2.6 Dynamical system . . . . .	73
1.3 Conclusion . . . . .	76
<b>2 Fluctuations and instability of a biological membrane induced by interaction with macro- molecules using geometric shape optimization</b>	<b>78</b>
2.1 Introduction . . . . .	78
2.2 Localization of multiple species of diffusion molecules on membrane surfaces . . . . .	79
2.2.1 Description of the mathematical problem . . . . .	80

2.2.2	Equation of the diffusive proteins on the surface membrane . . . . .	83
2.3	Fluctuations and instability of membrane in the presence in a diffusion field using shape optimization . . . . .	84
2.3.1	Mathematical Model . . . . .	85
2.3.2	Existence of optimal solution . . . . .	87
2.3.3	Differentiability with respect to domain . . . . .	92
2.4	Numerical Analysis . . . . .	96
2.4.1	Level-Set Method . . . . .	96
2.4.2	<b>Numerical Algorithm and Simulations</b> . . . . .	98
2.5	Conclusion . . . . .	98
<b>3</b>	<b>Dynamical Behavior of Vesicles in the Steady and Oscillatory Shear Flow</b>	<b>99</b>
3.1	Introduction . . . . .	99
3.2	A minimal model . . . . .	103
3.3	Analytical results . . . . .	108
3.3.1	Exact solutions . . . . .	108
3.3.2	Oscillating motions . . . . .	111
3.3.3	The bifurcation phenomena . . . . .	114
3.4	Rheology of vesicle suspension . . . . .	117
3.4.1	Reduced effective viscosity . . . . .	117
3.4.2	Normal stress differences . . . . .	121
3.5	Isotropic part of the tension . . . . .	122
3.6	Conclusion . . . . .	127
<b>4</b>	<b>Nonlinear parabolic equation having nonstandard growth condition with respect to the gradient and variable exponent</b>	<b>129</b>
4.1	Introduction . . . . .	129
4.2	Preliminaries results and notations . . . . .	132
4.2.1	Lebesgue-Sobolev spaces with variable exponent . . . . .	132
4.2.2	Functional framework and definitions . . . . .	134
4.3	An existence result with bounded nonlinearity . . . . .	136
4.4	An existence result with nonstandard growth nonlinearity . . . . .	142

4.4.1	Approximate problem . . . . .	143
4.4.2	A priori estimates . . . . .	145
4.4.3	Passing to the limit . . . . .	149
4.5	Appendix . . . . .	150
<b>5 Weak solution for quasilinear parabolic systems with variable exponents and critical growth</b>		
<b>nonlinearities with respect to the gradient</b>		<b>157</b>
5.1	Introduction . . . . .	157
5.2	Notations and Preliminaries. . . . .	160
5.3	Auxilliary Results . . . . .	165
5.4	An existence result for bounded nonlinearities . . . . .	168
5.5	An existence result for subquadratic growth . . . . .	173
5.5.1	Construction of the approximate problem . . . . .	174
5.5.2	A priori estimates . . . . .	177
5.5.3	Passing to the limit . . . . .	182
<b>6 Spherical Harmonics</b>		
6.0.4	Introduction . . . . .	185
6.1	Spherical harmonics on $S^1$ . . . . .	185
6.2	Spherical harmonics on $S^2$ . . . . .	189
6.3	Numerical implementation . . . . .	199
6.3.1	Computation of the spherical harmonics . . . . .	199
6.3.2	Visualization of the spherical harmonics . . . . .	200
<b>7 Application to Image Decomposition, Reconstruction and Fingerprints Identification.</b>		
7.0.3	Introduction . . . . .	202
7.1	Spherical representation . . . . .	203
7.2	Reconstruction . . . . .	204
7.2.1	Coefficients computation . . . . .	204
7.3	Numerical simulations . . . . .	205
7.3.1	Representation of an image on the sphere . . . . .	205
7.3.2	Reconstruction . . . . .	207

7.4	Fingerprints identification by a shape descriptor based on spherical harmonics . . . . .	208
7.4.1	Shape descriptor based on Spherical Harmonics . . . . .	213
7.4.2	Matlab Code . . . . .	218
7.4.3	Construction of the database . . . . .	219
7.4.4	Calculation of the descriptor vector . . . . .	219
7.4.5	Conclusion . . . . .	223
	<b>Bibliography</b>	<b>224</b>

# List of Figures

1	Human blood composition (source: <a href="https://ib.bioninja.com.au/standard-level/topic-6-human-physiology/62-the-blood-system/blood-composition.html">https://ib.bioninja.com.au/standard-level/topic-6-human-physiology/62-the-blood-system/blood-composition.html</a> ). . . . .	16
2	Red blood cells observed under the electron microscope. The biconcave shape is clearly visible. Link: <a href="https://www.nisenet.org/catalog/scientific-image-human-red-blood-cells-sem">https://www.nisenet.org/catalog/scientific-image-human-red-blood-cells-sem</a>	16
3	Molecular view of the cell membrane Link: <a href="https://www.britannica.com/science/membrane-biology">https://www.britannica.com/science/membrane-biology</a> . . . . .	17
4	A cross-section of a vesicle formed by phospholipids. . . . .	17
1.1	Scheme of a vesicle formed by phospholipids (source: article vesicle on Wikipedia. . . . .	27
1.2	A 3-D human red blood cell model (source: <a href="https://www.turbosquid.com/3d-models/3d-red-globule-blood/372582">https://www.turbosquid.com/3d-models/3d-red-globule-blood/372582</a> ). . . . .	28
1.3	Red blood cell capillary and cross-section view. Link: <a href="https://www.anatomynote.com/human-anatomy/cell-and-tissue/red-blood-cell-capillary-and-cross-section-view/">https://www.anatomynote.com/human-anatomy/cell-and-tissue/red-blood-cell-capillary-and-cross-section-view/</a> . . . . .	28
1.4	A normal red blood cell on the left and sickle cell disease on the right, very deformed erythrocyte and more rigid. Which causes the polymerization of the hemoglobin it contains in the absence of oxygen, then blocking blood flow . . . . .	28

1.5	Effect of the osmotic pressure on red blood cells. Three different solutions are shown: hypertonic solution, where a red blood cell is causing water to move out of the cell which make it contract and appear spiky, isotonic solution, where the concentration of solutes outside the cell is equal to the concentration of solutes inside the cell which make the red blood cell show it's normal discocyte shape, and hypotonic solution, where the red blood cell is causing water to move into the cell which make it expand and become more round (source: <a href="http://encyclopedia.lubopitko-bg.com/OsmosisAffectsCells.html">http://encyclopedia.lubopitko-bg.com/OsmosisAffectsCells.html</a> ). . . . .	29
1.6	Schematic illustrations of bending mode of a 2-D membrane . . . . .	30
1.7	Representation of the membrane in 2D with the used notations. . . . .	31
1.8	For a surface $S \in \mathbb{R}^3$ , the scalar mean curvature $H$ is given by the sum of $k_1$ and $k_2$ (principal curvatures defined by the curvatures of the green and red curves at the considered point $\mathbf{p}$ ). . . . .	32
1.9	Different vesicle shape depending on the reduced volume at equilibrium in the absence of flow in the three-dimensional case[121] . . . . .	40
1.10	A surface view and a cut view of a red blood cell (from Matlab simulations). . . . .	40
1.11	The curve defined by the function $h \in \Phi$ . Where, $h'(0) = 0$ , $h'(x_m) = -\infty$ are imposed conditions to ensure the symmetry. The curve $\Gamma_+$ is the continuous part of the curve, the rest of the curve (dashed) is constructed by symmetry . . . . .	41
1.12	$\kappa'$ curve as a function of $\kappa$ for $p = H_0 = 0$ , $\kappa'_0 = 0.3$ , and $\mu = 0.125$ . . . . .	48
1.13	This curve represent the function $h(x)$ in the case where $c_2 = 0$ . . . . .	53
1.14	The class of contours obtained by Evans Ref.[56] using equation (1.29), and the experimental data obtained by the interference microscopy method . . . . .	54
1.15	Diagram of the system resolution . . . . .	60
1.16	Plot $\Gamma$ of the function $h$ for different discretization steps . . . . .	61
1.17	Example of a function $h \in \Phi_m$ in 3D. We imposed to ensure the symmetry: $h'(0) = 0$ , $h'(r_m) = -\infty$ . Here we can see the $\Gamma_+$ curve . . . . .	63
1.18	Diagram of the problem and presentation of the $\Gamma$ curve. . . . .	63
1.19	Plot $\Gamma$ of the function $h$ for different discretization steps . . . . .	76
1.20	Plot of the function $h$ for different discretization steps . . . . .	76
1.21	Plot of the function $h$ for different discretization steps . . . . .	76
1.22	Plot of the function $h$ for different discretization steps . . . . .	76

1.23 Three-dimensional biconcave shape . . . . .	76
1.24 Three-dimensional biconcave shape . . . . .	76
2.1 Transport Across the Cell Membrane . . . . .	79
2.2 Transport Across the Cell Membrane: different adsorbate densities at or within the two head group layers. The lipid head groups are shown in blue, the lipid tails in red, and the adsorbate “particles” in dark gray. . . . .	80
2.3 The red part is the cell with membrane $\Gamma_0$ and the blue part represent the surrounding fluid containing the molecules . . . . .	86
2.4 Definition of a domain transported by a vector field $\theta$ . . . . .	93
2.5 Initial shape. . . . .	98
2.6 Shape evolution in time. . . . .	98
2.7 Final shape. . . . .	98
3.1 Scheme of a vesicle . . . . .	99
3.2 Ellipsoid membrane of a vesicle immersed in a viscous fluid a linear shear flow. . . . .	100
3.3 Different motion of vesicle [45] . . . . .	100
3.4 Spherical harmonics of order two . . . . .	105
3.5 (Color online) Illustration of the CW/CCW SW (solid red line) for a vesicle with excess area $\Delta = 0.437$ and parameters $h = 0.3, \Gamma = 0.99$ in response to the oscillatory shear rate (dashed black line, in arbitrary scale) with frequency $f_r = 0.02$ (period $T_{sh} = 50$ ) and shear rate amplitude $\dot{\gamma}_a = 0.55$ . A similar behavior is shown in Fig. 7 of Ref. [138] for microcapsules. . . . .	111
3.6 Plots of $\dot{\gamma}$ (dashed black line) and the orientation angle $\psi/\pi$ (red solid line). The vesicle exhibits alternatively TB and SW . Parameter $\dot{\gamma}_a = 1.5$ and other parameters are the same as in Figure 3.5. . . . .	113
3.7 Plots of $\dot{\gamma}$ (dashed black line) and the inclination angle (red solid line) at $\dot{\gamma}_a = \dot{\gamma}_a^2 \approx 2.351229$ , with same other parameters as in Figure 3.5. The vesicle periodically presents horizontal reversals ( $\psi = 0$ ) and vertical reversals ( $\psi = \pi/2$ ) separated by one TB. . . . .	114
3.8 Plots of $\dot{\gamma}$ (dashed black line) and $MOD_2$ behavior (red solid line) for $\dot{\gamma}_a = 2.37$ (just above $\dot{\gamma}_a^2$ ). The global maximum (see Figure 3.7) splits into two TB connected by a CCW/CW SW. . . . .	116

3.9	Time-dependent reduced viscosity $[\eta]$ during TB and VB regimes for different values of $\Gamma$ . Parameters are $\Delta = 0.437, h = 0.3, \dot{\gamma}_a = 2.37, \Gamma = 1.02$ (dashed red line) and $\Gamma = 0.91$ (solid blue line). . . . .	119
3.10	Time-dependent reduced viscosity $[\dot{\eta}]$ at $\tau$ during TB and VB regimes. Parameters are $\Delta = 0.437, h = 0.3, \dot{\gamma}_a = 2.37, \Gamma = 1.02$ (dashed red line) and $\Gamma = 0.91$ (solid blue line). . . . .	120
3.11	Time-dependent reduced viscosity $[\dot{\eta}]$ at $\tau$ during TB and VB regimes. Parameters are $\Delta = 0.437, h = 0.3, \dot{\gamma}_a = 1.5, \Gamma = 1.02$ (dashed red line) and $\Gamma = 0.91$ (solid blue line). . . . .	120
3.12	Time-dependent reduced viscosity $[\eta]$ during TB and VB regimes. Parameters are $\Gamma = 1.02, \Delta = 0.437, h = 0.3, \dot{\gamma}_a = 2.37$ and $f_r = 0.001$ . . . . .	120
3.13	Reduced average effective viscosity $\langle[\eta]\rangle$ as a function of $h$ for $\Delta = 1$ . The cusp singularity is due to the transition from <i>TB</i> or <i>VB</i> to <i>TT</i> . . . . .	122
3.14	Time evolution of the first normal stress difference for $\Delta = 0.5, h = 0.3$ , and $\Gamma = 0.95$ (tumbling oscillating regime). Parameters $\phi, \eta_{ext}$ , and $\dot{\gamma}$ are such that $\phi\eta_{ext}\dot{\gamma} = 0.2$ . . . . .	123
3.15	Time evolution of the isotropic tension (TT based oscillatory regime). Parameters are $\Delta = 0.01, \mathcal{C}_k = 0.5, f_r = 0.05$ and $h = 0.3$ . . . . .	124
3.16	(Color online) Time evolution of the isotropic tension for different values of $\Gamma$ . Parameters are $\Delta = 0.01, C_k = 0.5, f_r = 0.05$ and $h = 0.02$ . $\Gamma = 0.5$ for dotted black line (TB), 0.8 for dashed green line (TB), 1 for solid blue line (VB), and 3 for dashed-dotted red line (VB). . . . .	125
6.1	3D representation of the modulus of the $Y_l^m$ first terms. . . . .	197
6.2	Development of a spherical function in spherical harmonics . . . . .	198
6.3	Analytical representation of the real part of the first spherical harmonics . . . . .	199
7.1	The given image I . . . . .	203
7.2	Image I': sphere representation of the given image I . . . . .	204
7.3	Representation of one part of the image I by different degrees . . . . .	205
7.4	Representation of the image I on the sphere . . . . .	206
7.5	Henry Classification . . . . .	208
7.6	Arches, loops and whorls . . . . .	209
7.7	The components of a fingerprint . . . . .	209
7.8	Cores and deltas . . . . .	210

7.9	Events on an edge (minutiae) . . . . .	210
7.10	Automatic classification (pattern recognition) . . . . .	211
7.11	Basic model for fingerprint verification and identification process . . . . .	212
7.12	Eight prints of the same fingerprint from the FVC2002 database (Maio et al. 2002) with differences in operations, translation, rotation and image quality.) . . . . .	212
7.13	Top left: Original grayscale image. top right: the binary image. on the bottom left: the image to be thinned. on the bottom right: the image with thinned out with the core (green), delta (gold), bifurcations (blue for $\theta \in [0^\circ - 180^\circ)$ and purple for $\theta \in [180^\circ - 360^\circ)$ . crest endings (orange for $\theta \in [0^\circ - 180^\circ)$ and red for $\theta \in [180^\circ - 360^\circ)$ . . . . .	213
7.14	Extraction algorithm of the harmonic descriptor. . . . .	217
7.15	Illustration of the database made up of 4 people fingerprints . . . . .	218

## 0.1 Résumé Substantiel

Les travaux de ce mémoire présentent différents résultats dans trois domaines: la dynamique des membranes biologiques, la dynamique de certains fluides électro ou magnéto rhéologiques et le traitement d'images. Du point de vue mathématique le mémoire concern l'analyse théorique et numérique des équations différentielles ordinaires fortement non linéaires et des équations aux dérivées partielles non linéaires.

Ses travaux constituent une approche multidisciplinaire qui regroupe les mathématiques appliquées, la biologie, la physique et le traitement d'images. La thèse est donc divisée en trois parties indépendantes.

Le sujet de la partie principale de la thèse est concentré sur l'analyse de la dynamique et de la déformation des globules rouges et des membranes biologiques, telles que les vésicules. Plus précisément, l'analyse porte sur l'étude de la forme des globules rouges, sur l'effet des molécules sur la membrane biologique et sur la dynamique des vésicules sous un écoulement oscillatoire, qui sont considérés comme des modèles simples des globules rouges.

Le sang est le fluide vital qui circule dans notre corps. Les fonctions principales de ce fluide est de transporter de l'oxygène, ainsi que d'éliminer du dioxyde de carbone. Ce fluide est une suspension fortement concentrée en cellules. Il est composé de trois types de globules sanguins, les globules blancs qui assurent la défense immunitaire, les plaquettes qui participent à la coagulation et les globules rouges, ou les érythrocytes. 45 % de notre volume sanguin est composé de globules rouges. Cette composition confère à la circulation sanguine des propriétés d'écoulement, appelées propriétés rhéologiques, très complexes.

Un globule rouge est une petite quantité de solution d'hémoglobine encapsulée par une membrane viscoélastique spécifique. Les globules rouges ne contiennent pas de noyaux et leur membrane est composée de trois éléments principaux : une bicouche lipidique, un cytosquelette de spectrine et des protéines transmembranaires.

La structure de spectrine possède des propriétés élastiques qui ont un grand rôle dans la dynamique des globules rouges. Ce sont des cellules très déformables pouvant passer rapidement dans les plus petits capillaires afin d'approvisionner chaque partie du corps en oxygène. Ces cellules peuvent donc présenter une variété de formes (formes de parachutes axisymétriques ou formes asymétriques de pantouffles, ...).

En effet, au niveau cellulaire, la rhéologie du sang dépend de la réponse des globules rouges aux contraintes hydrodynamiques, et en particulier, de leur déformation, leur orientation, et de leur interaction

avec les parois des vaisseaux sanguines. Ce sont autant de facteurs qui influencent la fluidité du sang et sa capacité à irriguer correctement les tissus de l'organisme. Notamment, à faible vitesse de cisaillement, les globules rouges ont tendance à s'empiler en rouleaux comme des piles d'assiettes. Cela conduit à une augmentation de la viscosité du sang. Au fur et à mesure que la vitesse de cisaillement augmente, ils se séparent, s'alignent et s'étirent dans le flux, la viscosité du sang ainsi diminue. Le comportement microscopique des globules rouges a donc un impact direct sur les propriétés macroscopiques du sang.

Le principal objectif de cette partie est de se focaliser sur quelques aspects du comportement des globules rouges. Afin de faciliter l'analyse de la dynamique des globules rouges, souvent les études sont concentrées sur un modèle simplifié, les vésicules dont la membrane possède des propriétés mécaniques voisines de celles des globules rouges.

En effet, pour une structure complexe telle qu'une membrane de globule rouge où il existe deux types d'élasticité, l'élasticité due au cisaillement et l'élasticité de la flexion, la forme globale d'un élément de la membrane résulte de l'équilibre entre les deux forces d'élasticités. La forme d'équilibre du globule rouge (la forme au repos) est donc déterminée par la mécanique de la membrane sous contraintes de surface et de volume fixés. Au repos, les éléments de la membrane peuvent être soumis à des contraintes, mais les forces agissant sur tous les éléments sont en équilibre. Pour cela, le modèle de Canham et Helfrich, qui correspond à une énergie de courbure, est utilisé pour obtenir une description mathématique de la forme du globule rouge.

Afin d'expliquer la curieuse forme biconcave des globules rouges, Canham (1970) a combiné des résultats théoriques et expérimentaux. Canham a montré que les sphéroïdes du même volume évoluent vers un disque biconcave en minimisant l'énergie de courbure de la membrane. En 1973, Helfrich et al ont suggéré la nécessité d'une courbure spontanée avec une valeur négative pour la stabilité de la forme biconcave. Evans et ses collaborateurs (1972) ont proposé un modèle paramétrique pour caractériser la géométrie du globule rouge basée sur la symétrie et la continuité de la surface en utilisant le traitement d'image.

En présence de fluide, les propriétés mécaniques de la membrane jouent un rôle important sur la dynamique et la déformation des vésicules et des globules rouges. Donc pour modéliser de manière appropriée les globules rouges, certaines caractéristiques clés doivent être spécifiées: la forme biconcave au repos, la viscoélasticité de la membrane du globule rouge, l'équation constitutive de l'élasticité de flexion et du rapport de viscosité entre le fluide interne et le fluide externe.

Un certain nombre d'efforts ont été faits pour comprendre la dynamique complexe et la déforma-

bilité des globules rouges. Keller et Skalak (1982) ont fait un premier pas vers la compréhension de la dynamique des particules déformables telles que les capsules et les vésicules en étudiant un modèle d'ellipsoïde sous l'écoulement de cisaillement. Ils ont pu prédire une transition entre un mouvement de bascule et un mouvement de chenille de char. En ajoutant l'élasticité de la membrane au modèle de Keller et Skalak, un nouveau mouvement a été observé à l'aide des modèles analytiques de Skotheim et Secomb (2007) et Abkarian, Faivre et Viallat, appelé le mouvement "swinging", dans lequel l'orientation de la cellule en régime de chenille de char oscille autour d'une valeur moyenne. Dupire et al. (2012) ont étendu les travaux précédents, en tenant compte de la mémoire de la forme. Ils ont montré que le globule rouge conserve sa forme biconcave lors du mouvement de chenille de char en supposant que cela peut être due à des propriétés élastiques anisotropes de la membrane ou de la forme non homogène du globule rouge.

La première partie de la thèse s'inscrit dans le domaine de la rhéologie du sang. Bien que l'étude en générale est limitée à la présence d'un seul globule rouge ou vésicule (isolé), plusieurs contributions ont été apportées, puisqu'il représente une première étape vers une description plus complexe du sang.

La première contribution de ce travail concerne l'optimisation de forme du globule rouge. Il s'agit d'un problème d'optimisation sous contraintes. Nous avons dérivé l'équation d'équilibre. Cette équation est également obtenu par Simeoni (2011). C'est une équation différentielle fortement non linéaire du second ordre. L'analyse mathématique et numérique ont permis d'identifier les différentes formes de globules rouges. En particulier, nous avons mis en évidence le rôle de certains paramètres physiques dans la classification de ces formes qui correspondent à des minimums locaux de l'énergie de Canham (1970) et Helfrich (1973).

La deuxième contribution de cette partie concerne le développement d'un modèle qui inclut la diffusion des molécules sur la surface de la membrane (diffusion latérale). Ce modèle montre que le couplage entre la membrane et les molécules entraîne des instabilités morphologiques de la membrane.

La troisième contribution porte sur l'analyse du mouvement de vésicule sous l'effet d'un écoulement de cisaillement linéaire et oscillatoire dans la limite de petite déformation. Nous avons obtenu des solutions explicites ce qui a permis d'identifier différents régimes.

## **Partie 1: Modélisation des membranes biologiques et des globules rouges**

Cette partie est constitué de quatre chapitres

### **Chapitre 1: Modélisation de la forme d'équilibre des globules rouges**

Dans ce chapitre, nous nous sommes intéressés à la description du modèle mathématique des globules rouges et des vésicules en donnant quelques propriétés physiques de la membrane. Nous avons rappelé essentiellement quelques outils mathématiques permettant de décrire la forme de la membrane.

En suite, nous nous sommes concentrés sur la modélisation de la forme biconcave des globules rouges dans le domaine axisymétrique 2D et 3D. Dans un premier temps, nous avons étudié le problème d'existence d'une solution particulière à la fonctionnelle de Helfrich qui correspond à une surface de la forme du globule rouge. Cette fonctionnelle est aussi une perturbation de la fonctionnelle de Willmore impliquant certains paramètres ayant des significations physiques. En utilisant la symétrie de la surface des globules rouges (la forme biconcave), le problème se transforme en une ODE. Nous avons obtenu une condition suffisante sur les paramètres physiques qui assurent l'existence de la solution (forme biconcave). Ensuite, nous nous sommes concentrés sur la modélisation numérique de la forme d'un globule rouge en 2D et 3D. Le but de ce travail est de fournir une méthode quantitative pour interpréter les observations expérimentales de la forme des globules rouges obtenue par Evans (1972). Dans ce travail, nous proposons un nouvel algorithme qui combine la méthode lagrangienne et les réseaux de neurones, appelé réseau neuronal de programmation de Lagrange (LPNN) de Zhang et al (1992), qui est une technique de calcul neuronal analogique pour résoudre des problèmes d'optimisation sous contraintes non linéaires.

### **Chapitre 2: Fluctuations et instabilité d'une membrane biologique induites par l'interaction avec des macromolécules en utilisant l'optimisation de forme géométrique**

Dans ce chapitre, nous développons un modèle qui inclut la diffusion des molécules sur la surface de la membrane, afin de décrire les changements morphologiques également appelés fluctuations de la membrane induites par la présence de la diffusion des protéines sur la surface de la membrane. Ces protéines ont la capacité de s'adsorber et de se désorber de la membrane. Tout d'abord, nous commençons par la description énergétique de la distribution des molécules sur la surface de la membrane, puis nous définissons la courbure spontanée de la membrane en fonction de la concentration des molécules. Une équation de diffusion de la concentration des molécules sur la surface est obtenue. Le modèle exploité dans ce chapitre montre que le couplage entre la membrane et les molécules est fort ce qui implique une instabilité morphologique de la membrane.

### **Chapitre 3: Comportement dynamique des vésicules sous un écoulement de cisaillement oscillatoire**

Dans ce chapitre, nous étudions la réponse des vésicules à un cisaillement oscillatoire, dans le régime de petites déformations. L'interaction entre le taux de cisaillement et la fréquence donne lieu à une dynamique plus riche que nous classifions. Premièrement, notre résultat a mis en évidence des comportements de mouvement dynamique oscillatoire mixte où les mouvements de "tumbling" (TB) et de "swinging" (SW) se produisent alternativement de manière périodique ou régulière. Ce type de mouvement a été rapporté pour les globules rouges dans [Phys. Rev. Lett. 104, 168101 (2010)]. Plus important encore, nous dérivons une expression explicite des valeurs critiques de l'amplitude du taux de cisaillement, pour un mode oscillatoire mixte, caractérisé par une suite de  $n$  TB périodiquement interrompue par un SW. Nous avons également pu déterminer des expressions exactes de la viscosité effective et de la tension.

L'intérêt de comprendre la dynamique et la déformation du globule rouge permettra de mieux comprendre les maladies du sang comme la drépanocytose, caractérisées par une malformation des globules rouges, qui adoptent une forme de sécheresse et perdent leurs propriétés d'élasticité, cela malheureusement conduit à une mauvaise orientation de l'oxygène dans l'organisme, qui à son tour conduit à des maladies cardiovasculaires. Un autre intérêt est de pouvoir fabriquer des globules rouges artificiels ou des micro nageurs qui pourraient également servir de transporteurs. Ainsi, ils pourraient transporter de l'hémoglobine, sur laquelle se lie l'oxygène, mais aussi des molécules anticancéreuses ou des biocapteurs qui détecte les toxines.

## **Partie 2: Existence de certains problèmes paraboliques non linéaires ayant des conditions de croissance et un exposant variables**

Un des défis actuels de la science est d'adapter les techniques d'ingénierie pour manipuler l'unité de base d'un organisme vivant. De nos jours, grâce à l'introduction de dispositifs manipulables par des champs extérieurs au cœur de la cellule, celle-ci peut subir des manipulations d'origine physique. Par exemple, les cellules deviennent magnétiques en incorporant des nanoparticules d'oxyde de fer, elle peuvent être donc guidées de manière télécommandée grâce à des champs magnétiques externes. Il devient ainsi possible de contrôler la migration des cellules ou encore de construire des tissus fonctionnels. En clair, les cellules peuvent être dirigées dans l'organisme vers un site cible.

L'utilisation de champs magnétiques ou électriques n'ont pas seulement servi à manipuler les cellules pour les orientés mais aussi pour modifier la viscosité apparente de certains fluides, appelés fluides

magnéto ou électro rhéologiques qui sont des fluides intelligents dont la viscosité apparente peut être rapidement modifiée par l'application d'un champ magnétique ou électrique externe. Grâce à cette caractéristique unique, les embrayages à fluides magnéto-rhéologiques peuvent moduler rapidement le couple entre deux surfaces sans contact mécanique direct.

Le domaine d'application de ces fluides est très prometteur car il présente plusieurs avantages. La réponse est rapide et le phénomène est totalement réversible. Plusieurs applications ont été proposées (embrayage automobile, amortisseur, contrôle actif des vibrations, milieux poreux). Růžička (2000) a modélisé le mouvement de fluides électrorhéologiques, par une équation aux dérivées partielles stationnaire et instable avec une condition de croissance non standard décrivant l'écoulement d'un fluide visqueux spécial sensible au cisaillement, caractérisé par sa capacité à modifier violemment ses propriétés mécaniques lors de l'application d'un champ électrique.

L'étude des équations différentielles et des équations et systèmes d'équations aux dérivées partielles impliquant des conditions de croissance variables a toujours été motivée par leurs diverses applications. Depuis la découverte de Bingham (1920) que certaines peintures ne coulent pas comme du miel. Il a commencé à étudier ce comportement et a décrit un phénomène étrange où, il a remarqué qu'il y a des fluides qui s'écoulent d'abord, puis s'arrêtent spontanément, plus tard appelés fluides de Bingham. A l'intérieur de ces fluides, les forces qui créent l'écoulement n'atteignent pas un seuil. Cela permet au fluide de se déformer comme un solide. Grâce à l'invention du "médium flamand" au XVIIe siècle, la peinture peut être transformée en huile thixotrope. Elle coule sous la pression du pinceau, mais se fige dès qu'on la laisse reposer. Si la composition exacte du médium flamand reste inconnue, on sait que les liens se forment progressivement entre ses composants. C'est pourquoi l'image se fige en quelques minutes. Avec ce merveilleux médium, Rubens a pu peindre la Kermesse en seulement 24h.

L'étude récente des problèmes non linéaires à exposants variables est motivée par la description de plusieurs phénomènes pertinents qui surviennent dans les sciences appliquées. Par exemple, ce mécanisme peut être utilisé pour donner des modèles pour des fluides non newtoniens qui changent de viscosité en présence d'un champ électromagnétique, qui dans ce cas influence la taille de l'exposant variable, Ruzicka (2000). Des modèles similaires apparaissent dans la segmentation d'image, Chen, Levine et Rao (2006). Leur cadre est une combinaison du lissage gaussien et de la régularisation basée sur la variation totale.

Dans cette partie de la thèse, nous nous intéressons à l'étude des problèmes non linéaires dont les résultats sont les suivantes

**Chapitre 4: Équation parabolique non linéaire ayant une condition de croissance non standard par rapport au gradient et à l'exposant variable**

Dans ce chapitre, nous considérons les équations paraboliques quasi-linéaires suivantes ayant une non-linéarité de croissance critique par rapport au gradient et à l'exposant variable

$$\begin{cases} \partial_t u - \operatorname{div}(A(t, x, \nabla u)) = f(t, x, u, \nabla u) & \text{in } Q_T := ]0, T[ \times \Omega \\ u(0, x) = u_0(x) & \text{in } \Omega \\ u(t, x) = 0 & \text{on } \Sigma_T := (0, T) \times \partial\Omega. \end{cases} \quad (0.1)$$

En utilisant le théorème du point fixe de Schaeffer et la méthode des sous et sur solutions, nous prouvons l'existence de solutions faibles.

**Chapitre 5: Existence globale pour une classe de systèmes paraboliques dégénérés avec des exposants variables et des non-linéarités de croissance critiques par rapport au gradient**

Dans ce travail, nous établissons deux résultats d'existence intéressants pour le système parabolique dégénéré avec exposants variables suivant

$$\begin{cases} \forall i = 1, \dots, m, \\ \partial_t u_i - \operatorname{div}(A_i(t, x, \nabla u_i)) = f_i(t, x, u_1, \dots, u_m, \nabla u_1, \dots, \nabla u_m) & \text{in } Q_T \\ u_i(0, x) = u_{i0}(x) & \text{in } \Omega \\ u_i(t, x) = 0 & \text{on } \Sigma_T. \end{cases} \quad (0.2)$$

Le premier résultat concerne le cas où les non-linéarités sont bornées. Dans ce cas, nous prouvons l'existence de solutions en utilisant le théorème du point fixe de Schauder dans les espaces appropriés. La seconde résultat concerne le cas où les non-linéarités ont une croissance critique par rapport au gradient, l'existence d'une solution faible est obtenue via l'existence d'une sur-solution faible.

**Partie 3: Les harmoniques sphériques: application au traitement d'image**

Des outils avancés de modélisation et de visualisation d'objets 2D et 3D augmentent le nombre de modèles disponibles sur le WEB spécialement dans les bases de données. Le traitement efficace des objets géométriques nécessite, comme dans différents domaines de l'informatique, la conception de structures

de données appropriées. Pour chaque problème spécifique dans le traitement d'image, nous pouvons identifier un ensemble d'opérations par lesquelles le calcul est requis et nous devons donc choisir une représentation appropriée qui supporte efficacement l'exécution de ces opérations.

Dans la littérature, de nombreux travaux ont contribué au développement de méthodes efficaces pour représenter et manipuler des objets 2D ou 3D. On peut distinguer différents types de représentations d'objets 3D, mais ces représentations ne sont pas toujours satisfaisantes dans certaines applications, comme la reconnaissance de formes. L'une des représentations proposées d'objets 2D et 3D se concentre sur la décomposition en harmoniques sphériques. Ils sont utilisés dans diverses applications telles que la reconstitution, la reconnaissance de formes, l'identification, etc. Les travaux présentés dans cette partie s'inscrivent dans ce cadre.

L'utilisation des harmoniques sphériques a fait l'objet de nombreuses études dans le domaine de l'informatique graphique. Elle a été utilisée dans diverses applications telles que l'illumination globale, le calcul de descripteurs de forme, la reconstruction de surface s'approchant d'un ensemble de points étoilés par rapport à un point, la représentation fréquentielle et le filtrage de surfaces 3D, etc.

Dans la troisième partie de cette thèse, nous proposons de calculer une représentation directe et efficace en harmoniques sphériques en se limitant à des objets sphériques, nous nous intéressons d'abord aux objets 2D représentés sur une sphère. De tels objets ont une paramétrisation sphérique naturelle. De plus, nous montrons comment les coefficients de développement en harmoniques sphériques peuvent être calculés directement sur la description d'un échantillonnage. Cela nous permet de vérifier, à priori, la précision de la représentation de l'objet. On a pu pousser plus loin cette méthode de calcul en montrant que les coefficients d'harmoniques sphériques peuvent générer un descripteur de forme. Cela nous permet d'ajouter plus de contrôle sur l'exactitude de l'identification. Enfin, nous illustrons l'efficacité de notre représentation en harmoniques sphériques qui donnent un descripteur de forme efficace et qui permet de reconnaître des formes géométriques et même de les visualiser.

## **Chapitre 6: Harmoniques sphériques**

Ce chapitre, sera consacré à l'étude détaillée des harmoniques sphériques. Nous rappelons tout d'abord quelques définitions mathématiques utilisées dans cette partie. Nous présenterons la base du système de coordonnées harmoniques sphériques. Nous montrerons ensuite comment les fonctions sphériques sont décomposées à partir des harmoniques sphériques. Cette décomposition est appelée la transformation en harmoniques sphériques.

**Chapitre 7: Décomposition, reconstruction et identification d'images à en utilisant les harmoniques sphériques**

Dans ce chapitre, nous avons apporté une contribution au domaine de la représentation d'objets 2D et 3D à l'aide d'harmoniques sphériques. Ces représentations ont été utilisées dans deux types d'applications dans le domaine du traitement d'image: a) la décomposition et à la reconstitution d'images, b) l'identification des empreintes digitales.

# Introduction and Overview

This work was conducted with an interdisciplinary concern and the idea of establishing strong interactions between applied mathematics and other scientific fields such as biology, physics and image processing. The work synthesized in this thesis has been grouped into three parts which are successively articulated around, modeling red blood cells and biological membranes, mathematical modeling applied to magnetorheological fluids and digital image recognition.

The first part is devoted to the analysis of the dynamics and deformation of red blood cells and biological membranes, such as vesicles, in particular, the study of red blood cell shape at static equilibrium, the effect of molecules on the phospholipid membrane and vesicle dynamics under the action of an oscillatory shear flow.

Blood is the vital fluid that circulates in our body. This fluid is responsible for transporting oxygen, various components and nutrients, as well as removing carbon dioxide from the organs. This fluid is not a simple liquid, but a suspension highly concentrated in cells, it is made up of three types of blood cells, white blood cells which provide immune defense, platelets which participate in coagulation and red blood cells, or erythrocytes, which carry respiratory gases between the lungs and deeper tissue of the body, Fig.1. For instance, 45% of our blood volume is composed of red blood cells. This composition gives the blood flow properties, called rheological properties, which are very complex.

Indeed, the individual orientation of the cells, their interaction with the vascular wall and their shape at any given moment are all factors that influence the fluidity of the blood and, ultimately, its ability to properly irrigate the body's tissues. At the cellular level, the rheology of the blood depends on the response of red blood cells to the action of hydrodynamic stresses and, in particular, on their deformation and orientation in the blood stream. For example, at low shear velocity, red blood cells tend to pile up in rolls like stacks of plates. This leads to an increase in the viscosity of the blood. As the shear velocity

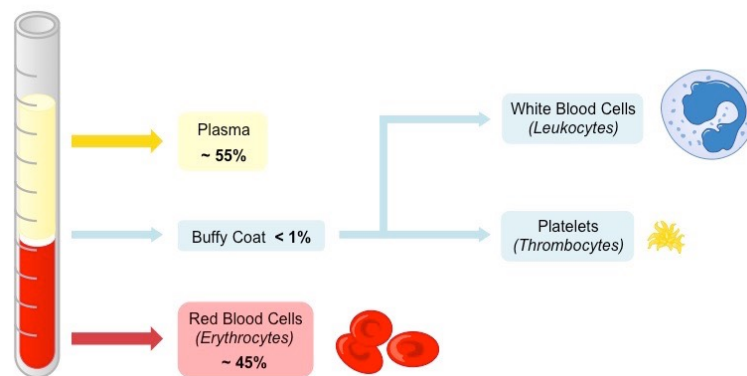


Figure 1: Human blood composition (source: <https://ib.bioninja.com.au/standard-level/topic-6-human-physiology/62-the-blood-system/blood-composition.html>).

increases, they separate from each other, align and stretch in the flow, the viscosity of the blood is lower. The microscopic behavior of red blood cells therefore has a direct impact on the macroscopic properties of the blood.

To best fulfill their function of transporting oxygen to deeper tissue of the body, red blood cells pass through very fine blood capillaries whose diameter is two times smaller than their own, to this end they must be very deformable. Observed under the microscope, a red blood cell reveals a very particular biconcave shape of  $7.5\mu\text{m}$  in diameter and  $2\mu\text{m}$  thickness (discocyte: disc where the central zone is thinner than the periphery fig. 2). Despite its laborious process construction and its extremely complex structure, the characteristic biconcave shape can only be explained by the properties of the RBC membrane.

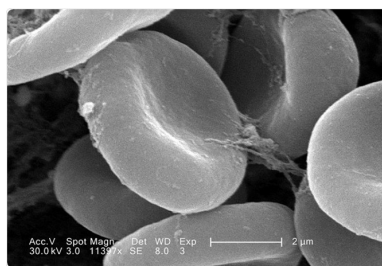


Figure 2: Red blood cells observed under the electron microscope. The biconcave shape is clearly visible. Link:<https://www.nisenet.org/catalog/scientific-image-human-red-blood-cells-sem>

Through its transport functions, the membrane that separates the outside of the cell from the inside plays a crucial role in cell metabolism. The membrane allows the absorption of nutrient substances, the excretion of wastes and maintain an internal ionic medium deeply distinct from the environment. These transport functions are of decisive importance for the survival of the cell.

The membrane is mainly composed of lipids, particularly phospholipids, between which proteins can be inserted. Phospholipids form a double layer (bilayer) which is relatively impermeable to the

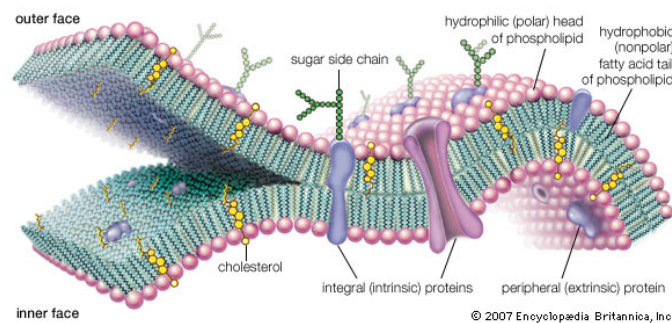


Figure 3: Molecular view of the cell membrane Link:<https://www.britannica.com/science/membrane-biology>

passage of most water soluble molecules. The double layer structure is directly due to the amphiphilic properties of phospholipids which have a hydrophilic end, that is to say water-loving, and a hydrophobic end, which on the contrary fears water. The quantities and types of proteins vary from cell to cell. These proteins are associated with the membrane in various ways and have many functions, such as transport of molecules across the membrane, reception of environmental signals, signaling in the cell, connection with the cytoskeleton and the most important is giving the membrane its elasticity.

Unlike bacteria and plant cell membranes, animal cell membranes contain cholesterol molecules, which rigidify them and increases their impermeability towards hydrophilic molecules.

Among mammals, the red blood cell is devoid of nucleus, which can reduce its deform-ability, since it is only filled with a solution of hemoglobin, the protein that associates with oxygen and carbon dioxide when transporting these gases. In this case red blood cells become a typical example of vesicles equipped with an additional internal structure playing the role of a skeleton inside the membrane fig. 4.

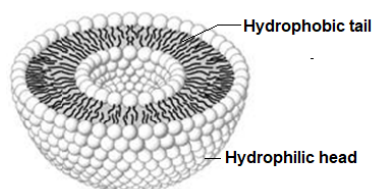


Figure 4: A cross-section of a vesicle formed by phospholipids.

At the local small deformations limit, the skeleton does not play any role which makes the red blood cell behaves like a vesicle. Otherwise, the skeleton acts as if a uniform bound on the curvature is imposed everywhere on the vesicle. Since the skeleton redistributes the excess of local stress on the whole surface

of the red blood cell.

For a complex structure such as an RBC membrane where there is two type of elasticity, the shear elasticity and the bending elasticity, the overall natural shape of an element of the membrane results from the balance between the bending and shear forces which means that the RBC equilibrium shape or rest shape is determined by the interplay between membrane area, enclosed volume, and membrane mechanics. At rest, membrane elements could be under stress, but the forces acting on all elements are in equilibrium. In order to explain the RBC curious biconcave shape, Canham [31] combined theoretical and experimental results, starting from the same volume spheroids will evolve into a biconcave disc by minimizing the bending energy of the membrane, while Helfrich et al.[72] suggested the necessity for a spontaneous curvature with negative value for the stability of the biconcave shape. Evans and co-workers [56] proposed a parametric mathematical model to characterize the RBC geometry based on symmetry and surface-continuity using image processing by minimizing of the difference between the model and the data image.

To appropriately model the RBC, some key features need to be specified, the biconcave rest shape of the cell, viscoelasticity of the RBC membrane, the natural state of each point on the RBC membrane, constitutive equation for bending elasticity and the viscosity ratio between the inner and outer fluids, which is the main purpose of this part.

A number of efforts have been made to understand the complex RBC dynamics and deformability. Keller and Skalak [77] made a first step toward the understanding of the dynamics of deformable particles such as capsules, vesicles, and cells by studying a model of an ellipsoid in shear, they were able to predict a transition between a tumbling motion to a tank-treading motion, as the viscosity of the inner fluid was decreased. By adding the contribution of the elasticity of the cell membrane to the Keller and Skalak model, a new motion has been revealed using analytical models by Skotheim and Secomb [1] and Abkarian, Faivre and Viallat, called the swinging motion, where the orientation of the cell in the tank-treading motion is seen to oscillate around a mean value. Dupire et al.[52] extended the previous works, taking into account the shape memory, they showed that the RBC maintains its biconcave shape even during tank-treading supposing that this effect may come from an inhomogeneous natural shape or anisotropic elastic properties.

The first part of the thesis fall within blood flow rheology problematic. Although we limit our study to the presence of a single red blood cell or vesicle, several contributions have been brought to this area of research, since it represents the first nucleus towards a more complex description of the blood.

The first contribution of this work concerns the geometric shape optimization which consists in finding the minimal surface that minimizes an energy functional dependent on the geometry under conditions for preserving constraints. We demonstrate an optimal result and we present a generalized condition of equilibrium of biological membranes for the mean curvature energy functional of Canham and Helfrich [31, 72].

The second contribution of this part is the development of a model that includes molecular diffusion in the surrounding environment, diffusion along the membrane (lateral diffusion) and the attachment and detachment to and from the membrane. This model shows that the coupling between the membrane and the molecules is strong and make the membrane suffer from morphological instabilities.

The third contribution is the analysis of a vesicle motion under the effect of a linear and oscillatory shear flow in the small deformation limit. The standard regimes of tank-treading, tumbling and vacillating breathing motion are found again.

## **Part 1: Modeling Biological Membranes and Red Blood Cells**

This part is organized as follows

### **Chapter 1: On the equilibrium shape of red blood cells**

In this chapter we are interested in the description of the mathematical model of red blood cells and vesicles by giving some physical properties of membranes. We essentially recall, some mathematical tools allowing to describe membranes, as a system that can have a large number of configurations.

Then we focus on the biconcave character of red blood cells modeling in 2D and 3D axisymmetric domain. At first, we study the existence problem of a special solution to the Helfrich functional which corresponds to a surface of the red blood cell shape. The Helfrich functional is also a perturbation of the Willmore functional involving some parameters with physical meanings. With the expected symmetry of the red blood cell surface, the problem reduces to an ODE analysis with certain shape requirements. We discover a sufficient condition on the parameters which ensures the existence of such special solution to the ODE. Then we focus on the shape identification and numerical modelisation of a single red blood cell in 3D axis-symmetric domain. The purpose of this work is to provide a quantitative method for interpreting experimental observations of the red blood cell shape under microscopy. In this work we give a new formulation based on classical theory of geometric shape determination which assumes that the curvature energy controls the shape of the red blood cell. To minimize this energy under con-

straints of volume and area, we propose a new algorithm which combines Lagrangian method and neural networks, called Lagrange programming neural network (LPNN) Ref.[136], which is an analog neural computational technique for solving nonlinear constrained optimization problems according to the Lagrange multiplier theory.

### **Chapter 2: Fluctuations and instability of a biological membrane induced by interaction with macromolecules using geometric shape optimization**

In this chapter, We develop a model that includes, besides hydrodynamics, molecular diffusion in the surrounding fluid, diffusion along the membrane and the kinetics of attachment and detachment to and from the membrane. In order to describe morphological changes also called fluctuations of bilayer membrane induced by the presence of a diffusion field of proteins in the crowded lipid environment which have the ability to adsorb on, and to desorb from, the membrane. First, we start with the energetic description of the distributions of molecules on the membrane surface, and define the spontaneous curvature of bilayer membrane as a function of the molecule concentrations on membrane surfaces. A diffusion equation governs the gradient flow of the surface molecule concentrations is obtained. The model exploited here for the case of a free membrane which is globally at equilibrium shows that the coupling between the membrane and the molecules is strong which make the membrane suffer from morphological instability.

### **Chapter 3: Dynamical behavior of vesicles in oscillatory shear flow**

In this chapter we investigate the responses of vesicle to a shear  $\dot{\gamma}_a$  and to oscillatory shear flow  $\dot{\gamma} = \dot{\gamma}_a \cos(2\pi f_r t)$  in the small deformation limit. The interplay between  $\dot{\gamma}_a$  and  $f_r$  gives rise to richer dynamics that we classify. At leading order, our result has evidenced mixed oscillating behaviors during which tumbling (TB) and swinging (SW) motions occur alternately, as has been reported for RBCs [Phys. Rev. Lett. 104, 168101 (2010)]. More importantly, we provide an explicit expression of critical values of the shear rate amplitude,  $\dot{\gamma}_a^n = (1 + 2n)\dot{\gamma}_a^0, n = 0, 1, 2, \dots$ , such that a mixed oscillating mode, characterized by a series of  $n$  TB periodically interrupted by a SW, is excited if  $\dot{\gamma}_a^n < \dot{\gamma}_a < \dot{\gamma}_a^{n+1}$ . We also report in detail on vesicle motion at  $\dot{\gamma}_a = \dot{\gamma}_a^n$ .

The interest of understanding the dynamics and deformation of the red blood cell will allow to better understand blood diseases such as sickle cell anemia or sickle cell disease, characterized by a malformation of the RBC, which adopt a shape of dryness and lose their elasticity properties and lead to a misdirection of oxygen in the body, another interest is to build artificial red blood cells or microswimmers that could also serve as transporters. Thus, they could transport hemoglobin, on which oxygen

binds, but also anticancer molecules or a biosensor that detects toxins.

## **Part 2: Existence of some nonlinear parabolic problems having a variable growth conditions and variable exponent**

One of the current challenges of science is to adapt engineering techniques to manipulate basic unit of a living organism. Nowadays, the cell can undergo manipulations of physical origin thanks to the introduction of manipulable devices by external fields at the heart of this latter. By incorporating oxide nanoparticles of iron, the cells become magnetic can be guided in a remotely controlled manner thanks to the of external magnetic fields. It becomes so possible to control cell migration or yet to build functional tissues. In clear, cells can be led in the organization to a target site.

The use of magnetic or electric fields have not only serve to manipulate the cells for reorientation but also to modify the apparent viscosity, called magneto-rheological fluids which are intelligent fluids whose apparent viscosity can be rapidly changed by the application of an external magnetic field. Using this unique feature, magneto-rheological fluids clutches can quickly modulate torque between two surfaces without direct mechanical contact.

The application field of this fluid is very promising because there are several advantages. The response is fast and the phenomenon is completely reversible. Several applications have been proposed(automotive clutch, shock absorber, active vibration control, porous media). Růžička [115, 116] modeled the movement of electrorheological fluids, special viscous fluids, characterized by their ability to violently change their mechanical properties on the application of an electric field by a stationary and unsteady partial differential equations with a condition of non-standard growth describing the flow of an electromological fluid sensitive to shear.

The second part of this thesis was motivated by these smart fluids a general model which takes into account various applications. In this part we study a family of equations and systems of partial differential equations is the presence of the operators of type- $p(x)$  Laplacian with non-standard growth conditions, this kind of problems are used to describe the flow of shear dependent magnetorheological or electrrheological fluids [115], to model porous medium [18] or even in the study of thin obstacle problems [29], and in image restoration [38].

The study of differential equations and variational problems involving variable growth conditions has always been motivated by their various applications. Since the discovery of Bingham, in 1920 when he

was surprised to discover that some paints do not run like honey. He became to study that behavior and described a strange phenomenon where, there are some fluids that first flow, then stop spontaneously, later called Bingham fluids. Inside these fluids, the forces that create the flows do not reach a threshold. As this threshold is not reached, the fluid flow deforms as a solid. Thanks to the "Flemish medium" invention in the 17th century, paint can be transformed into thixotropic oil, it flows under the pressure of the brush, but freezes as soon as it is left to rest. While the exact composition of the Flemish medium remains unknown, it is known that the links are gradually formed between its components, which is why the image freezes in a few minutes. With this wonderful medium, Rubens was able to paint La Kermesse in only 24 h. Recent studies of nonlinear problems with variable exponents are motivated by the description of several relevant phenomena arising in the applied sciences. This mechanism can be used to model non-Newtonian fluids which can influence the size of the variable exponent by changing their viscosity in the presence of an electromagnetic field as in Ref. [115]. Chen et al in Ref. [38] gives a similar model in image segmentation. In their model, they combine the Gaussian smoothing and regularization based on the total variation.

In this part of thesis, we are concerned with the study of a nonlinear problem whose features are the following:

**Chapter 4: Nonlinear parabolic equation having nonstandard growth condition with respect to the gradient and variable exponent**

In this chapter we consider the following quasilinear parabolic equations having critical growth non-linearity with respect to the gradient and variable exponent

$$\begin{cases} \partial_t u - \operatorname{div}(A(t, x, \nabla u)) = f(t, x, u, \nabla u) & \text{in } Q_T := ]0, T[ \times \Omega \\ u(0, x) = u_0(x) & \text{in } \Omega \\ u(t, x) = 0 & \text{on } \Sigma_T := (0, T) \times \partial\Omega. \end{cases} \quad (0.3)$$

Using Schaeffer's fixed point theorem and the sub- and super- solution method, we prove the existence results of weak solutions to the considered problem.

**Chapter 5: Global existence for a class of degenerate parabolic systems with variable exponents and critical growth nonlinearities with respect to the gradient**

In this work, we establish two interesting existence results for the following degenerate parabolic

system with variable exponents

$$\left\{ \begin{array}{l} \forall i = 1, \dots, m, \\ \partial_t u_i - \operatorname{div}(A_i(t, x, \nabla u_i)) = f_i(t, x, u_1, \dots, u_m, \nabla u_1, \dots, \nabla u_m) \text{ in } Q_T \\ u_i(0, x) = u_{i0}(x) \quad \text{in } \Omega \\ u_i(t, x) = 0 \quad \text{on } \Sigma_T. \end{array} \right. \quad (0.4)$$

The first result concerns the case where the non-linearities are bounded. In this case, we prove the existence of solutions using the Schauder fixed point theorem in appropriate spaces. The second relates to the case where the nonlinearities have a critical growth with respect to the gradient of the solution, the existence of a weak solution is obtained via the existence of a weak super-solution.

### **Part 3: Spherical Harmonics: Application to Image Processing**

Advanced tools in modeling, and visualization 2D and 3D objects increases the number of 2D or 3D models available on the WEB specially in databases. Efficient treatment of geometric objects requires, as in different areas of computer science, the conception of appropriate data structures. For each specific problem in the treatment, we can identify a set of operations by which the computation is required and therefore we need to choose an appropriate representation that efficiently supports the execution of these operations.

In the literature, many works has contributed to the development of efficient methods to represent and manipulate 2D or 3D objects. We can distinguish different types of representations of 3D objects, but these representations are not always satisfying in certain applications, such as shape recognition. One of the proposed representations of 2D and 3D objects focus on the decomposition into spherical harmonics. They are used in a variety of applications such as reconstruction, pattern recognition, identification, etc. The work presented in this part falls within this framework. the transform into spherical harmonics has been the subject of numerous studies in the field of computer science graphic.

It has been used in various applications such as global illumination, calculation of shape descriptors, surface reconstruction approximating a set of starred points with respect to a point, frequency representation and filtering of 3D surfaces, etc. In this manuscript, we propose to calculate a direct and efficient representation in spherical harmonics by limiting it to spherical objects, we are first interested in 2D

objects represented on a unit sphere. Such objects have a natural spherical parametrization. Moreover, we show how the coefficients of the expansion of this function in spherical harmonics can be calculated directly on the description of a sampling. This allows us to check, in advance, the precision of the representation of the object. We have then pushed this method of calculation further by showing that the coefficients of spherical harmonics can generate a shape descriptor. This allows us to add more control over the accuracy of the identification. Finally, we illustrate the efficiency of our representation in spherical harmonics which give an efficient shape descriptor and which allows to recognize geometric shapes and even visualized them.

In this part of the thesis we will study in details a very interesting geometric tool, the one introduced in the fifth chapter of the first part of this thesis which is the spherical harmonics and their applications in image processing.

### **Chapter 6: Spherical Harmonics**

This chapter, will be preserved to the itemized study of spherical harmonics. We first recall some mathematical definitions used in this project. We will present the basics of the coordinate system spherical as well as spherical harmonics. We will then show how the spherical functions are decomposed on the basis of the spherical harmonics, this decomposition is called the transform into spherical harmonics.

### **Chapter 7: Decomposition, reconstruction and identification of images using spherical harmonics**

In this chapter, we made a contribution to the field of 2D and 3D object representation using spherical harmonics. These representations have been used in two types of applications both in the field of image processing the first application is related to the decomposition and reconstruction of images and the other constitutes in fingerprints identification by building a strong shape descriptor using spherical harmonics.

# **Part 1: Modeling Biological Membranes and Red Blood Cells**

## On the equilibrium shape of red blood cells

The study of blood flow has always been at the center of interest of many mathematicians, physicists, biologists or industrialists. Indeed, the special interest of this large community science for blood behavior is widely due to a great wealth of dynamic behaviors. Scientists are using theoretical models to develop a higher understanding of biological systems. Computational simulations, and free energy functional uses mathematics to define abstract physical concepts into concrete mathematical expressions, and help us understand how components of the bio-molecular systems interact with one another. By solving these expressions, we may model overall many physical phenomena such as membrane dynamics, including cell movement and undulations in cell shape.

Most of these physical phenomena are governed by the geometry of their environment. The governing principle is usually modeled by some kind of energy minimization.

In this chapter, we are interested in the solutions to the red blood cell shape optimization problem, and in the determination of an accurate class of admissible shapes.

At rest, red blood cells take the shape of a disc with both sides slightly concave which is not the case when they have to slip into a fine capillary. They must then deform, and can look like a kind of parachute. Many questions then arise: how to explain such a shape? why not a simple sphere?. In this chapter we will explain that the particular shape of red blood cells, at rest, is the best solution to the minimization of the cell membrane curvature energy under constraints.

Whether at rest or deformed, the red blood cell is characterized by two physical quantities that are fixed. First, the quantity of the membrane that surrounds the cell, or more precisely its area  $A$ . Then, the volume  $V$  delimited by the cell membrane, since it is incompressible. To determine, among all the possible closed surfaces of area  $A$  and volume  $V$ , which one is selected by the red blood cell at rest, the

curvature energy of it's membrane must be minimized. This is the main objective of this chapter

## 1.1 Description of the mathematical model of red blood cells and vesicles

In this section, we will introduce the physical properties of the membrane. We will recall, essentially, some physical and mathematical tools allowing to describe membranes, as systems that can have a large number of configurations.

### 1.1.1 The biological structure of vesicles and Red blood cells

In cell biology, a phospholipid may be a certain type of lipid, and also a main ingredient constituting the membrane of any living cell. Its molecule structure consists of a hydrophilic head, on which are connected two hydrophobic tails.

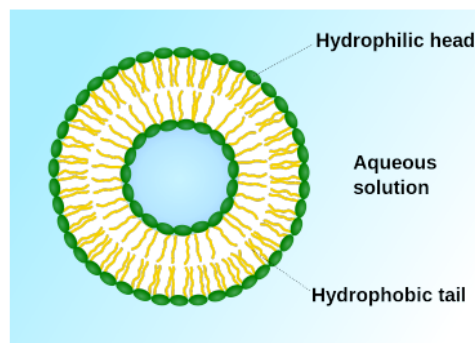


Figure 1.1: Scheme of a vesicle formed by phospholipids (source: article vesicle on Wikipedia).

Hence, when a sufficiently great amount of phospholipids is inserted in a very aqueous media, they immediately bring together in pairs to create bilayers also called vesicles, as illustrated in fig. 1.1.

Merely speaking, a vesicle may be a bag of viscous fluid itself contained in another viscous fluid. it corresponds to the essential membrane of all living cells. In fact, understanding it's behavior can be a primary fundamental step within the comprehension of general cells behavior.

Mammalian red blood cells are devoid of nucleus (fig. 1.2) and convey the oxygen and the carbon dioxide through the body via the blood. They are typical examples of vesicles, on which a network of proteins is fixed to play the role of a skeleton inside the membrane.

Observed with the electron microscope, the RBC reveals a very particular biconcave shape or discocyte (fig. 2). This shape gives it many properties, in particular a high elasticity enabling it to fulfill its function of transporting oxygen to the cells of the body, and gives it the possibility to sneak through

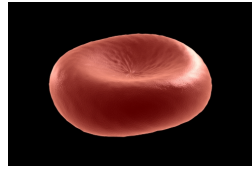


Figure 1.2: A 3-D human red blood cell model (source: <https://www.turbosquid.com/3d-models/3d-red-globule-blood/372582>).

capillaries of diameter up to two times smaller than its own diameter at rest.

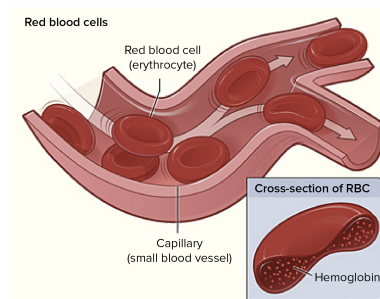


Figure 1.3: Red blood cell capillary and cross-section view. Link: <https://www.anatomynote.com/human-anatomy/cell-and-tissue/red-blood-cell-capillary-and-cross-section-view/>

The mathematical study of the particular shape of red blood cells is the subject of numerous research, with diverse motivations [72, 140]. Various models has been proposed to characterize this shape in order to better understand the properties of artificial vesicles or liposomes [120, 118], ideal objects are built in laboratories for the study of the physics or even in pharmacology as carriers of drugs within the blood circuit [88]. The analysis and the understanding of the red blood cell shape also lead to a better understanding of blood diseases such as sickle cell anemia or sickle cell disease, which is characterized by a malformation of the RBCs, which adopt a shape of dryness fig. 1.4, and lose their elasticity properties which can lead to a misdirection of oxygen in the body.

The problem of how a healthy RBC maintains the biconcave shape has been the object of many speculations ever since it was discovered that this ability is a property of the membrane itself. There are

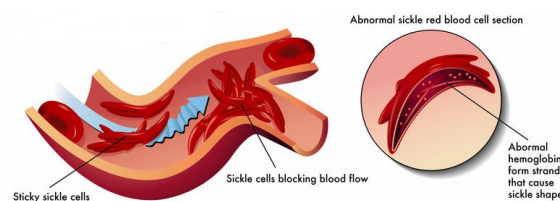


Figure 1.4: A normal red blood cell on the left and sickle cell disease on the right, very deformed erythrocyte and more rigid. Which causes the polymerization of the hemoglobin it contains in the absence of oxygen, then blocking blood flow

general agreements that the RBC shape is determined by the elasticity of curvature or bending [72] of the surrounding membrane but other studies have revealed that the shape of the RBC can be determined experimentally, using optical microscopy, and numerically, through microscopic, continuum model. E.Evans et al. [56] gives an improvement of resolution of optical microscopic dimensional determination of the RBC shape, where fifty to fifty-five cells for each tonicity were photographed and analyzed, in order to determine the geometry of the RBC, the principle was to use an interference microscope to capture the image of the RBC then analyzing the image according to the principles of holography.

In this study, we are mainly interested in some mathematical problems arising from the study of shapes associated with vesicles and red blood cells. For example, Figure 1.5 illustrates the effects of osmotic pressure on the human red blood cells shapes. From an optimization point of view, the red blood cell shape at rest minimizes a free bending energy under constraints, the surface of the bilayer and the volume of fluid it contains.

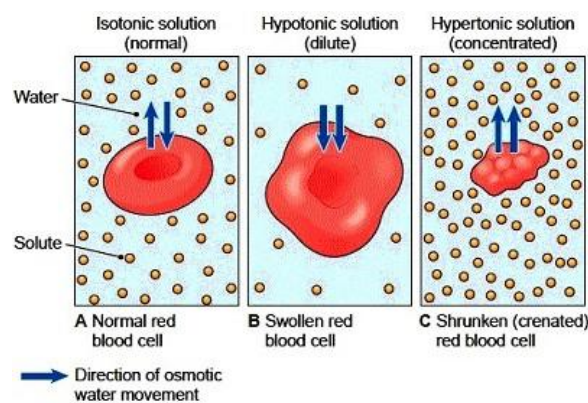


Figure 1.5: Effect of the osmotic pressure on red blood cells. Three different solutions are shown: hypertonic solution, where a red blood cell is causing water to move out of the cell which make it contract and appear spiky, isotonic solution, where the concentration of solutes outside the cell is equal to the concentration of solutes inside the cell which make the red blood cell show it's normal discocyte shape, and hypotonic solution, where the red blood cell is causing water to move into the cell which make it expand and become more round (source: <http://encyclopedia.lubopitko-bg.com/OsmosisAffectsCells.html>).

The study of artificial vesicles consists a starting point for modeling real biological membranes, especially their physical properties such as elasticity, shape transformations, transport and mutual interactions. The study of vesicle have succeeded mainly in: (i) explaining a large class of possible shapes of biological membranes, (ii) understanding the mechanism of exchange with the external environment, (iii) describing some types of unusual dynamical behavior of the membranes.

### 1.1.2 Construction of the physical model

In the 70s, Canham, Helfrich [31, 72] emphasized the important role of the curvature elasticity of membranes. The various configurations of red blood cells and their interactions with soft or rigid interfaces have become more and more obvious. The elastic properties of the membranes allowed to explain some cell properties, or certain aptitudes to perform movements

#### Elastic properties

A typical soft biomaterial like red blood cells shows a unique elastic properties characterizes there deform-ability when a force is applied. For RBCs the elastic properties are determined by the membrane structure. Although the deformation of RBC membrane is highly complex, since they characterizes its resistance to deformation. One type of elastic deformation, is the one perpendicular to the membrane plan, namely elasticity of curvature or bending mode which is determined by the energy needed to deform a membrane from its original curvature to some other curvature.

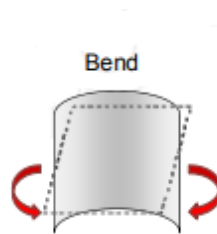


Figure 1.6: Schematic illustrations of bending mode of a 2-D membrane

In this framework, Helfrich and Canham proposed a simple model [72, 31], allowing to describe the bending model of bilayer membranes. In this model the energy of curvature plays a important role.

#### A minimal model

In this subsection, the two-dimensional model described in [32] is reproduced. To this end, we need first to understand the behavior of a vesicle once it is bent. Specifically, we try to model the effect of curvature on the elastic energy associated with the bilayer.

This tow-dimensional simplified model represent a small piece of a rectilinear membrane on the left in Fig. 1.7. The red and the yellow segments correspond to the space available respectively for the heads and the tails of the phospholipids. The same piece of the membrane is represented on the right, once bent.

In this first simplified approach, we consider the two-dimensional curvature generated in a plane

and neglect those generated in directions that are not in that plane. We only consider two dimensional

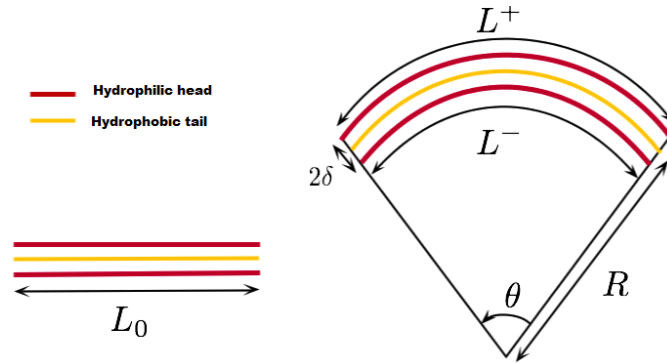


Figure 1.7: Representation of the membrane in 2D with the used notations.

space, all imposed deformations on the membrane are in the cutting plane. Initially, we consider that the membrane is not curved, which allows us to assimilate the phospholipid bilayer composed by three parallel segments of initial length  $L_0$ , separated by a distance  $\delta$  (fig. 1.7). Now we impose an elastic deformation to the membrane, which induces a curvature of this latter. Locally, the three curved layers can be seen as three arcs of concentric circles, of the same amplitude  $\theta$ . If we call  $L^+$ ,  $L$  and  $L^-$  the arcs length, the upper, the intermediate and the lower arc (respectively), then we have, due to the very low value of  $\theta$ :

$$L^+ = (R + \delta)\theta,$$

$$L = R\theta,$$

$$L^- = (R - \delta)\theta.$$

$R$  is the curvature radius of this portion of membrane. We can then model the mechanical energy of each layer by elastic energy of stiffness constant  $c$ . The elastic potential energy of the upper layer, slightly dilated, is  $E^+ = \frac{1}{2}c(L^+ - L_0)^2$ , where  $L_0$  is the length at rest of this portion membrane. Likewise, the elastic potential energy of the lower layer, slightly compressed is  $E^- = \frac{1}{2}k(L^- - L_0)^2$ . Finally, the biological considerations of section II allow us to conclude that the elongation of the intermediate layer is zero, and therefore its elastic potential energy too. Indeed, we know that the area of the membrane is preserved, so the mean elongation of the membrane must be zero, or  $L = L_0 = R\theta$ . If we consider the

total energy  $E$  of this piece of membrane we have:

$$\begin{aligned}
 E &= E^+ + E^-, \\
 &= \frac{c}{2L_0} ((L^+ - L_0)^2 + (L^- - L_0)^2), \\
 &= \frac{c}{2L_0} (((R + \delta)\theta - R\theta)^2 + ((R - \delta)\theta - R\theta)^2), \\
 &= \frac{2c}{L_0} (\delta\theta)^2, \\
 &= \frac{c\delta^2 L_0}{R^2}.
 \end{aligned}$$

By setting  $k = c\delta^2 L_0$  (quantity depending only on physical and geometric characteristics of the membrane) we obtain  $E = H^2$ , where  $H$  is the curvature of the membrane portion. To obtain the total energy of the membrane, it is necessary to integrate this expression on all the surface  $\Sigma$  (here it is actually a curve  $\Gamma$  since we are in a plane section).

$$E_{tot} = k \int_{\Gamma} H^2 dl. \quad (1.1)$$

The previous development can be generalized to a three-dimensional space  $\mathbb{R}^3$ . In this case, we replace the curvature  $H = \frac{1}{R}$  by the scalar mean curvature  $H = k_1 + k_2$ . In a geometrically point of view, the scalar mean curvature  $H(p)$  is obtained by summing the two principle curvatures associated with the green and red curves  $\Gamma$  called principal directions.  $k_1$  and  $k_2$  characterizes the local geometry of the surface  $S$ , they are formed by the intersection of the surface  $S$  with two orthogonal planes passing through the normal to the surface  $S$  at the point  $p$ .

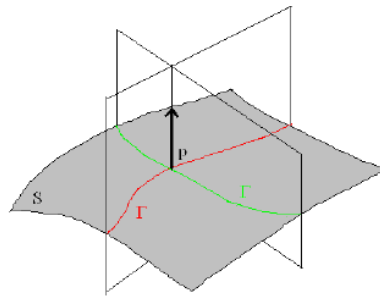


Figure 1.8: For a surface  $S \in \mathbb{R}^3$ , the scalar mean curvature  $H$  is given by the sum of  $k_1$  and  $k_2$  (principal curvatures defined by the curvatures of the green and red curves at the considered point  $p$ ).

The value of the scalar mean curvature in this case does not depend on the choice of the orthogonal planes. On the other hand, if we consider two planes having the highest and lowest curvature respectively, then they are orthogonal. Their associated curvatures denoted by  $k_1$  and  $k_2$  are called the principal

curvatures. From the above, their sum gives the mean curvature  $H = k_1 + k_2$  and their product  $K = k_1 k_2$  is referred to as the Gaussian curvature.

The energy expression is called Willmore energy

$$\mathcal{W}(\Sigma) = k \int_{\Sigma} H^2 ds, \quad (1.2)$$

where  $\Sigma$  is the surface membrane. In the following theorem Willmore proved that spheres are the only global minimizers of the Willmore energy (1.2)

**Theorem 1.1.1 (Willmore [134], Theorem 7.2 .2)**

*Let  $\Sigma$  be any compact  $C^2$ -surface of  $\mathbb{R}^3$ . Then, we have:*

$$\frac{1}{4} \int_{\Sigma} H^2 dA \geq 4\pi,$$

*where the equality holds if and only if  $\Sigma$  is a sphere.*

### A more elaborate model

The energy derived previously corresponds to Willmore energy, taking into account only the local curvature energy. It is possible to refine the expression of this energy, by introducing additional terms

#### Definition 1.1.1

The Willmore elaborate model seeks a closed surface  $\Sigma \subset \mathbb{R}^3$  that minimizes the functional

$$\mathcal{E}(\Sigma) = \frac{k}{2} \int_{\Sigma} (H - H_0)^2 ds - 2k_G \int_{\Sigma} K ds. \quad (1.3)$$

$H$  is the mean curvature,  $H_0$  is the spontaneous curvature,  $K$  is the Gaussian curvature,  $k > 0$  and  $k_G < 0$  are constants depending only on physical and geometrical characteristics of the membrane. When this energy is subject to constraints that the surface area of  $\Sigma$  or that the volume enclosed by  $\Sigma$  are prescribed, the model is referred to as the **Canham-Helfrich model**.

The spontaneous curvature  $H_0$  is introduced to take account of a possible asymmetry in the membrane (e.g. different chemical environments on both sides of the membrane). The integral over the Gaussian curvature is a topological invariant who take account the possible topological changes in the membrane and can be neglected if a minimizer is sought in a fixed topology class as shown in the following theorem.

**Theorem 1.1.2 (Gauss-Bonnet theorem)**

Let  $\Sigma$  be a 2-dimension compact riemannian manifold (without edges), then the integral of the Gaussian curvature  $K$  along  $\Sigma$  allows to find the Euler characteristic of the surface:

$$\begin{aligned} \int_{\Sigma} K ds &= 2\pi\chi(\Sigma) \\ &= 2 - 2g, \end{aligned}$$

where  $\chi(\Sigma)$  the Euler characteristic of  $\Sigma$  and  $g$  is the genus of the surface  $\Sigma$ .

The following proposition groups together several well known results for the existence of minimizer for (1.3) according to the spontaneous curvature [134, 13, 93].

**Proposition 1.1.1**

Let  $\Sigma \in \mathbb{R}^3$  be a compact surface of the class  $C^2$  such that  $k_G < 0 < k$ .

- Case where  $H_0 < 0$  : we have  $\mathcal{E}(\Sigma) > 4\pi(2k + k_G)$ , and  $\mathcal{E}(S_a) \xrightarrow{a \rightarrow 0^+} 4\pi(2k + k_G)$ , where  $S_a$  is a sequence of spheres with radius  $a > 0$ .
- Case where  $H_0 = 0$  : we have  $\mathcal{E}(\Sigma) \geq 4\pi(2k_B + k_G)$ , and the equality holds iff  $\Sigma$  is a sphere.
- Case where  $H_0 > 0$  : we have  $\mathcal{E}(\Sigma) \geq 4\pi k_G$ , and the equality holds iff  $\Sigma$  is the sphere  $S_{H_0}$  of radius  $\frac{1}{H_0}$ .

**Proof.**

Let  $\Sigma \in \mathbb{R}^3$  be a compact surface of the class  $C^2$  such that  $k_G < 0 < k$

- In the case where  $H_0 < 0$ , we have

$$\frac{1}{4} \int_{\Sigma} (H - H_0)^2 dA \geq \frac{1}{4} \int_{H \geq 0} (H - H_0)^2 dA > \frac{1}{4} \int_{H \geq 0} H^2 dA \geq \int_{H \geq 0} \max(0, K) dA \geq 4\pi,$$

where the last inequality is given by **Chern-Lashoff's Theorem** [94](Theorem 5.29) and by using Theorem (1.1.2) we get

$$2k \left( \frac{1}{4} \int_{\Sigma} (H - H_0)^2 dA \right) + k_G \int_{\Sigma} K dA > 8\pi k + 4\pi k_G [1 - g(\Sigma)] \geq 4\pi(2k + k_G).$$

By considering the sequence of spheres  $S_a$  with radius  $a > 0$ , we have

$$\frac{1}{4} \int_{S_a} (H - H_0)^2 dA = 4\pi \left( 1 - \frac{aH_0}{2} \right)^2 \xrightarrow{a \rightarrow 0^+} 4\pi^+.$$

As a conclusion, we have  $\inf_{\Sigma} \frac{1}{4} \int_{\Sigma} (H - H_0)^2 = 4\pi$  and the infimum is not a minimum. Finally, we have  $\mathcal{E}(S_a) = 8\pi k \left(1 - \frac{aH_0}{2}\right)^2 + 4\pi k_G$ , which converges to  $4\pi(2k + k_G)$  as  $a \rightarrow 0^+$ .

- In the case where  $H_0 = 0$ , By using Theorem 1.1.2 the energy becomes

$$\mathcal{E}(\Sigma) = \frac{k}{2} \int_{\Sigma} H^2 dA + 4\pi k_G = 2k\mathcal{W}(\Sigma) + 4\pi k_G.$$

$\mathcal{W}(\Sigma)$  is the Willmore energy. In this case we consider the original proof of Willmore Theorem 1.1.1 to obtain  $\mathcal{E}(\Sigma) \geq 4\pi(2k + k_G)$ . Furthermore, if the equality holds, then  $\int_{\Sigma} K dA = 4\pi = \frac{1}{4} \int_{\Sigma} H^2 dA$  and  $\frac{1}{4}H^2 = K$  on  $\Sigma$  i.e  $\Sigma$  is a sphere. Conversely, any sphere satisfies the equality case.

- In the case where  $H_0 > 0$ , with a constant scalar mean curvature  $H = H_0 > 0$ , such that  $\frac{1}{4} \int_{\Sigma} (H - H_0)^2 dA = 0$ . By combining the divergence theorem for surfaces ([93], Theorem 6.11) and the divergence theorem ([93], Theorem 5.31), we get

$$\begin{aligned} \int_{\Sigma} \frac{2}{H} dA &= \frac{2A(\Sigma)}{H_0} = \frac{1}{H_0} \int_{\Sigma} \operatorname{div}_{\partial\Omega}(\mathbf{x}) dA(\mathbf{x}) = \frac{1}{H_0} \int_{\Sigma} H(\mathbf{x}) \langle \mathbf{x} | \mathbf{n}(\mathbf{x}) \rangle dA(\mathbf{x}) \\ &= \int_{\Sigma} \langle \mathbf{x} | \mathbf{n}(\mathbf{x}) \rangle dA(\mathbf{x}) = \int_{\Omega} \operatorname{div}(\mathbf{x}) dV(\mathbf{x}) = 3V(\Omega). \end{aligned}$$

$\Omega$  is the inner domain enclosed by  $\Sigma$ . In the case where  $\Sigma$  is connected, we can apply the equality case in ([93], Theorem 6.16) (Heintze-Karcher's inequality) in order to get that  $\Sigma$  is the sphere  $S_{H_0}$  of radius  $\frac{2}{H_0}$ . Otherwise, by using the compactness argument,  $\Sigma$  has a finite number of connected components, each one being a copy of  $S_{H_0}$ , then from Theorem 1.1.1 and Theorem 1.1.2, we get  $\mathcal{E}(\Sigma) \geq 4\pi k_G$ . If the equality holds, we deduce that  $\int_{\Sigma} K dA = 4\pi$  and  $H = H_0$  on  $\Sigma$ , Hence, from Theorem 1.1.2,  $\Sigma$  has the topology of spheres. In particular,  $\Sigma$  is connected and the equality case of (Alexandrov [13]) ensures that  $\Sigma$  is the sphere  $S_{H_0}$  of radius  $\frac{1}{H_0}$ . To conclude, we conversely have  $\mathcal{E}(S_{H_0}) = 4\pi k_G$

The following table summarizes the existence results of Helfrich unconstrained problem

$$\inf_{\Sigma} \mathcal{H}(\Sigma) = \inf_{\Sigma} \frac{1}{4} \int_{\Sigma} (H - H_0) ds \tag{1.4}$$

$k_G < 0 < k$	$H_0 < 0$	$H_0 = 0$	$H_0 > 0$
Existence to (1.4)	no global minimizer	any sphere [134]	the sphere of radius $\frac{1}{H_0}$ [13]
$\inf_{\Sigma} \mathcal{H}(\Sigma)$	$4\pi$	$4\pi$	$0$
$\inf_{\Sigma} \mathcal{E}(\Sigma)$	$4\pi(2k + k_G)$	$4\pi(2k + k_G)$	$4\pi k_G$

### 1.1.3 A constrained optimization problem

In the previous section, we established the expression of Willmore energy (1.3) in the case of a more elaborate model taking into account a possible asymmetry in the membrane, where a spontaneous curvature is added (1.4). However, in the context of this study, we exclude any topological change of the red blood cells and by using Theorem 1.1.2, the energy of Helfrich, of a shape  $\Omega$  is as follows

$$\mathcal{H}(\Omega) = \frac{k}{2} \int_{\Sigma} (H - H_0)^2 ds. \quad (1.5)$$

The shape of the red blood cell  $\Omega^*$  is then a solution of the following optimization problem, or **Canham-Helfrich** problem

$$\Omega^* = \operatorname{argmin}_{\Omega \in \Lambda} \left\{ \frac{1}{2} \int_{\Sigma} (H - H_0)^2 ds \right\} \quad s.c. \quad \begin{cases} V = V_0, \\ A = A_0, \end{cases} \quad (1.6)$$

where  $\Lambda$  is the space of admissible shapes,  $V$  and  $A$  are the volume and the area of the red blood cell (respectively),  $V_0$  and  $A_0$  of the data of the problem. The constraint on the area is motivated by the biological study of the cell membrane conducted in Section I of this Chapter. The constraint on volume comes from the supposed incompressibility of the fluid contained in the globule red. We notice that we minimize the quantity  $\frac{1}{2} \int_{\Sigma} (H - H_0)^2 ds$  instead of  $\mathcal{H}$ , since  $k$  is a positive constant dependent only on physical and geometrical characteristics of the membrane.

An existence result for a class of axis-symmetric surfaces is given by the following theorem

**Theorem 1.1.3 ([41], Theorem 1.1)**

Let  $A_0, V_0 > 0$  be given such that

$$V_0 \leq \frac{A_0^{\frac{3}{2}}}{6\sqrt{\pi}}. \quad (1.7)$$

Assume that  $k > 0, k_G, H_0 \in \mathbb{R}$  such that  $\frac{k_G}{k} \in (-2, 0)$ . Let  $\mathcal{A}(A_0, V_0)$  denote the set of finite families  $S = (\Sigma_1, \dots, \Sigma_m)$ , for some  $m \in \mathbb{N}$  (not fixed), of axis-symmetric surfaces generated by disjoint curves and

satisfying the generalized area and volume constraints

$$\sum_{i=1}^m |\Sigma_i| = A_0, \quad \sum_{i=1}^m \text{Vol}(\Sigma_i) = V_0.$$

Let  $\mathcal{E}$  be the energy functional defined in (1.3) and let

$$\mathcal{F} : \mathcal{A}(A_0, V_0) \rightarrow \mathbb{R} \cup \{+\infty\}, \quad \mathcal{F}(S) := \sum_{i=1}^m \mathcal{E}(\Sigma_i).$$

Then the problem

$$\min \{ \mathcal{F}(S) : S \in \mathcal{A}(A_0, V_0) \}, \tag{1.8}$$

has a solution.

Condition (1.7) ensures that the constraints satisfy the isoperimetric inequality, so that the set  $\mathcal{A}(A_0, V_0)$  is not empty. When (1.7) becomes an equality instead of inequality, the only element in  $\mathcal{A}(A_0, V_0)$  is the sphere of area  $A$ , and if it becomes a strict inequality,  $\mathcal{A}(A_0, V_0)$  contains an infinite number of elements.

## 1.2 The biconcave character of red blood cells in 2D and 3D axis-symmetric domain

The study of human red blood cell shape properties is the most active field of research, theoretically, experimentally and numerically. Identifying the bio-physical parameters controlling such properties would be extremely important in the context of hematological diagnosis, specifically blood disorders.

In this section, particular attention has been paid to describe the particular shape of red blood cells. This latter can take many shapes in the blood but the most known are the biconcave shapes. Therefore, we are interested in this chapter in the geometric biconcave shape representing a plane of reflection in the two and three dimensional axis-symmetric domain.

### 1.2.1 Canham-Helfrich problem in two-dimensional axis-symmetric domain

We recall that in two-dimensional case, the surface " $\Sigma$ " is in fact a curve  $\Gamma$ , the volume  $V$  is the area of the domain  $\Omega$  delimited by  $\Gamma$ , "the area  $A$ " is the perimeter  $P$  of  $\Gamma$  and the surface element " $ds$ " is a length element  $dl$ .

### Mathematical formulation

In this case the problem (1.6) becomes

$$\Omega^* = \operatorname{argmin}_{\Omega \in \Lambda} \left\{ \frac{1}{2} \int_{\Gamma} (H - H_0)^2 dl \right\} \quad \text{under constraints} \quad \begin{cases} A = A_0, \\ P = P_0, \end{cases} \quad (1.9)$$

where the energy functional is defined by

$$\mathcal{H}(\Omega) = \frac{\kappa}{2} \int_{\Gamma} (H - H_0)^2 dl. \quad (1.10)$$

### Lagrange multiplier method

The constrained problem (1.9) can be transformed into a simple optimization problem using the Lagrange multiplier method. We introduce the Lagrangian of this problem as follows

$$\mathcal{L}(\Omega; \mu, p) = \frac{1}{2} \int_{\Gamma} (H - H_0)^2 dl + p(A - A_0) + \mu(P - P_0), \quad (1.11)$$

where  $\mu$  and  $p$  are Lagrange multipliers. Solving the constrained optimization problem (1.9) is equivalent to solve the following saddle point search problem

$$(\Omega^*; \mu^*, p^*) = \operatorname{argmin}_{\Omega \in \Lambda} \sup_{p, \mu \in \mathbb{R}} \{ \mathcal{L}(\Omega; \mu, p) \}. \quad (1.12)$$

In fact, the constrained optimization problem (1.9) is equivalent to the saddle point search problem (1.12). Since a shape  $\Omega \in \Lambda$  will never be a solution of the saddle point search problem (1.12) if  $\Omega$  do not verifies the conditions  $A = A_0$  and  $P = P_0$  because  $\sup_{p, \mu \in \mathbb{R}} \{ \mathcal{L}(\Omega; \mu, p) \} = \infty$ . Therefore, this shape will obviously not minimizes the value of the Lagrangian (1.11) for any shape  $\Omega \in \Lambda$ .

In order to study the dependence factors of the shape  $\Omega^*$  solution of the problem (1.12), we introduce the reduced volume.

### Reduced Volume

An interesting remark is that the Lagrangian (1.11) has a similarity property. To show this we consider

the case where  $H_0 = 0$  and we dimensionless the intervening quantities in (1.11)

Let  $R_0 = \frac{P_0}{2\pi}$  be the characteristic radius of a disc having the same Perimeter  $P_0$  as the shape  $\Omega^*$ . We denote by a "tilde" the dimensionless terms.

The expression of the Lagrangian (1.11) as a function of dimensionless variables is the following

$$\begin{aligned}\mathcal{L}(\Omega; \tilde{\mu}, \tilde{p}) &= \frac{1}{2} \int_{\tilde{\Gamma}} \frac{1}{R_0} \tilde{H}^2 \tilde{d}l + \tilde{p} R_0^2 (\tilde{A} - \tilde{A}_0) + \tilde{\mu} R_0 (\tilde{P} - \tilde{P}_0) \\ &= \frac{1}{R_0} \left( \frac{1}{2} \int_{\tilde{\Gamma}} \tilde{H}^2 \tilde{d}l + \tilde{p} R_0^3 (\tilde{A} - \tilde{A}_0) + \tilde{\mu} R_0^2 (\tilde{P} - \tilde{P}_0) \right),\end{aligned}$$

where,

$$\tilde{P} = \frac{P}{R_0}, \quad \tilde{A} = \frac{A}{R_0^2}, \quad \tilde{H} = R_0 H, \quad \tilde{d}l = \frac{dl}{R_0}, \quad \tilde{p} = R_0^3 p, \quad \text{and} \quad \tilde{\mu} = R_0^2 \mu.$$

In addition, we have

$$\tilde{P}_0 = \frac{P_0}{R_0} = 2\pi, \quad \tilde{A}_0 = \frac{A_0}{R_0^2} = \frac{4\pi^2 A_0}{P_0^2} = \pi v,$$

where  $v = \frac{4\pi A_0}{P_0^2}$  is the reduced volume, this parameter measures the degree of filling of the red blood cell, it is defined as the ratio between the area of  $\Omega^*$  and area of a disc which has the same perimeter as  $\Omega^*$ .

We finally get

$$\begin{aligned}\mathcal{L}(\Omega; \mu, p) &= \frac{1}{R_0} \left( \frac{1}{2} \int_{\tilde{\Gamma}} \tilde{H}^2 \tilde{d}l + \tilde{p} (\tilde{A} - \pi v) + \tilde{\mu} (\tilde{P} - 2\pi) \right) \\ &= \frac{1}{R_0} \tilde{\mathcal{L}}(\tilde{\Omega}; \tilde{\mu}, \tilde{p}).\end{aligned}$$

This show in particular that minimizing the Lagrangian  $\mathcal{L}$  is equivalent to minimize the dimensionless Lagrangian  $\tilde{\mathcal{L}}$ , given by

$$\tilde{\mathcal{L}}(\tilde{\Omega}; \tilde{\mu}, \tilde{p}) = \frac{1}{2} \int_{\tilde{\Gamma}} \tilde{H}^2 \tilde{d}l + \tilde{p} (\tilde{A} - \pi v) + \tilde{\mu} (\tilde{P} - 2\pi).$$

This similarity property shows that the red blood cell shape does not depend on the dimension of this latter, which means that we can substitute the two parameters  $A_0$  and  $P_0$  by the (unique) reduced volume  $v$ .

In summary, the shape  $\Omega^*$  does not depend on the problem dimension, since it minimizes both  $\mathcal{L}$  and  $\tilde{\mathcal{L}}$ . In addition, the dimensionless Lagrange multipliers  $\tilde{\mu}, \tilde{p}$  depend only on the reduced volume  $v$ . Indeed, they are mathematical parameters, introduced and chosen to verify conditions  $\tilde{P} = 2\pi$  and  $\tilde{A} = \pi v$ . To this end, we replace the dimensioned parameters  $A_0$  and  $P_0$  by a single dimensionless parameter  $v$ . In the three-dimensional case, the reduced volume is defined by  $v = \frac{3\pi^{\frac{1}{2}} V}{4A_0^{\frac{3}{2}}}$  this parameter

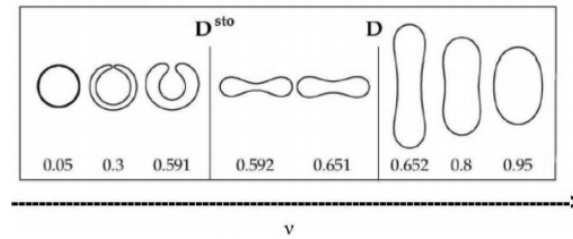


Figure 1.9: Different vesicle shape depending on the reduced volume at equilibrium in the absence of flow in the three-dimensional case[121]

can vary from 0 (the red blood cell is totally deflated) to 1 (sphere). Figure 1.9 shows the different shapes of vesicle at equilibrium as a function of  $v$ . In this figure, we observe three different families of shapes, for a reduced volume equal to 0.65, the vesicle has a biconcave shape, the similar shape observed for red blood cells.

### 1.2.2 The problem formulation in the two-dimensional axis-symmetric case

We assume that the red blood cell has an invariance by rotation around an axis. In this case, the surface of the red blood cell can be generated by a flat curve rotating around this axis. Then, we are in the presence of a so called axis-symmetric problem. To introduce the study of the three-dimensional axis-symmetric

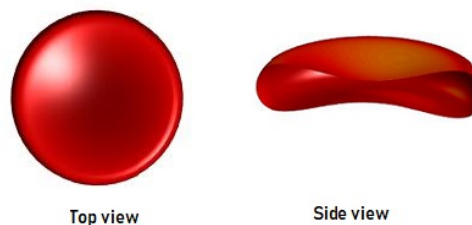


Figure 1.10: A surface view and a cut view of a red blood cell (from Matlab simulations).

case in the next section, we carried out a two-dimensional study by considering only one section of the red blood cell. We call  $\Gamma$  the curve obtained by making the intersection between a cutting plane containing the axis of rotation and the surface of the red blood cell (fig. 1.10). We assume that  $\Gamma$  has two axes of symmetry (which can be justified by the isotropy of physical constraints exercising on the red blood cell). We provide our cutting plan with a coordinate system  $(Oxy)$ , where the  $x$ -axis and the  $y$ -axis coincide with the two axes of symmetry (fig. 1.11). We limit our study to the top right half part of the curve  $\Gamma$ , called  $\Gamma_+$ , we can then, reconstruct the curve  $\Gamma$  from  $\Gamma_+$  by symmetry with respect to the  $x$  and  $y$  axes (fig. 1.11). In the top right half part,  $\Gamma_+$  can be seen as the graph of a function  $h$  and therefore admits the

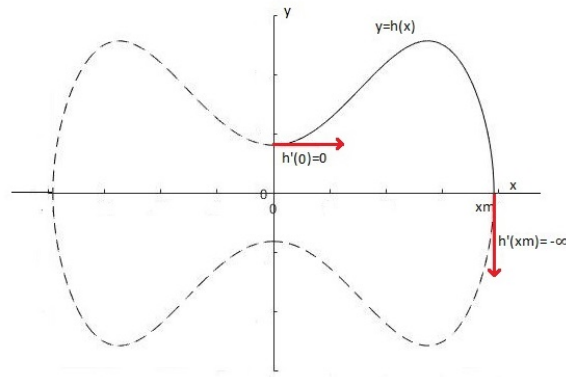


Figure 1.11: The curve defined by the function  $h \in \Phi$ . Where,  $h'(0) = 0$ ,  $h'(x_m) = -\infty$  are imposed conditions to ensure the symmetry. The curve  $\Gamma_+$  is the continuous part of the curve, the rest of the curve (dashed) is constructed by symmetry

following parametrization

$$\Gamma_+ = \{(x, y) \in \mathbb{R}^2 : y = h(x)\}.$$

Due to the perimeter and area constraints, the curve  $\Gamma_+$  is bounded on the x-axis, and we call  $x_m$  the maximum value reached, or the maximum elongation of  $\Gamma_+$ . To ensure the biconcave character of the red blood cell, we must also impose the following assumptions on the thickness  $h$

1.  $h(x) \geq 0$  for  $x \in [0, x_m]$ ,
2.  $h(x_m) = 0$ ,
3.  $h'(0) = 0$ ,  $h''(0) > 0$ ,
4.  $h'(x) \rightarrow -\infty$  when  $x \rightarrow x_m$ ,
5. there exist  $x_M \leq x_m$  such that  $h''(x) \geq 0$  for  $x \in ]0, x_M[$ , and  $h''(x) \leq 0$  for  $x \in ]x_M, x_m[$ .

In fact, a curve  $\Gamma$  that have the shape of a regular red blood cell is usually describe as a closed curve which is

1. symmetric with respect to x and y axis,
2. the "upper" half part  $\Gamma_+$  of the curve  $\Gamma$  satisfies the following conditions
  - (a) it intersects the tow axis of symmetry,
  - (b) it is a graph over its projection on the x-axis,

- (c) it is concave up near the y-axis,
- (d) it has a unique point of maximum and a unique point of inflection.

Finally, since the red blood cell is a physical system, we know that  $\Gamma$  cannot be too irregular, so we choose to take  $h \in \mathcal{C}^2(0, x_m)$ . Now we are able to describe all the admissible functions that parametrizes  $\Gamma_+$

$$\Phi_m = \{h \in \mathcal{C}^2(0, x_m) : h \text{ satisfies conditions 1 - 5}\}. \quad (1.13)$$

The framework of the problem thus defined, we can solve the Canham-Helfrich problem in the two-dimensional axis-symmetric case defined by (1.9).

We have seen that this problem under constraints can be transformed into a simple optimization problem using the Lagrange multiplier method, where the Lagrangian is defined by (1.11).

The problem is then to find the critical points  $(\Omega^*; \mu^*, p^*)$  of the Lagrangian  $\mathcal{L}$  that verifies

$$(\Omega^*; \mu^*, p^*) = \underset{\Omega \in \Lambda}{\operatorname{argmin}} \max_{p, \mu \in \mathbb{R}} \{\mathcal{L}(\Omega; \mu, p)\}. \quad (1.14)$$

The set  $\Lambda$  on which we minimize the energy of Canham-Helfrich is the set of  $\Omega$  shapes of curve  $\Gamma$  that can be obtained by successive symmetries from the curve  $\Gamma_+$ , parametrized by the function  $h \in \Phi$ .

Before tackling the problem (1.14), we must first express the Lagrangian involved quantities in two-dimensional axis-symmetric case, namely the area, the perimeter and the curvature.

**Lemma 1.2.1**

*The area, the perimeter and the curvature of the curve  $\Gamma$  are defined as follows*

$$\begin{aligned} A &= 4 \int_0^{x_m} h(x) dx, \\ P &= 4 \int_0^{x_m} (1 + h'^2(x))^{\frac{1}{2}} dx, \\ H &= \frac{h''(x)}{(1 + h'(x)^2)^{\frac{3}{2}}}. \end{aligned}$$

**Proof.**

In two-dimensional case, we have

$$dl = \sqrt{1 + h'^2(x)} dx.$$

Then the area  $A$  and the perimeter  $P$  are given by

$$\begin{aligned} A &= 4 \int_0^{x_m} h(x) dx, \\ P &= 4 \int_0^{x_m} dl, \\ &= 4 \int_0^{x_m} (1 + h'^2(x))^{\frac{1}{2}} dx. \end{aligned}$$

The expression of the curvature  $H$  of the curve  $\Gamma_+ = \{(x, y) \in \mathbb{R}^2 : \phi(x, y) = h(x) - y = 0\}$ , with a normal vector  $n$ , is the following

$$\begin{aligned} H &= \operatorname{div}(n) \\ &= \operatorname{div} \left( \frac{\nabla \phi(x, y)}{\|\nabla \phi(x, y)\|} \right) \\ &= \operatorname{div} \left( \begin{array}{c} \frac{h'(x)}{\sqrt{1+h'(x)^2}} \\ \frac{-1}{\sqrt{1+h'(x)^2}} \end{array} \right) \\ &= \frac{h''(x)\sqrt{1+h'(x)^2} - h'(x)^2 h''(x) (1+h'(x)^2)^{-1/2}}{1+h'(x)^2} \\ &= \frac{h''(x)}{(1+h'(x)^2)^{\frac{3}{2}}}. \end{aligned}$$

The Lagrangian (1.11), becomes

$$\mathcal{L}(x_m, h; \mu, p) = 2 \int_0^{x_m} \left[ \left( \frac{h''(x)}{(1+h'(x)^2)^{\frac{3}{2}}} - H_0 \right)^2 + 2\mu \right] (1+h'^2(x))^{\frac{1}{2}} dx - \mu P_0 + 4p \int_0^{x_m} h(x) dx - pA_0. \quad (1.15)$$

### 1.2.3 Variable change

Let  $\kappa(x) = \frac{h'(x)}{(1+h'^2(x))^{\frac{1}{2}}} = n_x(x)$ , be the principle curvature in the meridional direction, where  $n$  is the normalized gradient of the function  $h$  in the  $x$  direction. It is natural, and important, to look at the behavior of  $\kappa(x)$  instead of  $h(x)$ , where  $\kappa$  satisfy the following conditions

$$[C_1] \quad |\kappa| < 1,$$

$$[C_2] \quad \kappa \text{ is concave,}$$

$$[C_3] \quad \text{there exist a unique critical point } x_c, \text{ such that } \kappa'(x_c) = 0 \quad \text{and} \quad \kappa(x_c) > 0.$$

Using Lemma 1.2.1, the area, the perimeter and the curvature are given as a unction of  $\kappa$  by the

following expressions

$$\begin{aligned} A &= 4 \int_0^{x_m} h(x) dx \\ &= 4[xh(x)]_0^{x_m} - 4 \int_0^{x_m} xh'(x) dx \\ &= -4 \int_0^{x_m} \frac{x\kappa(x)}{(1-\kappa^2(x))^{\frac{1}{2}}} dx. \end{aligned}$$

Since  $h \in \Phi_m$ , we have  $h(x_m) = 0$  then  $[xh(x)]_0^{x_m} = 0$ ,

$$\begin{aligned} P &= 4 \int_0^{x_m} (1+h'(x)^2)^{\frac{1}{2}} dx \\ &= 4 \int_0^{x_m} \frac{1}{1-\kappa^2(x)} dx. \end{aligned}$$

Finally the main curvature  $H = \kappa'(x)$ .

By a straightforward computation in the case where  $H_0 = 0$ , one easily sees that the Lagrangian (1.15) becomes

$$\mathcal{L}(x_m, \kappa, \mu, p) = 2 \int_0^{x_m} \frac{\kappa'(x)^2 + 2\mu - 2px\kappa(x)}{\sqrt{1-\kappa(x)^2}} dx - pA_0 - \mu P_0. \quad (1.16)$$

The set describing all the admissible functions (1.13) becomes

$$\Psi_m = \{\kappa \in \mathcal{C}^1(0, x_m) : \kappa \text{ satisfies } [C_1] - [C_3]\}.$$

Looking for the saddle point of this Lagrangian, is equivalent to find the critical points  $(x_m, \kappa, \mu, p) \in \mathbb{R}^+ \times \Psi_m \times \mathbb{R} \times \mathbb{R}$  of the latter.

**Proposition 1.2.1 (Optimality conditions)**

At the critical points  $(x_m, \kappa, \mu, p) \in \mathbb{R} \times \Phi' \times \mathbb{R} \times \mathbb{R}$ , we have

$$\left\{ \begin{array}{l} \left[ \frac{d\mathcal{L}}{d\kappa}(\psi) \right] (x_m, \kappa; \mu, p) = 0 \quad \forall \psi \in \Psi_m, \\ \frac{\partial \mathcal{L}}{\partial x_m}(x_m, \kappa; \mu, p) = 0, \\ \frac{\partial \mathcal{L}}{\partial \mu}(x_m, \kappa; \mu, p) = 0, \\ \frac{\partial \mathcal{L}}{\partial p}(x_m, \kappa; \mu, p) = 0, \end{array} \right. \quad (1.17)$$

where  $\frac{d\mathcal{L}}{d\kappa}(\psi)$  is the directional derivative of  $\mathcal{L}$  with respect to  $\kappa$  in the direction  $\psi$

**Theorem 1.2.1 (Euler-Lagrange equation)**

The Euler-Lagrange equation for the problem (1.12) is given by

$$-2\kappa''(1-\kappa^2) - \kappa\kappa'^2 - 2px + (H_0^2 + 2\mu)\kappa = 0. \quad (1.18)$$

**Proof.**

In order to give the expression of the Euler-Lagrange equation for the problem (1.12), we have to compute the first optimality condition  $\left[\frac{d\mathcal{L}}{d\kappa}(\Psi)\right](x_m, \kappa; \mu, p) = 0$  for  $\Psi : \Phi' \rightarrow \mathbb{R}$ .

From the definition of  $\kappa$ , we have

$$\kappa'(x) = \frac{h''(x)}{(1+h^2(x))^{3/2}} = H(x),$$

where  $H(x)$  is the curvature of the curve  $\Gamma$  at  $x$  and

$$\kappa''(x) = \frac{h^{(3)}(x)}{(1+h^2(x))^{\frac{3}{2}}} - \frac{3h''^2(x)}{(1+h^2(x))^{\frac{5}{2}}}.$$

Then,

$$\begin{aligned} \left[\frac{k'^2 + 2\mu}{\sqrt{1-\kappa^2}}\right]'_{\Psi}(\kappa) &= \frac{2\kappa'\Psi'(1-\kappa^2) + (\kappa^2 + H_0^2 + 2\mu)k\Psi}{(1-\kappa^2)^{\frac{1}{2}}}, \\ \left[\frac{2xp\kappa}{\sqrt{1-\kappa^2}}\right]'_{\Psi}(\kappa) &= \frac{2px\Psi(1-\kappa^2) + 2px\kappa^2\Psi}{(1-\kappa^2)^{\frac{3}{2}}} = \frac{2px\Psi}{(1-\kappa^2)^{\frac{3}{2}}}. \end{aligned}$$

Then, we obtain

$$\begin{aligned} \left[\frac{d\mathcal{L}}{d\kappa}\right]_{\Psi}(x_m, \kappa, \mu, p) &= 2 \int_0^{x_m} \frac{2\kappa'\Psi'(1-\kappa^2) + (\kappa^2 + H_0^2 + 2\mu)k\Psi}{(1-\kappa^2)^{\frac{3}{2}}} dx - 2 \int_0^{x_m} \frac{2px\Psi}{(1-\kappa^2)^{\frac{3}{2}}} dx \\ &= 2 \int_0^{x_m} \frac{2\Psi\kappa'(1-\kappa^2) + \Psi(-2px + \kappa\kappa'^2 + (H_0^2 + 2\mu)\kappa)}{(1-\kappa^2)^{\frac{3}{2}}} dx \\ &= 4 \int_0^{x_m} \frac{\Psi\kappa'}{\sqrt{1-\kappa^2}} dx + 2 \int_0^{x_m} \frac{(-2px + \kappa\kappa'^2 + (H_0^2 + 2\mu)\kappa)\Psi}{(1-\kappa^2)^{\frac{3}{2}}} dx. \end{aligned}$$

Let  $T_1 = 4 \int_0^{x_m} \frac{\Psi\kappa'}{\sqrt{1-\kappa^2}} dx$  and  $T_2 = 2 \int_0^{x_m} \frac{(-2px + \kappa\kappa'^2 + (H_0^2 + 2\mu)\kappa)\Psi}{(1-\kappa^2)^{\frac{3}{2}}} dx$ , and by integrating  $T_1$  by part we obtain

$$T_1 = 4 \left( \left[ \frac{\kappa'}{\sqrt{1-\kappa^2}} \Psi \right]_0^{x_m} - \int_0^{x_m} \frac{\kappa''(1-\kappa^2) + \kappa'^2\kappa}{(1-\kappa^2)^{\frac{3}{2}}} \Psi dx \right).$$

Since  $\kappa$  and  $\psi$  are in  $\Psi_m$ , we set  $\psi(0) = \kappa(0) = 0$  and  $\psi(x_m) = \kappa(x_m) = -1$  ( $\psi$  is compact support).

We have

$$\left[ \frac{\kappa'(x)}{\sqrt{1-\kappa^2(x)}} \psi(x) \right]_0^{x_m} = \frac{\kappa'(x_m)}{\sqrt{1-\kappa^2(x_m)}} \psi(x_m) = 0.$$

Since

$$\frac{\kappa'(x_m)}{\sqrt{1-\kappa^2(x_m)}} = \frac{h''(x_m)}{1+h'^2(x_m)} \simeq \frac{C}{M} = 0,$$

where,  $C$  is a constant and  $M$  is a constant as large as we want, since  $h'(x_m) = -\infty$ .

Finally, we get

$$\begin{aligned} [\mathcal{L}]'_\psi &= T_1 + T_2 \\ &= 2 \int_0^{x_m} \psi \frac{-2\kappa''(1-\kappa^2) - \kappa\kappa'^2 - 2px + (H_0^2 + 2\mu)\kappa}{(1-\kappa^2)^{\frac{3}{2}}} dx. \end{aligned}$$

The first optimality condition from (1.17) is

$$\left[ \frac{d\mathcal{L}}{d\kappa}(\psi) \right] (x_m, \kappa; \mu, p) = \int_0^{x_m} \psi \frac{-2\kappa''(1-\kappa^2) - \kappa\kappa'^2 - 2px + (H_0^2 + 2\mu)\kappa}{(1-\kappa^2)^{\frac{3}{2}}} dx = 0, \quad \forall \psi \in \Psi_m.$$

This equality is verified for any  $\psi \in \Psi_m$ . The function  $\kappa \in \Psi_m$  that minimizes the Lagrangian  $\mathcal{L}$  verifies the following ordinary differential equation, called Euler-Lagrange equation

$$-2\kappa''(1-\kappa^2) - \kappa\kappa'^2 - 2px + (H_0^2 + 2\mu)\kappa = 0. \quad (1.19)$$

In addition, we have the following initial conditions

$$\kappa(0) = \frac{h'(0)}{(1+h'^2(0))^{\frac{1}{2}}} = 0, \quad \text{and} \quad \kappa'(0) = h''(0) = \kappa'_0 > 0.$$

The function  $\kappa$  is then a solution of the following problem

$$\begin{cases} \kappa''(x) = \frac{(H_0^2 + 2\mu)\kappa(x) - 2px - \kappa(x)\kappa'^2(x)}{2(1-\kappa^2(x))}, & x \in ]0, x_m[ \\ |\kappa| < 1, & x \in ]0, x_m[ \\ \kappa(0) = 0, \\ \kappa(x_m) = -1. \end{cases} \quad (1.20)$$

We introduce the following affine polynomial

$$P(\xi) = (H_0^2 + 2\mu) \xi - 2px.$$

The problem (1.20) becomes

$$\begin{cases} \kappa'' = \frac{P(\kappa) - \kappa\kappa'^2}{2(1-\kappa^2)}, & x \in ]0, x_m[ \\ |\kappa| < 1, & x \in ]0, x_m[, \\ \kappa(0) = 0, \\ \kappa(x_m) = -1. \end{cases}$$

We set  $Y = (y_1, y_2)^T$ , where  $y_1 = \kappa$  and  $y_2 = \kappa'$  we obtain the following **Cauchy-Lipschitz** problem

$$\begin{cases} Y'(x) = F(x, Y(x)) \\ Y(0) = (0, \kappa'_0)^T, \end{cases} \quad (1.21)$$

where  $\kappa'_0$  is a shooting parameter and

$$F \left( x, \begin{pmatrix} y_1 \\ y_2 \end{pmatrix} \right) = \begin{pmatrix} y_2 \\ \frac{(H_0^2 + 2\mu)y_1 - 2px - y_1 y_2^2(x)}{2(1-y_1^2(x))} \end{pmatrix}.$$

This singular initial value problem have a local unique solution according to the Cauchy-Lipschitz theorem for any fixed  $\kappa'_0 > 0$  and it depends continuously on the initial value  $\kappa'_0$ .

**Proposition 1.2.2 (Willmore solution)**

Consider  $\kappa$  a solution for the problem (1.20), such that  $p = 0$  and  $H_0^2 + 2\mu = \kappa_0'^2$ . Then the curve defined by  $h : \Phi \rightarrow \mathbb{R}$ , such that  $h'(x) = \frac{\kappa(x)}{(1-\kappa^2(x))^{1/2}}$ , must be a disc of radius  $x = \frac{1}{\sqrt{\kappa_0'}}$ .

**Proof.**

In the case where  $p = 0$ , and  $H_0, \mu \neq 0$ , the equation (1.18) verified by  $\kappa$  becomes autonomous

$$\kappa''(x) = \frac{(H_0^2 + 2\mu)\kappa - \kappa(x)\kappa'^2(x)}{2(1-\kappa^2(x))}, \quad \forall x \in ]0, x_m[. \quad (1.22)$$

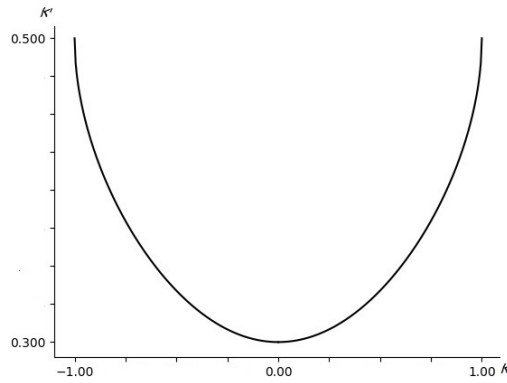


Figure 1.12:  $\kappa'$  curve as a function of  $\kappa$  for  $p = H_0 = 0$ ,  $\kappa'_0 = 0.3$ , and  $\mu = 0.125$

Suppose that  $\kappa' = F(\kappa)$ , we get  $\kappa'' = \kappa'F'(\kappa) = F(\kappa)F'(\kappa)$ . By using (1.22), we get

$$FF' = \frac{(H_0^2 + 2\mu)\kappa - F^2\kappa}{2(1 - \kappa^2)},$$

$$\left(\frac{1}{2}F^2\right)' = -\frac{F^2\kappa}{1 - \kappa^2} + \frac{(H_0^2 + 2\mu)\kappa}{2(1 - \kappa^2)}.$$

Let  $Y = \frac{F^2}{2}$ , we have

$$Y' + \frac{\kappa}{1 - \kappa^2}Y = \frac{(H_0^2 + 2\mu)\kappa}{2(1 - \kappa^2)}.$$

Then  $Y = \frac{H_0^2 + 2\mu}{2} + c_0(1 - \kappa^2)^{\frac{1}{2}}$ , where  $c_0$  is a derivation constant. As a consequence, we get

$$F(\kappa) = \pm\sqrt{H_0^2 + 2\mu + 2c_0(1 - \kappa^2)^{\frac{1}{2}}}.$$

We have,  $\kappa'(0) = F(0)$  since,  $\kappa(0) = 0$ , then,  $\kappa_0'^2 = H_0^2 + 2(\mu + c_0)$ , which implies that

$$\kappa' = \pm\sqrt{H_0^2 + 2\mu + (\kappa_0'^2 - H_0^2 - 2\mu)(1 - \kappa^2)^{\frac{1}{2}}}. \quad (1.23)$$

With this equation, we have the expression of  $x_m$

$$x_m = \int_0^1 \frac{ds}{\sqrt{H_0^2 + 2\mu + (\kappa_0'^2 - H_0^2 - 2\mu)(1 - s^2)^{\frac{1}{2}}}}.$$

Figure 4 represents the curve of  $\kappa'$  as a function of  $\kappa$  from equation 1.23

**Particular case:**  $\kappa_0'^2 = H_0^2 + 2\mu$  In this case  $\kappa' = \pm\sqrt{H_0^2 + 2\mu} = \pm\kappa_0' = \text{constant}$ , which gives

$$\kappa = \pm\kappa_0'x.$$

As a consequence, we get the circle parametrization (Willmore solution)

$$h(x) = \mp\frac{1}{\kappa_0'}\sqrt{1 - \kappa_0'^2x^2}.$$

Since an exact solution for (1.20) is not easy to find in a more general case (where  $H_0 \neq 0, \mu \neq 0$  and  $p \neq 0$ ), we study the global behavior of  $\kappa$  solution of (1.20) by finding necessary condition on the initial value  $\kappa_0'$ . For simplicity we assume in what follows that  $H_0 = 0$ .

**Theorem 1.2.2**

Let  $p, \mu > 0$ ,  $p < \left(\frac{2\mu}{3}\right)^{\frac{3}{2}}$ , we assume that  $0 < \kappa_0' < \frac{p}{\mu}$ . Then there exists  $x_m > 0$  such that  $\kappa \in \Psi_m$  is a solution to (1.20).

**Global behavior of solutions**

In the following, we assume that  $0 < \kappa_0' < \frac{p}{\mu}$ , and we mainly focus on the solutions of (1.20) in  $]0, x_m[$ , where  $x_m > 0$  and  $\kappa(0) = 0$ . Since the solution  $\kappa$  is completely parametrized by  $\kappa'(0) = \kappa_0'$ , we will simply refer to  $\kappa$  as the solution given by  $\kappa_0'$ .

**Lemma 1.2.2**

Under the assumptions of Theorem 1.2.2, we have

$$\kappa(x) < \frac{p}{\mu}x \quad \forall x > 0.$$

**Proof.**

Assume that there exist  $x_0 > 0$  such that  $\kappa(x_0) = \frac{p}{\mu}x_0$ . Let

$$f(x) = \frac{p}{\mu}x - \kappa(x).$$

We have  $f(0) = 0$ ,  $f'(0) = \frac{p}{\mu} - \kappa_0' > 0$ . Then  $f$  is an increasing function in a neighborhood of  $0^+$ . We suppose that  $f(x) > 0$  in  $(0, x_0)$

Since  $f(0) = f(x_0) = 0$ , there exists  $x_1$  such that

$$f'(x_1) = 0, \quad f(x_1) > 0 \quad \text{and} \quad f''(x_1) < 0,$$

which means that  $\kappa'(x_1) = \frac{p}{\mu}$  and  $\kappa''(x_1) > 0$ . From (1.18), we have

$$2(1 - \kappa^2)\kappa''(x_1) + \kappa(x_1)(\kappa'(x_1))^2 = 2\mu\kappa(x_1) - 2px_1.$$

Which implies that  $\kappa(x_1) > \frac{p}{\mu}x_1$  which impossible. Then  $\kappa(x) < \frac{p}{\mu}x \quad \forall x > 0$ .

**Lemma 1.2.3**

*We assume that there exist a critical point  $x_c^*$ , such that  $\kappa'(x_c^*) = 0$ , and  $0 < \kappa(x_c^*) < 1$ . Then  $\kappa' < 0$ , and  $\kappa'' < 0$ , for all  $x > x_c^*$ .*

**Proof.**

Assume that there exist a critical point  $x_c^*$  such that  $\kappa'(x_c^*) = 0$  and  $0 < \kappa(x_c^*) < 1$ .

We have from (1.18)  $2(1 - \kappa^2)\kappa''(x_c^*) = 2\mu\kappa(x_c^*) - 2px_c^*$ , and from lemma 1.2.2, we get  $\kappa''(x_c^*) < 0$ .

In a neighborhood  $x_c^* (x_c^*, x_c^* + \varepsilon)$ , we have  $\kappa' < 0$  and  $\kappa'' < 0$ . Now suppose that there exist  $x_2 > x_c^*$ , such that  $\kappa'(x_2) = 0$ ,  $\kappa^2(x_2) < 1$ , and  $\kappa' < 0$  in  $(x_c^*, x_2)$ . Then from (1.18), we get,  $2(1 - \kappa^2)\kappa''(x_2) = 2\mu\kappa(x_2) - 2px_2 < 0$ , which implies that  $\kappa'$  decreases in a neighborhood of  $x_2$ , since  $\kappa'(x_2) = 0$ , we get  $\kappa'(x) > 0$  in a neighborhood of  $x_2$ , which is impossible.

**Remark 1.2.1**

*We have,  $2(1 - \kappa^2)\kappa'' = 2\mu\kappa - 2px - \kappa\kappa'^2 < 0$ , if  $\kappa > 0$ .*

**Lemma 1.2.4**

*There exist a unique critical point  $x_c$  such that,  $\kappa'(x_c) = 0$ , and  $0 < \kappa(x_c) < 1$ .*

**Proof.**

Assume that  $\kappa' > 0$  and  $\kappa$  is bounded  $\forall x \in [0, +\infty[$ . Since  $\kappa$  is a bounded increasing function, and  $\kappa'' < 0$  (Remark1.2.1), we deduce that  $\kappa'(x) \xrightarrow{x \rightarrow +\infty} 0$ , and there exists a sequence  $(x_n)_n$  such that  $\kappa''(x_n) \xrightarrow{x_n \rightarrow +\infty} 0$ .

According to (1.18), we get,

$$2(1 - \kappa^2)\kappa''(x_n) \xrightarrow{x_n \rightarrow +\infty} -\infty,$$

which is absurd.

Then, there exist  $x_0$  such that  $\kappa(x_0) = 1$ , again by using equation (1.18), we get

$$2(1 - \kappa^2(x_0))\kappa''(x_0) = 2\mu - 2px_0 - \kappa'^2(x_0) < 0,$$

which implies that  $\kappa'' \sim \frac{c}{1-\kappa}$ ,  $c < 0$ . So that

$$\frac{1}{2}\kappa'^2 + c_0 \underset{x \rightarrow x_0}{\sim} |c| \ln(1 - \kappa),$$

which is impossible.

### Proof of Theorem 1.2.2

Assume that  $p < \left(\frac{2\mu}{3}\right)^{\frac{3}{2}}$  and  $\kappa$  satisfies (1.19) with  $\kappa(0) = 0$  and  $0 < \kappa'_0 < \frac{p}{\mu}$ . Since the solution  $\kappa$  is completely parametrized by  $\kappa'(0) = \kappa'_0$ , we will simply refer to  $\kappa$  as the solution given by  $\kappa'_0$  and most of the study will be conducted in the neighborhood of 0.

Near  $x = 0$ ,  $\kappa$  can be approximated by,  $\kappa(x) \simeq \kappa'_0 x + ax^3 + o(x)^3$ , since it's an odd function from (1.18), where  $a = \frac{1}{3}\kappa^{(3)}(0) = -\frac{1}{12}(\kappa_0'^3 - 2\mu\kappa'_0 + 2p)$ .

The polynomial  $\kappa_0'^3 - 2\mu\kappa'_0 + 2p$  admits two positive roots, since  $p < \left(\frac{2\mu}{3}\right)^{\frac{3}{2}}$ , and by using the condition  $0 < \kappa'_0 < \frac{p}{\mu}$ . We get  $\lim_{x \rightarrow 0} \frac{\kappa''(x)}{x} = 6a < 0$ , since  $\kappa_0'^3 - 2\mu\kappa'_0 + 2p > 0$ . It follow immediately that  $\kappa$  is concave near 0. Using Lemma 1.2.4 There exist a unique critical point  $x_c$  such that  $\kappa'(x_c) = 0$  and  $0 < \kappa(x_c) < 1$ . Then from Lemma 1.2.3, we get  $\kappa' < 0$  and  $\kappa'' < 0$  for all  $x > x_c$ . Which proves that  $\kappa$  is concave and have a unique critical point. We are now reduced to proving that  $|\kappa| < 1$ .

From Lemma 1.2.3 and Lemma 1.2.4, there exists  $x_m^*$  such that  $\kappa(x_m^*) = 0$ ,  $\kappa < 0 \forall x > x_m^*$ ,  $\kappa < 0$ ,  $\kappa'' < 0 \forall x > x_m^*$ .

Next we define  $\widehat{\kappa} = -\kappa$ . Therefore,  $\widehat{\kappa}$  satisfies

$$\begin{cases} 2(1 - \widehat{\kappa}^2)\widehat{\kappa}'' = 2\mu\widehat{\kappa} + 2px - \widehat{\kappa}\widehat{\kappa}'^2, & x > x_m^*, \\ \widehat{\kappa}(x_m^*) = 0, \widehat{\kappa}'(x_m^*) > 0, \widehat{\kappa}''(x_m^*) > 0. \end{cases}$$

Firstly, it should be noted that it is easy to show that  $\widehat{\kappa}'(x_m^*) > 0$  as soon as  $0 < \widehat{\kappa} < 1$ .

In the similar way as in the proof of lemma 1.2.4, we assume that  $\widehat{\kappa}$  is bounded by  $M < 1$ . Since  $\widehat{\kappa} > 0$  and bounded then there exists  $x_n$  such that

$$\widehat{\kappa}'(x_n) \underset{x_n \rightarrow +\infty}{\longrightarrow} 0. \tag{1.24}$$

It follows that  $\widehat{\kappa}'(x) \underset{x \rightarrow +\infty}{\longrightarrow} 0$  if  $\widehat{\kappa}'$  is monotonic. By using the equation of  $\widehat{\kappa}$  we deduce that  $\widehat{\kappa}'' > 0$  for large  $x$ , which is absurd ( $\widehat{\kappa}' > 0$  increasing and tends to 0).

Now if  $\widehat{\kappa}'$  is not monotonic for large  $x$ , there exist a sequence  $y_n$  such that  $\widehat{\kappa}''(y_n) = 0$  and  $\widehat{\kappa}'(y_n)$  is a local minimum. Using again equation of  $\widehat{\kappa}$  one deduces that  $\widehat{\kappa}'(y_n) \xrightarrow{y_n \rightarrow +\infty} 0$  and then  $\widehat{\kappa}'(x) \xrightarrow{x \rightarrow +\infty} 0$ , which contradicts equation (1.24).

Then, there exist  $x_m$  such that  $\widehat{\kappa}(x_m) = 1$ , which gives  $\kappa(x_m) = -1$  and then  $|\kappa| < 1$  for  $0 < x < x_m$ , which ends the proof of the Theorem.

Let us note that, since  $h' = \frac{\kappa}{\sqrt{1-\kappa^2}}$  we have,  $h'(x_m) = -\infty$ .

**Remark 1.2.2**

*The condition  $p < \left(\frac{2\mu}{3}\right)^{\frac{3}{2}}$  is necessary to ensure the biconcave character. Indeed, if  $p = \left(\frac{2\mu}{3}\right)^{\frac{3}{2}}$ , we get the spherical shape which is also a solution to the problem, but in our case we are rather interested in the biconcave character. otherwise, if  $p > \left(\frac{2\mu}{3}\right)^{\frac{3}{2}}$  we obtain complex shapes that are not physically admissible.*

**An approximation solution**

let  $\kappa$  be a solution of (1.20). Near 0,  $\kappa$  can be approximated as the following polynomial, since  $\kappa$  is an odd function and it is completely parametrized by  $\kappa'(0) = \kappa'_0$

$$\kappa(x) \simeq \kappa'_0 x + ax^3 + o(x)^3.$$

Using the equation (1.18) we get  $a = \frac{1}{3}\kappa^{(3)}(0) = -\frac{1}{12}(\kappa_0'^3 - 2\mu\kappa_0' + 2p) < 0$ , and by using the fact that  $h'(x) = \frac{\kappa(x)}{(1-\kappa^2)^{1/2}}$ , we obtain

$$h'(x) \simeq \frac{\kappa'_0 x + ax^3}{(1 - \kappa_0'^2 x^2)^{1/2}} + o(x)^3.$$

Integrating this quantity over  $]0, x_m[$  for fixed  $x_m$ , we get

$$h(x) = \sqrt{1 - (\kappa_0' x)^2} [c_0 + c_2 x^2], \tag{1.25}$$

where  $c_0 = h(0) = \frac{1}{\kappa_0'} + \frac{2|a|}{3\kappa_0'^4}$ ,  $c_2 = \frac{|a|}{3\kappa_0'^2}$  and  $a = -\frac{1}{12}(\kappa_0'^3 - 2\mu\kappa_0' + 2p)$ .

In the case where  $c_2 = 0$ , we have

$$h(x) = x_m \sqrt{1 - \left(\frac{x}{x_m}\right)^2}. \tag{1.26}$$

Which is a disk parametrization with radius  $x_m = \frac{1}{\kappa_0'}$  (spherical shape of red blood cells in 2 dimensions)

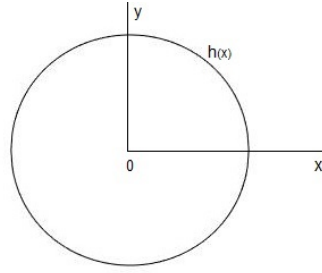


Figure 1.13: This curve represent the function  $h(x)$  in the case where  $c_2 = 0$

It is obviously seen that  $h$  is a solution of the minimization problem, where  $\mu = p = H_0 = 0$ , which agree with results given by Willmore in Theorem 1.1.1.

Now, let  $x_m = \frac{1}{\kappa_0}$ , Therefore, from (1.25), we get

$$h(x) = \sqrt{1 - \left(\frac{x}{x_m}\right)^2} \left[ C_0 + C_2 \left(\frac{x}{x_m}\right)^2 \right], \quad (1.27)$$

where  $C_0 = x_m + 2C_2$  and  $C_2 = \frac{|a|x_m^4}{3}$ , and if we increase the order of the Taylor expansion up to five order we get

$$h(x) = \sqrt{1 - \left(\frac{x}{x_m}\right)^2} \left[ C_0 + C_2 \left(\frac{x}{x_m}\right)^2 + C_4 \left(\frac{x}{x_m}\right)^4 \right], \quad (1.28)$$

where  $C_0 = x_m + \frac{2|a|x_m^4}{3} - \frac{8bx_m^6}{15}$ ,  $C_2 = +\frac{5|a|x_m^4 - 4bx_m^6}{15}$  and  $C_4 = \frac{-3bx_m^6}{15}$  such that  $a = -\frac{1}{12x_m^3}(1 - 2\mu x_m^2 + 2px_m^3)$  and  $b = \frac{5a}{40x_m^2}$ .

This approximation is similar to the parametric representation proposed by Evans and co-workers [56] to characterize the red blood cell geometry based on symmetry and surface-continuity.

The experimental data by Evans namely the diameter, the maximum and the minimum thickness, the surface area, and volume were easily computed using the interference microscopy method. This method allows to measure the phase change which a light wave undergoes when passing through a blood cell along the direction parallel to the rotational axis. The phase change is not simply proportional to the thickness of the cell but is related to the contour  $z(x)$  in a much more complicated way due to diffraction effects. To allow these effects, Evans et al. [56] computed the phase shift for the class of contours given by the following parametric equation

$$z(x) = \pm R \sqrt{1 - \left(\frac{x}{R}\right)^2} \left( C_0 + C_2 \left(\frac{x}{R}\right)^2 + C_4 \left(\frac{x}{R}\right)^4 \right), \quad (1.29)$$

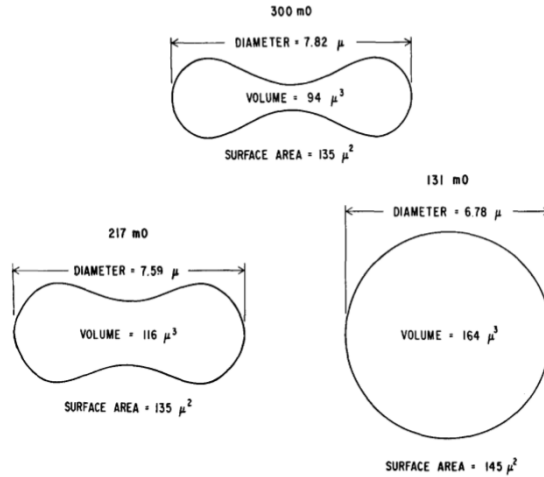


Figure 1.14: The class of contours obtained by Evans Ref.[56] using equation (1.29), and the experimental data obtained by the interference microscopy method

where  $R$  is the radius,  $x$  is the horizontal distance; and,  $C_0$ ,  $C_2$ , and  $C_4$  are three parameters that determine the RBC shape.

The free model parameters  $R, C_0, C_2, C_4$  were determined by fitting the phase shift for the class of contours (fig.1.14) given by equation (1.29) to the measured phase shift.

### 1.2.4 Numerical simulations

This section describes simulations of the red blood cell biconcave shape, using a combination of the Lagrangian multiplier method and artificial neural networks [83, 86].

A general model was first discussed by S. Zhang et al.[136]. In our study, we aim to determine the biconcave solutions of the problem (1.9). In fact we are looking for minimizers of the curvature energy (1.10), under area and perimeter constraints, among the functions that satisfy (1.28).

The problem resumes in seeking  $x_m, C_0, C_2, C_4$  that minimize the following energy

$$\mathcal{H}(x_m, C_0, C_2, C_4) = 2 \int_0^{x_m} \frac{h''^2(x)}{(1 + h'^2(x))^{\frac{5}{2}}} dx,$$

under constraints

$$\begin{aligned} 4 \int_0^{x_m} h(x) dx &= A_0, \\ 4 \int_0^{x_m} (1 + h'^2(x))^{\frac{1}{2}} dx &= P_0. \end{aligned} \tag{1.30}$$

Where  $A_0, P_0$  are initial data and  $h(x)$  is given by

$$h(x) = \sqrt{1 - \left(\frac{x}{x_m}\right)^2} \left[ C_0 + C_2 \left(\frac{x}{x_m}\right)^2 + C_4 \left(\frac{x}{x_m}\right)^4 \right]. \quad (1.31)$$

This optimization problem is not easy to tackle by the classical methods since the energy  $\mathcal{H}$  depends on the parameters  $x_m, C_0, C_2$  and  $C_4$  which are unknown and must themselves be determined in solving the problem.

In order to give the expression of  $\mathcal{H}$  as function of  $x_m, C_0, C_2$  and  $C_4$ , we have to calculate the first and the second derivatives of  $h(x)$  which is a difficult task. To overcome this difficulty we computed  $h'(x)$  and  $h''(x)$  formally in our algorithm using Matlab's formal calculations.

This work originates in an attempt to circumvent this difficulty by making use of the dynamical system obtained by combining the Lagrangian multiplier method and artificial neural networks as an alternative approach to the numerical analysis of our problem.

We consider  $\rho(u) = \sqrt{1 - (u)^2}$  where  $u = \frac{x}{x_m}$ . We get

$$\tilde{h}(u) = \rho(u) [C_0 + C_2 u^2 + C_4 u^4], \quad (1.32)$$

where  $\tilde{h}(u) = h(x_m u)$ . By a straightforward calculation, the derivatives of  $h$  are given by

$$\begin{cases} \tilde{h}'(u) = \frac{1}{x_m \rho(u)} ((2C_2 - C_0)u + (4C_4 - 3C_2)u^3 - 5C_4 u^5), \\ \tilde{h}''(u) = \frac{1}{x_m^2 \rho(u)^3} ((2C_2 - C_0) - 3(4C_4 - 3C_2)u^2 + (6C_2 - 33C_4)u^4 + 20C_4 u^6), \end{cases}$$

with the initial conditions

$$\begin{cases} \tilde{h}'(0) = 0, \\ \tilde{h}''(0) = \frac{1}{x_m^2} (2C_2 - C_0) > 0. \end{cases}$$

Therefore, necessary conditions to insure the biconcave shape becomes

$$C_0 > 0, C_2 > 0 \text{ and } 2C_2 - C_0 > 0. \quad (1.33)$$

Let  $x_c$  in  $(0, x_m)$  be a critical point such that  $h'(x_c) = 0$ . Then, we have

$$\frac{1}{x_m \rho(x_c/x_m)} \left( (2C_2 - C_0) \frac{x_c}{x_m} + (4C_4 - 3C_2) \left(\frac{x_c}{x_m}\right)^3 - 5C_4 \left(\frac{x_c}{x_m}\right)^5 \right) = 0.$$

Therefore

$$(2C_2 - C_0) + (4C_4 - 3C_2) \left(\frac{x_c}{x_m}\right)^2 - 5C_4 \left(\frac{x_c}{x_m}\right)^4 = 0.$$

We solve this equation, by sitting  $X = \left(\frac{x_c}{x_m}\right)^2$ . We have

$$\Delta = (4C_4 - 3C_2)^2 + 20C_4(2C_2 - C_0).$$

Using conditions  $C_4 > 0$  and  $2C_2 - C_0 > 0$  gives  $\Delta > 0$

$$v_0 = \sqrt{\frac{(4C_4 - 3C_2) + \sqrt{\Delta}}{10C_4}},$$

where  $0 < v_0 < 1$  gives  $0 < \frac{(4C_4 - 3C_2) + \sqrt{\Delta}}{10C_4} < 1$ , we get the following necessary condition

$$5C_2 - C_0 - C_4 < 0. \tag{1.34}$$

The Helfrich energy functional is defined by

$$\mathcal{H}(x_m, C_0, C_2, C_4) = \int_0^1 \frac{1}{\rho(u)} K_{\mathcal{H}}(x_m, C_0, C_2, C_4) du, \tag{1.35}$$

where

$$K_{\mathcal{H}}(x_m, C_0, C_2, C_4) = \frac{x_m^2 \cdot ((2C_2 - C_0) + (12C_4 - 9C_2)u^2 + (6C_2 - 33C_4)u^4 + 20C_4u^6)^2}{\left(x_m^2 \rho(u)^2 + ((2C_2 - C_0)u + (4C_4 - 3C_2)u^3 - 5C_4u^5)^2\right)^{\frac{5}{2}}}. \tag{1.36}$$

The area and the perimeter constraint becomes

$$A = 4 \int_0^1 x_m \cdot \rho(u) [C_0 + C_2u^2 + C_4u^4] du, \tag{1.37}$$

that can be written as follows

$$A = x_m(L_1 \cdot C_0 + L_2 \cdot C_2 + L_3 \cdot C_4),$$

where

$$L_1 = 4 \int_0^1 u \cdot \rho(u) du, \quad L_2 = 4 \int_0^1 u^3 \cdot \rho(u) du, \quad L_3 = 4 \int_0^1 u^5 \cdot \rho(u) du,$$

and

$$P = 4 \int_0^1 \frac{1}{\rho(u)} \left[ x_m \rho^2(u) + ((2C_2 - C_0)u + (4C_4 - 3C_2)u^3 - 5C_4u^5)^2 \right]^{\frac{1}{2}} du, \quad (1.38)$$

or equivalently

$$P = \int_0^1 \frac{1}{\rho(u)} K_P(x_m, C_0, C_2, C_4), \quad (1.39)$$

where

$$K_P(x_m, C_0, C_2, C_4) = 4 \left[ x_m \rho^2(u) + ((2C_2 - C_0)u + (4C_4 - 3C_2)u^3 - 5C_4u^5)^2 \right]^{\frac{1}{2}}.$$

The minimization problem becomes

$$\text{Min } \mathcal{H}(x_m, C_0, C_2, C_4) \quad \text{under constraints} \quad \begin{cases} A - A_0 = 0, \\ P - P_0 = 0, \\ C_4 \geq 0, x_m \geq 0, \\ 2C_2 - C_0 \geq 0, \\ 5C_2 - C_0 - C_4 < 0. \end{cases} \quad (1.40)$$

The Lagrangian function  $\mathcal{L}(x_m, C_0, C_2, C_4, p, \mu)$  is defined by

$$\mathcal{L}(C_0, C_2, C_4, x_m, \mu, \sigma, \eta) = \mathcal{H} + p(A - A_0) + \mu(P - P_0) - \eta_1 C_4 - \eta_2(C_0 - 2C_2) - \eta_3(5C_2 - C_0 - C_4) - \eta_4 x_m, \quad (1.41)$$

where  $\mathcal{H} = \mathcal{H}(x_m, C_0, C_2, C_4)$ ,  $A = A(C_0, C_2, C_4, x_m)$ ,  $P = P(C_0, C_2, C_4, x_m)$  and  $\eta = (\eta_1, \eta_2, \eta_3; \eta_4)$ .

Since (1.40) contains inequality constraints, we introduce the additional variables  $y$  to transform the inequality constraints into equalities as in [136].

The following nonlinear programming problem involves equality constraints

$$\text{Min } \mathcal{H}(C_0, C_2, C_4, x_m) \quad \text{under constraints} \quad \begin{cases} A - A_0 = 0, \\ P - P_0 = 0, \\ -C_4 + y_1^2 = 0, \\ C_0 - 2C_2 + y_2^2 = 0, \\ 5C_2 - C_0 - C_4 + y_3^2 = 0, \\ -x_m + y_4^2 = 0. \end{cases}$$

The Lagrangian  $\mathcal{L}$  rewrites

$$\begin{aligned} \mathcal{L}(x_m, C_0, C_2, C_4, p, \mu, y_1, y_2, y_3, y_4, \eta_1, \eta_2, \eta_3, \eta_4) = & \mathcal{H} + p(A - A_0) + \mu(P - P_0) + \\ & \eta_1(-C_4 + y_1^2) + \eta_2(C_0 - 2C_2 + y_2^2) + \eta_3(5C_2 - C_0 - C_4 + y_3^2) + \eta_4(-x_m + y_4^2). \end{aligned} \quad (1.42)$$

The dynamical system based on the Lagrangian function  $\mathcal{L}(x_m, C_0, C_2, C_4, p, \mu, y_1, y_2, y_3, y_4, \eta_1, \eta_2, \eta_3, \eta_4)$  of the transformed problem is the main topic of the following section.

### Dynamical system

Note that  $x_m, C_0, C_2, C_4$  and  $y$  are primal variables and  $p, \mu, \eta_1, \eta_2, \eta_3$  and  $\eta_4$  are Lagrange multipliers.

The dynamic system is written as follows

$$\left\{ \begin{array}{l} \frac{dC_i}{dt} = -\frac{\partial}{\partial C_i} \mathcal{L}(x_m, C_i, p, \mu, y, \eta), \quad \text{for } i = 0, 2, 4 \\ \frac{dx_m}{dt} = -\frac{\partial}{\partial x_m} \mathcal{L}(x_m, C_i, p, \mu, y, \eta) \\ \frac{dy_j}{dt} = -\frac{\partial}{\partial y_j} \mathcal{L}(x_m, C_i, p, \mu, y, \eta), \quad \text{for } j = 1, 2, 3, 4 \\ \frac{dp}{dt} = \frac{\partial}{\partial p} \mathcal{L}(x_m, C_i, p, \mu, y, \eta) \\ \frac{d\mu}{dt} = \frac{\partial}{\partial \mu} \mathcal{L}(x_m, C_i, p, \mu, y, \eta) \\ \frac{d\eta_j}{dt} = \frac{\partial}{\partial \eta_j} \mathcal{L}(x_m, C_i, p, \mu, y, \eta), \quad \text{for } j = 1, 2, 3, 4 \end{array} \right. \quad (1.43)$$

where  $y = (y_1, y_2, y_3, y_4)$  and  $\eta = (\eta_1, \eta_2, \eta_3, \eta_4)$

In the following, we give the expression of the derivatives of each quantity arising in the Lagrangian.

The derivative of the energy, the area and the perimeter with respect to  $C_0$  are given by

$$\begin{aligned} \frac{\partial}{\partial C_0} \mathcal{H}(x_m, C_0, C_2, C_4) &= \int_0^1 \frac{1}{\rho(u)} \frac{\partial}{\partial C_0} K_{\mathcal{H}}(x_m, C_0, C_2, C_4) du, \\ \frac{\partial}{\partial C_0} A(x_m, C_0, C_2, C_4) &= x_m \cdot L_1, \\ \frac{\partial}{\partial C_0} P(x_m, C_0, C_2, C_4) &= \int_0^1 \frac{1}{\rho(u)} \frac{\partial}{\partial C_0} K_P(x_m, C_0, C_2, C_4) du. \end{aligned} \quad (1.44)$$

This allows us to give the expression of  $\frac{\partial}{\partial C_0} \mathcal{L}(x_m, C_0, C_2, C_4)$ , as follows

$$\frac{\partial}{\partial C_0} \mathcal{L}(x_m, C_0, C_2, C_4, p, \mu, y, \eta) = \int_0^1 \frac{1}{\rho(u)} \left[ \frac{\partial}{\partial C_0} K_{\mathcal{H}} + \mu \frac{\partial}{\partial C_0} K_P \right] + px_m \cdot L_1 + \eta_2 - \eta_3.$$

The derivatives of the energy the area and the perimeter with respect to  $C_2$  are given by

$$\begin{aligned}\frac{\partial}{\partial C_2} \mathcal{H}(x_m, C_0, C_2, C_4) &= \int_0^1 \frac{1}{\rho(u)} \frac{\partial}{\partial C_2} K_{\mathcal{H}}(x_m, C_0, C_2, C_4) du, \\ \frac{\partial}{\partial C_2} A(x_m, C_0, C_2, C_4) &= x_m \cdot L_2, \\ \frac{\partial}{\partial C_2} P(x_m, C_0, C_2, C_4) &= \int_0^1 \frac{1}{\rho(u)} \frac{\partial}{\partial C_2} K_P(x_m, C_0, C_2, C_4) du.\end{aligned}\tag{1.45}$$

This allows us to give the expression of  $\frac{\partial}{\partial C_2} \mathcal{L}(x_m, C_0, C_2, C_4)$

$$\frac{\partial}{\partial C_2} \mathcal{L}(x_m, C_0, C_2, C_4, p, \mu, y, \eta) = \int_0^1 \frac{1}{\rho(u)} \left[ \frac{\partial}{\partial C_2} K_{\mathcal{H}} + \mu \frac{\partial}{\partial C_2} K_P \right] + px_m \cdot L_2 - 2\eta_2 + 5\eta_3.$$

The derivatives of the energy the area and the perimeter with respect to  $C_4$  are given by

$$\begin{aligned}\frac{\partial}{\partial C_4} \mathcal{H}(x_m, C_0, C_2, C_4) &= \int_0^1 \frac{1}{\rho(u)} \frac{\partial}{\partial C_4} K_{\mathcal{H}}(x_m, C_0, C_2, C_4) du \\ \frac{\partial}{\partial C_4} A(x_m, C_0, C_2, C_4) &= x_m \cdot L_3 \\ \frac{\partial}{\partial C_4} P(x_m, C_0, C_2, C_4) &= \int_0^1 \frac{1}{\rho(u)} \frac{\partial}{\partial C_4} K_P(x_m, C_0, C_2, C_4) du.\end{aligned}\tag{1.46}$$

This allows us to give the expression of  $\frac{\partial}{\partial C_4} \mathcal{L}(x_m, C_0, C_2, C_4)$

$$\frac{\partial}{\partial C_4} \mathcal{L}(x_m, C_0, C_2, C_4, p, \mu, y, \eta) = \int_0^1 \frac{1}{\rho(u)} \left[ \frac{\partial}{\partial C_2} K_{\mathcal{H}} + \mu \frac{\partial}{\partial C_2} K_P \right] + px_m \cdot L_3 + \eta_1 - \eta_3.$$

We derivative also the energy, the area and the perimeter with respect to  $x_m$  as follows

$$\begin{aligned}\frac{\partial}{\partial x_m} \mathcal{H}(x_m, C_0, C_2, C_4) &= \int_0^1 \frac{1}{\rho(u)} \frac{\partial}{\partial x_m} K_{\mathcal{H}}(x_m, C_0, C_2, C_4) du, \\ \frac{\partial}{\partial x_m} P(x_m, C_0, C_2, C_4) &= \int_0^1 \frac{1}{\rho(u)} \frac{\partial}{\partial x_m} K_P(x_m, C_0, C_2, C_4) du, \\ \frac{\partial}{\partial x_m} A(x_m, C_0, C_2, C_4) &= 2x_m(L_1 \cdot C_0 + L_2 \cdot C_2 + L_3 \cdot C_4).\end{aligned}\tag{1.47}$$

This allows us to give the expression of  $\frac{\partial}{\partial x_m} \mathcal{L}(x_m, C_0, C_2, C_4)$

$$\frac{\partial}{\partial x_m} \mathcal{L}(x_m, C_0, C_2, C_4, p, \mu, y, \eta) = \int_0^1 \frac{1}{\rho(u)} \left[ \frac{\partial}{\partial x_m} K_{\mathcal{H}} + \mu \frac{\partial}{\partial x_m} K_P \right] + 2px_m(L_1 \cdot C_0 + L_2 \cdot C_2 + L_3 \cdot C_4) - \eta_4.$$

Then, the dynamics system is finally given by

$$\left\{ \begin{array}{l} \frac{dC_0}{dt} = -\int_0^1 \frac{1}{\rho(u)} \left[ \frac{\partial}{\partial C_0} K_{\mathcal{H}} + \mu \frac{\partial}{\partial C_0} K_P \right] - px_m \cdot L_1 - \eta_2 + \eta_3 \\ \frac{dC_2}{dt} = -\int_0^1 \frac{1}{\rho(u)} \left[ \frac{\partial}{\partial C_2} K_{\mathcal{H}} + \mu \frac{\partial}{\partial C_2} K_P \right] - px_m \cdot L_2 + 2\eta_2 - 5\eta_4 \\ \frac{dC_4}{dt} = -\int_0^1 \frac{1}{\rho(u)} \left[ \frac{\partial}{\partial C_4} K_{\mathcal{H}} + \mu \frac{\partial}{\partial C_4} K_P \right] - px_m \cdot L_3 - \eta_1 + \eta_3 \\ \frac{dx_m}{dt} = -\int_0^1 \frac{1}{\rho(u)} \left[ \frac{\partial}{\partial x_m} K_{\mathcal{H}} + \mu \frac{\partial}{\partial x_m} K_P \right] - 2px_m(L_1 \cdot C_0 + L_2 \cdot C_2 + L_3 \cdot C_4) + \eta_4 \\ \frac{dp}{dt} = x_m(L_1 \cdot C_0 + L_2 \cdot C_2 + L_3 \cdot C_4) - A_0 \\ \frac{d\mu}{dt} = \int_0^1 \frac{1}{\rho(u)} \frac{\partial}{\partial x_m} K_P(x_m, C_0, C_2, C_4) du - P_0 \\ \frac{dy_1}{dt} = -2\eta_1 y_1 \\ \frac{dy_2}{dt} = -2\eta_2 y_2 \\ \frac{dy_3}{dt} = -2\eta_3 y_3 \\ \frac{dy_4}{dt} = -2\eta_4 y_4 \\ \frac{d\eta_1}{dt} = -C_4 + y_1^2 \\ \frac{d\eta_2}{dt} = C_0 - 2C_2 + y_2^2 \\ \frac{d\eta_3}{dt} = 5C_2 - C_0 - C_4 + y_3^2 \\ \frac{d\eta_4}{dt} = -x_m + y_4^2. \end{array} \right. \quad (1.48)$$

In order to solve this dynamical system we use the classical fourth-order Runge-Kutta method.

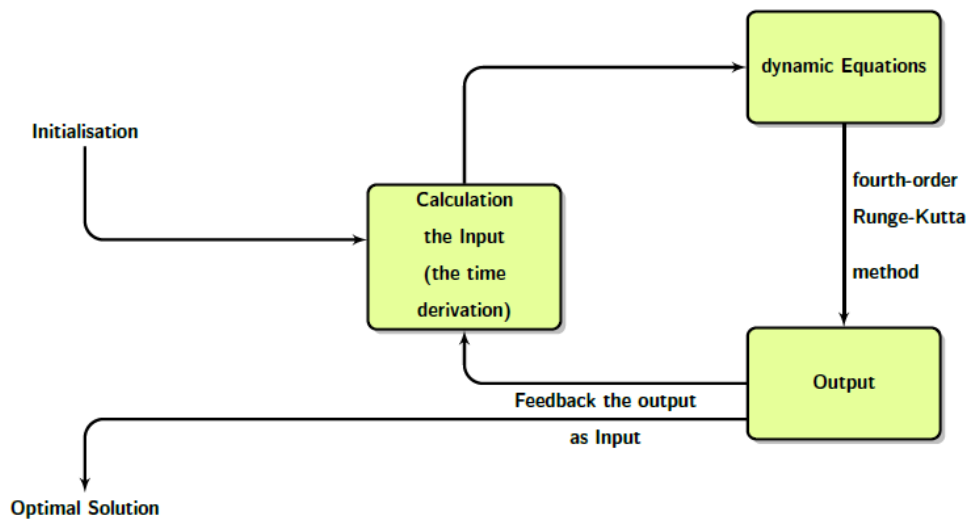


Figure 1.15: Diagram of the system resolution

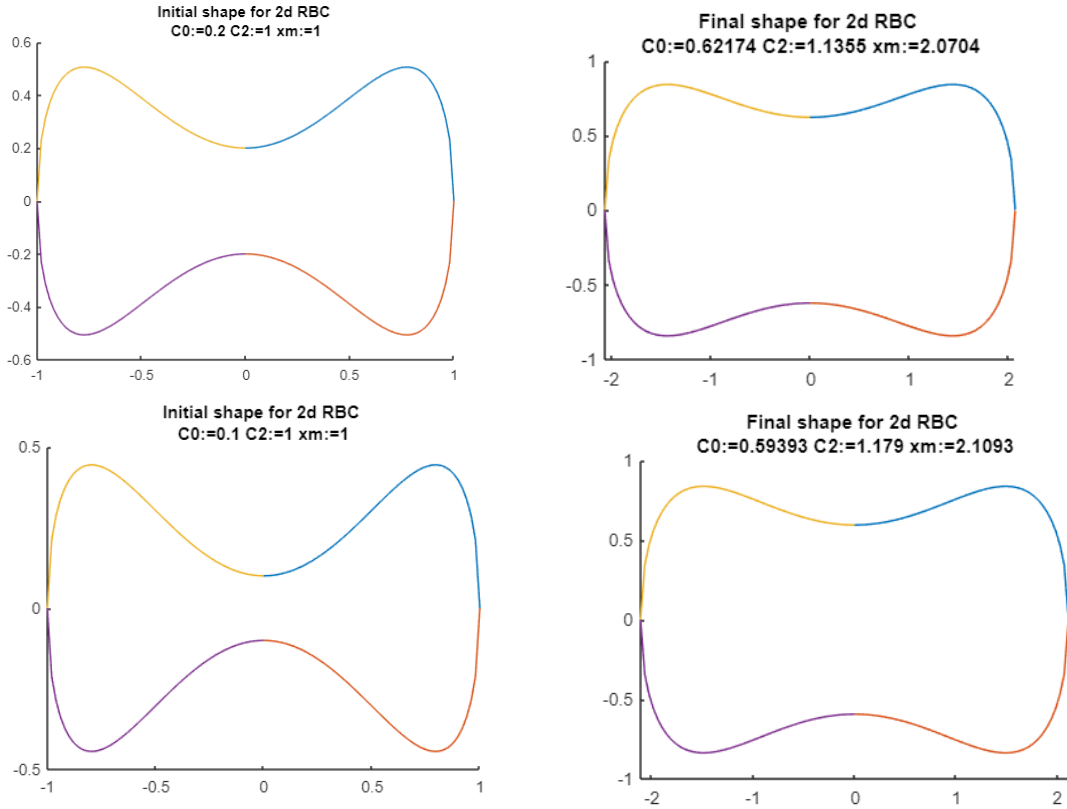


Figure 1.16: Plot  $\Gamma$  of the function  $h$  for different discretization steps

### Simulation Results

The implementation procedure for our algorithm based on Lagrange multiplier method is simulated by solving the dynamical system (1.48) using the classical fourth-order Runge-Kutta method (fig. 1.15) which is embedded in MATLAB ode solver. Figure 1.2.4 represents: in the left the initial biconcave shape with initial given coefficients  $x_m$ ,  $C_0$  and  $C_2$ , in the right the final biconcave shape resulting from injecting the new coefficients obtained by solving the dynamical system in the shape parametrization.

### 1.2.5 Canham-Helfrich problem in three-dimensional axi-symmetric Domain

Note that the approach used in the three-dimensional case is very similar to that implemented in the two-dimensional case. We will therefore rely on the developments carried out in the previous section and will not detail all the calculation steps so that we do not overload with unnecessary development.

In this section, we use the same parameterization of the red blood cell shape in three dimensions which allows having a simple expression of the curvature, then we adopt the theoretical study of Canham-Helfrich in the 1970s ([46],[31]) which represents the red blood cell shape as a minimum of the curvature

energy for fixed area and volume. After a mathematical formulation of the problem, we come across a complex minimization problem since the energy is written as function of the shape parameters which themselves must be determined by solving the problem. The classical optimization methods are not adapted to this type of problems, therefore we carried out numerical simulations to investigate the shape properties of RBC using a combination of the Lagrange multiplier method and fourth order Runge Kutta method.

As seen in the above section, the equilibrium configuration of red blood cells minimizes the energy of curvature proposed by Canham [31] and Helfrich [72] and given by the following functional

$$\mathcal{H}(\Omega) = \frac{\kappa}{2} \int_{\Gamma} H^2 ds. \quad (1.49)$$

$\Gamma$  represents the membrane (a closed surface) of the cell  $\Omega$  (the inner domain),  $H$  is the mean curvature and  $\kappa$  is the rigidity modulus of the membrane  $\Gamma$ .

Red blood cell equilibrium configurations will be determined by the minimization of the curvature energy under constraints, conserved volume (incompressible fluid inside the cell) and conserved area (inextensible membrane). Therefore, we solve the following optimization problem

$$\Omega^* = \arg \min_{\Omega \in \Lambda} \left\{ \frac{1}{2} \int_{\Gamma} H^2 ds \right\} \quad \text{under constraints} \quad \begin{cases} V = V_0, \\ A = A_0. \end{cases} \quad (1.50)$$

With  $\Lambda$  is the space of  $\Omega$  admissible shapes,  $\Omega^*$  is the optimal shape,  $V$  and  $A$  are the volume and the area of the red blood cell respectively and  $V_0$  and  $A_0$  represent the reference volume and area respectively.

We notice that minimizing the quantity  $\frac{1}{2} \int_{\Gamma} H^2 ds$  amounts to minimize  $\mathcal{H}(\Omega)$ , since  $\kappa$  is a positive constant depending only on the physical and geometrical characteristics of the membrane.

### **Formulation of the problem**

In this subsection, we are interested in the mechanical equilibrium of a single red blood cell in three-dimensional axis-symmetric case considering only a cut of the red blood cell.

To obtain the curve  $\Gamma$  (the membrane in 3D axis-symmetric case) we intersect a cutting plane containing the axis of rotation and the surface of the red blood cell see (Figure 1.10) that we obtain by numerical simulation to show the cut view.

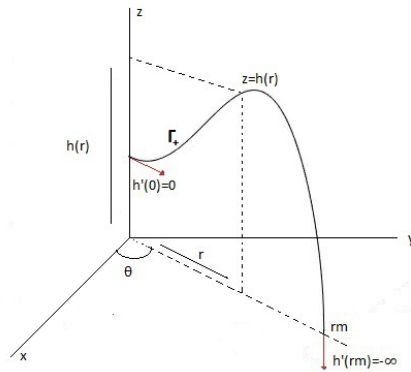


Figure 1.17: Example of a function  $h \in \Phi_m$  in 3D. We imposed to ensure the symmetry:  $h'(0) = 0$ ,  $h'(r_m) = -\infty$ . Here we can see the  $\Gamma_+$  curve

We assume that this curve has two axes of symmetry (Figure 1.17). Therefore, it suffices to study  $\Gamma$  in the upper dial, and we call  $\Gamma_+$  the  $\Gamma$  restriction on the upper dial. Then we can reconstruct the  $\Gamma$ -curve from  $\Gamma_+$  by symmetry (Figure 1.18). We use the cylindrical coordinates and we consider that, in the upper

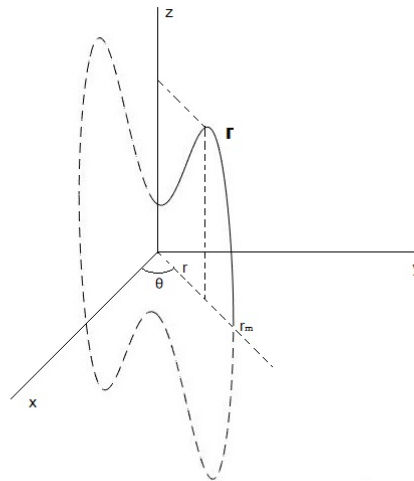


Figure 1.18: Diagram of the problem and presentation of the  $\Gamma$  curve.

half-space,  $\Gamma_+$  can be seen as the graph of a function  $h(r)$  which describes the thickness of the RBC.

The goal now is to numerically determine parameters  $r_m$ ,  $C_0$ ,  $C_2$  and  $C_4$  that can be used to describe the equilibrium state as above. Values of  $r_m$ ,  $C_0$ ,  $C_2$  and  $C_4$  will be obtained by solving numerically an optimization problem. We recall that  $r_m$  is the final radius of the RBC given by  $h(r_m) = 0$ . The equation

of the membrane  $\Gamma$  of the red blood cell is expressed in the following parametric form

$$\Gamma_+ = \{(r, \theta, z) \in [0, r_m] \times [0, 2\pi] \times [0, +\infty] : z = h(r), z \geq 0\}, \quad (1.51)$$

where fixed  $\theta$  is defined in figure 1.17.

In order to ensure the biconcave character for the solution of the problem (1.50), we must look for a solution  $z = h(r)$  such that  $h$  satisfy the following conditions.

1.  $h(r) \geq 0$  for  $r \in [0, r_m]$ ,
2.  $h(r_m) = 0$ ,
3.  $h'(0) = 0$ ,
4.  $h'(r) \rightarrow -\infty$  when  $r \rightarrow r_m$ ,
5. there exist  $r_M \leq r_m$  such that  $h''(r) \geq 0$  for  $r \in [0, r_M[$ , and  $h''(r) \leq 0$  for  $r \in ]r_M, r_m[$ .

The third and the last conditions imply that  $h'(r)$  has a unique maximum and that  $h(r)$  has a unique single inflection point  $r_I$ . This means that the function  $h(r)$  also has a unique maximum in  $r \in [0, r_m]$  (noted by  $r_M$ ).

Now we are able to describe the set of admissible functions to parametrize the curve  $\Gamma_+$

$$\Phi_m = \{h \in \mathcal{C}^2(0, r_m) : h \text{ satisfies } 1 - 5\}. \quad (1.52)$$

The framework of the problem thus defined allows us to solve the Canham-Helfrich problem in the three-dimensional case, which is written

$$\Omega^* = \operatorname{argmin}_{\Omega \in \mathbb{A}} \left\{ \frac{1}{2} \int_{\Gamma} (H - H_0)^2 ds \right\} \quad \text{under constraints} \quad \begin{cases} V = V_0, \\ A = A_0. \end{cases}$$

We have seen in the previous section that this constrained optimization problem can be transformed into a simple optimization problem using the Lagrange multipliers method. We then introduce the Lagrangian

$$\mathcal{L}(\Omega; \mu, p) = \frac{1}{2} \int_{\Omega} (H - H_0)^2 ds + p(V - V_0) + \mu(A - A_0),$$

with  $\mu$  and  $p$  are Lagrange multipliers. The problem is then to find the critical points  $(\Omega^*, \mu^*, p^*)$  of the Lagrangian  $\mathcal{L}$  verifying

$$(\Omega^*; \mu^*, p^*) = \operatorname{argmin}_{\Omega \in \Lambda} \max_{\mu, p \in \mathbb{R}} \{\mathcal{L}(\Omega; \mu, p)\}.$$

### Lagrangian Formulation

Before proceeding to the search for the saddle points, we compute the expressions in the three-dimensional case of the intervening quantities in the Lagrangian, namely the volume, the area and the curvature. In the three-dimensional case, we have the volume  $V$  and the area  $A$  which are given by:

$$\begin{aligned} V &= 2 \int_0^{2\pi} \int_0^{r_m} rh(r) dr d\theta, \\ A &= 2 \int_0^{2\pi} \int_0^{r_m} r \left(1 + (h'(r))^2\right)^{\frac{1}{2}} dr d\theta. \end{aligned}$$

By integrating the volume by parts we find

$$\begin{aligned} V &= 2 \int_0^{2\pi} \int_0^{r_m} rh(r) dr d\theta \\ &= 4\pi \left[ \frac{r^2}{2} h(r) \right]_0^{r_m} - 4\pi \int_0^{r_m} \frac{r^2}{2} h'(r) dr. \end{aligned}$$

Now, given that  $h \in \Phi_m$ , we have  $h(r_m) = 0$  then we get  $\left[ \frac{r^2}{2} h(r) \right]_0^{r_m} = 0$  and by setting  $\omega(r) = h'(r)$  we finally obtain the following expressions for the volume and the area

$$\begin{aligned} V &= -2\pi \int_0^{r_m} r^2 \omega(r) dr, \\ A &= 4\pi \int_0^{r_m} r \left(1 + \omega(r)^2\right)^{\frac{1}{2}} dr. \end{aligned}$$

Let's compute the curvature in the three dimensional case. The curvature  $H$  of the surface  $\Omega_+ \subset \mathbb{R}^3$  is defined as follows

$$H = \operatorname{trace}(\nabla n) = \operatorname{div}(n),$$

where  $n = \frac{\nabla \phi}{|\nabla \phi|}$ , is the normalized gradient of the la function  $\phi$  parameterizing  $\Omega_+$ . Here we have

$$\Omega_+ = \{(r, \theta, z) \in \mathbb{R}^3 : \phi(r, \theta, z) = h(r) - z = 0, \quad z \geq 0\},$$

then

$$n = \frac{1}{\sqrt{1+h'(r)^2}} \begin{pmatrix} h'(r) \\ 0 \\ -1 \end{pmatrix}.$$

In cylindrical coordinates, the divergence operator is expressed as follows

$$\operatorname{div}(n) = \frac{1}{r} \frac{\partial (rn_r)}{\partial r} + \frac{1}{r} \frac{\partial n_\theta}{\partial \theta} + \frac{\partial n_z}{\partial z},$$

which gives

$$\begin{aligned} H &= \operatorname{div}(n) \\ &= \frac{1}{r} \frac{\partial}{\partial r} \left( \frac{rh'(r)}{\sqrt{1+h'(r)^2}} \right). \end{aligned}$$

After computation we get

$$H = \frac{h''}{(1+h'^2)^{3/2}} + \frac{h^3+h'}{r(1+h'^2)^{3/2}}.$$

By replacing  $A$  and  $V$  by their expressions the Lagrangian becomes

$$\frac{\mathcal{L}(r_m, h; \mu, p)}{2\pi} = \int_0^{r_m} r \left[ (H - H_0)^2 + 2\mu \right] (1+h'^2(r))^{\frac{1}{2}} dr - \mu A_0 - p \int_0^{r_m} r^2 h'(r) dr - pV_0.$$

By setting once again

$$\kappa(r) = \frac{h'(r)}{r(1+h'^2(r))^{1/2}}. \tag{1.53}$$

We notice that this variable change is not defined at  $r = 0$ . However we can deduce from (1.53) that  $\kappa(r)$  tends to  $h''_0$  as  $r$  goes to 0.

We calculate the first and second derivatives

$$\begin{aligned} \kappa'(r) &= \frac{h''(r)}{r(1+h'^2(r))^{3/2}} - \frac{\kappa}{r}, \\ \kappa''(r) &= \frac{h'''(r)}{r(1+h'^2(r))^{\frac{3}{2}}} - \frac{\kappa'}{r} - \frac{3h'(r)h''^2(r)}{r(1+h'(r)^2)^{\frac{5}{2}}}. \end{aligned}$$

This will be also very useful for the numerical calculation of the curvature

$$H(r) = -2\kappa(r) - r\kappa'(r).$$

Therefor the Lagrangian becomes

$$\frac{\mathcal{L}(r_m, \kappa; \mu, p)}{2\pi} = \int_0^{r_m} r \left[ (H(\kappa) + H_0)^2 + 2\mu \right] (1 - r^2 \kappa^2(r))^{-\frac{1}{2}} dr - \mu A_0 - p \int_0^{r_m} \frac{r^3 \kappa(r)}{(1 - r^2 \kappa^2(r))^{\frac{3}{2}}} dr - pV_0.$$

It remains now to minimize this Lagrangian, which is equivalent to find the critical points  $(r_m, \kappa, \mu, p) \in \mathbb{R}^+ \times \Psi_m \times \mathbb{R} \times \mathbb{R}$  of this latter. At such a point, we have

$$\left\{ \begin{array}{l} \left[ \frac{d\mathcal{L}}{d\kappa}(\psi) \right] (r_m, \kappa, \mu, p) = 0 \quad \forall \psi \in \Psi_m, \\ \frac{\partial \mathcal{L}}{\partial r_m}(r_m, \kappa, \mu, p) = 0, \\ \frac{\partial \mathcal{L}}{\partial \mu}(r_m, \kappa, \mu, p) = 0, \\ \frac{\partial \mathcal{L}}{\partial p}(r_m, \kappa, \mu, p) = 0, \end{array} \right.$$

where  $\frac{d\mathcal{L}}{d\omega}(\psi)$  the directional derivative within the meaning of Gateau  $\mathcal{L}$  in the  $\psi$ , direction, where  $\Psi_m = \{ \psi \in \mathcal{C}^0(\mathbb{R}) : \psi(0) = 0, \psi(r_m) = -\infty \}$ .

Again, the two conditions  $\frac{\partial \mathcal{L}}{\partial x}(r_m, \kappa, \mu, p) = 0$  et  $\frac{\partial \mathcal{L}}{\partial p}(r_m, \kappa, \mu, p) = 0$  give respectively  $V = V_0$  and  $A = A_0$ . Now let's focus on the first condition :  $\left[ \frac{d\mathcal{L}}{d\kappa}(\psi) \right] (r_m, \kappa, \mu, p) = 0 \forall \psi \in \Psi_m$ . For the rest of the computations, we will write  $\kappa$  instead of  $\kappa(r)$  in order to simplify the notations. By following the same procedure as in the two-dimensional case, first, we have

$$\begin{aligned} \left[ (H - H_0)^2 \right]'_{\psi}(\kappa) &= 2H'_{\psi}(\kappa) (H(\kappa) - H_0), \\ \left[ (1 - r^2 \kappa^2)^{-\frac{1}{2}} \right]'_{\psi}(\kappa) &= \frac{r^2 \kappa \psi}{(1 - r^2 \kappa^2)^{\frac{3}{2}}}. \end{aligned}$$

Then, we obtain

$$\frac{1}{2\pi} \left[ \frac{d\mathcal{L}}{d\kappa} \right]_{\psi} = \int_0^{r_m} r \left[ 2H'_{\psi}(\kappa) (H(\kappa) - H_0) \right] (1 - r^2 \kappa^2)^{-\frac{1}{2}} dr + \int_0^{r_m} r \psi \frac{r^2 \kappa \left[ (H(\kappa) - H_0)^2 + 2\mu \right] - pr^2}{(1 - r^2 \kappa^2)^{\frac{3}{2}}} dr.$$

Since

$$H'_{\psi} = \left[ -2\kappa - r\kappa' \right]'_{\psi}(\kappa) = -2\psi - r\psi',$$

we get,

$$\begin{aligned} \frac{1}{2\pi} \left[ \frac{d\mathcal{L}}{d\kappa} \right]_{\psi} &= \int_0^{r_m} r\psi \frac{4(2\kappa + r\kappa' + H_0)(1 - r^2\kappa^2) + r^2\kappa \left[ (H(\kappa) - H_0)^2 + 2\mu \right] - pr^2}{(1 - r^2\kappa^2)^{\frac{3}{2}}} dr \\ &\quad + \int_0^{r_m} \psi' \frac{4r^2\kappa + 2r^3\kappa' + 2r^2H_0}{(1 - r^2\kappa^2)^{\frac{1}{2}}} dr. \end{aligned}$$

Using the integration by part, we have

$$\int_0^{r_m} \psi' \frac{4r^2\kappa + 2r^3\kappa' + 2r^2H_0}{(1 - r^2\kappa^2)^{\frac{1}{2}}} dr = \left[ \psi \frac{4r^2\kappa + 2r^3\kappa' + 2r^2H_0}{(1 - r^2\kappa^2)^{\frac{1}{2}}} \right]_0^{r_m} - \int_0^{r_m} \psi \left[ \frac{4r^2\kappa + 2r^3\kappa' + 2r^2H_0}{(1 - r^2\kappa^2)^{\frac{1}{2}}} \right]' dr.$$

Since  $\psi(0) = \psi(r_m) = -\infty$  ( $\psi$  is a compact support function). We get

$$\begin{aligned} \int_0^{r_m} \psi' \frac{4r^2\kappa + 2r^3\kappa' + 2r^2H_0}{(1 - r^2\kappa^2)^{\frac{1}{2}}} dr &= - \int_0^{r_m} \psi \left[ \frac{(8r\kappa + 4r^2\kappa' + 6r^2\kappa'' + 2r^3\kappa''' + 4rH_0)(1 - r^2\kappa^2)}{(1 - r^2\kappa^2)^{\frac{3}{2}}} \right] dr \\ &\quad - \int_0^{r_m} \psi \left[ \frac{(r\kappa^2 + r^2\kappa\kappa')(4r^2\kappa + 2r^3\kappa' + 2r^2H_0)}{(1 - r^2\kappa^2)^{\frac{3}{2}}} \right] dr. \end{aligned}$$

Thus the Lagrangian becomes

$$\begin{aligned} \frac{1}{2\pi} \left[ \frac{d\mathcal{L}}{d\kappa} \right]_{\psi} &= \int_0^{r_m} r\psi \frac{4(2\kappa + r\kappa' + H_0)(1 - r^2\kappa^2) + r^2\kappa \left[ (2\kappa + r\kappa' + H_0)^2 + 2\mu \right] - pr^2}{(1 - r^2\kappa^2)^{\frac{3}{2}}} dr \\ &\quad - \int_0^{r_m} r\psi \left[ \frac{(8\kappa + 4r\kappa' + 6r\kappa'' + 2r^2\kappa''' + 4H_0)(1 - r^2\kappa^2)}{(1 - r^2\kappa^2)^{\frac{3}{2}}} \right] dr \\ &\quad - \int_0^{r_m} r\psi \left[ \frac{(\kappa^2 + r\kappa\kappa')(4r^2\kappa + 2r^3\kappa' + 2r^2H_0)}{(1 - r^2\kappa^2)^{\frac{3}{2}}} \right] dr. \end{aligned}$$

By simplifying this expression we obtain

$$\left[ \frac{d\mathcal{L}}{d\kappa} \right]_{\psi} = 2\pi \int_0^{r_m} r^2\psi \frac{-2(3\kappa' + r\kappa'')(1 - r^2\kappa^2) - r\kappa(r\kappa' + \kappa)^2 + r\kappa^3 + 2rH_0\kappa^2 + r(H_0^2 + 2\mu)\kappa - pr}{(1 - r^2\kappa^2)^{\frac{3}{2}}} dr.$$

Therefore, the optimality condition  $\left[ \frac{d\mathcal{L}}{d\kappa}(\psi) \right](r_m, \kappa, \mu, p) = 0 \forall \psi \in \Phi'$ , becomes

$$\int_0^{r_m} \psi \left( \frac{-2(3\kappa' + r\kappa'')(1 - r^2\kappa^2) - r\kappa(r\kappa' + \kappa)^2 + r\kappa^3 + 2rH_0\kappa^2 + r(H_0^2 + 2\mu)\kappa - pr}{(1 - r^2\kappa^2)^{\frac{3}{2}}} \right) dr = 0, \quad \forall \psi \in \Phi'.$$

This equality must be verified for every  $\psi \in \Phi'$ . The function  $\kappa$  which minimizes the Lagrangian  $\mathcal{L}$  then satisfies the following ordinary differential equation

$$2(r\kappa'' + 3\kappa')(1 - r^2\kappa^2) = r\kappa^3 + 2rH_0\kappa^2 + r(H_0^2 + 2\mu)\kappa - pr - r\kappa(r\kappa' + \kappa)^2.$$

The above equation has to be solved subject to the following initial conditions (for small  $\varepsilon$ )

$$\kappa(\varepsilon) = h_0'' \text{ and } \kappa'(\varepsilon) = -\varepsilon h_0''' ,$$

with  $h_0''$  is the shouting parameter. Then we introduce the following polynomial

$$Q(\xi) = \xi^3 + 2H_0\xi^2 + (H_0^2 + \mu)\xi - p.$$

The function  $\kappa$  is then solution of the following Cauchy-Lipschitz problem

$$\begin{cases} \kappa'' = \frac{Q(\kappa) - \kappa(r\kappa' + \kappa)^2}{2(1 - r^2\kappa^2)} - \frac{3\kappa'}{r}, & r \in [\varepsilon, r_m], \\ \kappa(\varepsilon) = h_0'', \\ \kappa'(\varepsilon) = -\varepsilon h_0'''. \end{cases} \quad (1.54)$$

This is the main problem of this chapter. Once  $\kappa$  is known  $h'$  will be determined from (1.53), and then  $h$  will be deduced by a simple integration. The expression of  $h'(r)$  can be deduced from  $\kappa$  using the formula,  $h' = \frac{r\kappa}{\sqrt{(1 - r^2\kappa^2)}}$ .

**Remark 1.2.3**

As in 2Ds case, we excluded the solution,  $h' = -\frac{r\kappa}{\sqrt{(1 - r^2\kappa^2)}}$ .

Indeed, in a fixed plane  $\theta = \theta_0$ , we can interpret  $r\kappa$  as a component of the normalize gradient  $n$  to the curve, therefore  $r\kappa$  and  $h'$  have the same sign because they both reflect variations of  $h$  in this plane.

Unfortunately, the problem (1.54) is a second order nonlinear differential equation that we are not capable of finding an exact solution. TK. Au et al in Ref.[19] gives a sufficient condition on the parameters which ensures the existence of a special solution to the problem (1.54) that corresponds to a surface of the shape of a red blood cell. Note that the purpose of this section is not to exploit all possible shapes but to provide semi-explicit solutions in order to validate the proposed algorithm which characterize the physical solutions and to conform these solutions to the known physical results. The essential point is to show that

the solutions are physically acceptable, this implies that we have a closed surface that doesn't necessary have intersections of purely mathematical origins. This induces, the knowledge of the first zero of the solution  $h(r)$ , the number of zeros, the number of critical points, etc.

In the next section we propose to obtain numerical solution of  $h(r)$  by using an idea of Evans et al. [56]. As mentioned before, the authors in [56] claimed that

$$h(r) = \sqrt{1 - \left(\frac{r}{r_m}\right)^2} \left[ C_0 + C_2 \left(\frac{r}{r_m}\right)^2 + C_4 \left(\frac{r}{r_m}\right)^4 \right]. \quad (1.55)$$

Our contribution here is to numerically calculate  $r_m, C_0, C_2$  and  $C_4$  such that function  $h$ , given by (1.55), is a minimizer of the energy (1.49).

### Numerical method

As in the numerical implementation of the two-dimensional case, we consider  $\sigma(v) = \sqrt{1 - v^2}$  where  $v = \frac{r}{r_m}$  and  $r \in [0, r_m]$ . We have

$$\tilde{h}(v) = \rho(v) [C_0 + C_2 v^2 + C_4 v^4], \quad (1.56)$$

with  $\tilde{h}(v) = h(r)$ ,  $r_m > 0, C_0, C_2$ , and  $C_4 \geq 0$ . As in the previous section, we get

$$\begin{cases} \tilde{h}'(v) = \frac{1}{r_m \rho(v)} ((2C_2 - C_0)v + (4C_4 - 3C_2)v^3 - 5C_4 v^5), \\ \tilde{h}''(v) = \frac{1}{r_m^2 \rho(v)^3} ((2C_2 - C_0) - 3(4C_4 - 3C_2)v^2 + (6C_2 - 33C_4)v^4 + 20C_4 v^6). \end{cases}$$

At  $r = 0$ , we have the following initial conditions

$$\begin{cases} h'(0) = 0, \\ h''(0) = \frac{1}{r_m^2} (2C_2 - C_0) > 0 \quad \text{then } 2C_2 - C_0 > 0. \end{cases}$$

Therefore the necessary conditions for the biconcave shape are

$$0 \leq C_0, C_2, C_4 \quad \text{and} \quad 2C_2 - C_0 > 0. \quad (1.57)$$

Again, by considering a critical point  $r_c \in (0, r_m)$ , such that  $h'(r_c) = 0$ . We obtain the following condition

$$5C_2 - C_0 - C_4 < 0. \quad (1.58)$$

The Helfrich energy becomes

$$\begin{aligned} \mathcal{H}(r_m, C_0, C_2, C_4) &= 2\pi \int_0^{r_m} \frac{r(h''(r))^2}{(1+h'(r)^2)^{\frac{5}{2}}} + \frac{(h'(r))^2}{r(1+h'(r)^2)^{\frac{1}{2}}} dr \\ &= 2\pi \int_0^1 \frac{1}{\rho(v)} K_{\mathcal{H}}(r_m, C_0, C_2, C_4) dv, \end{aligned} \quad (1.59)$$

where

$$\begin{aligned} K_{\mathcal{H}}(r_m, C_0, C_2, C_4) &= \frac{r_m^3 \cdot v \left( (2C_2 - C_0) - 3(4C_4 - 3C_2)v^2 + (6C_2 - 33C_4)v^4 + 20C_4v^6 \right)^2}{\left( r_m^2 \rho(v)^2 + ((2C_2 - C_0)v + (4C_4 - 3C_2)v^3 - 5C_4v^5)^2 \right)^{\frac{5}{2}}} \\ &+ \frac{v \cdot \left( (2C_2 - C_0) + (4C_4 - 3C_2)v^2 - 5C_4v^4 \right)^2}{r_m \cdot \left( r_m^2 \rho(v)^2 + ((2C_2 - C_0)v + (4C_4 - 3C_2)v^3 - 5C_4v^5)^2 \right)^{\frac{1}{2}}}. \end{aligned}$$

The volume constraint becomes

$$V = 4\pi \int_0^1 r_m^2 \cdot v \cdot \rho(v) [C_0 + C_2v^2 + C_4v^4] dv, \quad (1.60)$$

that can be written as follows

$$V = r_m^2 (L_1 \cdot C_0 + L_2 \cdot C_2 + L_3 \cdot C_4),$$

where

$$L_1 = 4\pi \int_0^1 v \cdot \rho(v) dv; \quad L_2 = 4\pi \int_0^1 v^3 \cdot \rho(v) dv; \quad L_3 = 4\pi \int_0^1 v^5 \cdot \rho(v) dv.$$

The area constraint also becomes

$$A = 4\pi \int_0^1 \frac{v \cdot r_m}{\rho(v)} \left[ r_m(1 - v^2) + ((2C_2 - C_0)v + (4C_4 - 3C_2)v^3 - 5C_4v^5)^2 \right]^{\frac{1}{2}} dv, \quad (1.61)$$

that can be written as

$$A = \int_0^1 \frac{1}{\rho(v)} K_A(r_m, C_0, C_2, C_4) dv, \quad (1.62)$$

where

$$K_A(r_m, C_0, C_2, C_4) = v \cdot r_m \left[ r_m(1 - v^2) + ((2C_2 - C_0)v + (4C_4 - 3C_2)v^3 - 5C_4v^5)^2 \right]^{\frac{1}{2}}.$$

The minimization problem thus becomes

$$\text{Min } \mathcal{H}(r_m, C_0, C_2, C_4) \text{ under constraints } \begin{cases} V - V_0 = 0, \\ A - A_0 = 0, \\ C_4 \geq 0, x_m \geq 0, \\ 2C_2 - C_0 \geq 0, \\ 5C_2 - C_0 - C_4 < 0. \end{cases}$$

The Lagrangian function  $\mathcal{L}(r_m, C_0, C_2, C_4, p, \mu)$  is defined by

$$\mathcal{L}(r_m, C_0, C_2, C_4, p, \mu) = \mathcal{H} + p(V - V_0) + \mu(A - A_0) - \eta_1 C_4 - \eta_2(C_0 - 2C_2) - \eta_3(5C_2 - C_0 - C_4) - \eta_4 r_m, \quad (1.63)$$

where  $\mathcal{H} = \mathcal{H}(r_m, C_0, C_2, C_4)$ ,  $V = V(r_m, C_0, C_2, C_4)$  and  $\eta = (\eta_1, \eta_2, \eta_3; \eta_4)$ .

Since the problem contains inequality constraints, we introduce the additional variables  $y$  to transform the inequality constraints into equalities as in [83].

The minimization problem becomes.

$$\text{Min } \mathcal{H}(r_m, C_0, C_2, C_4) \text{ under constraints } \begin{cases} V - V_0 = 0, \\ A - A_0 = 0, \\ -C_4 + y_1^2 = 0, \\ C_0 - 2C_2 + y_2^2 = 0, \\ 5C_2 - C_0 - C_4 + y_3^2 = 0, \\ -r_m + y_4^2 = 0. \end{cases}$$

The Lagrangian function  $\mathcal{L}(r_m, C_0, C_2, C_4, p, \mu, y, \eta)$  becomes

$$\begin{aligned} &\mathcal{L}(r_m, C_0, C_2, C_4, \sigma, y_1, y_2, y_3, y_4, y_5, \mu_1, \mu_2, \mu_3, \mu_4, \mu_5) \\ &= J + \sigma(V - V_0) + \mu_1(-C_4 + y_1^2) + \mu_2(C_0 - 2C_2 + y_2^2) + \mu_3(5C_2 - C_0 - C_4 + y_3^2) + \mu_4(-r_m + y_4^2). \end{aligned} \quad (1.64)$$

The following dynamical system based on the Lagrangian function  $\mathcal{L}(r_m, C_0, C_2, C_4, p, \mu, y_1, y_2, y_3, y_4, \eta_1, \eta_2, \eta_3, \eta_4)$  of the transformed problem is the principle of the following section.

### 1.2.6 Dynamical system

Note that  $r_m, C_0, C_2, C_4, y$  are primal variables and  $p, \mu, \eta_1, \eta_2, \eta_3$  and  $\eta_4$  are Lagrange multipliers. The dynamic system can be briefly written as

$$\left\{ \begin{array}{l} \frac{dC_i}{dt} = -\frac{\partial}{\partial C_i} \mathcal{L}(r_m, C_i, p, \mu, y, \eta), \quad \text{for } i = 0, 2, 4 \\ \frac{dr_m}{dt} = -\frac{\partial}{\partial r_m} \mathcal{L}(r_m, C_i, p, \mu, y, \eta) \\ \frac{dy_j}{dt} = -\frac{\partial}{\partial y_j} \mathcal{L}(r_m, C_i, p, \mu, y, \eta), \quad \text{for } j = 1, 2, 3, 4 \\ \frac{dp}{dt} = \frac{\partial}{\partial p} \mathcal{L}(r_m, C_i, p, \mu, y, \eta) \\ \frac{d\mu}{dt} = \frac{\partial}{\partial \mu} \mathcal{L}(r_m, C_i, p, \mu, y, \eta) \\ \frac{d\eta_j}{dt} = \frac{\partial}{\partial \eta_j} \mathcal{L}(r_m, C_i, p, \mu, y, \eta), \quad \text{for } j = 1, 2, 3, 4 \end{array} \right. \quad (1.65)$$

where  $y = (y_1, y_2, y_3, y_4)$  and  $\eta = (\eta_1, \eta_2, \eta_3, \eta_4)$

Now, let's compute the expressions of the partial derivatives of each quantity occurring in the Lagrangian. The expressions of the derivatives of the energy, the volume and the area with respect to  $C_0$  are as follows

$$\begin{aligned} \frac{\partial}{\partial C_0} \mathcal{H}(r_m, C_0, C_2) &= \int_0^1 \frac{1}{\rho(u)} \frac{\partial}{\partial C_0} K_{\mathcal{H}}(r_m, C_0, C_2, C_4) dv, \\ \frac{\partial}{\partial C_0} V(r_m, C_0, C_2, C_4) &= r_m^2 \cdot L_1, \\ \frac{\partial}{\partial C_0} A(r_m, C_0, C_2, C_4) &= \int_0^1 \frac{1}{\rho(u)} \frac{\partial}{\partial C_0} K_A(r_m, C_0, C_2) dv. \end{aligned}$$

This allows to give the expression of  $\frac{\partial}{\partial C_0} \mathcal{L}(r_m, C_0, C_2, C_4)$

$$\frac{\partial}{\partial C_0} \mathcal{L}(r_m, C_0, C_2, C_4, y, \sigma, \mu) = \int_0^1 \frac{1}{\rho(u)} \left[ \frac{\partial}{\partial C_0} K_{\mathcal{H}} + \mu \frac{\partial}{\partial C_0} K_A \right] + \sigma r_m^2 \cdot L_1 + \mu_2 - \mu_3.$$

The expressions of the derivatives of the energy, the volume and the area with respect to  $C_2$  are

$$\begin{aligned} \frac{\partial}{\partial C_2} \mathcal{H}(r_m, C_0, C_2, C_4) &= \int_0^1 \frac{1}{\rho(u)} \frac{\partial}{\partial C_2} K_{\mathcal{H}}(r_m, C_0, C_2, C_4) dv, \\ \frac{\partial}{\partial C_2} V(r_m, C_0, C_2, C_4) &= r_m^2 \cdot L_2, \\ \frac{\partial}{\partial C_2} A(r_m, C_0, C_2, C_4) &= \int_0^1 \frac{1}{\rho(u)} \frac{\partial}{\partial C_2} K_A(r_m, C_0, C_2, C_4) dv. \end{aligned}$$

This allows to give the expression of  $\frac{\partial}{\partial C_2} \mathcal{L}(r_m, C_0, C_2, C_4)$

$$\frac{\partial}{\partial C_2} \mathcal{L}(r_m, C_0, C_2, C_4, p, \mu, y, \eta) = \int_0^1 \frac{1}{\rho(u)} \left[ \frac{\partial}{\partial C_2} K_{\mathcal{H}} + \mu \frac{\partial}{\partial C_2} K_A \right] dv + pr_m^2 \cdot L_2 - 2\eta_2 + 5\eta_3.$$

The expressions of the derivatives of the energy, the volume and the area with respect to  $C_4$  are

$$\begin{aligned} \frac{\partial}{\partial C_4} \mathcal{H}(r_m, C_0, C_2, C_4) &= \int_0^1 \frac{1}{\rho(u)} \frac{\partial}{\partial C_4} K_{\mathcal{H}}(r_m, C_0, C_2, C_4) dv, \\ \frac{\partial}{\partial C_4} V(r_m, C_0, C_2, C_4) &= r_m^2 \cdot L_3, \\ \frac{\partial}{\partial C_4} A(r_m, C_0, C_2, C_4) &= \int_0^1 \frac{1}{\rho(u)} \frac{\partial}{\partial C_4} K_A(r_m, C_0, C_2, C_4) dv. \end{aligned}$$

This allows to give the expression of  $\frac{\partial}{\partial C_4} \mathcal{L}(r_m, C_0, C_2, C_4)$

$$\frac{\partial}{\partial C_4} \mathcal{L}(r_m, C_0, C_2, C_4, p, \mu, y, \eta) = \int_0^1 \frac{1}{\rho(u)} \left[ \frac{\partial}{\partial C_2} K_{\mathcal{H}} + \mu \frac{\partial}{\partial C_2} K_A \right] dv + pr_m^2 \cdot L_3 + \eta_1 - \eta_3.$$

The expressions of the derivatives of the energy, the volume and the area with respect to  $r_m$  are

$$\begin{aligned} \frac{\partial}{\partial r_m} \mathcal{H}(r_m, C_0, C_2, C_4) &= \int_0^1 \frac{1}{\rho(u)} \frac{\partial}{\partial r_m} K_{\mathcal{H}}(r_m, C_0, C_2, C_4) dv, \\ \frac{\partial}{\partial r_m} A(r_m, C_0, C_2, C_4) &= \int_0^1 \frac{1}{\rho(u)} \frac{\partial}{\partial r_m} K_A(r_m, C_0, C_2, C_4) dv, \\ \frac{\partial}{\partial r_m} V(r_m, C_0, C_2, C_4) &= 2r_m(L_1 \cdot C_0 + L_2 \cdot C_2 + L_3 \cdot C_4). \end{aligned}$$

This allows to give the expression of  $\frac{\partial}{\partial r_m} \mathcal{L}(r_m, C_0, C_2, C_4)$

$$\frac{\partial}{\partial r_m} \mathcal{L}(C_0, C_2, C_4, r_m, p, \mu, y, \eta) = \int_0^1 \frac{1}{\rho(u)} \left[ \frac{\partial}{\partial r_m} K_{\mathcal{H}} + \mu \frac{\partial}{\partial r_m} K_A \right] dv + 2pr_m(L_1 \cdot C_0 + L_2 \cdot C_2 + L_3 \cdot C_4) - \eta_4.$$

Then the dynamics system is finally given by

$$\left\{ \begin{array}{l} \frac{dC_0}{dt} = -\int_0^1 \frac{1}{\rho(v)} \left[ \frac{\partial}{\partial C_0} K_{\mathcal{H}} + \mu \frac{\partial}{\partial C_0} K_A \right] dv - pr_m^2 \cdot L_1 - \eta_2 + \eta_3, \\ \frac{dC_2}{dt} = -\int_0^1 \frac{1}{\rho(v)} \left[ \frac{\partial}{\partial C_2} K_{\mathcal{H}} + \mu \frac{\partial}{\partial C_2} K_A \right] dv - pr_m^2 \cdot L_2 + 2\eta_2 - 5\eta_4, \\ \frac{dC_4}{dt} = -\int_0^1 \frac{1}{\rho(v)} \left[ \frac{\partial}{\partial C_4} K_{\mathcal{H}} + \mu \frac{\partial}{\partial C_4} K_A \right] dv - pr_m^2 \cdot L_3 - \eta_1 + \eta_3, \\ \frac{dr_m}{dt} = -\int_0^1 \frac{1}{\rho(v)} \left[ \frac{\partial}{\partial r_m} K_{\mathcal{H}} + \mu \frac{\partial}{\partial r_m} K_A \right] dv - 2pr_m(L_1 \cdot C_0 + L_2 \cdot C_2 + L_3 \cdot C_4) + \mu_4, \\ \frac{dp}{dt} = r_m^2(L_1 \cdot C_0 + L_2 \cdot C_2 + L_3 \cdot C_4) - V_0, \\ \frac{d\mu}{dt} = \int_0^1 \frac{1}{\rho(u)} \frac{\partial}{\partial r_m} K_A(C_0, C_2, C_4, r_m) dv - A_0, \\ \frac{dy_1}{dt} = -2\eta_1 y_1, \\ \frac{dy_2}{dt} = -2\eta_2 y_2, \\ \frac{dy_3}{dt} = -2\eta_3 y_3, \\ \frac{dy_4}{dt} = -2\eta_4 y_4, \\ \frac{d\eta_1}{dt} = -C_4 + y_1^2, \\ \frac{d\eta_2}{dt} = C_0 - 2C_2 + y_2^2, \\ \frac{d\eta_3}{dt} = 5C_2 - C_0 - C_4 + y_3^2, \\ \frac{d\eta_4}{dt} = -r_m + y_4^2. \end{array} \right. \quad (1.66)$$

Again in order to solve this dynamical system we use the classical fourth-order Runge-Kutta method.

### Simulation Results

Implementations procedure of our method is simulated using the classical fourth-order Runge-Kutta method which is embedded in MATLAB ode solver to solve the dynamical system (1.66) differential equations.

We reconstruct the 3D profile of some of the solution forms previously encountered. Note that the shapes are obtained by rotating the  $\Gamma$  curves around the  $z$  axis since it is a surface revolution, then by symmetry with respect to the plane  $z = 0$ . The details of the Matlab code are provided in figure 1.2.6

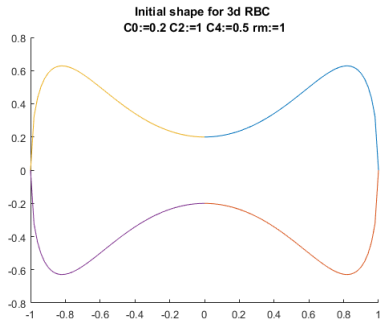


Figure 1.19: Plot  $\Gamma$  of the function  $h$  for different discretization steps

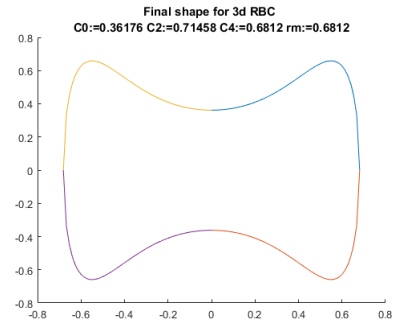


Figure 1.20: Plot of the function  $h$  for different discretization steps

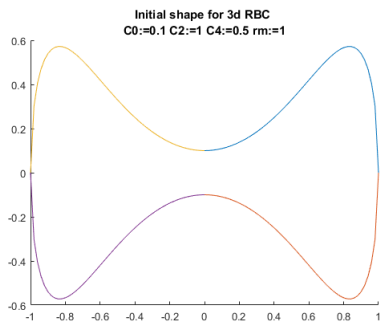


Figure 1.21: Plot of the function  $h$  for different discretization steps

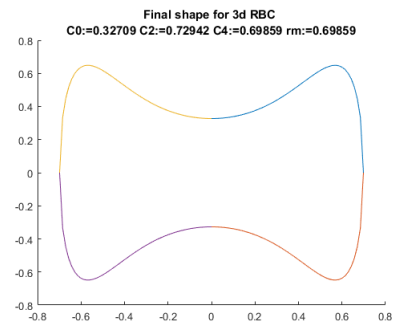


Figure 1.22: Plot of the function  $h$  for different discretization steps

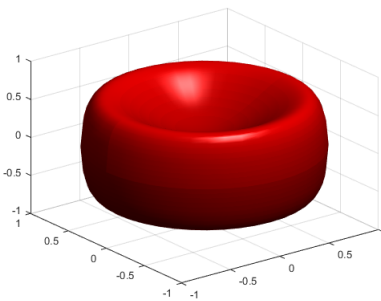


Figure 1.23: Three-dimensional biconcave shape

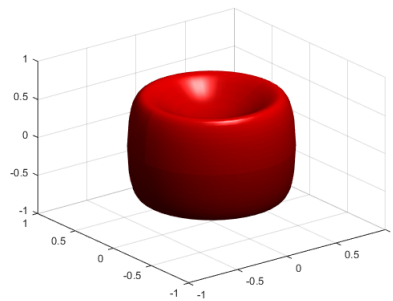


Figure 1.24: Three-dimensional biconcave shape

### 1.3 Conclusion

A majority of studies considered the Euler-Lagrange equilibrium equation given in [80] to characterize the RBC shape. In this work we have focused on the geometrical properties of the red blood cell shape. Our contributions is to determine particular solutions of the form (1.55) that minimizes the curvature energy numerically. Using our algorithm we are able to calculate coefficients  $x_m, C_0, C_2, C_4$  in two-dimensional

case and  $r_m, C_0, C_2, C_4$  in the three-dimensional case in order to obtain the biconcave shape of the red blood cell. The novelty of our proposed method is seen in the fact that

- We have a simple parametrization of the surface of the RBC.
- We don't need to go through the equilibrium equation which is not easy to solve.
- We develop an efficient algorithm based on a dynamical system to find the coefficients  $x_m, C_0, C_2, C_4$  in two-dimensional case and  $r_m, C_0, C_2, C_4$  in the three-dimensional case that minimize the curvature energy model.

In this work we found new results that do not require using the usual analytical description of the curvature energy. We found that our numerical results are closely similar to the results given by Evans and co-workers.

# Fluctuations and instability of a biological membrane induced by interaction with macromolecules using geometric shape optimization

## 2.1 Introduction

Biological membranes consist of molecular bilayers with two layers that are usually exposed to different aqueous environments and may differ in molecular density or composition. Due to these asymmetries, the membranes prefer to bend in a certain way as quantitatively described by their spontaneous curvature. Experiments shows that diffusive proteins within lipid membranes play an important role in producing and regulating membrane curvature [22, 17]. Scientific revelations shows that, about 30–90% of all membrane proteins can diffuse along the membrane [58]. Therefore, they induce various curvatures to the membrane they attach. Some of these proteins have an intrinsic curvature and, upon attachment, the membrane bends to match the protein curvature. In a similar fashion, several proteins can oligomerize to create a rigid shape and bend the membrane, this mechanism could be responsible for the morphological transformations and instabilities of membranes as frequently observed during protein adsorption onto vesicles. The same mechanism could be a generation of spontaneous curvature provided by asymmetric adsorption onto the bilayer membranes two surfaces.

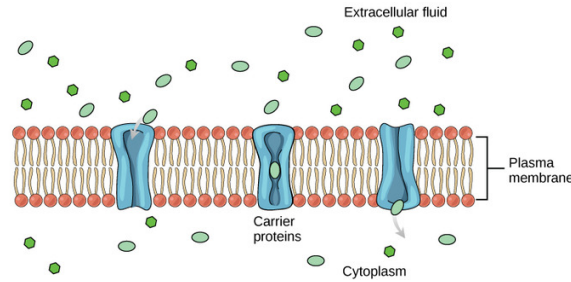


Figure 2.1: Transport Across the Cell Membrane

The induced membrane curvature is due to a difference between the thickness of the hydrophobic core of the lipid bilayer in which proteins are embedded and the length of the hydrophobic region of a membrane protein [108]. Moreover, the exposing of the two sides of the bilayer membranes to aqueous solutions that differ in their ionic or molecular composition can make an asymmetry between the two layers. This mechanism should induce a preferred or spontaneous curvature in the bilayer membranes which could make these latter try to adapt their shape to this curvature.

In the context of lipid bilayers the classical bending energy was first considered by Canham [31], and Helfrich et al. [72], depends only on the membrane mean and spontaneous curvature. The spontaneous curvature describes the intuitive notion that thin layers with two chemically different sides tend to bend or bulge towards one of these sides [114]. However, when topological changes in the membrane surface are produced by certain forces, such as the one induced by proteins, a discontinuity in the energy functional will be created. In this case, an explicit parameterization of the surface is impossible, since the changes in topology requires a discontinuous surface for a moment.

To treat topological changes, we choose to implicitly track the surface as a level set of a three-dimensional function. The level set method is such an implicit and diffuse-interface method, and it has been very successful in modeling membrane dynamics [51, 5]. In the level set method, the membrane is defined by the level sets of a function  $\phi$ , and the motion of the membrane is governed by gradient flow of the energy functional, ensuring a decrease in energy in time.

## 2.2 Localization of multiple species of diffusion molecules on membrane surfaces

In this section, we give the formulation of the total energy for the diffusion of molecules on membrane surface. Then we introduce the molecule concentration dependent spontaneous curvature in the bending

energy of the bilayer membrane. Finally, we derive the transport equation for diffusive molecules which represent the gradient flow of the total energy as in [90].

### 2.2.1 Description of the mathematical problem

Let  $\Gamma$  be a structureless surface that corresponds to an enclosed bilayer membrane. The membrane  $\Gamma$  separates the entire domain  $\Omega \in \mathbb{R}^3$  into two sub-domains (the inside and the outside of the membrane).

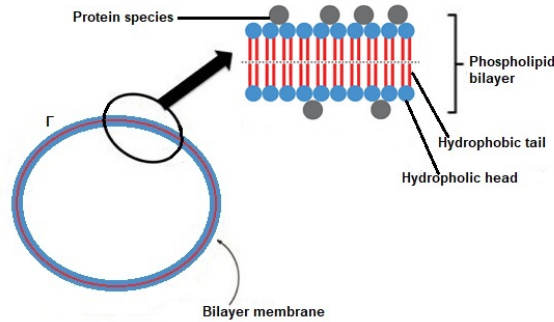


Figure 2.2: Transport Across the Cell Membrane: different adsorbate densities at or within the two head group layers. The lipid head groups are shown in blue, the lipid tails in red, and the adsorbate “particles” in dark gray.

$n + 1$  distinct protein species with concentrations  $c_i$ ,  $0 = 1, i, n$ , are distributed on the membrane figure 2.2. The total energy of the system is the sum of the bending energy  $E_{\text{mem}}$  that includes the effects of the multiple protein species on the membrane and the entropy energy  $E_{\text{ent}}$  for the distribution of proteins

$$E_{\text{tot}} = E_{\text{mem}} + E_{\text{ent}} . \quad (2.1)$$

The membrane bending energy  $E_{\text{mem}}$  is the Canham-Helfrich energy derived from the elasticity of bending of the membrane [31, 72]

$$E_{\text{mem}} = \frac{k}{2} \int_{\Gamma} (H - H_0)^2 ds, \quad (2.2)$$

where  $H$  is the mean curvature of the membrane  $\Gamma$ ,  $H_0$  is the spontaneous curvature, and  $k$  is the bending modulus.

Following the Boltzmann relation, the entropy energy for the membrane with embedded proteins is

defined by

$$E_{\text{ent}} = \frac{1}{\beta} \int_{\Gamma} \left( \sum_{i=0}^n c_i \left[ \ln \left( c_i (\Lambda_i)^2 \right) - 1 \right] \right) ds, \quad (2.3)$$

where  $\beta = 1/(k_B T)$  is the inverse thermal energy and  $\Lambda_i$  are the constants effective sizes of proteins for  $i = 1, \dots, n..$

The total energy becomes,

$$E_{\text{tot}} = \frac{k}{2} \int_{\Gamma} (H - H_0)^2 ds + \frac{1}{\beta} \int_{\Gamma} \left( \sum_{i=0}^n c_i \left[ \ln \left( c_i (\Lambda_i)^2 \right) - 1 \right] \right) ds. \quad (2.4)$$

On the membrane, the particles concentration cannot exceed the available entire surface space, for this, the following saturation condition must be satisfied

$$\sum_{i=0}^n (\Lambda_i)^2 c_i = 1. \quad (2.5)$$

Following the general mass conservation law, the variation of a general surface concentration of proteins  $c$  on the membrane  $\Gamma$ , if  $\Gamma$  evolves only in its normal direction at a velocity  $\mathbf{v} \cdot \mathbf{n}$ , is defined by

$$\frac{Dc}{Dt} + (\nabla_s \cdot \mathbf{v}) c = -\nabla_s \cdot \mathbf{J}, \quad (2.6)$$

where  $D/Dt$  is the material derivative of the advective surface,  $\mathbf{v}$  is a divergence free velocity field in  $\Omega$ ,  $\nabla_s$  is the surface divergence, and  $\mathbf{J}$  is the flux vector on the surface.

Since the fluid in which the membrane is immersed is incompressible, the divergence free velocity field is what the membrane experiences. The surface advection diffusion equation is the following

$$\frac{\partial c}{\partial t} + \mathbf{v} \cdot \nabla_s c = -\nabla_s \cdot \mathbf{J}. \quad (2.7)$$

This equation is not as relevant to the transport of proteins on the membrane surface, since it assumes a steady surface in a velocity field  $\mathbf{v}$ , thus,  $\mathbf{v} \cdot \mathbf{n} = 0$  and  $\nabla \cdot \mathbf{v} = \nabla_s \cdot \mathbf{v}$ .

Using Nernst-Planck formula as an extension of Fick's first law, the flux is given by

$$\mathbf{J} = -D_{\Gamma} \beta c \nabla_s \mu, \quad (2.8)$$

where  $\mu$  is the diffusion potential,  $D_{\Gamma}$  is the lateral diffusion coefficient which is a constant and  $\nabla_s$ , is the

surface gradient.  $\mu$  is defined as the variation of the total energy with respect to the surface concentration as follows

$$\mu_i = \frac{\delta E_{\text{tot}}}{\delta c_i}, \quad i = 1, \dots, n. \quad (2.9)$$

Thanks to the saturation condition (2.5), solving the surface concentrations variation equation for the concentration of the 0th species of proteins will not be necessary. In order to compute the entropic portion of the diffusion potentials, we solve (2.5) to obtain  $(\Lambda_0)^2 c_0$  which we substitute in the entropic energy (2.3) to set a form that facilitate differentiation. Then we obtain

$$E_{\text{ent}} = \frac{1}{\beta} \int_{\Gamma} \left( \frac{1}{(\Lambda_0)^2} \left( 1 - \sum_{i=1}^n (\Lambda_i)^2 c_i \right) \times \left[ \ln \left( 1 - \sum_{i=1}^n (\Lambda_i)^2 c_i \right) - 1 \right] + \sum_{i=1}^n c_i \left[ \ln \left( (\Lambda_i)^2 c_i \right) - 1 \right] \right) ds, \quad (2.10)$$

for the  $i$  th species,  $1 \leq i \leq n$ . Its derivative is

$$\begin{aligned} \frac{\delta E_{\text{ent}}}{\delta c_i} &= \frac{1}{\beta} \left( \frac{1}{(\Lambda_0)^2} \left( -(\Lambda_j)^2 \right) \left[ \ln \left( 1 - \sum_{j=1}^n (\Lambda_j)^2 c_j \right) - 1 \right] + \frac{1}{(\Lambda_0)^2} \left( 1 - \sum_{j=1}^n (\Lambda_j)^2 c_j \right) \left[ \frac{-\Lambda_j^2}{1 - \sum_{j=1}^n (\Lambda_j)^2 c_j} \right] + \ln \left( (\Lambda_j)^2 c_j \right) \right) \\ &= \frac{1}{\beta} \left[ \frac{-\Lambda_j^2}{(\Lambda_0)^2} \ln \left( 1 - \sum_{j=1}^n (\Lambda_j)^2 c_j \right) + \ln \left( (\Lambda_j)^2 c_j \right) \right]. \end{aligned} \quad (2.11)$$

When proteins are induced in the bilayer, the spontaneous curvature should depend on the structure and the distribution of proteins [58]. This biological nature motivates to model the local membrane spontaneous curvature as a parameter that depends on the concentration of proteins. To this end, each protein species  $i$  has its intrinsic spontaneous curvature, denoted  $H_0(c_i)$  and defined as in [90] by

$$H_0 = \left( \frac{\sum_{i=0}^n H_0^i (\Lambda_i)^2 c_i}{\sum_{i=0}^n (\Lambda_i)^2 c_i} \right). \quad (2.12)$$

$H_0^i$  are the spontaneous curvature constants pertaining to protein structures. We modeled every specie as a hard disk occupying some surface area on the membrane see Fig. 2.2, so we take  $(\Lambda_i)^2$  for an effective surface area.

Using this condition (2.5) the spontaneous curvature defined by (2.12) can be simplified as

$$H_0 = \left( \sum_{i=0}^n H_0^i (\Lambda_i)^2 c_i \right). \quad (2.13)$$

The variation of the bending energy of the membrane with respect to the concentrations represents the curvature driven portion by of the diffusion potential. Using the expression of the bending energy given in (2.2) and equation (2.13), the variation is computed as

$$\frac{\delta E_{\text{memn}}}{\delta c_i} = k(H_0 - H) \frac{\partial H_0}{\partial c_i} = kH_0^i (\Lambda_i)^2 (H_0 - H). \quad (2.14)$$

The potential for each species is given by summing (2.11) and (2.14)

$$\mu_i = \frac{1}{\beta} \left[ \frac{-(\Lambda_i)^2}{(\Lambda_0)^2} \ln \left( 1 - \sum_{j=1}^n c_j (\Lambda_j)^2 \right) + \ln \left( c_i (\Lambda_i)^2 \right) \right] + H_0^i (\Lambda_i)^2 (H_0 - H), \quad (2.15)$$

### 2.2.2 Equation of the diffusive proteins on the surface membrane

Now, we rearrange the diffusion equation (2.7). We define

$$L^i(c_i) = \ln \left( c_i (\Lambda_i)^2 \right), \quad (2.16)$$

$$R^i(c_i) = \frac{-(\Lambda_i)^2}{(\Lambda_0)^2} \ln \left( 1 - \sum_{j=1}^m c_j (\Lambda_j)^2 \right), \quad (2.17)$$

$$P(c_i) = (H_0(c_i) - H). \quad (2.18)$$

$L$  indicates the leading order term for proteins,  $R$  corresponds to the size restrictions and  $P$  is the term corresponding to the curvature function. Using equations (2.16), (2.17) and (2.18), the diffusion potential (2.15) becomes

$$\mu_i = \frac{1}{\beta} (L^i + R^i) + H_0^i (\Lambda_i)^2 P. \quad (2.19)$$

In order to compute the flux (2.8), we have

$$\nabla_s \mu_i = \frac{1}{\beta} (\nabla_s L^i + \nabla_s R^i) + H_0^i (\Lambda_i)^2 \nabla_s P, \quad (2.20)$$

The derivative of the leading term is the following

$$\nabla_s L^i = \frac{\nabla_s c_i}{c_i}. \quad (2.21)$$

We define

$$M_i = \beta H_0^i (\Lambda_i)^2. \quad (2.22)$$

If we consider the equation on a stationary membrane ( $v = 0$ ) and neglect the size effect term involving  $R$ , the diffusion equation (2.7) for each protein species becomes

$$\frac{\partial c}{\partial t} = D \nabla_s \cdot (\nabla_s c + M c \nabla_s (H_0 - H)). \quad (2.23)$$

This equation shows that the curvature driven diffusive species is due to the difference in the actual membrane curvature and the spontaneous curvature of the membrane  $H_0 - H$ . This term is the one responsible for driving the localization of proteins to the position on the membrane surface where the preferred mean curvature is observed.

### 2.3 Fluctuations and instability of membrane in the presence in a diffusion field using shape optimization

In this section we study the geometric shape optimization of membrane in the presence of a diffusion field of protein molecules, which have the ability to adsorb on, and to desorb from the membrane. The main idea of this study is to vary the position of the boundaries of a given initial shape of the membrane, without changing its topology which remains the same as the initial shape. We develop a model that includes, molecular diffusion along the membrane as well as the attachment and detachment of molecules to and from the membrane.

Geometric shape optimization theory based on the boundary variation method, dates back to J. Hadamard in 1907 [71]. It has been very classic since then. The first results of existence of an optimal shape under constraint of geometric regularity are due to D. Chenaïs [39], F. Murat and J. Simon [95],[96]. More recently, some results of existence under topological constraint for flat shapes have been obtained by V. Sverak [128] for a membrane model, then by A. Chambolle [34] for the elasticity model. There are other types of additional constraints for the existence of optimal shapes. For example, the work of L. Ambrosio and G. Buttazzo [15] where an upper bound on the perimeter is imposed, which prevents the creation of too many holes.

In this work we follow the method of F. Murat and J. Simon [96] based on the study of optimal control problems where the control is the shape of a domain in which the state of the system is defined

by a partial differential equation. Compared to other optimization problems, many new difficulties arise. In particular, the mathematical representation of the shape. For example, a shape can be represented by the characteristic function of its domain (which is 1 inside and 0 outside), but in this case, we don't know how we can represent shape variations. Indeed, a linear combination of characteristic functions is not, in general, a characteristic function. Therefore we can not do "variations computation" in the space of the characteristic functions, and compute the gradient. This is a typical difficulty in geometric shape optimization that is important to focus on for both theoretical and numerical reasons.

A new numerical implementation of geometric shape optimization problem has been used in this work. It is based on the level set method of S. Osher and J. Sethian [104]. The main idea is to represent the membrane as the set of zero level of a discretized function on a fixed mesh. This method is based on capturing shapes in an Eulerian fixed mesh. The main advantage of this method is that it allows to considerably reduce the cost of the computations and gives a simple expression of the normal vector and the curvature.

We present in this study a model of membrane ( $\Gamma_0$ ) in the presence of a diffusion field of molecules  $c_{\Omega_0}$ . The aim of this work is to understand the effect of molecules on the membrane shape. First we proved the existence of an optimal shape then we computed the first derivative with respect to the domain of the free energy of the membrane in presence of diffusion and finally we did numerical simulation to see the morphological instability of the membrane induced by interaction with molecules.

### 2.3.1 Mathematical Model

At rest, the membrane ( $\Gamma_0$ ) represent the variable part of the border of a reference domain  $\Omega_0$  whose border is divided into tow disjointed parts (see figure2.3)

$$\partial\Omega_0 = \Gamma_0 \cup \Gamma_D,$$

where  $\Gamma_0$ (the membrane) is the variable part of the boundary (Neumann boundary condition),  $\Gamma_D$  is the fixed part of the boundary (Dirichlet boundary condition). The tow parts of the boundary are assumed to be non-empty. We assumed that the variable part  $\Gamma_0$  of the border is free of any effort, which means that the membrane is supposed to be impermeable and the molecules can just adsorb on, or desorb from the membrane(homogeneous Neumann boundary condition).

The concentration of the molecules in the surrounding environment (see Figure2.3: the blue part)

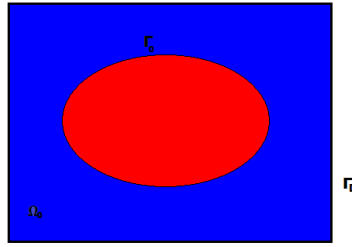


Figure 2.3: The red part is the cell with membrane  $\Gamma_0$  and the blue part represent the surrounding fluid containing the molecules

verifies the following system

$$\begin{cases} \eta c_{\Omega_0} - d\Delta c_{\Omega_0} = f & \text{in } \Omega_0, \\ \frac{\partial c_{\Omega_0}}{\partial n} = 0 & \text{on } \Gamma_0, \\ c_{\Omega_0} = 0 & \text{on } \Gamma_D. \end{cases} \quad (2.24)$$

where

- $d$  is diffusion coefficient
- $f$  is the reaction term
- $\eta$  is a positive parameter

The total free energy of the membrane is given by [49]

$$E(\Omega_0) = \frac{k}{2} \int_{\partial\Omega_0} (K_{\Omega_0} - K_0)^2 ds - \int_{\partial\Omega_0} k\Lambda K_{\Omega_0} c_{\Omega_0} ds + \int_{\partial\Omega_0} \frac{\alpha}{2} (c_{\Omega_0} - c_0)^2 ds. \quad (2.25)$$

The first term represents the curvature energy of the membrane, the second one represents the coupling term between curvature and surface concentration and the last term represent the concentration deviation of adsorbed molecules from its equilibrium value  $c_0$ .

The physical parameters in (2.25) are

- $K$  is the mean local curvature,
- $K_0$  is the spontaneous curvature,
- $k$  is the bending rigidity,

- $\Lambda$  is the molecule size,
- $\alpha$  is supposed to be positive constant.

**Remark 2.3.1**

*In this section we have changed the notation of the mean curvature  $H$  to  $K$ , to not be confused with the Hilbert spaces*

The geometric shape optimization problem is written us follows

$$\inf_{\Omega \in \mathcal{D}_{ad}} E(\Omega), \tag{2.26}$$

where it remains to define the set of admissible shapes  $\mathcal{D}_{ad}$ .

This work is organized as follows. In the next subsection we will consider the existence of the optimal shape under some regularity constraints. In this subsection we will also introduce a framework for mathematical shape representation that will be useful to define a notion of derivation with respect to the domain. Then we will develop this derivation theory which will allows to write the optimality conditions, and finally construct numerical simulation.

**2.3.2 Existence of optimal solution**

The problem is rather the absence of an optimal shape than its existence. However, if additional constraints of a regularity nature are added, then there exist an optimal shape in a restricted class of admissible shapes.

**Existence under a condition of regularity**

We give here some notions of topology on a domain of regular boundary, using the perturbations of the identity. Taking inspiration from the approach developed in [95] and [96] to demonstrate the existence result. We will take this framework further to establish a concept of derivation with respect to the domain.

Let  $\Omega_0$  be a reference domain, which we assumed to be a connected bounded open set of  $\mathbb{R}^n$ , of the class  $W^{2,\infty}$ . As in the introduction, we suppose that the border of  $\Omega_0$  is divided into tow disjointed parts (not empty)

$$\partial\Omega_0 = \Gamma_0 \cup \Gamma_D,$$

where  $\Gamma_D$  is fixed and only  $\Gamma_0$  is variable.

The main idea is to define a set of admissible shapes  $\mathcal{D}_{ad}$  from which any element  $\Omega$  is obtained by applying a regular diffeomorphism to the reference domain  $\Omega_0$ . Thus the space of admissible shapes is very significantly restricted, but we gain a very simple representation of the shape in terms of diffeomorphisms.

Let us first remind that,  $W^{2,\infty}(\mathbb{R}^n, \mathbb{R}^n)$  is the space of Lipschitz functions  $\phi$  from  $\mathbb{R}^n$  to  $\mathbb{R}^n$  such that  $\phi$ ,  $\nabla\phi$ , and  $\Delta\phi$  are uniformly bounded in  $\mathbb{R}^n$  to which we associate the following norm which makes it a Banach space

$$\|\phi\|_{W^{2,\infty}(\mathbb{R}^n, \mathbb{R}^n)} = \sup_{x \in \mathbb{R}^n} \text{ess} (\sum_{0 < |\alpha| \leq 2} |D^\alpha \phi(x)|_{\mathbb{R}^n}^2)^{\frac{1}{2}}. \quad (2.27)$$

We define a space of diffeomorphisms as follows

$$\tau^{2,\infty} = \left\{ T \text{ such that } (T - Id) \in W^{2,\infty}(\mathbb{R}^n, \mathbb{R}^n), (T^{-1} - Id) \in W^{2,\infty}(\mathbb{R}^n, \mathbb{R}^n) \right\}. \quad (2.28)$$

Somehow we can see diffeomorphisms of  $\tau^{2,\infty}$  as perturbations of the identity.

Now we can then introduce a space of admissible shapes obtained by deformation of  $\Omega_0$

$$\mathcal{D}_{\Omega_0}^{2,\infty} = \left\{ \Omega \text{ such that } \exists T \in \tau^{2,\infty}, \Omega = T(\Omega_0) \right\}. \quad (2.29)$$

Each admissible shape  $\Omega \in \mathcal{D}_{\Omega_0}^{2,\infty}$ , is represented by a diffeomorphism  $T \in \tau^{2,\infty}$ . This representation is not unique because it is possible that two diffeomorphisms  $T \neq T_2$  in  $\tau^{2,\infty}$  lead to the same open set  $\Omega = T(\Omega_0) = T_2(\Omega_0)$ . Since the functions of  $W^{2,\infty}(\mathbb{R}^n, \mathbb{R}^n)$  are continuous, the applications  $T$  of  $\tau^{2,\infty}$  are also homomorphisms, which implies that they preserve the topology of the domains to which they are applied. Thus, all admissible shapes of  $W^{2,\infty}(\mathbb{R}^n, \mathbb{R}^n)$  have the same topology as  $\Omega_0$ . Therefore this approach is not helpful to optimize the topology (number of holes or connected components of the boundary). We can then introduce a pseudo-distance on  $\mathcal{D}_{\Omega_0}^{2,\infty}$  (it verifies only a weak version of the triangular inequality)

$$d^{2,\infty}(\Omega, \Omega_2) = \inf_{T \in \tau | T(\Omega) = \Omega_2} \left( \|T - Id\|_{W^{2,\infty}(\mathbb{R}^n, \mathbb{R}^n)} + \|T^{-1} - Id\|_{W^{2,\infty}(\mathbb{R}^n, \mathbb{R}^n)} \right). \quad (2.30)$$

We can now define a condition of uniform regularity of the admissible shapes by being limited to open

sets  $\Omega$  close to  $\Omega_0$  in the sense of this pseudo-distance  $d^{2,\infty}$ . More precisely, for  $R > 0$  we define

$$\mathcal{D}_{ad} = \left\{ \Omega \in \mathcal{D}_{\Omega_0}^{2,\infty} / d^{2,\infty}(\Omega, \Omega_0) \leq R, \Gamma_0 \cup \Gamma_D \subset \partial\Omega_0, |\Omega| = V_0 \right\}. \quad (2.31)$$

The choice of the regularity constant  $R$  is arbitrary as well as the choice of the reference domain  $\Omega_0$ .

**Theorem 2.3.1**

*If we assume that*

$$\left\{ \begin{array}{l} \Omega_0 \text{ is a connected bounded open set of } \mathbb{R}^n \text{ of the class } W^{2,\infty}, \\ f \in L^2(\mathbb{R}^n), \quad K_0 \in H^1(\mathbb{R}^n) \quad \text{and} \quad c_0 \in H^1(\mathbb{R}^n). \end{array} \right. \quad (2.32)$$

*There exist an optimal shape  $\Omega^*$ , such that*

$$\Omega^* \in \mathcal{D}_{ad}, \quad E(\Omega^*) \leq E(\Omega), \quad \forall \Omega \in \mathcal{D}_{ad}. \quad (2.33)$$

**Remark 2.3.2**

The proof of this theorem rests on a compactness argument. The essential idea is that the admissible shapes of  $\mathcal{D}_{ad}$  can not change their topology, and the uniform regularity bound  $R$  prevents the boundaries of the  $\Omega$  shape from being too oscillating.

**Proof.**

Let  $\Omega_0$  be a fixed connected bounded open set of  $\mathbb{R}^n$  of the class  $W^{2,\infty}$  such that  $|\Omega_0| = V_0$ , every domain  $\Omega \in \mathcal{D}^{2,\infty}$  is a connected bounded open set of the class  $W^{2,\infty}$  [96]. We will prove that

- $\mathcal{D}_{ad}$  is a compact of  $\mathcal{D}^{2,\infty}$
- $E(\Omega)$  is a continuous functional of  $\mathcal{D}^{2,\infty}$

For the compactness of  $\mathcal{D}_{ad}$ , let  $\Omega \in \mathcal{D}_{ad}$  and  $R \geq 0$  fixed. For all sequence  $\{\Omega_n\}_{n \in \mathbb{N}}$  of  $\mathcal{D}_{ad}$  such that  $d^{2,\infty}(\Omega_n, \Omega) \leq R$  and  $|\Omega_n| = V_0$ , we can extract a subsequence that we can also call  $\Omega_n$  that converges to  $\Omega_* \in \mathcal{D}^{2,\infty}$  such that  $d^{2,\infty}(\Omega_*, \Omega) \leq R$  in Ref.[96](theorem 2,4), it remains to show that  $|\Omega_*| = V_0$ . Let  $K_1$  and  $K_2$  be closed subsets of  $\mathbb{R}^n$  such that  $K_1 \subset \Omega_*$  and  $K_2 \subset \mathbb{R}^n - \overline{\Omega_*}$ . Then, according to the definition of the Hausdorff distance,  $K_1 \subset \Omega_n$  and  $K_2 \subset \mathbb{R}^n - \overline{\Omega_n}$  for  $n$  large enough.

We consider closed subsets reduced to a single point, since  $mes(\partial\Omega_*) = 0$  it results that

$$\chi(\Omega_n) \longrightarrow \chi(\Omega_*) \quad a.e \quad \text{in } \mathbb{R}^n$$

Using Lebesgue's theorem,  $\Omega_*$  is bounded and the sequence  $\Omega_n$  is bounded in  $L^\infty(\mathbb{R}^n)$  it comes that

$$\chi(\Omega_n) \longrightarrow \chi(\Omega_*) \quad \text{in } L^\infty(\mathbb{R}^n) \quad \text{starweak and strongly in } L^p(\mathbb{R}^n) \quad 1 \leq p < \infty.$$

which means that  $|\Omega_*| = V_0$  and so  $\Omega_* \in \mathcal{D}_{ad}$ . Hence the compactness of  $\mathcal{D}_{ad}$ .

For the continuity of the functional  $E$  we will use the variable change  $\Omega = T(\Omega_0)$ ,  $T \in \tau^{2,\infty}$ , where  $\Omega \in \mathcal{D}^{2,\infty}$  is a connected bounded open set of the class  $W^{2,\infty}$ , such that  $|\Omega| = V_0$ .

Let  $\Omega_n$  be a sequence of  $\mathcal{D}_{\Omega_0}^{2,\infty}$  that converges to  $\Omega \in \mathcal{D}_{\Omega_0}^{2,\infty}$ , as a result of [96](theorem 2.4) we can extract a subsequence  $\Omega_m$ , then we have

$$\Omega_m = T_m(\Omega_0), \quad \Omega = T(\Omega_0) \quad \text{where } T_m, T \in \tau^{2,\infty}. \quad (2.34)$$

Now we need the continuity of the state transport  $c_{\Omega_m}$  to the fixed domain  $\Omega_0$ . The function  $c_{\Omega_m}$  is a unique solution of the following equation in the domain  $\Omega_m = T_m(\Omega_0)$

$$\begin{cases} c_{\Omega_m} \in H^1(\Omega_m), \\ \int_{\Omega_m} d \nabla c_{\Omega_m} \nabla \varphi + \eta c_{\Omega_m} \varphi = \int_{\Omega_m} f \varphi \quad \forall \varphi \in H^1(\Omega_m). \end{cases} \quad (2.35)$$

Applying the variable change  $T_m$  to equation (2.35) in order to return back to the fixed domain  $\Omega_0$ , as in Ref.[96](lemma 4.1), we deduce that

$$\begin{cases} c(\Omega_m) \circ T_m \in H^1(\Omega_0), \\ \int_{\Omega_0} d \langle {}^t [T'_m]^{-1} \nabla (c(\Omega_m) \circ T_m), {}^t [T'_m]^{-1} \nabla \varphi \rangle | \det [T'_m] | + \eta \langle c(\Omega_m) \circ T_m, \varphi \rangle | \det [T'_m] | \\ = \int_{\Omega_0} \langle f \circ T_m, \varphi \rangle | \det [T'_m] | \quad \forall \varphi \in H^1(\Omega_0). \end{cases} \quad (2.36)$$

As a result see Ref.[96](lemma 4.2, 4.3 and 4.4), we get

$$\begin{cases} {}^t [T'_m]^{-1} \longrightarrow {}^t [T']^{-1} \quad \text{in } L^\infty(\mathbb{R}^n, \mathbb{R}^{2n}), \\ | \det [T'_m] | \longrightarrow | \det [T'] | \quad \text{in } L^\infty(\mathbb{R}^n, \mathbb{R}^{2n}), \\ f \circ T_m \longrightarrow f \circ T \quad \text{in } L^2(\Omega_0). \end{cases} \quad (2.37)$$

The continuity of the solution of equation (2.36) with respect to its coefficients and to the second member

(2.37) and the fact that  $\Omega_m \longrightarrow \Omega$  implies that

$$c_{\Omega_m} \circ T_m \longrightarrow c_{\Omega} \circ T \quad \text{in } H^1(\Omega_0).$$

The uniform ellipticity of the equation (2.36) in  $m$  gives

$$\left\{ \begin{array}{l} \|{}^t [T'_m]^{-1}\|_{W^{1,\infty}(\mathbb{R}^n, \mathbb{R}^{2n})} \leq C \quad \forall m, \\ | \det [T'_m] |_{W^{1,\infty}(\mathbb{R}^n)} \leq C \quad \forall m, \\ \| f \circ T_m \|_{L^2(\Omega_0)} \leq C \quad \forall m. \end{array} \right. \quad (2.38)$$

Since  $\Omega_0$  is a bounded open set of the class  $W^{2,\infty}$ , the sequence  $c_{\Omega_m} \circ T_m$  is bounded in  $H^2(\Omega_0)$ . We have then

$$c_{\Omega_m} \circ T_m \longrightarrow c_{\Omega} \circ T \quad \text{in } H^2(\Omega_0) \quad \text{Weak.} \quad (2.39)$$

Lets now verify the continuity of the functional E. We denote by  $n_{\Omega}$  the exterior normal vector to  $\partial\Omega$ , we have

$$E(\Omega_m) = \int_{\partial\Omega_m} \frac{k}{2} (K_{\Omega_m} - K_0)^2 - k\Lambda K_{\Omega_m} c_{\Omega_m} + \frac{\alpha}{2} (c_{\Omega_m} - c_0)^2 ds. \quad (2.40)$$

Where  $K_{\Omega_m} = \text{div}(n_{\Omega_m})$ . We apply the variable changes  $T_m$

$$E(\Omega_m) = \int_{\partial\Omega_0} \left[ \frac{k}{2} (K_{\Omega_m} \circ T_m - K_0 \circ T_m)^2 - k\Lambda K_{\Omega_m} \circ T_m c_{\Omega_m} \circ T_m + \frac{\alpha}{2} (c_{\Omega_m} \circ T_m - c_0 \circ T_m)^2 \right] \times | \det [T'_m] | |{}^t [T'_m]^{-1} n(\Omega_0) |_{\mathbb{R}^n} ds. \quad (2.41)$$

The convergence results of (2.37) also holds in  $L^\infty(\partial\Omega_0)$ , since  $T_m$  and  $T$  are  $C^1(\mathbb{R}^n, \mathbb{R}^n)$ . Furthermore, we have

$$|{}^t [T'_m]^{-1} n(\Omega_0) |_{\mathbb{R}^n} \geq \frac{1}{\| [T'_m] \|_{L^\infty(\mathbb{R}^n, \mathbb{R}^{2n})}} \quad \text{pp on } \partial\Omega_0.$$

Finally by the results obtained in (2.38) and the continuity Lemma 4.4 i) in Ref.[96] we have

$$K(\Omega_m) \circ T_m \longrightarrow K(\Omega) \circ T \quad \text{in } L^2(\partial\Omega_0) \quad \text{strongly,}$$

$$K_0 \circ T_m \longrightarrow K_0 \circ T \quad \text{in } L^2(\partial\Omega_0) \quad \text{strongly,}$$

$$c(\Omega_m) \circ T_m \longrightarrow c(\Omega) \circ T \quad \text{in } L^2(\partial\Omega_0) \quad \text{strongly.}$$

which implies that

$$E(\Omega_m) \longrightarrow E(\Omega).$$

This convergence lies for all sequence  $\{\Omega_n\}_{n \in \mathbb{N}}$  which ends the proof

### 2.3.3 Differentiability with respect to domain

In this subsection we take again the shape representation introduced in section 2, which will allow us to naturally define the notion of derivation with respect to the domain. Once we are able to differentiate, we can write the optimality conditions that we will use to characterize the optimal shape and compute the gradient to implement a numerical optimization method. It is therefore a fundamental concept both from the theoretical and practical point of view.

Let  $\Omega_0$  (reference domain) be a regular bounded open set of  $\mathbb{R}^n$ . We consider the class of admissible shapes  $\mathcal{D}_{\Omega_0}^{2,\infty}$  as defined before. It is natural to consider the variable  $\theta$  defined by

$$T = Id + \theta \quad \text{where } \theta \in W^{2,\infty}(\mathbb{R}^n, \mathbb{R}^n) \text{ small enough.}$$

With this notation  $\Omega$  is defined by

$$\Omega = (Id + \theta)(\Omega_0).$$

We can see  $\theta(x)$  as a vector field which transports or displaces the reference domain  $\Omega_0$  (fig. 2.3.3). In other words, each admissible shape  $\Omega \in \mathcal{D}_{\Omega_0}^{2,\infty}$  is represented by a vector field  $\theta(x)$  of  $\mathbb{R}^n$  in  $\mathbb{R}^n$ . We can then define a notion of differentiability in  $\Omega_0$  by using the derivation with respect to  $\theta(x)$ .

**Remark 2.3.3**

-If  $\theta(x)$  is small enough then  $T = Id + \theta$  belongs to the set  $\tau^{2,\infty}$  of diffeomorphisms on  $\mathbb{R}^n$ .

-A function  $E$  defined in  $\mathcal{D}_{\Omega_0}^{2,\infty}$  is differentiable at  $\Omega_0$  if the function  $\theta \longrightarrow E((I + \theta)(\Omega_0)) = E(\Omega)$  is Frechet Differentiable (in the usual sense) from  $W^{2,\infty}$  to  $\mathbb{R}$  in 0, and its derivative is defined by

$$\frac{\partial E}{\partial \Omega}(\Omega_0) = \frac{\partial E((I + \theta)(\Omega_0))}{\partial \theta}(0) \in \mathcal{L}_c(W^{2,\infty}(\mathbb{R}^n, \mathbb{R}^n), \mathbb{R}).$$

We consider the equation defined by (2.24) in  $\Omega$  which admits a unique solution  $c_\Omega \in H^1(\Omega)$ . The

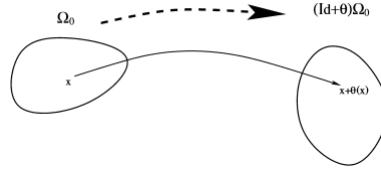


Figure 2.4: Definition of a domain transported by a vector field  $\theta$ .

variational formulation of (2.24) in  $\Omega$  is to find  $c \in H^1(\Omega)$  such that

$$\begin{cases} c \in H^1(\Omega), \\ \int_{\Omega} d\nabla c \nabla \varphi + \eta c \varphi = \int_{\Omega} f \varphi \quad \forall \varphi \in H^1(\Omega). \end{cases} \quad (2.42)$$

### Theorem 2.3.2

Let  $\Omega_0$  be a regular open set. The total free energy of the membrane  $E(\Omega_0)$ , defined by (2.25), is differentiable from  $\mathcal{D}^{2,\infty}$  to  $\mathbb{R}$ , and its derivative with respect to the domain is defined by

$$\begin{aligned} E'(\Omega_0)(\theta) &= \int_{\partial\Omega_0} (\theta \cdot n) \left\{ \eta c p + d\nabla c \nabla p - f p + k(K - K_0 - \Lambda c) \frac{\partial K}{\partial n} \right. \\ &\quad \left. + \frac{k}{2} K (K - K_0)^2 - k \Lambda K^2 c + \frac{\alpha}{2} K (c - c_0)^2 + k(\Delta_{\partial\Omega_0} K - \Lambda \Delta_{\partial\Omega_0} c) \right\}. \end{aligned}$$

Where  $n$  is the normal vector,  $\Delta_{\partial\Omega_0}$  is the Laplace Beltrami operator defined by  $\Delta_{\partial\Omega_0} c_{\Omega_0} = \Delta c_{\Omega_0} - K \frac{\partial c_{\Omega_0}}{\partial n} - \frac{\partial^2 c_{\Omega_0}}{\partial n^2}$  on  $\Gamma_0$ , and  $p_{\Omega_0}$  is the solution of the adjoint state

$$\begin{cases} \eta p_{\Omega_0} - d\Delta p_{\Omega_0} = 0 & \text{in } \Omega_0 \\ d \frac{dp_{\Omega_0}}{dn} = k \Lambda K - \alpha (c_{\Omega_0} - c_0) & \text{on } \Gamma_0 \\ p_{\Omega_0} = 0 & \text{on } \Gamma_D \end{cases} \quad (2.43)$$

where  $\partial\Omega_0 = \Gamma_0 \cup \Gamma_D$

### Remark 2.3.4

The rigorous computation of the derivative of an objective function requires the ability to derive the solution of the state equation (c) even though this derivative ( $\tilde{C}$ (Eulerian derivative of c) or  $\bar{C}$ (Lagrangian derivative of c)) does not appear in the final result [96]. There is a certain waste, especially since the computation of  $\tilde{C}$  or  $\bar{C}$  is quite delicate and tedious. Fortunately, there is a method faster to derive (at least formally) an objective function called the Lagrangian method, developed by J. Cea in [33]. This method

also allows to define the adjoint state  $p_{\Omega_0}$  in a very simple way. In practice, this is the most used method and easy to compute.

**Proof.**

The proof of this theorem is based on the Lagrangian method.

$$E(\Omega) = \int_{\partial\Omega} \frac{k}{2}(K - K_0)^2 - k\Lambda Ku + \frac{\alpha}{2}(u - u_0)^2. \quad (2.44)$$

We suppose first that  $u$  is a solution of (2.24) in  $\Omega$  which means that  $u$  verifies (2.41)  $\forall q \in H^1(\Omega)$ . We introduce the Lagrangian which is the sum of the objective function and the variational formulation of the equation of state

$$\mathcal{L}(\Omega, u, q) = E(\Omega) + \int_{\Omega} \eta u q + d\nabla u \nabla q - f q dx, \quad (2.45)$$

with  $u$  and  $q$  in  $H^1(\mathbb{R}^n)$ . It is important to note that the space  $H^1(\mathbb{R}^n)$  does not depend on  $\Omega$  then the three variables of the Lagrangian  $\mathcal{L}$  are independent. The partial derivative of  $\mathcal{L}$  with respect to  $q$  in the direction  $\phi \in H^1(\mathbb{R}^n)$  is

$$\left\langle \frac{\partial \mathcal{L}}{\partial q}(\Omega, u, q), \phi \right\rangle = \int_{\Omega} \eta u q + d\nabla u \nabla q - f q dx, \quad (2.46)$$

which, when it vanishes, gives (by construction) the variational formulation of the equation of state (2.24). The partial derivative of  $\mathcal{L}$  with respect to  $u$  in the direction  $\phi \in H^1(\mathbb{R}^n)$  is

$$\left\langle \frac{\partial \mathcal{L}}{\partial u}(\Omega, u, q), \phi \right\rangle = \int_{\Omega} \eta \phi q - d\phi \Delta q dx + \int_{\partial\Omega} d \frac{dq}{dn} \phi ds + \int_{\partial\Omega} \alpha(u - u_0)\phi - k\Lambda K \phi ds. \quad (2.47)$$

Which, when it vanishes, gives nothing else than the variational formulation of the adjoint state equation (2.43). Finally, the derivative of  $\mathcal{L}$  with respect to the domain, evaluated by assuming that  $u$  and  $q$  are fixed (i.e. as a partial derivative), in the direction  $\theta$  is

$$\begin{aligned} \frac{\partial \mathcal{L}}{\partial \Omega}(\Omega_0, u, q)(\theta) &= \int_{\partial\Omega_0} (\theta \cdot n) \left\{ \eta u q + d\nabla u \nabla q - f q + K \left( \frac{k}{2}(K - K_0)^2 - k\Lambda Ku + \frac{\alpha}{2}(u - u_0)^2 \right) \right. \\ &+ \left. \frac{\partial}{\partial n} \left( \frac{k}{2}(K - K_0)^2 - k\Lambda Ku + \frac{\alpha}{2}(u - u_0)^2 \right) \right\} ds + \int_{\partial\Omega_0} k((K - K_0) - \Lambda u) \frac{\partial K}{\partial \Omega}(\Omega_0)(\theta) ds. \end{aligned}$$

Where (see for example Ref.[80])

$$\frac{\partial K}{\partial \Omega}(\Omega_0)(\theta) = \frac{\partial(\operatorname{div}(n))}{\partial \Omega}(\Omega_0)(\theta) = \operatorname{div}\left(\frac{\partial n}{\partial \Omega}(\Omega_0)(\theta)\right) = -\nabla \cdot (\nabla_{\partial \Omega_0}(\theta \cdot n)).$$

And

$$\frac{\partial}{\partial n}\left(\frac{k}{2}(K - K_0)^2 - k\Lambda Ku + \frac{\alpha}{2}(u - u_0)^2\right) = k(K - K_0 - \Lambda u)\frac{\partial K}{\partial n}.$$

When it comes to evaluate this derivative at the state  $c_{\Omega_0}$  and the adjoint state  $p_{\Omega_0}$ , we find exactly the value of the derivative of the objective function

$$\frac{\partial \mathcal{L}}{\partial \Omega}(\Omega_0, c, p)(\theta) = E'(\Omega_0). \quad (2.48)$$

This equation is not a coincidence. Indeed, for all  $q \in H^1(\mathbb{R}^n)$

$$\mathcal{L}(\Omega, c_{\Omega}, q)(\theta) = E(\Omega). \quad (2.49)$$

Since  $c_{\Omega}$  verifies the variational formulation of the state system (2.24) which depends on  $\Omega$ , but not  $q$ , by deriving this expression and using the composite derivative theorem, it comes

$$E'(\Omega_0) = \frac{\partial \mathcal{L}}{\partial \Omega}(\Omega_0, c(\Omega_0), q)(\theta) + \left\langle \frac{\partial \mathcal{L}}{\partial u}(\Omega_0, c(\Omega_0), q), c'(\Omega_0)(\theta) \right\rangle. \quad (2.50)$$

Taking  $q = p_{\Omega_0}$  solution of the adjoint state (2.43), the last term vanishes and we obtain

$$\begin{aligned} E'(\Omega_0) &= \frac{\partial \mathcal{L}}{\partial \Omega}(\Omega_0, c_{\Omega_0}, p_{\Omega_0})(\theta) \\ &= \int_{\partial \Omega_0} (\theta \cdot n) \left\{ \eta c_{\Omega_0} p_{\Omega_0} + d \nabla c_{\Omega_0} \nabla p_{\Omega_0} - f p_{\Omega_0} + \frac{k}{2} K (K - K_0)^2 - k \Lambda K^2 c_{\Omega_0} + \frac{\alpha}{2} K (c_{\Omega_0} - c_0)^2 \right. \\ &\quad \left. + k (K - K_0 - \Lambda c_{\Omega_0}) \frac{\partial K}{\partial n} \right\} ds + \int_{\partial \Omega_0} k ((K - K_0) - \Lambda c_{\Omega_0}) (-\nabla \cdot (\nabla_{\partial \Omega_0}(\theta \cdot n))) ds \\ &= \int_{\partial \Omega_0} (\theta \cdot n) \left\{ \eta c_{\Omega_0} p_{\Omega_0} + d \nabla c_{\Omega_0} \nabla p_{\Omega_0} - f p_{\Omega_0} + \frac{k}{2} K (K - K_0)^2 - k \Lambda K^2 c_{\Omega_0} + \frac{\alpha}{2} K (c_{\Omega_0} - c_0)^2 \right. \\ &\quad \left. + k (K - K_0 - \Lambda c_{\Omega_0}) \frac{\partial K}{\partial n} + k (\Delta_{\partial \Omega_0} K - \Lambda \Delta_{\partial \Omega_0} c_{\Omega_0}) \right\} ds. \end{aligned} \quad (2.51)$$

Thanks to this simple computation, we obtain a "good" result for  $E'(\Omega_0)$  without going through the Eulerian derivative or material derivative which are rather complicated to establish. However, this quick

calculation of the derivative  $E'(\Omega_0)$  is only formal. In fact, it assumes that we already know the differentiability of  $c$  with respect to the domain, and that we can apply the rule of composed derivation

## 2.4 Numerical Analysis

### 2.4.1 Level-Set Method

In order to evolve the shape we will consider the variable part of the border  $\Gamma$  and look for a function  $\phi$  such that  $\Gamma = \{x \in \mathbb{R}^2 / \phi(x) = 0\}$ . So, instead of deforming the shape by studying the evolution of  $\Gamma$ , we will transform the function  $\phi$  into  $\tilde{\phi}$  then take as a new border the set  $\{x \in \mathbb{R}^2 / \tilde{\phi}(x) = 0\}$ . The advantage is that many geometric properties of  $\Gamma$  are expressed more easily using  $\phi$ . For example, the vector normal to  $\Gamma$  is defined by  $n = \frac{\nabla\phi}{\|\nabla\phi\|}$  and the mean curvature defined by  $K = \nabla \cdot \left( \frac{\nabla\phi}{\|\nabla\phi\|} \right)$ . Many  $\phi$  functions are suitable, we will then impose conditions which without leading to the uniqueness of  $\phi$ , will allow us to work with better functions. So we ask  $\phi$  to be negative inside  $\Gamma$  and positive outside. In practice, we choose a function whose gradient does not vanish on  $\Gamma$ . In fact, we try to work with a function close to the signed distance function at  $\Gamma$ .

We want to evaluate a shape  $\Omega_0$  with border  $\Gamma_0 = \{x \in \mathbb{R}^2 / \phi_0(x) = 0\}$  along the vector field

$$\vec{V} = V \cdot \frac{\nabla\phi_0}{\|\nabla\phi_0\|},$$

where  $V$  is obtained by Theorem 2.3.2 (Eq. (2.51)) as follows

$$V = \eta c p + d \nabla c \nabla p - f p + k(K - K_0 - \Lambda c) \frac{\partial K}{\partial n} + \frac{k}{2} K(K - K_0)^2 - k \Lambda K^2 c + \frac{\alpha}{2} K(c - c_0)^2 + k(\Delta_{\partial\Omega_0} K - \Lambda \Delta_{\partial\Omega_0} c). \quad (2.52)$$

For that we will solve the system

$$\begin{cases} \partial_t \Phi + \vec{V} \cdot \nabla \Phi = 0, \\ \Phi(t_0, 0) = \phi_0. \end{cases} \quad (2.53)$$

As a new border we will take  $\Gamma = \{x \in \mathbb{R}^2 / \phi(x) = 0\}$ , where  $\phi = \Phi(t_0 + \Delta t, \cdot)$ .

#### Remark 2.4.1

To know the evolution of  $\phi$  in time. In practice, the problem lies from the fact that if  $x$  is a mesh node,

$x + \vec{V}(t, x)$  is not necessarily one. However, we prefer to work with a fix mesh. That's why we will use the operator *Convect*.

With *FreeFem++*, it is very easy to perform this operation because an operator does it. Let's consider a transport equation defined by (15).

If the solution is  $\phi_0$  at time  $t_0$ , then we get  $\phi = \Phi(t_0 + \Delta t, \cdot)$  by

$$\phi = \text{convect} \left( \left[ -\vec{V} \cdot e_x, -\vec{V} \cdot e_y \right], \Delta t, \phi_0 \right). \quad (2.54)$$

This technique will also be used in the program to reset the function delimiting the domain  $\Omega$ .

**Remark 2.4.2**

When we modify a function that serves only to delimit the curve  $\{x \in \mathbb{R}^2 : \phi(x) = 0\}$ .  $\phi$  can become less suitable than other functions delimiting the same curve. In practice, we want that the gradient of  $\phi$  has approximately a constant norm in a neighborhood of the curve  $\Gamma$ . For this reason, we reset the function  $\phi$ , which means, that we substitute to  $\phi$  a more interesting function which delimits the same curve  $\Gamma$  but approaches of the ideal function which is the signed distance to  $\Gamma$ .

We denote  $\phi_{old}$  the function that we want to improve and we solve the equation whose stationary solution is the signed distance at  $\Gamma$

$$\begin{cases} \partial_t \Phi + \text{sing}(\phi_{old})(\|\nabla \Phi\| - 1) = 0, \\ \Phi(t_0, 0) = \phi_{old}. \end{cases} \quad (2.55)$$

Then we replace  $\phi_{old}$  by  $\phi = \Phi(t_0 + \Delta t, \cdot)$ . So on the set  $\{x \in \mathbb{R}^2 : \phi_{old}(x) = 0\}$  as  $\text{sing}(\phi_{old}) = 0$ , the equation reduces to  $\partial_t \Phi = 0$  and the curve  $\{x \in \mathbb{R}^2 : \phi(x) = 0\}$  is then equal to  $\{x \in \mathbb{R}^2 : \phi_{old}(x) = 0\}$ , the border of the shape remains unchanged by this modification. Moreover, in a neighborhood of this curve,  $\partial_t \Phi$  is weak so the gradient is almost unit. To solve this system, we start by linearizing the equation by the following approximation

$$\partial_t \Phi + \text{sing}(\phi_{old}) \left( \frac{\nabla \phi_{old}}{\|\nabla \phi_{old}\|} \cdot \nabla \Phi - 1 \right) = 0.$$

Then we proceed in two steps, we solve the equation without the source term then we add  $dt \times \text{sing}(\phi_{old})$  to the solution found. By repeating this process, we get a function closer to the signed distance at  $\Gamma$ .

## 2.4.2 Numerical Algorithm and Simulations

---

**Algorithm 1** Representation of the shape of the membrane by Level Set method

---

1. Initialization of the level set function  $\phi_0$  by solving (2.55).

2. Iteration until convergence for  $k \geq 1$  :

(a) Compute the direct stat  $c_{\Omega_0}$  solution of (2.24) and the adjoint stat  $p_{\Omega_0}$  solution of (2.43) for the shape  $\phi_k$ .

Deduce the shape gradient = normal velocity  $=V_k$  (2.52)

(b) Advect the shape with  $V_k$  (solving the Hamilton Jacobi equation (2.54)) to obtain a new shape  $\phi_{k+1}$ .

---

## 2.5 Conclusion

Using geometrical shape optimization we have analyzed the coupling of the membrane to a diffused molecules, we prove the existence of the optimal shape of a membrane and we computed its first derivative with respect to the domain. We have focused on the situation where the system is in global equilibrium. When the membrane is stable we have analyzed the effect of the various processes on the membrane fluctuations by using level-set method. Numerical simulations show that the coupling between the membrane and adsorbed molecules makes the membrane suffers from morphological instabilities.

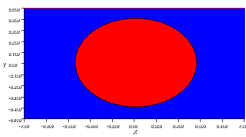


Figure 2.5: Initial shape.

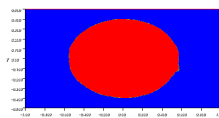


Figure 2.6: Shape evolution in time.

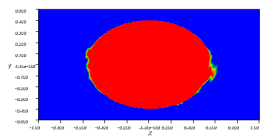


Figure 2.7: Final shape.

# Dynamical Behavior of Vesicles in the Steady and Oscillatory Shear Flow

## 3.1 Introduction

Vesicles (also known as fluid membranes) are closed membranes suspended in an aqueous medium fig. 3.1. They are often evoked as a simplified model for understanding various intricate dynamics exhibited by red blood cells (RBCs) and blood rheology, by including a minimal set of physical ingredients. Nevertheless, vesicles have been and remain a challenge for different disciplines ranging from biology to mathematics. The difficulty is that the vesicle shape is not known *a priori* and is determined dynamically via a subtle interplay between the local flow and interfacial forces, which gives rise to a large variety of shapes and dynamics for which exact analytical solutions in most cases are impossible and numerical treatments are inevitable. When placed in a linear shear flow of the form  $\mathbf{u}_0 = (\dot{\gamma}y, 0, 0)$ , where  $\dot{\gamma}$  is the steady shear rate see figure 3.1, vesicles have attracted extensively experimental, theoretical and numerical

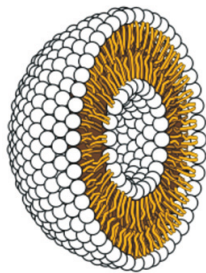


Figure 3.1: Scheme of a vesicle

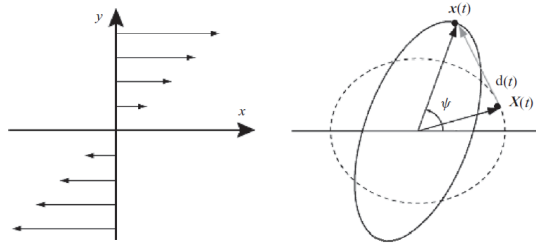


Figure 3.2: Ellipsoid membrane of a vesicle immersed in a viscous fluid a linear shear flow.

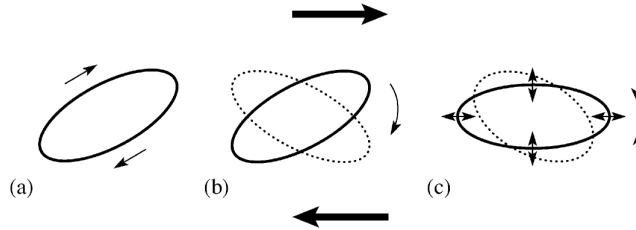


Figure 3.3: Different motion of vesicle [45]

studies (see Refs. [132]–[4] and the references therein).

The general picture is that vesicles share with RBCs and capsules in their behavior under flow a variety of different regimes of motions, depending on three control parameters: (i) the excess area  $\Delta = (A - 4\pi r_0^2)/r_0^2$ , where  $A$  is the vesicle area and  $r_0 = (3V/4\pi)^{1/3}$  is the effective vesicle radius defined via its volume  $V$ , (ii) the viscosity contrast  $\lambda = \eta_{\text{int}}/\eta_{\text{ext}}$ , where  $\eta_{\text{int}}$  and  $\eta_{\text{ext}}$  are the viscosities of the internal and the external fluids, respectively, and (iii) the bending number  $\mathcal{C}_\kappa = \eta_{\text{ext}}\dot{\gamma}r_0^3/\kappa$ , that plays the role of a capillary number, where the surface tension is replaced by the bending rigidity modulus  $\kappa$ . Due to the impermeability and inextensibility of the membrane the volume and the surface area of the vesicle are conserved.

At low deform ability (which means small enough  $\mathcal{C}_\kappa$ ), the perturbation theory of Misbah [91] revealed that a quasi spherical vesicle (i.e., its excess area  $\Delta$  is small) exhibits three major types of motions: (a) tank-treading (TT) regime, (b) tumbling (TB) regime, and (c) vacillating-breathing (VB) regime see figure 3.1. In the TT mode, the vesicle deforms into a prolate ellipsoid inclined at a stationary angle with the flow direction, while its membrane undergoes a tank-treading motion. During the TB regime, the vesicle undergoes a flipping motion like a rigid particle. The VB mode is an intermediate regime between TT and TB. During this mode the inclination angle of the vesicle oscillates around zero in the interval  $[-\pi/4, \pi/4]$ , whereas its shape makes a breathing motion. The selection between these three modes of motions depends only on two control parameters;  $\Delta$  and  $\lambda$ . For small enough  $\lambda$ , the TT motion

is predicted. For large enough  $\lambda$ , the TT mode disappears in favor of TB which coexists with VB. At low deformability, the TT-to-TB/VB transition occurs at a critical value  $\lambda_c = \lambda_c(\Delta)$ . A fourth classical mode, not observed in the small deformation limit, is the swinging mode during which the main axis oscillates about a non-zero mean value. Sometimes, the VB regime is also called swinging (SW), or trembling, and is qualified as a SW mode with a superimposed shape change resulting from the inclusion of deformability in the model. The SW mode has been discovered by Abkarian *et al.* for RBCs [1].

Besides the classical TT, TB and SW or VB modes, experimental work of Abkarian *et al.* [1] showed that the TB-to-SW transition occurred via a narrow intermediate, or the so-called intermittent behavior, during which both SW and TB happen alternately in time evolution, where the numbers of SW and TB depend on the shear rate, a mechanism similar to type-I intermittency of Pomeau-Manneville [109]. Based on the theoretical model of Keller and Skalak (KS) [77], phenomenological models which approximate RBCs or capsules by an ellipsoid of fixed shape predicted TB and SW, as well as intermittent motions [1], [125], [2]. Intermittent regimes, however, have generated certain debated questions and remain controversial [132], [130], [76]–[42]. Some works, which allow shape deformation, predict new regimes and also recover various regimes of motions, except intermittency. In Ref. [132], where a deformable capsule was considered, the authors pointed out that the intermittency reported in Refs. [1] and [125] is an artifact of the shape preservation. An intermittent behavior was found only if the capsule deforms in the shear plane; the intermittency disappears if the shape is free to undergo breathing (a deformation along the vorticity direction). Similar conclusion can be found in Ref. [103]. In Ref. [63] the authors found that the deformation of the capsule shape plays a large part in its dynamics, at odds with Ref. [101] in which the author concluded that deformability does not qualitatively change the dynamics. In Ref. [53] the authors pointed out that the cell shape remains almost biconcave in the region where the intermittent is expected to occur. Very recently, Cordasco and Bagchi [42] have observed intermittent motions for deformable RBCs in a simple (steady) shear, by performing 3D numerical simulations using a front-taking numerical method.

Recently, RBCs have been reported to also exhibit an intermittent regime by imposing a time-periodic shear flow. More precisely, in order to explore the response of RBCs, or their biomimetic analogs, to flow conditions in microcirculation, Dupire *et al.* [52] have analyzed the motion of nondeformable RBCs subject to an oscillatory shear flow described by the velocity field ( $\dot{\gamma} = \dot{\gamma}_a \sin(2\pi f_r t)$ )

$$\mathbf{u}_0 = (\dot{\gamma}_a \sin(2\pi f_r t)y, 0, 0), \quad (3.1)$$

with shear rate amplitude  $\dot{\gamma}_a$  and shear oscillatory frequency  $f_r$  (period  $T_{os} = 1/f_r$ ). The authors showed that the time-dependent external flow allows the cell to have a complex, even chaotic motion, using experiments supported by theoretical description. For analytical investigations, the authors used a nonautonomous model of two coupled equations for the inclination angle  $\psi$  and the Lagrangian angular location (the shape remains unchanged over time), by extending the model giving in Ref. [1] or Ref. [125]. It is reported that RBCs can present either stable motions characterized by intermittent behaviors or chaotic motions. For specific values of  $\dot{\gamma}_a$  and  $f_r$ , an unstable nonperiodic motion that is highly sensitive to initial conditions is also predicted. In Ref. [138], Zhao and Bagchi described numerically the dynamics of deformable capsules with both qualitative agreement and discrepancy with Ref. [52].

Deformable vesicles under an oscillatory shear flow have been considered by Noguchi [99]. The dynamics is described in terms of the Taylor deformation parameter and inclination angle  $\psi$ . It is shown, for example, that during the TB regime (high  $\lambda$ )  $\psi$  rotates clockwise and then rotates back. For middle  $\lambda$  and high  $\dot{\gamma}_a$  the vesicle shape and the inclination angle oscillate. In Ref. [62], Farutin and Misbah pointed out that under the oscillatory shear rate

$$\dot{\gamma} = \dot{\gamma}_a \cos(2\pi f_r t), \quad (3.2)$$

with small enough  $\dot{\gamma}_a$ , the oscillatory shear flow has no influence on the vesicle motion, in the sense that the vesicle undergoes oscillations without exhibiting TT, TB or VB and that the application of the pure oscillatory (3.2) misses several interesting microscopic features of the suspension.

Sparked by the above results, we would like to examine responses of deformable vesicles as a function of time to an oscillatory shear flow. As in Ref. [62], the case that we shall consider in the present work is the oscillatory shear rate (3.2), which also yields the constant shear rate at the limit  $f_r = 0$  (for an easy steady shear testing). A time-dependent shear rate of the form (3.2) is the commonly used one in analysis of viscoelastic effects of many complex fluids. Note that the corresponding strain  $\gamma$  is then

$$\gamma(t) = \frac{\dot{\gamma}_a}{2\pi f_r} \sin(2\pi f_r t). \quad (3.3)$$

Therefore, the peak strain (or the shear strain amplitude) is given by  $\gamma_a = \dot{\gamma}_a/2\pi f_r$ .

Vesicle motions, under (3.2) or (3.3), are expected to deviate from the classical regimes as for capsules and RBCs. Here, we focus on quasispherical vesicles at low deformability which allows for analytical

tractability. The physical problem is described via a simplified model that is obtained by including oscillating shear rate (3.2) to the small deformation model derived by Misbah [91]. This facilitates the formulation of exact analytical solutions for the vesicle orientation and its shape. Here, particular attention is paid to vesicles which exhibit TB modes under steady shear rate. We report that the competition between shape rate amplitude  $\dot{\gamma}_a$  and frequency  $f_r$  inhibits or modifies the classical TB motion and excites a variety of interesting and complex motions. More precisely, the small theory approach will allow us to easily distinguish one motion from another in a predictable manner by varying  $\dot{\gamma}_a$  and  $f_r$  independently, or by varying  $\dot{\gamma}_a/f_r$ . In other words, imposing the oscillatory shear rate (3.2), or (3.1), leads to completely different results (comparing with the steady shear flow), as for RBCs and capsules, which could have an impact on the rheological response of suspensions.

### 3.2 A minimal model

In the spirit of Refs. [91], [44] and [69], we consider a nearly spherical vesicle and adapt the small deformation theory, which describes reasonably the TT, TB and VB modes under a steady share rate (figure 3.1). The fluid motion outside and inside the vesicle is described by the Stokes equations with the stress balance, continuity of the velocity at the membrane and membrane inextensibility boundary conditions. The induced velocity fields (outside and inside the vesicle) are given by the classical Lamb solution [91]. The contribution of thermal fluctuations is neglected in this analysis. At low deformability, the equations of vesicle dynamics are expanded into perturbative series using  $\varepsilon = \sqrt{\Delta}$  as the small expansion parameter (unlike capsules where  $\varepsilon \approx \mathcal{C}_a$ ). In the small deformation theory (or the lowest order of a perturbation theory), the deviation of the shape from a sphere is parametrized by ( $r_0 = 1$ , or in other words lengths are measured in unit of  $r_0$ )

$$r = 1 + \sum_{|m| \leq 2} F_{2m} \mathcal{Y}_{2m}, \quad (3.4)$$

where  $\mathcal{Y}_{2m}$ ,  $|m| = 0, 1, 2$ , are the usual spherical harmonics of order two. Note that for a quasispherical shape  $F_{1m}$  can be set to zero since it corresponds to a solid translation.  $F_{2m}$  are unknown time-dependent coefficients satisfying the constraint of fixed total area

$$\frac{\Delta}{2} = \sum_{|m| \leq 2} |F_{2m}|^2. \quad (3.5)$$

The evolution equations for  $F_{2m}$  are given by [130]

$$\frac{dF_{2m}}{dt} = \dot{\gamma}_a \cos(2\pi f_r t) \left\{ -i \frac{m}{2} h \delta_{2|m|} + i \frac{m}{2} F_{2m} - h \sqrt{\frac{6}{5\pi}} \mathcal{C}_k^{-1} (6 + \sigma_0) F_{2m} \right\}, \quad (3.6)$$

where  $i^2 = -1$ ,  $|m| \leq 2$ ,  $h = \sqrt{\frac{2\pi}{15} \frac{60}{(32+23\lambda)}}$ , and  $\sigma_0$  is the isotropic part of the tension (or a Lagrange multiplier). Here the bending number  $\mathcal{C}_k$  is given by  $\mathcal{C}_k = \eta_{\text{ext}} \dot{\gamma}_a r_0^3 \cos(2\pi f_r t) / k$ , which can be written as  $\mathcal{C}_k = \mathcal{C}_k^* \cos(2\pi f_r t)$ , where  $\mathcal{C}_k^*$  is the bending number in the steady shear flow.

The constraint of fixed total area leads to

$$\sigma_0 = -6 - \mathcal{C}_k^* \Delta^{-1} \sqrt{\frac{40\pi}{3}} \cos(2\pi f_r t) \text{Im}(F_{22}). \quad (3.7)$$

Therefore, Eq. (3.6) reads as

$$\frac{dF_{2m}}{dt} = \dot{\gamma}_a \cos(2\pi f_r t) \left\{ -i \frac{m}{2} h \delta_{2|m|} + i \frac{m}{2} F_{2m} + \frac{4h}{\Delta} \text{Im}(F_{22}) F_{2m} \right\}, \quad (3.8)$$

which is independent of the bending number  $\mathcal{C}_k$ . This is the main evolution equation for the quasispherical vesicle shape to the leading order [91],[44]. The evolution in time of the vesicle shape configuration in the shear plane is given by the dynamics of  $F_{22}$ .  $F_{2\pm 1}$  and  $F_{20}$  modes describe deformations out of the shear plane. More precisely, the out-of-plane deformation along the vorticity direction is described by the  $F_{20}$  mode. Usually,  $F_{2\pm 1}$  modes are ignored for simplicity. In this case, it is shown that the three classical regimes (TT, TB, and VB) are qualitatively described by a two-dimensional model [91] satisfied by  $\mathcal{R}$  and  $\psi$ , which are defined by  $F_{22} = \frac{\sqrt{\Delta}}{2} \mathcal{R} e^{-2i\psi}$ . The orientation angle  $\psi$  coincides with the inclination angle of the long axis (with respect to the flow direction) of the vesicle in the flow and  $\mathcal{R}$  is the amplitude of deformation of the vesicle. This quantity measures the ellipticity of the vesicle contour in the shear plane

In this study we consider the vesicle problem (when  $F_{21} = 0$ ), so the two order spherical harmonics will be limited to  $\mathcal{Y}_2^m, m = -2, 0, 2$ , Fig. 3.4.

Then the deformed membrane is represented by the following spherical harmonic expansion around a sphere ( $r_0 = 1$ )

$$r = 1 + \mathcal{R} e^{2i\psi} \mathcal{Y}_2^{-2} + F_{20} \mathcal{Y}_2^0 + \mathcal{R} e^{-2i\psi} \mathcal{Y}_2^2, \quad (3.9)$$

$F_{20}$  mode, which describes the out-of-plane deformation along the vorticity, can be obtained from the area

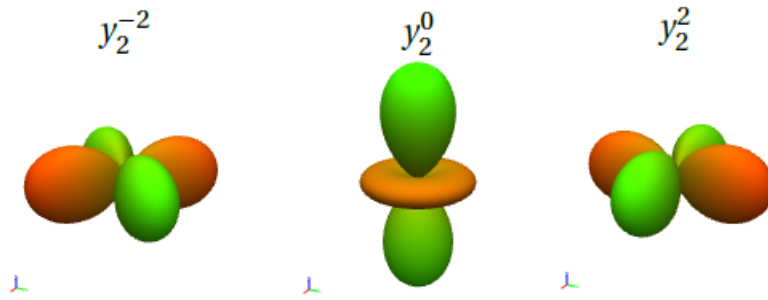


Figure 3.4: Spherical harmonics of order two

conservation constraint

$$\Delta = 4|\mathcal{R}|^2 + 2|F_{20}|^2. \quad (3.10)$$

The simplified equations, that were firstly reported in Ref. [91] still hold at low deformability. The only difference is that, as for RBCs and capsules [52], [99], [75], [102], [100],  $\dot{\gamma}$  is not a constant but a time-periodic function satisfying (3.2). Therefore, the minimal model describing the dynamics of the vesicle in the quasispherical approach at low deformability is the following coupled equations

$$\frac{d\mathcal{R}}{dt} = \dot{\gamma}_a \cos(2\pi f_r t) \left( h \left[ 1 - 4 \frac{\mathcal{R}^2}{\Delta} \right] \sin(2\psi) \right), \quad (3.11)$$

$$\frac{d\psi}{dt} = \dot{\gamma}_a \cos(2\pi f_r t) \left( -\frac{1}{2} + \frac{h}{2\mathcal{R}} \cos(2\psi) \right), \quad (3.12)$$

where  $h = 60\sqrt{2\pi/15}/(32 + 23\lambda)$  and the unknown functions  $\psi$  and  $\mathcal{R}$  are, respectively, the vesicle inclination angle and its shape deformation.

Eqs. (3.11) and (3.12) are deduced from the shape evolution equation derived in Refs. [91] and [43], which can be written as

$$\frac{dF_{22}}{dt} = \dot{\gamma}_a \cos(2\pi f_r t) [-ih + iF_{22} + 4h\Delta^{-1} \text{Im}(F_{22})F_{22}], \quad (3.13)$$

where  $F_{22} = \mathcal{R} \exp(-2i\psi)$ . Eq. (3.13) can also be deduced from the evolution equation for the vesicle conformation  $\mathbf{f}$  which can be written in a compact form (at leading order) [61], [43], [70];

$$\frac{\mathcal{D}\mathbf{f}}{\mathcal{D}t} = \frac{20}{(23\lambda + 32)\sqrt{\Delta}} \mathbf{e} - \frac{24\kappa}{23\lambda + 32} (Z_0 + 6\kappa)\mathbf{f}, \quad (3.14)$$

$$\mathbf{e} = \frac{\nabla \otimes \mathbf{u}_0 + (\nabla \otimes \mathbf{u}_0)^T}{2}, \quad (3.15)$$

in which  $\mathbf{u}_0$  is the imposed flow,  $Z_0$  is the isotropic part of the local surface tension (which is a Lagrange multiplier ensuring local membrane incompressibility) and  $\frac{\mathcal{D}\mathbf{f}}{\mathcal{D}t}$  is the Jaumann (or corotational) derivative defined as

$$\frac{\mathcal{D}\mathbf{M}}{\mathcal{D}t} = \frac{1}{2} (\mathbf{M}_{(-)} + \mathbf{M}_{(+)}), \quad (3.16)$$

where  $\mathbf{M}_{(-)}$  and  $\mathbf{M}_{(+)}$  are, respectively, the upper and lower convected derivatives, defined for a second-order  $\mathbf{M}$  as follows

$$\mathbf{M}_{(-)} = \frac{D\mathbf{M}}{Dt} - M \cdot (\nabla \otimes \mathbf{u}_0) - (\nabla \otimes \mathbf{u}_0)^T \cdot M, \quad (3.17)$$

$$\mathbf{M}_{(+)} = \frac{D\mathbf{M}}{Dt} + M \cdot (\nabla \otimes \mathbf{u}_0) + (\nabla \otimes \mathbf{u}_0)^T \cdot M, \quad (3.18)$$

where  $DM/Dt$  is the usual material derivative. The value of  $Z_0$  is determined by the demand that  $d\Delta/dt = 0$ . From this condition it follows that  $Z_0 + 6\kappa = 8\pi(\mathbf{f} : \mathbf{e})/\kappa\sqrt{\Delta}$ . Therefore, the equation for the vesicle dynamics reads

$$\frac{\mathcal{D}\mathbf{f}}{\mathcal{D}t} = \frac{20}{(23\lambda + 32)\sqrt{\Delta}} \mathbf{e} - \frac{192\pi}{(23\lambda + 32)\sqrt{\Delta}} (\mathbf{f} : \mathbf{e}) \mathbf{f}. \quad (3.19)$$

In fact, Eq (3.19) is the general evolution equation of the vesicle conformation for an arbitrary linear flow at low deformability. The rheological relation is obtained by performing the spatial average of the stress over the total volume  $V$ :  $\langle \sigma_{ij} \rangle = \frac{1}{V} \int_V \sigma_{ij} dV$  [44], where

$$\frac{\sigma_{ij}}{2\eta} = e_{ij} + \phi \left( \frac{5}{2} - 2h\sqrt{\frac{15}{2\pi}} \right) e_{ij} + \phi h \sqrt{\frac{15\pi}{2}} \frac{96f_{12}f_{ij}}{5\Delta}. \quad (3.20)$$

$\sigma_{ij}$  is the average stress tensor,  $e_{ij} = \frac{\partial u_j + \partial_j u_i}{2}$  is the symmetric part of the velocity gradient of the unperturbed flow,  $\phi$  is the volume fraction of the suspension and  $f_{ij}$  are the time-dependent amplitude in terms of Cartesian coordinates,  $r_i$  such that

$$\sum_{m=-2}^2 F_{2m}(t) y_{2m}(\theta, \phi) = \sum_{i,j=x,y,z} 3f_{ij}(t) r_i r_j$$

$f_{ij}$  are linear combinations of  $F_{2m}$ .

Equations (3.19) and (3.20) summarize the rheological equations of the composed fluid. In principle

$f_{ij}$  is determined from Eq. (3.19). Plugging the result into Eq. (3.20) determines the stress tensor. The deviation of the shape from a sphere is parametrized by the quadratic form  $r_i r_j f_{ij}(t)$ , where  $r_i$  is the  $i$ th Cartesian component of the position vector  $\mathbf{r}$ ;

$$r = 1 + \sum_{i,j=x,y,z} 3r_i r_j f_{ij}. \quad (3.21)$$

Functions  $f_{ij}$  are linear combinations of  $F_{2m}$ . In particular,  $F_{22}$  is given by [45]

$$\text{Re}(F_{22}) = \sqrt{\frac{6\pi}{5}}(f_{11} - f_{22}), \quad \text{Im}(F_{22}) = -\sqrt{\frac{24\pi}{5}}f_{12}. \quad (3.22)$$

Let us return to the minimal model. Eqs. (3.11) and (3.12) contain four control parameters  $\Delta, h, \dot{\gamma}_a$  and  $f_r$  which may induce a complex motion. In this work, we will qualitatively investigate vesicle responses by varying parameters  $\dot{\gamma}_a$  and  $f_r$ , for small enough  $h$  (or large enough  $\lambda$ ). Note that Eqs. (3.11) and (3.12) at  $f_r = 0$ , correspond to the constant shear rate case ( $\dot{\gamma} = \dot{\gamma}_a$ ). In this case, it is found, as mentioned before, that the three primary regimes (TT, TB and VB) are, at leading order, controlled only by the two parameters  $\lambda$  and  $\Delta$ , and not by  $\dot{\gamma}_a$  [91].  $\dot{\gamma}_a^{-1}$  is used as unit of time. The TT motion is predicted when  $\lambda < \lambda_c = -\frac{32}{23} + \frac{120}{23}(2\pi/15\Delta)^{1/2}$  (the KS critical ratio). The shape and the inclination angle of the vesicle relax to a certain steady state, which depends on parameters  $\lambda$  and  $\Delta$ . Above  $\lambda_c$ , the vesicle dynamics relaxes to TB/VB [132], [91]. Recently, the steady shear model ( $f_r = 0$ ) has been solved exactly [69]. In particular, it is showed that TB and VB are distinguishable via a control parameter  $\Gamma$  (depending on initial conditions as well as on  $h$  and  $\Delta$ );

$$\Gamma = \frac{4h^2}{\Delta} \frac{\frac{\Delta}{4h} - \xi_0}{\sqrt{\omega^2 \zeta_0^2 + (\xi_0 - h)^2}}, \quad (3.23)$$

where  $\omega = |1 - 4h^2/\Delta|^{1/2}$ ,  $\xi_0 = \mathcal{R}(0) \cos(2\psi(0))$  and  $\zeta_0 = \mathcal{R}(0) \sin(2\psi(0))$ . It is found that  $|\Gamma| \geq \frac{2h}{\Delta}$ . If  $\frac{2h}{\Delta} \leq |\Gamma| < 1$ ,  $\psi$  describes a TB regime, while a VB regime is obtained if  $|\Gamma| > 1$ . The transition between TB and VB occurs at  $\Gamma = \pm 1$ .

We turn to the unsteady shear rate case. Note that if there is no deformation along the vorticity direction (i.e.,  $F_{20} = 0$ ), we have  $\mathcal{R} = \sqrt{\Delta}/2$  (fixed vesicle shape). In this case Eqs. (3.11) and (3.12)

reduce to a nonautonomous Jeffery equation (or a nonautonomous (KS) equation)

$$\frac{d\psi}{dt} = \cos(2\pi f_r t) (A + B \cos(2\psi)), \quad (3.24)$$

where  $A = -\dot{\gamma}_a/2$  and  $B = \dot{\gamma}_a h/\sqrt{\Delta}$ . At  $f_r = 0$ , we get the classical Jeffery equation

$$\frac{d\psi}{dt} = A + B \cos(2\psi). \quad (3.25)$$

The above equation, which is solved in a closed form [77], describes very well the dynamics of TT and TB modes for a rigid particle. The nonautonomous Jeffery equation can also be viewed as a reference model for physical dynamics under oscillatory shear flow. When  $-A/B < 1$  (i.e.,  $h > \sqrt{\Delta}/2$ ), both Eqs. (3.24) and (3.25) have two steady states (the pure TT motion)  $\psi_0^\pm = \pm \cos^{-1}(\sqrt{\Delta/2h})$ . In steady shear rate the "+" solution is stable and the "-" solution is unstable. However, for Eq. (3.24), as an intuitive consequence of the presence of  $\cos(2\pi f_r t)$ , is that the inclination angle should oscillate without reaching  $\psi_0^\pm$ . For  $h < \sqrt{\Delta}/2$ , both Eqs. (3.24) and (3.25) have no steady state. The well known explicit general solution to (3.25), the KS formula [77], showed that the vesicle tumbles and the period is easily obtained as  $\dot{\gamma}_a T_{ks} = 2\pi/\omega$  ( $T_{ks} = \pi/\sqrt{A^2 - B^2}$ ). In contrast, Eq. (3.24) may present a new type of motion in which the oscillatory shear flow disturbs the TB motion under certain conditions on  $f_r$  and  $\dot{\gamma}_a$ . When the tumbling frequency is small enough in comparison to the non-dimensional frequency flow (i.e.,  $\omega/2\pi < f_r/\dot{\gamma}_a$ ), we may naively deduce that the oscillatory shear flow (3.2) could prevent a vesicle from tumbling. The vesicle oscillates with the same frequency as the applied shear flow without exhibiting the TB motion, as predicted in [62] for small enough  $\dot{\gamma}_a$ . This regime, which is known as the "linear" response, is expected for small amplitude oscillatory shear (SAOS). There is insufficient time for the vesicle to tumble. This constituted the motivation for the present work. We shall explore the complex vesicle dynamics that results from the application of the pure oscillatory shear rate (3.2), for arbitrary  $\dot{\gamma}_a$  and  $f_r$ .

### 3.3 Analytical results

#### 3.3.1 Exact solutions

As in [69], the small deformation approach will allow us to easily discuss the dependence on shear rate amplitude  $\dot{\gamma}_a$  and shear frequency  $f_r$ , and to identify specific dynamical features that can be viewed as

physical essential for vesicles in the spirit of [52] and [138], by exploring a wide range of parameters  $\dot{\gamma}_a$  and  $f_r$ . In particular, condition  $\omega/2\pi < f_r/\dot{\gamma}_a$ , will be refined. Although Eqs. (3.11) and (3.12) are nonautonomous, the vesicle orientation and its shape deformation can be obtained as follows.

Firstly, we define  $\tau = \frac{\dot{\gamma}_0}{2\pi f_r} \sin(2\pi f_r t)$ , and then Eqs. (3.11) and (3.12) become

$$\frac{d\mathcal{R}}{d\tau} = h \left[ 1 - 4 \frac{\mathcal{R}^2}{\Delta} \right] \sin(2\psi), \quad (3.26)$$

$$\frac{d\psi}{d\tau} = -\frac{1}{2} + \frac{h}{2\mathcal{R}} \cos(2\psi). \quad (3.27)$$

This coupled equations were firstly reported in Ref.[91] in the quasispherical approach at low deformability. As in Ref. [70] the solution to Eqs. (3.26) and (3.27) are found to be

$$\psi(t) = \frac{1}{2} \arctan \left( \omega \frac{\Delta \left[ e^{\frac{\omega \dot{\gamma}_a}{2\pi f_r} \sin(2\pi f_r t)} - C_1 e^{-\frac{\omega \dot{\gamma}_a}{2\pi f_r} \sin(2\pi f_r t)} \right]}{4h^2 C_2 + \Delta \left[ d s e^{\frac{\omega \dot{\gamma}_a}{2\pi f_r} \sin(2\pi f_r t)} + C_1 e^{-\frac{\omega \dot{\gamma}_a}{2\pi f_r} \sin(2\pi f_r t)} \right]} \right), \quad (3.28)$$

and

$$\mathcal{R}^2(t) = \frac{\Delta}{4} + \frac{\omega^2 \Delta^3}{16h^2} \left[ \frac{4h^2 C_2^2}{\Delta} - 4C_1 \right] \frac{1}{\left( C_2 + e^{\frac{\omega \dot{\gamma}_a}{2\pi f_r} \sin(2\pi f_r t)} + C_1 e^{-\frac{\omega \dot{\gamma}_a}{2\pi f_r} \sin(2\pi f_r t)} \right)^2}, \quad (3.29)$$

for  $\lambda < \lambda_c$ , where  $C_1$  and  $C_2$  are constants. For  $\lambda > \lambda_c$ , the inclination angle and the vesicle shape satisfy

$$\psi(t) = \beta(t) + \frac{1}{2} \arctan \left( \omega \frac{\cos(\dot{\gamma}_a \frac{f_r^*}{f_r} \sin(2\pi f_r t))}{\Gamma + \sin(\dot{\gamma}_a \frac{f_r^*}{f_r} \sin(2\pi f_r t))} \right), \quad (3.30)$$

where

$$\beta(t) = \frac{\pi}{4} \frac{\cos(\dot{\gamma}_a \frac{f_r^*}{f_r} \sin(2\pi f_r t))}{|\cos(\dot{\gamma}_a \frac{f_r^*}{f_r} \sin(2\pi f_r t))|} \left[ 1 - \frac{\Gamma + \sin(\dot{\gamma}_a \frac{f_r^*}{f_r} \sin(2\pi f_r t))}{|\Gamma + \sin(\dot{\gamma}_a \frac{f_r^*}{f_r} \sin(2\pi f_r t))|} \right], \quad (3.31)$$

and

$$\mathcal{R}^2(t) = \frac{\Delta}{4} - \frac{\omega^2 \Delta^3}{64h^4} \left[ \Gamma^2 - \frac{4h^2}{\Delta} \right] \frac{1}{\left( \Gamma \frac{\Delta}{4h^2} + \sin(\dot{\gamma}_a \frac{f_r^*}{f_r} \sin(2\pi f_r t)) \right)^2}, \quad (3.32)$$

where  $f_r^* = \omega/2\pi$  is the TB/VB frequency (under constant shear rate).  $\beta$  takes values  $\pm\pi/2, 0$ , and parameter  $\Gamma$ , which is assumed here to be positive, is given by (3.23). That is to mean the vesicle under (3.2) starts its motion from the identical initial condition as in the constant shear rate case. The method of obtaining expressions (3.28)-(3.32) has used a similar procedure as in [69] for constant shear rate. As for constant shear rate Eq. (3.32) implies that  $\Gamma \geq 2h/\sqrt{\Delta} = \Gamma_c$  by using constraint (3.10). It should

be noted that for  $\Gamma = \Gamma_c$ , which corresponds to the shape-preserving solution, the general solution to the nonautonomous KS equation (3.24) can be written simply as

$$\psi(t) = \arctan \left( \frac{A+B}{\sqrt{A^2-B^2}} \tan \left[ \sqrt{A^2-B^2} \frac{\sin(2\pi f_r t) - \sin(2\pi f_r t_0)}{2\pi f_r} \right] \right). \quad (3.33)$$

As far as we know, the general solution to the nonautonomous KS equation has never been reported before.

In the limit  $f_r \rightarrow 0$  we recover the well known KS solution and the general solution reported in [69] for vesicles under the constant shear rate ( $\dot{\gamma} = \dot{\gamma}_a$ ), since the quantity  $\sin(2\pi f_r t)/2\pi f_r$  tends to  $t$ , as  $f_r \rightarrow 0$ .

As the main purpose of the present work is to examine the effect of (3.2) on TB vesicles, we shall present, in the next section, a panel of scenarios for  $\lambda > \lambda_c$  and  $\Gamma < 1$ . The case  $\Gamma > 1$  (VB phase) is not reported in this work, and the case  $\lambda < \lambda_c$  (TT phase) leading to oscillating profiles can be found in Ref. [99] (see also Ref. [100]). For reader convenience, we provide here only a brief account (for TT phase).

It is transparent from (3.28) that the inclination angle oscillates with the frequency of the imposed oscillatory shear flow between

$$\psi_{os}^{\pm} = \frac{1}{2} \arctan \left( \omega \frac{\Delta \left[ e^{\pm \frac{\omega \dot{\gamma}_a}{2\pi f_r}} - C_1 e^{\mp \frac{\omega \dot{\gamma}_a}{2\pi f_r}} \right]}{4h^2 C_2 + \Delta \left[ d s e^{\pm \frac{\omega \dot{\gamma}_a}{2\pi f_r}} + C_1 e^{\mp \frac{\omega \dot{\gamma}_a}{2\pi f_r}} \right]} \right). \quad (3.34)$$

Imposing (3.2) induces no preferable orientation for the vesicles (for  $\lambda < \lambda_c$ ). This behavior qualitatively corresponds to a VB or SW motion in simple (steady) shear flow. Expression (3.34) indicates that the amplitude oscillation of the orientation depends on the initial conditions.

The maximum and minimum values of  $\psi$  are obtained at  $t = 0.25f_r$  and  $t = 0.753f_r$ , respectively, when the oscillatory flow changes direction. As a function of the non-dimensional frequency  $f_r/\dot{\gamma}_a$ , the oscillation amplitude,  $[\psi]$ , decreases with increasing  $f_r/\dot{\gamma}_a$ , and both  $\psi_{os}^{\pm}$  converge to  $\frac{1}{2} \arctan \left( \omega \frac{\Delta(1-C_1)}{4h^2 C_2 + \Delta(1+C_1)} \right)$  for large enough  $f_r/\dot{\gamma}_a$  ( $[\psi] \rightarrow 0$  as  $f_r/\dot{\gamma}_a \rightarrow \infty$ ). In the limit  $f_r/\dot{\gamma}_a \rightarrow 0$ ,  $\psi_{os}^{\pm}$  tend to the fixed inclination angles (the pure TT regime)  $\psi_0^{\pm} = \pm \frac{1}{2} \arctan \omega$ . This result is qualitatively identical to the predicted results reported in Refs [99] and [100].

In the limit of the spherical case  $\Delta = 0$ , we have  $\psi_{os}^{\pm} = \pm \pi/4$ . The vesicle behaves exactly as rigid body and oscillates between  $\pm \pi/4$ , while for the constant shear flow the orientation angle is  $\pi/4$ .

Note that,  $\zeta = Re(F_{22})$  and  $\xi = Im(F_{22})$  are fixed to be as in [69].

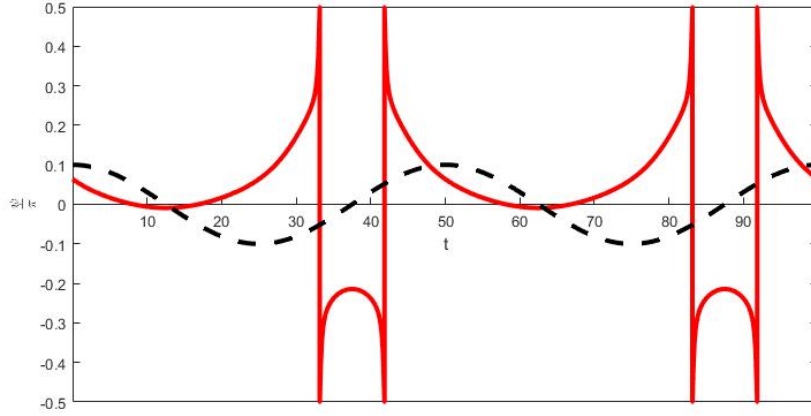


Figure 3.5: (Color online) Illustration of the CW/CCW SW (solid red line) for a vesicle with excess area  $\Delta = 0.437$  and parameters  $h = 0.3, \Gamma = 0.99$  in response to the oscillatory shear rate (dashed black line, in arbitrary scale) with frequency  $f_r = 0.02$  (period  $T_{sh} = 50$ ) and shear rate amplitude  $\dot{\gamma}_a = 0.55$ . A similar behavior is shown in Fig. 7 of Ref. [138] for microcapsules.

For  $\lambda < \lambda_c$

$$\zeta(t) = \frac{\Delta\omega}{4h} \frac{(e^{\frac{\dot{\gamma}_a\omega}{2\pi f_r} \sin(2\pi f_r t)} - C_1 e^{-\frac{\dot{\gamma}_a\omega}{2\pi f_r} \sin(2\pi f_r t)})^2}{(C_2 + e^{\frac{\dot{\gamma}_a\omega}{2\pi f_r} \sin(2\pi f_r t)} + C_1 e^{-\frac{\dot{\gamma}_a\omega}{2\pi f_r} \sin(2\pi f_r t)})^2}, \quad (3.35)$$

and

$$\xi(t) = \frac{\Delta}{4h} + \frac{\Delta\omega^2}{4h} \frac{C_2}{C_2 + e^{\frac{\dot{\gamma}_a\omega}{2\pi f_r} \sin(2\pi f_r t)} + C_1 e^{-\frac{\dot{\gamma}_a\omega}{2\pi f_r} \sin(2\pi f_r t)}}. \quad (3.36)$$

For  $\lambda > \lambda_c$

$$\zeta(t) = \frac{\Delta\omega}{4h} \frac{\cos\left(\frac{\dot{\gamma}_a f_r^*}{f_r} \sin(2\pi f_r t) + C_3\right)}{C_4 + \sin\left(\frac{\dot{\gamma}_a f_r^*}{f_r} \sin(2\pi f_r t) + C_3\right)}, \quad (3.37)$$

and

$$\xi(t) = \frac{\Delta}{4h} + \frac{\Gamma + \sin\left(\frac{\dot{\gamma}_a f_r^*}{f_r} \sin(2\pi f_r t) + C_3\right)}{C_4 + \sin\left(\frac{\dot{\gamma}_a f_r^*}{f_r} \sin(2\pi f_r t) + C_3\right)}, \quad (3.38)$$

where,  $C_j, j = 1, 2, 3, 4$ , are constants depending on the initial conditions, with  $C_4 = \frac{\Delta}{4h^2}\Gamma$ ,

### 3.3.2 Oscillating motions

We investigate now the vesicle motion for  $\lambda > \lambda_c$ , with the aim to easily identify minimal ingredients that are needed for an MOD type behavior. In this work, by MOD type behavior we mean a mixed oscillatory dynamic motion (MOD) in which the alternation between TB and VB (or SW) modes occurs in a periodic or regular manner.

Although simple in appearance, expression (3.30) should be a significant help in clarifying the complexity of motions that could be developed by quasispherical vesicles at low deformability. A number of nontrivial features is described below on the basis of a family of solution curves obtained for fixed  $\Delta = 0.437, h = 0.3, \Gamma = 0.99$  and for some specific values of  $\dot{\gamma}_a$ . We have kept  $f_r$  fixed at  $f_r = 0.02$ , despite it may play an important role in the dynamics. The types of motions obtained here are representative of those that are obtained (not shown here) with different values of  $\Gamma$  in the range  $1 > \Gamma \geq \Gamma_c = 2h/\sqrt{\Delta}$ .

As mentioned before, Farutin and Misbah [62] showed that imposing (3.2), with small enough  $\dot{\gamma}_a$ , induces no preferable orientation of the vesicles. The vesicle oscillates about its initial position. In addition, the amplitude of these oscillations is small if  $f_r/\dot{\gamma}_a \gg 1$ . Here, we firstly find that below a first critical value,  $\dot{\gamma}_a < \dot{\gamma}_a^0 \approx 0.4702$ , Eq. (3.30) describes one type of unsteady motion: a SW motion in which the vesicle inclination undergoes a continuous periodic motion around a mean value between 0 and  $\pi/4$  (not shown here). In the case of low  $\dot{\gamma}_a$ , which corresponds to high  $f_r$ , the SW regime is accompanied by a small angular amplitude. The inclination angle behaves as

$$\psi(t) \approx \frac{1}{2} \arctan \left( \frac{\omega}{\Gamma} \left( 1 - \frac{\dot{\gamma}_a f_r^*}{\Gamma f_r} \sin(2\pi f_r t) \right) \right), \quad (3.39)$$

for small enough  $\dot{\gamma}_a$ . When  $\dot{\gamma}_a$  increases to  $\dot{\gamma}_a^0$ , the amplitude oscillation of  $\psi$  increases significantly and reaches  $\pi/2$ .

The situation, however, changes when  $\dot{\gamma}_a$  is large. As the shear amplitude is further increased above  $\dot{\gamma}_a^0$ , the vesicle does not tumble. It rather performs a new unsteady periodic motion. The vesicle undergoes a new SW regime. In this regime, the angle undergoes sudden discontinuous jumps over the course of time, as we see from Figure 3.5, in marked contrast with the usual VB and SW modes, in which the angle evolves continuously. In fact, the vesicle tries to tumble. However, the oscillatory shear flow (3.2) prevents the vesicle from tumbling when the flow changes direction and the vesicle rotates back to the initial position. The imposed periodic flow acts as a spring element. The flow reverses before the vesicle could exhibit a full ( $180^\circ$ ) TB. Therefore, the vesicle makes clockwise (CW) from  $\pi/2$  and counterclockwise (CCW) back to  $\pi/2$ , and CCW from  $-\pi/2$  and CW back to  $-\pi/2$  (without making a full  $2\pi$  rotation). As for nondeformable RBCs [52] and capsules [138], the vesicle exhibits CW during the forward motion ( $\dot{\gamma} > 0$ ) and CCW during the backward motion ( $\dot{\gamma} < 0$ ). The inclination angle has local extrema at the same moment when  $\dot{\gamma} = 0$ , and its responses during CW/CCW and CCW/CW SW are not identical and have unequal time-steps.

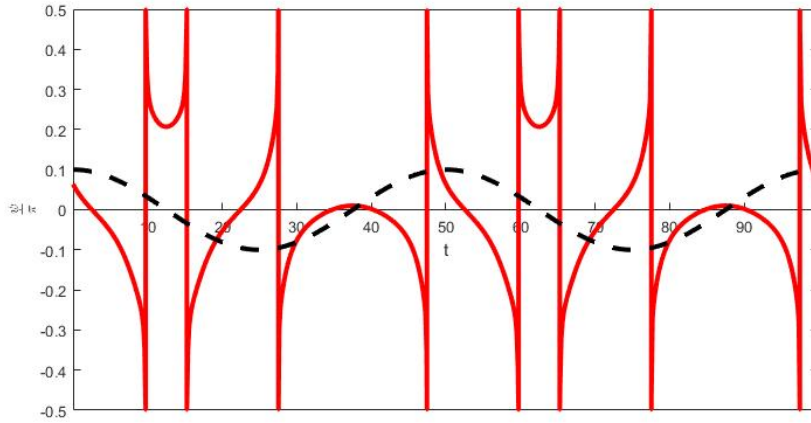


Figure 3.6: Plots of  $\dot{\gamma}$  (dashed black line) and the orientation angle  $\psi/\pi$  (red solid line). The vesicle exhibits alternatively TB and SW. Parameter  $\dot{\gamma}_a = 1.5$  and other parameters are the same as in Figure 3.5.

Just above a second critical value  $\dot{\gamma}_a^1 \approx 1.4107$ , the vesicle dynamics enters into a different regime. The motion is characterized by a successive transitions from CW/CCW SW to CCW TB to CCW/CW SW to CW TB and then to CW/CCW SW, over the course of time in one cycle. In this mode, referred here to as  $\text{MOD}_1$ , the vesicle switch between TB and SW periodically. The vesicle performs exactly one (CW or CCW) TB between two SW described above, as long as  $\dot{\gamma}_a$  takes place in the range from  $\dot{\gamma}_a^1$  to  $\dot{\gamma}_a^2$  (region for  $\text{MOD}_1$ ), where  $\dot{\gamma}_a^2 \approx 2.3512$  (the third critical value). A net  $\text{MOD}_1$  is illustrated in Fig. 3.6 for  $\dot{\gamma} = 1.5$ .

In the range  $\dot{\gamma}_a > \dot{\gamma}_a^2$ , the vesicle presents sequences of alternating TB and SW. The vesicle exhibits different mixed oscillating motions, which can be classified according to the number of TB before the vesicle swings. For each MOD motion the number of CW TB and the number of CCW TB are equal (over a period). SW modes are located in regions where  $\dot{\gamma} = 0$ . A MOD solution having  $n$  CW (or  $n$  CCW) TB is referred here to as  $\text{MOD}_n$  (mixed oscillatory motion that displays a ratio of 1: $n$ , SW to TB). The vesicle swings once after  $n$  tumblings. A  $\text{MOD}_2$  tendency has been observed experimentally for nondeformable RBCs in sinusoidal shear flow [52] (see Fig. 4(a) of [52]).

A question naturally arises: Can we define a criterion of the selection of  $\text{MOD}_n$ ? It is checked here that the mixed oscillatory mode transition occurs continuously in the parameter space of  $\dot{\gamma}_a$  (at fixed frequency), and that the MOD region width  $\Lambda$  of  $\text{MOD}_n$  is independent of  $n$  ( $\Lambda$  is defined as the absolute value of the difference between  $\dot{\gamma}_a^n$  and  $\dot{\gamma}_a^{n+1}$ ). For the set of parameters explored here it is found  $\Lambda \approx 0.9405$ , irrespective of  $n$ . This suggests that the critical value for the transition from  $\text{MOD}_{n-1}$  to

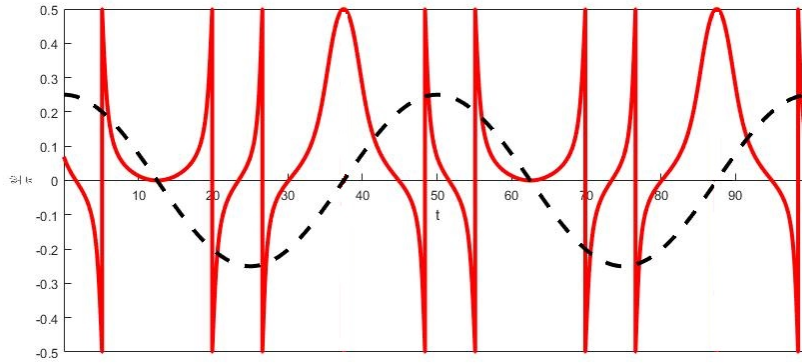


Figure 3.7: Plots of  $\dot{\gamma}$  (dashed black line) and the inclination angle (red solid line) at  $\dot{\gamma}_a = \dot{\gamma}_a^2 \approx 2.351229$ , with same other parameters as in Figure 3.5. The vesicle periodically presents horizontal reversals ( $\psi = 0$ ) and vertical reversals ( $\psi = \pi/2$ ) separated by one TB.

$\text{MOD}_n$ , should obey an equation of the form

$$\dot{\gamma}_a^n = \dot{\gamma}_a^0 + n\Lambda. \quad (3.40)$$

An important consequence of the above equation, which is justified rigorously later, is that a cascade of doubling period, or a catastrophe solution, should not be favored. The interruption between TB and SW are not based on chaotic dynamics. Recall that the shape-preserving assumption leads to nonautonomous Jeffery equation (3.24). This equation resembles the nonautonomous Jeffery equation for non deformable RBCs, in the limit where Lagrangian angular location remains very small [52]. In this case, the authors pointed out that chaos is no longer possible.

### 3.3.3 The bifurcation phenomena

To demonstrate (3.40), we seek to study the time evolution of the inclination angle during the  $\text{MOD}_{n-1}$ -to- $\text{MOD}_n$  transition. Perhaps, the most interesting feature of Eq. (3.30) is obtained when looking more closely at the vesicle motion at  $\dot{\gamma}_a = \dot{\gamma}_a^n$ . For  $n = 2$ , we have firstly observed that, during  $\text{MOD}_1$ , the local smooth minimum (resp. maximum) of SW decreases (resp. increases), upon increasing  $\dot{\gamma}_a$  up to  $\dot{\gamma}_a^2$ , while the times for local extrema are independent of  $\dot{\gamma}_a$  ( $t = 0.25/f_r$ , and  $t = 0.75/f_r$ ) as for RBCs [100]. At  $\dot{\gamma}_a = \dot{\gamma}_a^2$ , the local smooth maxima becomes global ( $\psi = \pi/2$ ), and the local smooth minimum value vanishes (see Figure 3.7). That is to say that the vesicle exhibits periodically vertical and horizontal reversals (at the same moment when the flow changes direction). More generally, at  $\dot{\gamma}_a = \dot{\gamma}_a^n$  one of

the local smooth extrema becomes global and periodically reaches  $\pi/2$  or  $-\pi/2$ , while the second one reaches 0. For  $\dot{\gamma}_a$  slightly below  $\dot{\gamma}_a^n$ , the local smooth extremum does not significantly change, however, the global smooth extremum splits into CCW and CW TB connected by a CCW/CW SW (with small inclination oscillation amplitude), and then a new regime with additional one CCW TB and one CW TB, progressively appears as in Figure 3.8. As a result, the numbers of CCW and CW TB increase and remain equal. Critical value  $\dot{\gamma}_a^n$  can be estimated by solving  $|\psi| = \pi/2$  and  $d\psi/dt = 0$ , from which one sees that  $\dot{\gamma}_a^n$  has to be

$$\dot{\gamma}_a^n = \frac{\pi}{2} \frac{f_r}{f_r^*} (1 + 2n), \quad (3.41)$$

irrespective of  $\Gamma$ . Using again the equation  $|\psi| = \pi/2$ , we deduce that the vesicle exhibits an  $\text{MOD}_n$  only for  $\dot{\gamma}_a^n < \dot{\gamma}_a < \dot{\gamma}_a^{n+1}$ , Eq. (3.41) shows that the width is given by  $\Lambda = \pi f_r / f_r^*$ . At fixed frequency, the threshold shear rate between SAOS and LAOS regimes is given by  $\dot{\gamma}_a^0 = \pi f_r / 2 f_r^*$ . Interval  $(0, \pi f_r / 2 f_r^*)$  can be referred to as the plateau region from the view point of linear viscosity theory. Note that Eq. (3.41) can be rewritten as  $\dot{\gamma}_a^n = (1 + 2n) \dot{\gamma}_a^0$ . Parameter  $\dot{\gamma}_a^1 = 3\pi f_r / (2 f_r^*)$  is the threshold shear rate between SW regimes and MOD behaviors. Eq. (3.41) indicates, in particular, that an MOD behavior is excited whenever the oscillating frequency is equal to an integer multiple of the TB frequency. Beyond the critical values of the shear rate, Eq. (3.41) allows us, also for an experimental testability, to estimate (at leading order) the number of CW TB (or CCW TB), during each period, as a function of the ratio of  $\dot{\gamma}_a$  to  $f_r$ ;

$$n = \left\lfloor \frac{\dot{\gamma}_a f_r^*}{\pi f_r} - \frac{1}{2} \right\rfloor, \quad (3.42)$$

where  $\lfloor \cdot \rfloor$  stands for the floor function ( $\lfloor z \rfloor$  is obtained by omitting the fractional part of  $z$ ). A higher  $\dot{\gamma}_a / f_r$  forces the vesicle to tumble more frequently. Note that Eq. (3.42) is valid as soon as  $\dot{\gamma}_a > \dot{\gamma}_a^0$  (or  $\dot{\gamma}_a > \pi^2 f_r$ ). Of course, there is no TB for  $\dot{\gamma}_a^0 < \dot{\gamma}_a < \dot{\gamma}_a^1$ . Note that number  $n$  goes to infinity as  $f_r$  approaches 0.

Analogous to (3.41), the transition also occurs, for any fixed  $\dot{\gamma}_a$ , at critical frequencies,

$$f_r^n = \frac{2}{\pi} \frac{\dot{\gamma}_a f_r^*}{1 + 2n} = \frac{1}{1 + 2n} f_r^0. \quad (3.43)$$

The above expression indicates, in particular, that no (periodic) MOD can occur for  $f_r > f_r^0 = 2\dot{\gamma}_a f_r^* / \pi$ . Eq. (3.43) can also be used to estimate (at leading order) the critical values of the shear strain amplitude

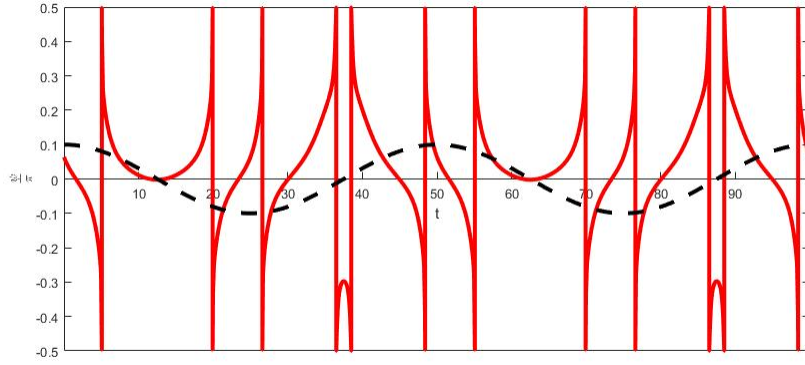


Figure 3.8: Plots of  $\dot{\gamma}$  (dashed black line) and  $\text{MOD}_2$  behavior (red solid line) for  $\dot{\gamma}_a = 2.37$  (just above  $\dot{\gamma}_a^2$ ). The global maximum (see Figure 3.7) splits into two TB connected by a CCW/CW SW.

(see Eq. (3.3)) for the MOD transition;

$$\dot{\gamma}_a^n = (1 + 2n) \frac{\pi}{2} \left( 1 - \frac{4h^2}{\Delta} \right)^{-1/2}, \quad (3.44)$$

by knowing  $h$ ,  $\Delta$  and  $n$ .

Finally, we shall examine how the viscosity ratio in turn influences the dynamics of the vesicle. From (3.41) and (3.43) or (3.44), the viscosity ratio is also of special interest. Given the importance of this parameter we need a more refined analysis of Eq. (3.41). We have fixed parameters  $\dot{\gamma}_a$  and  $f_r$ , such that  $\dot{\gamma}_a > \pi^2 f_r$ , and found that transitions between MOD behaviors take place at critical values

$$\lambda_c^n = -\frac{32}{23} + \frac{120}{23} \left( 1 - \frac{\pi^4 f_r^2}{\dot{\gamma}_a^2} (1 + 2n)^2 \right)^{-1/2} \sqrt{2\pi/15\Delta}, \quad (3.45)$$

provided that  $n \leq \mathcal{N} = \left\lfloor \left( \frac{\dot{\gamma}_a}{\pi^2 f_r} - 1 \right) / 2 \right\rfloor$ . When  $1 < \mathcal{N} = \left( \frac{\dot{\gamma}_a}{\pi^2 f_r} - 1 \right) / 2$ , we have an  $\text{MOD}_{\mathcal{N}-1}$  behavior for any  $\lambda > \lambda_c^{\mathcal{N}-1}$ , while if  $\mathcal{N} < \left( \frac{\dot{\gamma}_a}{\pi^2 f_r} - 1 \right) / 2$  the vesicle exhibits an  $\text{MOD}_{\mathcal{N}}$  behavior, for any  $\lambda > \lambda_c^{\mathcal{N}}$ . That is to say a large  $\lambda$  ensures the saturation of the MOD behavior. This result indicates, in particular, that the viscosity contrast is no longer sufficient to induce the  $\text{MOD}_n$  behavior for arbitrary  $n$ . In contrast, the vesicle tends to undergo a saturated mixed oscillatory behavior for large enough viscosity contrast  $\lambda$  (the number of TB remains constant over one cycle), and this saturation depends only on the ratio of  $\dot{\gamma}_a$  to  $f_r$ .

### 3.4 Rheology of vesicle suspension

We have seen above that the viscosity contrast  $\lambda$  and the time-dependent shear flow play a crucial role in the vesicle dynamics. Once the exact expressions of solutions of each regime are obtained, the rheology of a dilute suspension will be easily analyzed. More precisely we investigate the time variation of the effective viscosity and normal stress differences for a dilute suspension in different regimes

#### 3.4.1 Reduced effective viscosity

Danker and Misbah [44] and Danker et al. [43] reported on analytical and numerical observations of the effective viscosity for steady shear flow. The time-average of the reduced effective viscosity  $[\eta]$  (see below) over one period has been determined. This quantity is a function of  $\lambda$  and  $\Delta$ , for the three regimes, and is denoted  $\langle[\eta]\rangle$ . It is found that  $\langle[\eta]\rangle$  decreases with increasing  $\lambda$  and attains a minimum at  $\lambda_c$ . For  $\lambda > \lambda_c$ ,  $\langle[\eta]\rangle$  exhibits a sudden increase, in agreement with experiments [62]. Here, as mentioned above, we study the time-dependent effective viscosity in the case where the shear flow is given by (3.2). From the rheological equations (3.19) and (3.20), it is easy to show that the full expression of the time-dependent effective viscosity  $\eta_{eff}$  is defined by  $\eta_{eff} = \frac{\sigma_{xy}}{\dot{\gamma}_a}$ , with  $\sigma_{xy}$  given in Eq (3.20).

$$\eta_{eff}(t) = \eta_{ext} \cos(2\pi f_r t) \left[ 1 + \frac{5}{2} \varphi \left( 1 - \frac{4}{5} \sqrt{\frac{15}{2\pi}} h \right) + \frac{\varphi}{\Delta} h \sqrt{\frac{480}{\pi}} \mathcal{R}^2(t) \sin^2(2\psi) \right], \quad (3.46)$$

which is equivalent to,

$$\eta_{eff}(t) = \eta_{ext} \cos(2\pi f_r t) \left[ 1 + \frac{5}{2} \varphi \left( 1 - \frac{4}{5} \sqrt{\frac{15}{2\pi}} h \right) + \frac{\varphi}{\Delta} h \sqrt{\frac{480}{\pi}} \zeta^2(t) \right], \quad (3.47)$$

since,  $\zeta(t) = R(t) \sin(2\psi)$ .

Note that in the limit  $f_r \rightarrow 0$  we recover the time-dependent effective viscosity for vesicles under the constant shear rate in [70].

$$\dot{\eta}_{eff}(t) = \eta_{ext} \left[ 1 + \frac{5}{2} \varphi \left( 1 - \frac{4}{5} \sqrt{\frac{15}{2\pi}} h \right) + \frac{\varphi}{\Delta} h \sqrt{\frac{480}{\pi}} \dot{\zeta}^2(t) \right], \quad (3.48)$$

where,  $\dot{\zeta}(t) = \dot{\mathcal{R}}(t) \sin(2\dot{\psi}(t))$ ,  $\dot{\psi}$  and  $\dot{\mathcal{R}}$  are, respectively, the vesicle inclination angle and its shape

deformation under the constant shear rate [69]. For  $f_r \neq 0$  we have

$$\eta_{eff}(t) = \cos(2\pi f_r t) \dot{\eta}_{eff} \left( \frac{\dot{\gamma}_a}{2\pi f_r} \sin(2\pi f_r t) \right). \quad (3.49)$$

According to Ref.[97] the effective viscosity is given by

$$\eta_{eff} = \eta_{ext} (1 + [\eta]\varphi), \quad (3.50)$$

where  $[\eta]$  is the normalized viscosity (called the intrinsic viscosity when  $\varphi \rightarrow 0$ ) which represents the contribution of the vesicle to the viscosity and  $\varphi$  is the volume fraction of the suspension (the volume occupied by the vesicles over the total volume).

From Eq. (3.50) the reduced effective viscosity, or the normalized viscosity is defined by

$$[\eta] = \frac{\eta_{eff} - \eta_{ext}}{\eta_{ext} \varphi}, \quad (3.51)$$

Using eq. (3.47) The reduced effective viscosity reads

$$[\eta] = \frac{5}{2} \left(1 - \frac{4}{5} \sqrt{\frac{15}{2\pi}} h\right) \cos(2\pi f_r t) + \frac{h}{\Delta} \sqrt{\frac{480}{\pi}} \cos(2\pi f_r t) \zeta^2(t) + \frac{\cos(2\pi f_r t) - 1}{\varphi}. \quad (3.52)$$

Let us now evaluate the time-dependent effective viscosity. Making use the expression of  $\zeta(t)$  that

$$[\eta] = \cos(2\pi f_r t) \left[ \frac{5}{2} \left(1 - \frac{4}{5} \sqrt{\frac{15}{2\pi}} h\right) + |4h^2 - \Delta| \sqrt{\frac{480}{\pi}} \frac{1}{16h} \mathcal{G} \left( \frac{\dot{\gamma}_a \omega}{2\pi f_r} \sin(2\pi f_r t) \right) \right] + \frac{\cos(2\pi f_r t) - 1}{\varphi}, \quad (3.53)$$

where the function  $\mathcal{G}$  is given by

$$\mathcal{G}(s) = \frac{(e^s - C_1 e^{-s})^2}{(C_2 + e^s + C_1 e^{-s})^2}. \quad (3.54)$$

For  $\lambda < \lambda_c$  and, for  $\lambda > \lambda_c$

$$\mathcal{G}(s) = \frac{(\cos(s + C_3))^2}{(C_4 + \sin(s + C_3))^2}. \quad (3.55)$$

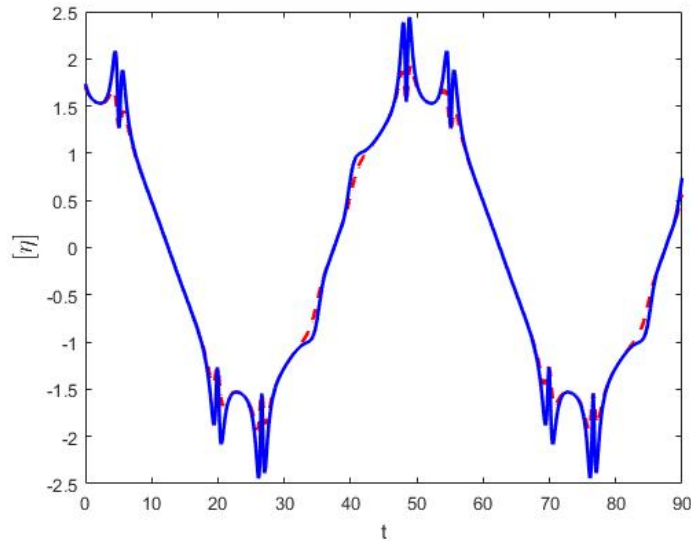


Figure 3.9: Time-dependent reduced viscosity  $[\eta]$  during TB and VB regimes for different values of  $\Gamma$  . Parameters are  $\Delta = 0.437$ ,  $h = 0.3$ ,  $\dot{\gamma}_a = 2.37$ ,  $\Gamma = 1.02$  (dashed red line) and  $\Gamma = 0.91$  (solid blue line).

This expression displays several interesting properties. As a function of  $t$ .

The time-dependent effective viscosity can also expressed as function of the effective viscosity under the constant shear rate given in [70] by the following expression

$$[\eta](t) = \cos(2\pi f_r t) [\hat{\eta}](\tau) + \frac{\cos(2\pi f_r t) - 1}{\varphi}, \quad (3.56)$$

where

$$\tau = \frac{\dot{\gamma}_a}{2\pi f_r} \sin(2\pi f_r t). \quad (3.57)$$

We plotted in Fig. 3.4.1 the time evolution of the reduced effective viscosity (during TB and VB regimes) for different values of the parameter ( $\Gamma = \frac{4h^2}{\Delta} C_4$ ). In Fig.3.4.1 we plotted the quantity  $[\hat{\eta}] = [\hat{\eta}](\tau)$  to indicates the maximum and the minimum possible value of the instantaneous reduced effective viscosity as it is reported in Ref. [70] that

$$\frac{5}{2} \left( 1 - \frac{4}{5} \sqrt{\frac{15}{2\pi} h} \right) \leq [\hat{\eta}] \leq \frac{5}{2}. \quad (3.58)$$

From eq. 3.56 and 3.58 we clearly see that  $[\eta]$  oscillates between  $-\frac{5}{2}$  and  $\frac{5}{2}$ .

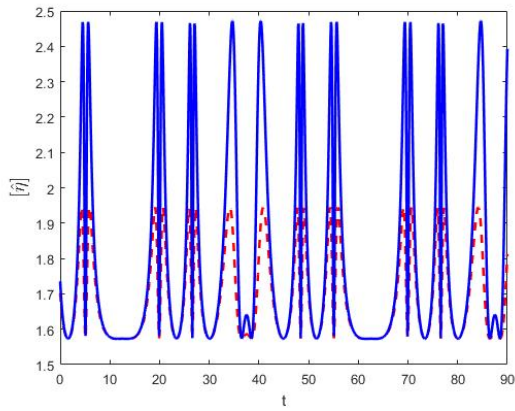


Figure 3.10: Time-dependent reduced viscosity  $[\hat{\eta}]$  at  $\tau$  during TB and VB regimes. Parameters are  $\Delta = 0.437$ ,  $h = 0.3$ ,  $\dot{\gamma}_a = 2.37$ ,  $\Gamma = 1.02$  (dashed red line) and  $\Gamma = 0.91$  (solid blue line).

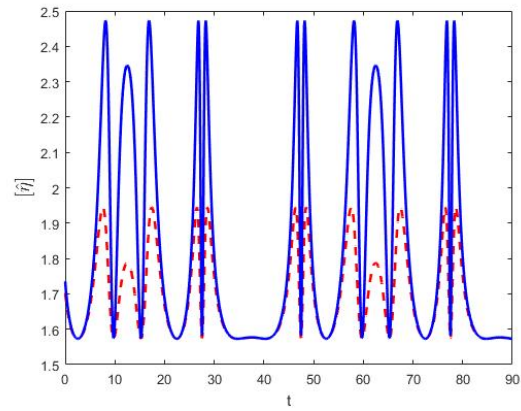


Figure 3.11: Time-dependent reduced viscosity  $[\hat{\eta}]$  at  $\tau$  during TB and VB regimes. Parameters are  $\Delta = 0.437$ ,  $h = 0.3$ ,  $\dot{\gamma}_a = 1.5$ ,  $\Gamma = 1.02$  (dashed red line) and  $\Gamma = 0.91$  (solid blue line).

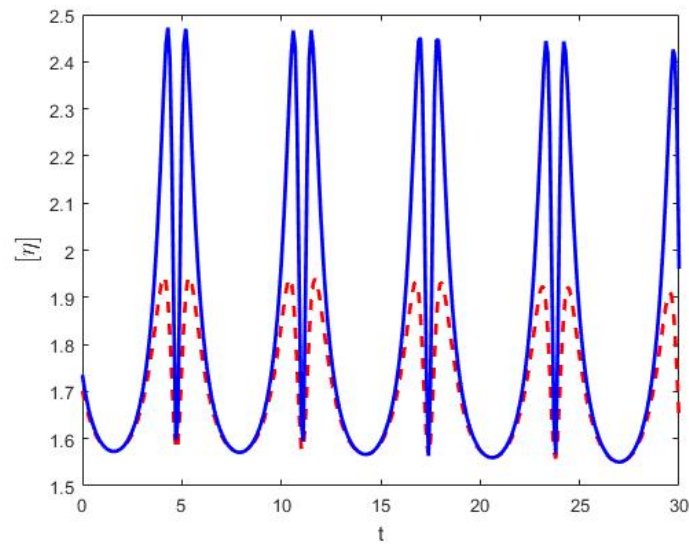


Figure 3.12: Time-dependent reduced viscosity  $[\eta]$  during TB and VB regimes. Parameters are  $\Gamma = 1.02$ ,  $\Delta = 0.437$ ,  $h = 0.3$ ,  $\dot{\gamma}_a = 2.37$  and  $f_r = 0.001$ .

As in Ref. [70], we are also interested in the time average over one period. From eq. (3.53). We get

$$\langle[\eta]\rangle = \frac{5}{2}\left(1 - \frac{4}{5}\sqrt{\frac{15}{2\pi}}h\right) + (4h^2 - \Delta)\sqrt{\frac{480}{\pi}}\frac{1}{16h}\frac{C_4 - \sqrt{C_4^2 - 1}}{\sqrt{C_4^2 - 1}}. \quad (3.59)$$

For  $\lambda < \lambda_c$  and, for  $\lambda > \lambda_c$

$$\langle[\eta]\rangle = \frac{5}{2}\left(1 - \frac{4}{5}\sqrt{\frac{15}{2\pi}}h\right) + (\Delta - 4h^2)\sqrt{\frac{480}{\pi}}\frac{1}{16h}\frac{\sqrt{4C_1 - C_2^2 - C_2^2}}{\sqrt{4C_1 - C_2^2}}, \quad (3.60)$$

where  $C_4 > 0$ . A similar expression has been derived in Ref. [70]. From Eq. (3.59) and (3.60) the reduced effective viscosity first decreases, reaching the minimum at the critical value  $\lambda = \lambda_c$ ,

$$\langle[\eta]\rangle = \frac{5}{2} - \sqrt{\frac{15\Delta}{2\pi}}. \quad (3.61)$$

Then increases with increasing  $\lambda$ , with a cusp singularity at  $\lambda = \lambda_c$  see Fig. 3.13.

### 3.4.2 Normal stress differences

As an interesting supplemental physical investigation and another consequence of the exact explicit solutions is to compute the first normal stress difference  $N_1 = \sigma_{11} - \sigma_{22}$  and the second normal stress difference  $N_2 = \sigma_{22} - \sigma_{33}$ . According to Ref.[44],  $N_1$  and  $N_2$  are given by

$$N_1 = -2N_2 = \frac{16\varphi\dot{\gamma}\eta_{ext}}{\Delta}\sqrt{\frac{15}{32\pi}}\mathcal{R}^2\sin(4\psi). \quad (3.62)$$

Using the identity  $\sin(2x) = 2\sin x \cos x$ , Eq. (3.62) can be written simply as

$$N_1 = -2N_2 = \frac{32\varphi\dot{\gamma}_a\eta_{ext}}{\Delta}\sqrt{\frac{15}{32\pi}}\cos(2\pi f_r t)\xi(t)\zeta(t). \quad (3.63)$$

In the TB and VB based oscillatory regimes, the exact solutions (3.37)-(3.38) yield

$$N_1 = -2N_2 = \frac{\varphi\dot{\gamma}_a\eta_{ext}}{2}\sqrt{\frac{15}{2\pi}}\frac{\Delta}{h^2}\frac{\cos(\omega\tau + C_3)[\Gamma + \sin(\omega\tau + C_3)]}{[C_4 + \sin(\omega\tau + C_3)]^2}\cos(2\pi f_r t), \quad (3.64)$$

where

$$\tau = \frac{\dot{\gamma}_a}{2\pi f_r}\sin(2\pi f_r t). \quad (3.65)$$

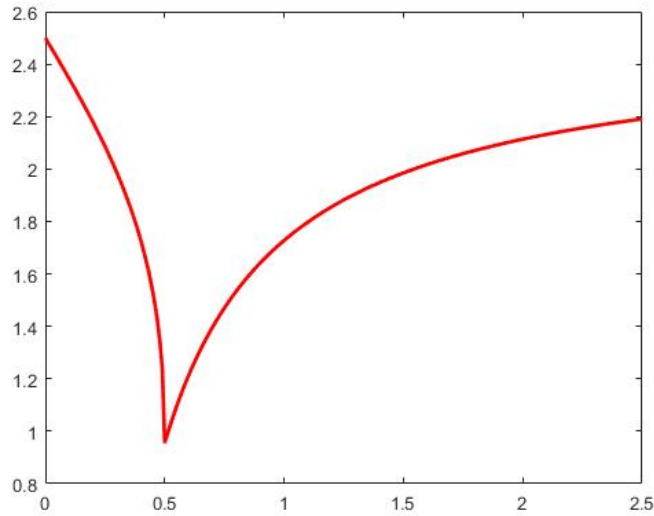


Figure 3.13: Reduced average effective viscosity  $\langle[\eta]\rangle$  as a function of  $h$  for  $\Delta = 1$ . The cusp singularity is due to the transition from  $TB$  or  $VB$  to  $TT$ .

It follows from (3.64) that the time-averaged (over a period) of  $N_1$  and  $N_2$  vanishes;  $\langle N_1 \rangle = \langle N_2 \rangle = 0$  (there is no preferred orientation of the vesicle). In Fig.3.4.2 the first normal stress difference  $N_1$  is plotted by using the exact explicit solution (3.37)-(3.38).

### 3.5 Isotropic part of the tension

In this section, we investigate the time-dependent dynamics of the isotropic part of the tension (3.7). In terms of  $\mathcal{R}$  and  $\psi$ , the isotropic part of the tension  $\sigma_0$  reads

$$\sigma_0 = -6 + \mathcal{C}_k \Delta^{-1} \sqrt{\frac{40\pi}{3}} \mathcal{R} \sin(2\psi). \quad (3.66)$$

Making use the expressions of  $\psi$  and  $\mathcal{R}$  we obtain

$$\sigma_0 = -6 + \mathcal{C}_k^* \Delta^{-1} \sqrt{\frac{40\pi}{3}} \frac{\Delta\omega}{4h} \cos(2\pi f_r t) \mathcal{G} \left( \frac{\dot{\gamma}_a \omega}{2\pi f_r} \sin(2\pi f_r t) \right), \quad (3.67)$$

where the function  $\mathcal{G}$  is given by Eq. (3.54) and Eq. (3.55).

In the limit  $f_r \rightarrow 0$  we recover the time-dependent dynamics of the isotropic part of the tension under

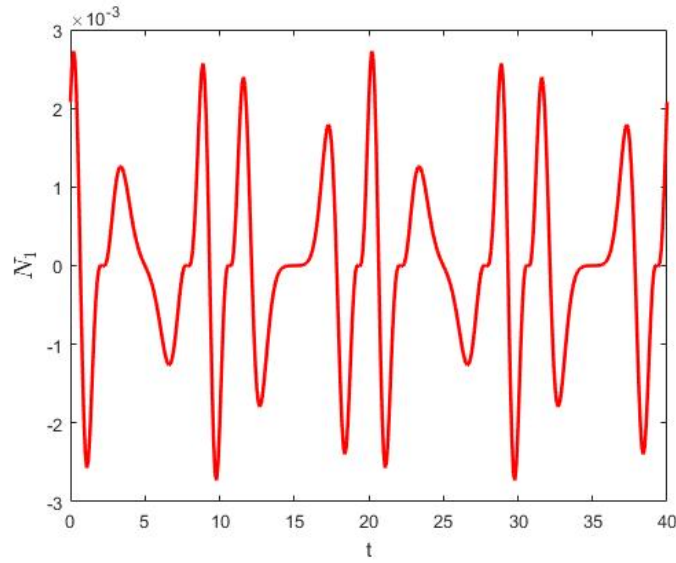


Figure 3.14: Time evolution of the first normal stress difference for  $\Delta = 0.5$ ,  $h = 0.3$ , and  $\Gamma = 0.95$  (tumbling oscillating regime). Parameters  $\varphi$ ,  $\eta_{ext}$ , and  $\dot{\gamma}$  are such that  $\varphi\eta_{ext}\dot{\gamma} = 0.2$ .

the constant shear rate given in [69]

$$\dot{\sigma}_0 + 6 = \mathcal{C}_k^* \Delta^{-1} \sqrt{\frac{40\pi}{3} \frac{\Delta\omega}{4h}} \mathcal{G}(\omega t). \quad (3.68)$$

The isotropic part of the tension under the oscillatory shear rate reads

$$\sigma_0 + 6 = \cos(2\pi f_r t) (\dot{\sigma}_0 + 6)(\tau), \quad (3.69)$$

where  $\tau$  is given by Eq.(3.65).

For  $\lambda < \lambda_c$  (TT based oscillatory regime)

$$\sigma_0 = -6 + \mathcal{C}_k^* \Delta^{-1} \sqrt{\frac{40\pi}{3} \frac{\Delta\omega}{4h}} \frac{e^{\frac{\dot{\gamma}\omega}{2\pi f_r} \sin(2\pi f_r t)} - C_1 e^{-\frac{\dot{\gamma}\omega}{2\pi f_r} \sin(2\pi f_r t)}}{C_2 + e^{\frac{\dot{\gamma}\omega}{2\pi f_r} \sin(2\pi f_r t)} + C_1 e^{-\frac{\dot{\gamma}\omega}{2\pi f_r} \sin(2\pi f_r t)}} \cos(2\pi f_r t), \quad (3.70)$$

when  $f_r$  tends to 0

$$\sigma_0 + 6 = (\dot{\sigma}_0 + 6)(t), \quad (3.71)$$

as  $t$  tends to infinity, which corresponds indeed to a pure TT regime where the shape is fixed. Quantity

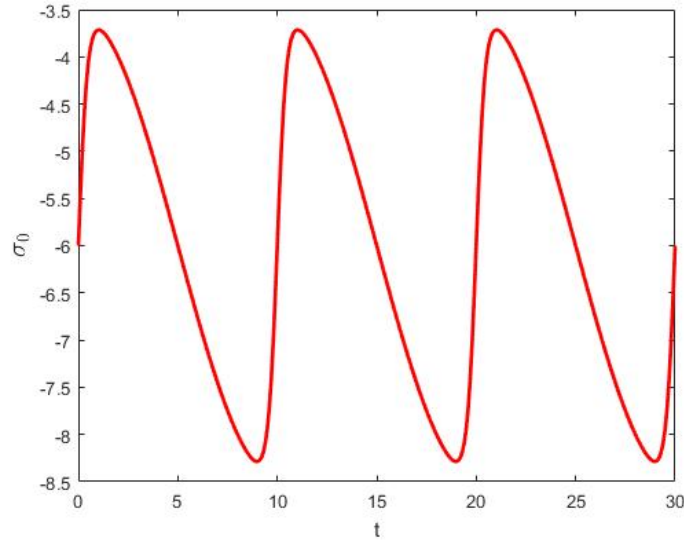


Figure 3.15: Time evolution of the isotropic tension (TT based oscillatory regime). Parameters are  $\Delta = 0.01$ ,  $\mathcal{C}_k = 0.5$ ,  $f_r = 0.05$  and  $h = 0.3$ .

$\sin(2\pi f_r t)$  oscillates with frequency  $\frac{1}{f_r}$ , and as  $f_r$  tends to zero,  $\sigma_0$  takes the stationary value

$$\sigma_0^\infty = -6 + \frac{\mathcal{C}_k^*}{4h} \sqrt{\frac{40\pi}{3}} \sqrt{\frac{4h^2}{\Delta} - 1}. \quad (3.72)$$

The quantity  $\sigma_0^\infty$  increases linearly with  $\mathcal{C}_k^*$ , takes the limit value  $-6$  at  $h = h_c$ , and monotonically approaches  $-6 + \frac{\mathcal{C}_k^*}{\sqrt{\Delta}}$  for large  $h$ . For  $f_r \neq 0$  using eq.(3.69) we can easily see that  $\sigma_0$  oscillates between  $-\sigma_0^\infty$  and  $+\sigma_0^\infty$ . From this, we may deduce that decreasing the bending number leads to the apparition of a negative tension. More precisely, there exists a range of values of the bending number for which the isotropic part of the tension is negative. That is to say, during a TT regime the membrane undergoes compression for

$$\mathcal{C}_k^* \leq \mathcal{C}_c^* = \sqrt{\frac{54\Delta}{5\pi}}. \quad (3.73)$$

In TB and VB based oscillatory dynamics ( $\lambda > \lambda_c$ ), we use expression (3.55) of  $\mathcal{G}$  to get from Eq. (3.67) that

$$\sigma_0 = -6 + \mathcal{C}_k^* \Delta^{-1} \sqrt{\frac{40\pi}{3}} \frac{\Delta \omega \cos(\frac{\gamma_a f_r^*}{f_r} \sin(2\pi f_r t) + C_3)}{4h C_4 + \sin(\frac{\gamma_a f_r^*}{f_r} \sin(2\pi f_r t) + C_3)} \cos(2\pi f_r t). \quad (3.74)$$

Figure (3.16) shows the evolution of  $\sigma_0$  for  $\mathcal{C}_k^* = 0.5$  and for different values of  $\Gamma$  ( $\Gamma = 0.5, 0.8, 1, 3$ ).

As for capsules [69] it is instructive to study the maximum value of the isotropic tension over one period. it is instructive to study the maximum value of the isotropic tension over one period. The min-

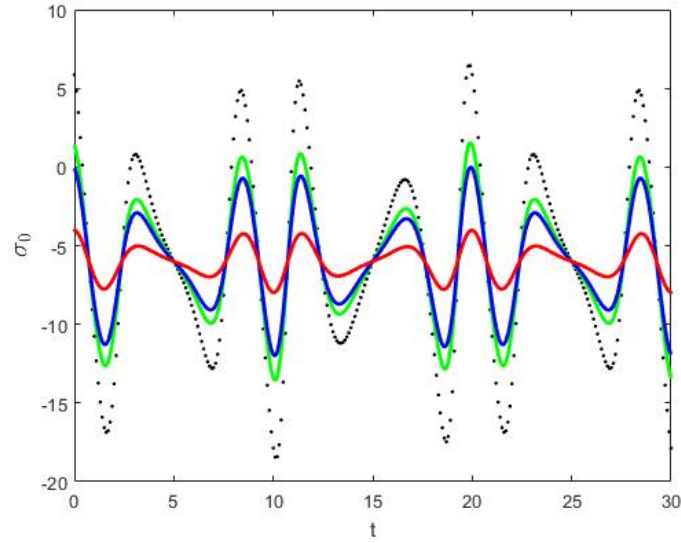


Figure 3.16: (Color online) Time evolution of the isotropic tension for different values of  $\Gamma$ . Parameters are  $\Delta = 0.01, C_k = 0.5, f_r = 0.05$  and  $h = 0.02$ .  $\Gamma = 0.5$  for dotted black line (TB),  $0.8$  for dashed green line (TB),  $1$  for solid blue line (VB), and  $3$  for dashed-dotted red line (VB).

imum value is always negative, indicating that the membrane is (momentarily) under compression and then buckling may occur. First, we calculate the averaged value of  $\sigma_0$  over a period. From Eq. (3.74) we immediately see that

$$\langle \sigma_0 \rangle = \langle \sigma_0^\circ \rangle = -6, \quad (3.75)$$

for both the TB and VB based oscillatory regimes. As a function of  $h$ ,  $\sigma_0$  behaves as the normal stress differences (at the small deformation) [44], We note from Eq. (3.67) that  $\sigma_0 = -6$  at  $\psi = 0$  (where the vesicle aligns with the flow) and at  $\psi = \frac{\pi}{2}$  (where the shape elongation is minimal). During the tumbling KS solution ( $\Gamma = \frac{2h}{\sqrt{\Delta}}$ ) since  $\zeta$  oscillates between  $\pm \frac{\sqrt{\Delta}}{2}$ ,  $\sigma_0$  oscillates between  $-6 \pm \mathcal{C}_k^* \frac{10\pi}{3\Delta}$ . Therefore, the isotropic tension is negative for all times for the shape-preserving regime if Eq. (3.74) holds. For  $\Gamma > \frac{2h}{\sqrt{\Delta}}$  the maximum value of  $\sigma_0$ , noted  $\sigma_0^{\max}$ , is given explicitly by

$$\sigma_0^{\max} = -6 + \frac{\mathcal{C}_k \omega h}{\Delta} \sqrt{\frac{40\pi}{3}} \frac{1}{\sqrt{\Gamma_0^2 - \frac{16h^4}{\Delta^2}}}, \quad (3.76)$$

which decays monotonically to the limiting value  $\sigma_0 \rightarrow -6$  as  $\Gamma$  tends to infinity (see Fig.3.16). Therefore, the isotropic part of the tension is negative for large enough  $\Gamma$ . Expression (3.76) also indicates that

$\sigma_0^{\max}$  is negative for small enough  $\mathcal{C}_k^*$ , i.e.,

$$\mathcal{C}_k^* < \mathcal{C}_c^*(\Gamma), \quad (3.77)$$

where  $\mathcal{C}_c^*(\Gamma)$  is the  $\Gamma$ -critical bending number

$$\mathcal{C}_c^*(\Gamma) = \frac{\Delta}{h\omega} \sqrt{\frac{27}{10\pi}} \sqrt{\Gamma^2 - \frac{16h^4}{\Delta^2}}, \quad (3.78)$$

below which the membrane undergoes compression during the  $\Gamma$  solution. Since  $\Gamma^2 \geq \frac{4h^2}{\Delta}$ , one sees that  $\sigma_0 < 0$  if Eq. (3.73) holds. This means that negative tension occurs in the three regimes for values of  $\mathcal{C}_k^*$  below  $\mathcal{C}_c^*$ . A related question is the effect of the bending number on the formation of wrinkles on a membrane at low deformability. For capsules, it was reported in Ref. [133] that the most extensive wrinkling is seen to occur as  $\mathcal{D}_{12}$  approaches 0 (transition regime). When quasispherical vesicles are placed in nonstationary elongation flows, it is shown theoretically that the relaxational dynamics of the vesicle is accompanied by high-order membrane deformation modes (wrinkles) which have been attributed to the appearance of negative surface tension and that during a stage (third stage) the maximal amplitude of wrinkles is observed at a time when  $F_{22} = 0$ . This corresponds to  $\mathcal{D}_{12} = 0$ . As mentioned above, quantitative three-dimensional analysis of vesicles under flow are presented in Ref. [25]. Numerical solutions, for vesicles with the reduced volume  $v = 0.95$  ( $\Delta = 0.437$ ), showed that the VB mode is damped as long long as  $0.5 < \mathcal{C}_k^* < 2$ . Beyond a value of the order of  $\mathcal{C}_k^* = 2$ , the VB band exhibits a sudden ample widening. In Ref.[60] it was reported that when

$$\sigma_0 + 20 \frac{\sqrt{\Delta}}{\mathcal{C}_k^*} < 0, \quad (3.79)$$

the fourth-order harmonic is excited. In addition, the authors found numerically that close to the VB-to-TB transition at some times during the oscillation, quantity  $-\frac{\sigma_0 \mathcal{C}_k^*}{\sqrt{\Delta}}$  exceeds 20. Here, we find that at the circular shape in the shear plane, quantity  $\sigma_0 + 20 \frac{\sqrt{\Delta}}{\mathcal{C}_k^*}$  is negative for

$$\mathcal{C}_k^* > \frac{10}{3} \sqrt{\Delta}. \quad (3.80)$$

This constitutes a possible explanation of a wrinkled structure during the VB-TB phase transition for quasispherical vesicles. As an example, if we take  $\Delta = 0.437$  [ ] we obtain, during the VB-TB phase

border that quantity  $-\frac{\sigma_0 \mathcal{C}_k}{\sqrt{\Delta}}$  momentarily exceeds 20 for  $\mathcal{C}_k > 2.203$ .

### 3.6 Conclusion

In conclusion, we analytically studied the dynamics of a deformable vesicle under a pure oscillating shear flow. The investigation used the small deformation theory [91]. The advantage of this approach is that a complete set of exact closed solutions for the vesicle orientation in the flow and its shape evolution are derived (to leading order). As a result, a mixed oscillatory dynamics ( $\text{MOD}_n$ ) regime, during which a series of  $n$  TB is periodically interrupted by a SW is found (for  $\lambda > \lambda_c$ ), in a reasonable agreement with the result for RBCs [52]. Overall, we estimated  $n$ , as a function of the ratio of  $\dot{\gamma}_a$  to  $f_r$ , and obtained an unbounded sequence of critical values ( $\dot{\gamma}_a^n$ ) at which the transition between  $\text{MOD}_{n-1}$  and  $\text{MOD}_n$  occurs. Also, we noted that the mixed oscillatory structure is insensitive to initial conditions, and no cascade of doubling period motion is observed as well as the parameters vary (at least to leading order). The present results can be considered as a (relative) simplistic picture when compared to the actual complex nature of RBCs. However, we strongly believe that our results can be used as a starting point to study the mixed oscillatory dynamics behaviors for vesicles and microcapsules under oscillatory flow taking into account higher-order contributions or/and thermal fluctuations in the shape deformation equations, even for small amplitude oscillatory shear. We hope to investigate this matter further in a future work. Finally, beyond the scope of this work, Eq. (3.30) or (3.33) can be considered as a simple analytical example that describes a sequence of tumbles interrupted (periodically) by swinging. The exact closed solutions also may provide a more elegant and simple way for analyzing the vesicle dynamics in the case where the shear flow oscillates and is unbounded in the course of time. This problem is currently under investigation.

**Part 2: Existence of some  
nonlinear parabolic problems  
having a variable growth  
conditions and variable  
exponent**

# Nonlinear parabolic equation having nonstandard growth condition with respect to the gradient and variable exponent

## 4.1 Introduction

In the last decade, theoretical studies of partial differential equations have given birth to a new type of problem with nonstandard growth conditions. This new type of problem is often linked to the name "variable exponent" which means that the equation and their operator has a variable growth condition. Mathematical analysis of PDEs with variable exponent has undergone a great evolution in several fields of applied science. Among which dynamics fluid, image processing [38, 57, 115, 123], pidemiology models and their related predator-prey models [6, 14, 23]. The functional framework involving these type of problems are  $L^{p(x)}(\Omega)$  and  $W^{m,p(x)}(\Omega)$  which called respectively Lebesgue and Sobolev space with variable exponent, for more details on these spaces, we refer the readers to see [57, 79, 67].

The purpose of this work is to study the existence of weak solution for a class of quasilinear parabolic equation with variable exponent modeled by

$$\begin{cases} \partial_t u - \operatorname{div}(A(t, x, \nabla u)) = f(t, x, u, \nabla u) & \text{in } Q_T := (0, T) \times \Omega \\ u(0, x) = u_0(x) & \text{in } \Omega \\ u(t, x) = 0 & \text{on } \Sigma_T := (0, T) \times \partial\Omega \end{cases} \quad (4.1)$$

where  $\Omega$  is an open bounded subset of  $\mathbb{R}^N$ , with smooth boundary  $\partial\Omega$ ,  $T > 0$ , the initial data  $u_0$  is assumed to be a measurable function belonging in  $L^2(\Omega)$ . The operator  $-\operatorname{div}(A(t, x, \nabla u))$  is of the type Leray-Lions with variable exponent  $p(x)$ . We assume that  $p$  is a continuous function on  $\overline{\Omega}$  with  $\inf_{x \in \overline{\Omega}} p(x) > 1$  and  $A : Q_T \times \mathbb{R}^N \rightarrow \mathbb{R}^N$  is a Carathéodory function satisfying

$$(H_1) \quad |A(t, x, \xi)| \leq H(t, x) + |\xi|^{p(x)-1}$$

$$(H_2) \quad A(t, x, \xi)\xi \geq d|\xi|^{p(x)}$$

$$(H_3) \quad \langle A(t, x, \xi) - A(t, x, \xi^*), \xi - \xi^* \rangle > 0$$

for almost every  $(t, x)$  in  $Q_T$  and for every  $\xi, \xi^*$  in  $\mathbb{R}^N$  ( $\xi \neq \xi^*$ ), with  $H \in L^{\frac{p(x)}{p(x)-1}}(Q_T)$  and  $d > 0$ . For the nonlinearity  $f$ , we assume that

$$(H_4) \quad f : Q_T \times [0, +\infty) \times \mathbb{R} \times \mathbb{R}^N \rightarrow \mathbb{R} \text{ is a Carathéodory function.}$$

$$(H_5) \quad (s, r) \mapsto f(t, x, s, r) \text{ is locally Lipschitz continuous for a.e } (t, x) \text{ in } Q_T.$$

$$(H_6) \quad f(t, x, s, 0) = \min \{f(t, x, s, r), r \in \mathbb{R}^N\} = 0.$$

Quasilinear partial differential equations has pulled the attention of several authors and great works have been published not only for initial data [12, 10, 64, 113, 112, 67, 105, 85] but also for stationary and periodic case (see for example the works [11, 36, 37, 35, 54]). To present the novelty and the originality of our work, we propose to recall some recent works which have been dealt with the particular cases of the problem (4.1). We start by the paper of Bendahmane et al [24], where the authors studied (4.1) when  $u_0$  belong to  $L^1(\Omega)$ ,  $f$  belongs to  $L^1(Q_T)$  and does not depend on  $(u, \nabla u)$ . Based on the semigroup theory, they established well-posedness (existence and uniqueness) of a renormalized solution to (4.1). They proved that the obtained solution is also the entropy solution of the considered problem. Zhang and Zhou in [137] were studied the existence-uniqueness of renormalized and entropy solution of the same equation (4.1). They used the semi-discretization time method to prove the well-posedness of an approximate weak solution to (4.1). Thereafter, they obtained the existence of a renormalized solution to (4.1) as a limit of an approximate problem. Based on the choice of the used test function, the authors showed the uniqueness of the obtained solution and they demonstrated the equivalence between the renormalized solution and the entropy solution to (4.1). The results of [24, 137] was generalized by Li and Gao in their paper [84], where they studied the existence of solutions to (4.1) with a particular sign assumption on the nonlinearity  $f(u, \nabla u)$ . Via the convergence of truncation, they obtained the existence of renormalized solution to

the considered problem. In [85] Li et al studied the equation (4.1) with smooth initial condition and  $f$  depends only on  $\nabla u$ . Under the De Giorgi iteration technique, the authors proved the critical a priori  $L^\infty$ -estimates and thus established the existence of weak solutions to (4.1). Note that all these work examined the  $p(x)$ -Laplacian operator which is a particular case of the considered operator in the equation (4.1). Therefore, the case of the Leray-Lions operator was discussed in the current literature. In particular, Ouaro et al. [105] proved the existence and uniqueness of the entropy solutions to (4.1) with  $L^1$ -data. Their proof based on the nonlinear semigroup theory and involved Lebesgue and Sobolev spaces with variable exponent. In view of the semilinear case of (4.1) ( $f$  depending only on  $u$ ), Rădulescu et al [67] have been proposed a qualitative analysis on the existence and uniqueness of a weak solution to (4.1). The authors assumed that  $f(x, u)$  is a Carathéodory function with respect to  $x$  and locally Lipschitz with respect to  $u$ . Under a suitable assumption on the variable exponent, they established the existence and uniqueness of the weak solution to (4.1). The authors discussed also the global behavior of the obtained solutions, more precisely the convergence to a stationary solution as  $t \rightarrow \infty$ .

$L^2$ -solutions for PDEs with variable exponent was also examined by several authors. In [7] Akagi and Matsuura proposed a mathematical analysis of parabolic  $p(x)$ -Laplacian equation with  $L^2$  data. Using the subdifferential calculus, They proved the existence and uniqueness of  $L^2$ -solution to the considered problem and they studied the large-time behavior of the obtained solution. Shangerganesh and Balachandran [123] considered the reaction-diffusion model with variable exponents and  $L^2$  data and without growth conditions on  $(u, \nabla u)$ . The authors studied the existence of weak solutions to the considered model when the nonlinearities does not depend on  $\nabla u$ . Based on the standard Galerkin's method and Gronwall lemma, the authors established the existence and uniqueness of a weak solution to the considered model. However in contrast to the earlier mentioned works, here we present two existence results of a weak solution to the quasilinear parabolic equation (4.1). For the first one, we will assume that  $f(u, \nabla u)$  is bounded in  $Q_T$ . Under the application of Schaeffer's fixed point theorem in a suitable Banach space, we prove the existence of a weak solution to (4.1). Concerning the second existence result, we will assume that  $f(u, \nabla u)$  has a critical growth with respect to the gradient. By combining the truncation technics with the sub-and super-solution method, we establish the existence of a weak solution to (4.1).

We start initially with a recall in which we state the interesting results and properties of Lebesgue-Sobolev spaces with exponents variables. Thereafter, we prove in section 3 the existence result of a weak solution to the proposed equation with bounded nonlinearity. This is done with the help of Schaeffer's

fixed point theorem. In section 4, we use the method of sub- and super-solution to consider an approximate problem of (4.1), the existence of a weak solution to the last one is ensured by the result of section 3. After that, we give a suitable estimates on the approximate solutions and we pass to the limit in the approximate problem. Section 5, is devoted to prove some auxiliaries results, the first result concerns the existence and uniqueness result of a weak parabolic equation with  $L^2$  data. The second result presents an interesting compactness result of a class of parabolic equations with variable exponent.

## 4.2 Preliminaries results and notations

### 4.2.1 Lebesgue-Sobolev spaces with variable exponent

We begin this section by a brief recall of Lebesgue and Sobolev spaces with variable exponent. Let  $p : \bar{\Omega} \rightarrow [1, +\infty[$  be a continuous function, we define

$$p^- = \inf_{x \in \bar{\Omega}} p(x) \quad \text{and} \quad p^+ = \sup_{x \in \bar{\Omega}} p(x).$$

Throughout this chapter, we assume that

$$1 < p^- \leq p(x) \leq p^+ < \infty. \tag{4.2}$$

The variable exponent Lebesgue space is introduced such as

$$L^{p(x)}(\Omega) = \left\{ u : \Omega \rightarrow \mathbb{R}; u \text{ is measurable with } \rho_{p(x)}(u) < \infty \right\},$$

where  $\rho_{p(x)}(\cdot)$  define the following convex modular

$$\rho_{p(x)}(u) = \int_{\Omega} |u(x)|^{p(x)} dx.$$

We equip the Lebesgue space  $L^{p(x)}(\Omega)$  with the Luxemburg norm

$$\|u\|_{p(x)} = \inf \left\{ \alpha > 0 : \rho_{p(x)}\left(\frac{u}{\alpha}\right) \leq 1 \right\}.$$

From the hypothesis (4.2), the space  $L^{p(x)}(\Omega)$  come to be a separable, uniformly convex Banach space, the dual space of  $L^{p(x)}(\Omega)$  is introduced as  $L^{p'(x)}(\Omega)$  with  $p'(x) = \frac{p(x)}{p(x)-1}$ . Let  $u \in L^{p(x)}(\Omega)$  and  $v \in L^{p'(x)}(\Omega)$ ,

then the following Hölder inequality

$$\int_{\Omega} |uv| dx \leq \left( \frac{1}{p} + \frac{1}{p'} \right) \|u\|_{p(x)} \|v\|_{p'(x)},$$

holds true. The following proposition gives us the useful interesting properties of Lebesgue spaces with variable exponent.

**Proposition 4.2.1**

1.  $\min \left\{ \|u\|_{p(x)}^{p^-}, \|u\|_{p(x)}^{p^+} \right\} \leq \rho_{p(x)}(u) \leq \max \left\{ \|u\|_{p(x)}^{p^-}, \|u\|_{p(x)}^{p^+} \right\}$ .
2. *If  $\Omega$  is bounded, the inclusion result between  $L^{p(x)}(\Omega)$  spaces still holds. Furthermore, let  $p_1, p_2$  be two variables exponents, such that  $p_1(x) \leq p_2(x)$  almost everywhere in  $\Omega$ , we have the following continuous embedding  $L^{p_2(x)}(\Omega) \hookrightarrow L^{p_1(x)}(\Omega)$ .*
3. *Let  $q \in C(\bar{\Omega})$  such that  $1 \leq q(x) < p^*(x)$ , for all  $x \in \bar{\Omega}$ , then the embedding  $W_0^{1,p(x)}(\Omega) \hookrightarrow L^{q(x)}(\Omega)$  is continuous and compact, where*

$$p^*(x) := \begin{cases} \frac{Np(x)}{N-p(x)}, & p(x) < N, \\ +\infty, & p(x) \geq N. \end{cases}$$

To extend the variable exponent  $p : \bar{\Omega} \rightarrow [1, \infty)$  to the general case  $\bar{Q}_T = [0, T] \times \bar{\Omega}$ , we set  $p(t, x) := p(x)$  for all  $(t, x) \in \bar{Q}_T$ . Hence, the variable exponent Lebesgue space  $L^{p(x)}(Q_T)$  is presented as follows

$$L^{p(x)}(Q_T) = \left\{ u : Q_T \rightarrow \mathbb{R} \text{ measurable with } \int_{Q_T} |u(t, x)|^{p(x)} dx dt < \infty \right\},$$

equipped with the norm

$$\|u\|_{p(x)} = \inf \left\{ \alpha > 0, \int_{Q_T} \left| \frac{u(t, x)}{\alpha} \right|^{p(x)} dx dt \leq 1 \right\},$$

which is a separable, uniformly convex Banach space. The variable exponent Sobolev space  $W^{1,p(x)}(\Omega)$  is defined such as

$$W^{1,p(x)}(\Omega) = \left\{ u \in L^{p(x)}(\Omega), \quad |\nabla u| \in L^{p(x)}(\Omega)^N \right\},$$

where its norm is presented as follows

$$\|u\|_{1,p(x)} = \|u\|_{p(x)} + \|\nabla u\|_{p(x)}.$$

Due to this norm, the space  $W^{1,p(x)}(\Omega)$  is a separable and reflexive Banach space. We assume that  $p(x)$  satisfies the log-Hölder-continuity condition, i.e. there exists a constant  $C$  such that for all  $x_1, x_2 \in \Omega$

$$|p(x_1) - p(x_2)| \leq \frac{C}{-\log|x_1 - x_2|}, \quad \forall x_1, x_2 \in \Omega, \quad \text{with } |x_1 - x_2| < \frac{1}{2}. \quad (4.3)$$

Under the assumption (4.3), the space of smooth functions  $\mathcal{C}_c^\infty(\Omega)$  is dense in the variable exponent Sobolev space  $W^{1,p(x)}(\Omega)$ . For the sake of convenience, we define  $W_0^{1,p(x)}(\Omega)$  as the closure of  $\mathcal{C}_c^\infty(\Omega)$  in  $W^{1,p(x)}(\Omega)$ . For any  $u \in W_0^{1,p(x)}(\Omega)$  the  $p(x)$ -Poincaré inequality

$$\|u\|_{L^{p(x)}(\Omega)} \leq C \|\nabla u\|_{L^{p(x)}(\Omega)},$$

holds true, where the constant  $C$  depends only on  $p$  and  $\Omega$ . Thus, we define the norm on  $W_0^{1,p(x)}(\Omega)$  such as

$$\|u\|_{W_0^{1,p(x)}(\Omega)} = \|\nabla u\|_{p(x)}.$$

For more properties of Lebesgue and Sobolev spaces with variable exponent, we refer the reader to the book [113].

## 4.2.2 Functional framework and definitions

In this paragraph, we present the functional framework used in this work and we enunciate the notion of weak solution adapted to solve the problem (4.1).

For any  $0 < T < +\infty$ , we define the time space

$$L^{p^-}(0, T; W_0^{1,p(x)}(\Omega)) = \left\{ u \in L^{p(x)}(Q_T) : \int_0^T \|\nabla u\|_{p(x)}^{p^-} dt < \infty \right\},$$

endowed with the norm

$$\|u\|_{L^{p^-}(0, T; W_0^{1,p(x)}(\Omega))} = \left( \int_0^T \|\nabla u\|_{p(x)}^{p^-} dt \right)^{\frac{1}{p^-}}.$$

Now, let us introduce the space  $\mathcal{V}$  which is already considered in the studies of a parabolic problems with variable exponent

$$\mathcal{V} = \left\{ v \in L^{p^-} \left( 0, T; W_0^{1,p(x)}(\Omega) \right) : |\nabla v| \in L^{p(x)}(Q_T)^N \right\},$$

endowed with the norm

$$\|u\|_{\mathcal{V}} = \|\nabla u\|_{L^{p(x)}(Q_T)}.$$

Due to the  $p(x)$ -Poincaré inequality and the continuity of the embedding  $L^{p(x)}(Q_T) \hookrightarrow L^{p^-}(0, T; W_0^{1,p(x)}(\Omega))$

the norm  $\|\cdot\|_{\mathcal{V}}$  is equivalent to the following norm

$$\|v\|_{\mathcal{V}} = \|v\|_{L^{p^-}(0, T; W_0^{1,p(x)}(\Omega))} + \|\nabla v\|_{p(x)}.$$

The space  $\mathcal{V}$  is a separable and reflexive Banach space and  $\mathcal{V}^*$  denoted its dual space. Some interesting properties of the space  $\mathcal{V}$  are stating in the following lemma

**Lemma 4.2.1**

[24] Let  $\mathcal{V}$  be the space defined as above. Then,

i) we have the following continuous dense embedding

$$L^{p^+}(0, T; W_0^{1,p(x)}(\Omega)) \hookrightarrow \mathcal{V} \hookrightarrow L^{p^-}(0, T; W_0^{1,p(x)}(\Omega)). \quad (4.4)$$

In particular, since  $\mathcal{C}_c^\infty(Q_T)$  is dense in  $L^{p^+}(0, T; W_0^{1,p(x)}(\Omega))$ , it is dense in  $\mathcal{V}$  and for the corresponding dual spaces we have

$$L^{(p^-)'}(0, T; (W_0^{1,p(x)}(\Omega))^*) \hookrightarrow \mathcal{V}^* \hookrightarrow L^{(p^+)'}(0, T; (W_0^{1,p(x)}(\Omega))^*). \quad (4.5)$$

ii) Moreover, the elements of  $\mathcal{V}^*$  are represented as follow: For all  $\zeta \in \mathcal{V}^*$ , there exists  $\xi = (\xi_1, \dots, \xi_N) \in (L^{p'(x)}(Q_T))^N$  such that:  $\zeta = \operatorname{div}(\xi)$  and

$$\langle \zeta, \varphi \rangle_{\mathcal{V}^*, \mathcal{V}} = \int_{Q_T} \xi \nabla \varphi \, dxdt,$$

for any  $\varphi \in \mathcal{V}$ . Furthermore, we have

$$\|\zeta\|_{\mathcal{V}^*} = \max\{\|\xi_i\|_{L^{p(x)}(Q_T)}, i = 1, \dots, N\}.$$

iii) For any  $u \in \mathcal{V}$  the following relationship holds true

$$\min \left\{ \|u\|_{\mathcal{V}}^{p^-}, \|u\|_{\mathcal{V}}^{p^+} \right\} \leq \int_{Q_T} |\nabla u|^{p(x)} dxdt \leq \max \left\{ \|u\|_{\mathcal{V}}^{p^-}, \|u\|_{\mathcal{V}}^{p^+} \right\}. \quad (4.6)$$

**Definition 4.2.1**

A measurable function  $u : Q_T \rightarrow \mathbb{R}$  is said to be a weak solution to the problem (4.1) if it satisfies the following properties

$$u \in \mathcal{V} \cap L^\infty(Q_T), \quad \partial_t u \in \mathcal{V}^* + L^1(Q_T),$$

$$f(t, x, u, \nabla u) \in L^1(Q_T), \quad u(0, x) = u_0(x) \text{ in } L^2(\Omega),$$

$$\int_0^T \langle \partial_t u, \varphi \rangle + \int_{Q_T} A(t, x, \nabla u) \nabla \varphi = \int_{Q_T} f(t, x, u, \nabla u) \varphi,$$

for every test function  $\varphi \in \mathcal{V} \cap L^\infty(Q_T)$ .

**Remark 4.2.1**

According to the result of [24], we have the following embedding

$$\{u \in \mathcal{V} \cap L^\infty(Q_T); \partial_t u \in \mathcal{V}^* + L^1(Q_T)\} \hookrightarrow \mathcal{C}([0, T]; L^2(\Omega)),$$

which gives that the initial condition makes sense in the definition 4.2.1.

**Lemma 4.2.2**

[85] Assuming that  $\pi : \mathbb{R} \rightarrow \mathbb{R}$  is  $C^1$  piecewise function such that  $\pi(0) = 0$  and  $\pi' = 0$  outside a compact set. Let  $\Pi(s) = \int_0^s \pi(\sigma) d\sigma$ . If  $u \in \mathcal{V}$  with  $\partial_t u \in \mathcal{V}^* + L^1(Q_T)$ , then

$$\int_0^T \langle \partial_t u, \pi(u) \rangle dt = \langle \partial_t u, \pi(u) \rangle_{\mathcal{V}^* + L^1(Q_T), \mathcal{V} \cap L^\infty(Q_T)} = \int_\Omega \Pi(u(T)) dx - \int_\Omega \Pi(u(0)) dx$$

Before closing this section, we state some truncation functions which will be useful in this work. For every positive real number  $k$ , we set  $T_k(s) = \min(k, \max(s, -k))$  and  $S_k(r) = \int_0^r T_k(s) ds$ .

**4.3 An existence result with bounded nonlinearity**

The purpose of this section is to establish the existence of a weak solution to the problem (4.1) when the nonlinearity  $f$  is bounded almost everywhere. We state in the following theorem the main result of this section.

**Theorem 4.3.1**

Under the hypotheses  $(H_1)$ - $(H_6)$ , we assume the existence of a nonnegative function  $M \in L^\infty(Q_T)$  such that for a.e.  $(t, x)$  in  $Q_T$ ,

$$|f(t, x, r, \xi)| \leq M(t, x) \quad \text{for all } (r, \xi) \in \mathbb{R} \times \mathbb{R}^N. \quad (4.7)$$

Then for every  $u_0 \in L^2(\Omega)$ , the problem (4.1) has a weak solution.

**Proof.**

In order to prove the result of Theorem 4.3.1, we propose to apply Schaeffer fixed point method. We set  $\mathcal{X} := [0, 1] \times \mathcal{V}$  and we consider the following mapping

$$\begin{aligned} \mathcal{H} : \mathcal{X} &\longrightarrow \mathcal{V}, \\ (\lambda, v) &\longmapsto u. \end{aligned}$$

where  $u$  is a weak solution of the following parabolic equation

$$\begin{cases} \partial_t u - \operatorname{div}(t, x, \nabla u) = f(t, x, v, \lambda \nabla v) & \text{in } Q_T \\ u(0, x) = \lambda u_0(x) & \text{in } \Omega \\ u(t, x) = 0 & \text{on } \Sigma_T \end{cases} \quad (4.8)$$

Due to the assumption (4.7), the function  $f(t, x, v, \lambda \nabla v)$  belongs to  $L^2(Q_T)$  and the initial condition  $\lambda u_0$  belongs to  $L^2(Q_T)$ . Moreover, for  $(\lambda, v) \in \mathcal{X}$  fixed, we deduce from Lemma 4.5.1 the existence of a unique weak solution  $u \in \mathcal{V}$  to the problem (4.8) in the sense that

$$\begin{aligned} \partial_t u &\in \mathcal{V}^* + L^2(Q_T), \quad u(0, x) = \lambda u_0(x) \text{ in } L^2(\Omega), \\ \int_0^T \langle \partial_t u, \varphi \rangle + \int_{Q_T} A(t, x, \nabla u) \nabla \varphi &= \int_{Q_T} f(t, x, v, \lambda \nabla v) \varphi, \end{aligned} \quad (4.9)$$

for every test function  $\varphi \in \mathcal{V} \cap L^2(Q_T)$ . As a consequence, the mapping  $\mathcal{H}$  is well defined. Furthermore, from the assumption  $(H_6)$  and (4.9), it is easy to verify that for all  $v \in \mathcal{V}$ , we have  $\mathcal{H}(0, v) = 0$ . We set

$$\mathcal{U} = \left\{ u \in \mathcal{V} : u = \mathcal{H}(\lambda, u) \text{ for some } \lambda \in [0, 1] \right\}.$$

To apply Schaeffer's fixed point Theorem, we proceed by three steps:

**Step 1: the mapping  $\mathcal{H}$  is continuous**

Let  $(\lambda_n, v_n)$  be a sequence in  $\mathcal{X}$  such that

$$(\lambda_n, v_n) \rightarrow (\lambda, v) \text{ strongly in } \mathcal{X}.$$

Let us define  $u_n = \mathcal{H}(\lambda_n, v_n)$ , which means that  $u_n$  satisfies the following weak formulation

$$\begin{aligned} \partial_t u_n &\in \mathcal{V}^* + L^2(Q_T), \quad u_n(0, x) = \lambda_n u_0(x) \text{ in } L^2(\Omega), \\ \int_0^T \langle \partial_t u_n, \varphi \rangle + \int_{Q_T} A(t, x, \nabla u_n) \nabla \varphi &= \int_{Q_T} f(t, x, v_n, \lambda_n \nabla v_n) \varphi, \end{aligned} \quad (4.10)$$

for all  $\varphi \in \mathcal{V} \cap L^2(Q_T)$ . To prove the continuity of  $\mathcal{H}$  it suffices to prove that  $(u_n)$  converges strongly to  $u$  in  $\mathcal{V}$ . According to the result of Lemma 4.5.1, one obtains

$$\begin{aligned} \|u_n\|_{\mathcal{V}} &\leq C(\Omega, T) \left( \|\lambda_n u_0\|_{L^2(\Omega)} + \|f(t, x, v_n, \lambda_n \nabla v_n)\|_{L^2(Q_T)} \right), \\ \|\partial_t u_n\|_{\mathcal{V}^* + L^2(Q_T)} &\leq C(\Omega, T) \left( \|H\|_{p'(x)} + \|\lambda_n u_0\|_{L^2(\Omega)} + \|f(t, x, v_n, \lambda_n \nabla v_n)\|_{L^2(Q_T)} \right). \end{aligned}$$

By using the assumption (4.7), it follows that  $(u_n)$  is bounded in  $\mathcal{V}$  and  $(\partial_t u_n)$  is bounded in  $\mathcal{V}^* + L^2(Q_T)$ . On the other hand, due to the compactness result of Lemma 4.5.2, there exists a subsequence of  $(u_n)$  still denoted by  $(u_n)$  for simplicity such that

$$\begin{aligned} u_n &\rightarrow u \text{ strongly in } L^{p^-}(Q_T) \text{ and a.e. in } Q_T, \\ \nabla u_n &\rightarrow \nabla u \text{ a.e. in } Q_T, \end{aligned} \quad (4.11)$$

therefore,

$$A(t, x, \nabla u_n) \rightharpoonup A(t, x, \nabla u) \text{ weakly in } L^{p'(x)}(Q_T).$$

From the strong convergence of  $(\lambda_n, v_n)$  in  $\mathcal{X}$ , it follows that

$$f(t, x, v_n, \lambda_n \nabla v_n) \rightarrow f(t, x, v, \lambda \nabla v) \text{ a.e in } Q_T,$$

using hypotheses (4.7) and Lebesgue convergence theorem, one has

$$f(t, x, v_n, \lambda_n \nabla v_n) \rightarrow f(t, x, v, \lambda \nabla v) \text{ strongly in } L^{(p^-)'}(Q_T). \quad (4.12)$$

We Subtract the equation (4.10) for different indexes  $n$  and  $m$ , one gets

$$\begin{aligned} & \int_0^T \langle \partial_t(u_n - u_m), \varphi \rangle + \int_{Q_T} (A(t, x, \nabla u_n) - A(t, x, \nabla u_m)) \nabla \varphi \\ &= \int_{Q_T} (f(t, x, v_n, \lambda_n \nabla v_n) - f(t, x, v_m, \lambda_m \nabla v_m)) \varphi. \end{aligned}$$

Setting  $\varphi = (u_n - u_m)$ , one obtains

$$\begin{aligned} & \int_{Q_T} (A(t, x, \nabla u_n) - A(t, x, \nabla u_m)) (\nabla u_n - \nabla u_m) \leq \frac{1}{2} \int_{\Omega} |(\lambda_n u_0 - \lambda_m u_0)|^2 \\ &+ \int_{Q_T} (f(t, x, v_n, \lambda_n \nabla v_n) - f(t, x, v_m, \lambda_m \nabla v_m)) (u_n - u_m) \end{aligned} \quad (4.13)$$

Using Hölder's inequality on the right-hand side of (4.13), we get

$$\begin{aligned} & \int_{Q_T} (A(t, x, \nabla u_n) - A(t, x, \nabla u_m)) (\nabla u_n - \nabla u_m) \leq \frac{|\lambda_n - \lambda_m|^2}{2} \int_{\Omega} |u_0|^2 \\ &+ \|f(t, x, v_n, \lambda_n \nabla v_n) - f(t, x, v_m, \lambda_m \nabla v_m)\|_{L^{(p-)'}(Q_T)} \|u_n - u_m\|_{L^{p-}(Q_T)}. \end{aligned} \quad (4.14)$$

By employing the almost everywhere convergence of  $(\nabla u_m)$  in  $Q_T$ , the assumption  $(H_3)$  and (4.12), we may employ Fatou's Lemma in order to the limit in (4.14) as  $m \rightarrow \infty$

$$\begin{aligned} & \int_{Q_T} (A(t, x, \nabla u_n) - A(t, x, \nabla u)) (\nabla u_n - \nabla u) \leq \frac{|\lambda_n - \lambda|^2}{2} \int_{\Omega} |u_0|^2 \\ &+ \|f(t, x, v_n, \lambda_n \nabla v_n) - f(t, x, v, \lambda \nabla v)\|_{L^{(p-)'}(Q_T)} \|u_n - u\|_{L^{p-}(Q_T)}. \end{aligned} \quad (4.15)$$

From (4.11) and (4.12), it follows that

$$\lim_{n \rightarrow \infty} \int_{Q_T} (A(t, x, \nabla u_n) - A(t, x, \nabla u)) (\nabla u_n - \nabla u) \leq 0.$$

In view of the result [26], we deduce that  $(u_n)$  converges strongly to  $u$  in  $\mathcal{V}$ . Passing to the limit in (4.10), one gets

$$\begin{aligned} & \partial_t u \in \mathcal{V}^* + L^2(Q_T), \quad u(0, x) = \lambda u_0(x) \text{ in } L^2(\Omega), \\ & \int_0^T \langle \partial_t u, \varphi \rangle + \int_{Q_T} A(t, x, \nabla u) \nabla \varphi = \int_{Q_T} f(t, x, v, \lambda \nabla v) \varphi, \end{aligned} \quad (4.16)$$

for all  $\varphi \in \mathcal{V} \cap L^2(Q_T)$ . Using the uniqueness of the weak solution of (4.16), we deduce that  $\mathcal{H}(\lambda, v) = u$ , which gives the continuity of  $\mathcal{H}$ .

**Step 2: the mapping  $\mathcal{H}$  is compact**

We consider  $(\lambda_n, v_n)$  a bounded sequence in  $\mathcal{X}$ , we will prove that  $u_n = \mathcal{H}(\lambda_n, v_n)$  is relatively compact in  $\mathcal{V}$ , we have

$$\begin{aligned}\lambda_n &\rightarrow \lambda^*, \\ v_n &\rightarrow v \text{ weakly in } \mathcal{V}.\end{aligned}$$

In this step, the difficulties come back in the absence of the almost everywhere convergence of  $(\nabla v_n)$  in  $Q_T$ , but we can overcome these difficulties by employing the assumption (4.7). By following the same reasoning of the first step, one gets

- $u_n$  is bounded in  $\mathcal{V}$
- $\partial_t u_n$  is bounded in  $\mathcal{V}^* + L^2(Q_T)$
- $\left( f(t, x, v_n, \lambda_n \nabla v_n) \right)_n$  is bounded in  $L^2(Q_T)$

Thanks to the compactness result of Lemma 4.5.2, there exist a subsequence still denoted by  $u_n$  for simplicity such that for

$$\begin{aligned}u_n &\rightarrow u \text{ strongly in } L^{p^-}(Q_T) \text{ and a.e. in } Q_T. \\ \nabla u_n &\rightarrow \nabla u \text{ and a.e. in } Q_T.\end{aligned}$$

Furthermore, we have

$$A(t, x, \nabla u_n) \rightharpoonup A(t, x, \nabla u) \text{ weakly in } L^{p'(x)}(Q_T).$$

We shall prove that  $(u_n)$  converges strongly in  $\mathcal{V}$ . We follow the same reasoning of the first step, for different index  $m$  and  $n$ , one has

$$\begin{aligned}\int_{Q_T} (A(t, x, \nabla u_n) - A(t, x, \nabla u_m))(\nabla u_n - \nabla u_m) &\leq \frac{|\lambda_n - \lambda_m|^2}{2} \int_{\Omega} |u_0|^2 \\ &+ \int_{Q_T} (f(t, x, v_n, \lambda_n \nabla v_n) - f(t, x, v_m, \lambda_m \nabla v_m))(u_n - u_m).\end{aligned}\tag{4.17}$$

To deal with the right-hand side of (4.17), we apply the assumption (4.7) and Hölder's inequality, we have

$$\begin{aligned}\int_{Q_T} (f(t, x, v_n, \lambda_n \nabla v_n) - f(t, x, v_m, \lambda_m \nabla v_m))(u_n - u_m) &\leq 2\|M\|_{L^\infty(Q_T)} \int_{Q_T} |u_n - u_m| \\ &\leq C\|u_n - u_m\|_{L^{p^-}(Q_T)}.\end{aligned}$$

Therefore,

$$\begin{aligned} \int_{Q_T} (A(t, x, \nabla u_n) - A(t, x, \nabla u_m))(\nabla u_n - \nabla u_m) &\leq \frac{|\lambda_n - \lambda_m|^2}{2} \int_{\Omega} |u_0|^2 \\ &+ C \|u_n - u_m\|_{L^{p^-}(Q_T)}. \end{aligned} \quad (4.18)$$

In view of the almost everywhere convergence of  $(\nabla u_m)$  and thanks to the assumption  $(H_3)$ , we can apply Fatou's Lemma to pass to the limit in (4.18) as  $m \rightarrow \infty$ , one obtains

$$\begin{aligned} \int_{Q_T} (A(t, x, \nabla u_n) - A(t, x, \nabla u))(\nabla u_n - \nabla u) &\leq \frac{|\lambda_n - \lambda^*|^2}{2} \int_{\Omega} |u_0|^2 \\ &+ C \|u_n - u\|_{L^{p^-}(Q_T)}. \end{aligned} \quad (4.19)$$

Using the strong convergence of  $(u_n)$  in  $L^{p^-}(Q_T)$ , one deduce

$$\lim_{n \rightarrow \infty} \int_{Q_T} (A(t, x, \nabla u_n) - A(t, x, \nabla u))(\nabla u_n - \nabla u) \leq 0.$$

With the help of the result of [26], we conclude that  $(u_n)$  converges strongly to  $u$  in  $\mathcal{V}$  which implies the compactness of the mapping  $\mathcal{H}$ .

**Step 3: the set  $\mathcal{U}$  is bounded in  $\mathcal{V}$**

Let  $u \in \mathcal{V}$  such that  $u = \mathcal{H}(\lambda, u)$  for some  $\lambda \in [0, 1]$ , we aim to prove that  $u$  is bounded in  $\mathcal{V}$  independently of  $\lambda$ . By taking  $\varphi = u$  as a test function in (4.9), it comes that

$$\frac{1}{2} \int_{\Omega} u^2(T) + \int_{Q_T} A(t, x, \nabla u) \nabla u = \frac{\lambda^2}{2} \int_{\Omega} u_0^2 + \int_{Q_T} f(t, x, u, \lambda \nabla u) u.$$

Thanks to the coercivity assumption  $(H_2)$  and by using (4.7), we get

$$d \int_{Q_T} |\nabla u|^{p(x)} \leq \int_{\Omega} u_0^2 + \int_{Q_T} |Mu|.$$

Hölder's inequality leads to

$$d \int_{Q_T} |\nabla u|^{p(x)} \leq \|u_0\|_{L^2(\Omega)} + C \|M\|_{L^\infty(Q_T)} \|u\|_{L^{p^-}(Q_T)}.$$

Applying the result of (4.4) and (4.6), one has

$$\min \left\{ \|u\|_{\mathcal{V}}^{p^-}, \|u\|_{\mathcal{V}}^{p^+} \right\} \leq C(\|u_0\|_{L^2(\Omega)} + \|M\|_{L^\infty(Q_T)} \|u\|_{\mathcal{V}}).$$

Using Young's inequality, one obtains

$$\min \left\{ \left( \frac{p^- - 1}{p^-} \right) \|u\|_{\mathcal{V}}^{p^-}, \left( \frac{p^+ - 1}{p^+} \right) \|u\|_{\mathcal{V}}^{p^+} \right\} \leq C.$$

where  $C$  is a constant depending only on  $T, \Omega, p^-, p^+, d, \|u_0\|_{L^2(\Omega)}$  and  $\|M\|_{L^\infty(Q_T)}$ . As a consequence,  $\mathcal{U}$  is bounded in  $\mathcal{V}$ , then, a direct application of Schaeffer's fixed point theorem (see e.g [107]) permit us to deduce the existence of a weak solution to the problem (4.1).

#### 4.4 An existence result with nonstandard growth nonlinearity

In this section, we are concerned by the existence result of a weak solution to (4.1) in the case when the nonlinearity  $f$  is nonnegative and has a critical growth with respect to the gradient namely

$$|f(t, x, r, \xi)| \leq c(|r|) \left[ G(t, x) + |\xi|^{p(x)} \right], \quad (4.20)$$

where  $c : [0, +\infty) \rightarrow [0, +\infty)$  is a non-decreasing function and  $G$  is a nonnegative function belonging to  $L^1(Q_T)$ .

Under the assumption that an order couple of sub- and super-solution existent, we prove the existence of a weak solution to (4.1), which is a SOLA solution (Solution obtained as a limit of approximation).

First of all, let us define the notion of weak sub- and super-solution to (4.1).

##### Definition 4.4.1

A weak sub-solution of problem (4.1) is a function  $\underline{u} \in \mathcal{V} \cap L^\infty(Q_T)$ ,  $\partial_t \underline{u} \in \mathcal{V}^* + L^1(Q_T)$  such that

$$\begin{cases} \partial_t \underline{u} - \operatorname{div}(A(t, x, \nabla \underline{u})) \leq f(t, x, \underline{u}, \nabla \underline{u}) & \text{in } Q_T, \\ \underline{u} = 0 & \text{on } \Sigma_T, \\ \underline{u}(0, x) \leq u_0(x) & \text{in } \Omega. \end{cases} \quad (4.21)$$

A weak super-solution of problem (4.1) is a function  $\bar{u}$  satisfying (4.21) with  $\leq$  is replaced by  $\geq$ .

In the following theorem, we state the main result of this section.

**Theorem 4.4.1**

*Assume that  $(H_1)$ - $(H_6)$  and the nonlinearity  $f$  satisfies the growth assumption (4.20). Moreover, we assume the existence of  $(\underline{u}, \bar{u})$  sub- and super solution such as  $\underline{u} \leq \bar{u}$ . Then, for any  $u_0 \in L^\infty(\Omega)$  such that  $\underline{u}(0) \leq u_0 \leq \bar{u}(0)$ , the system (4.1) has a weak solution  $u$  such that  $\underline{u} \leq u \leq \bar{u}$  a.e. in  $Q_T$ .*

To establish the result of Theorem 4.4.1, we will truncate the nonlinearity  $f(t, x, u, \nabla u)$  to become bounded, thereafter we consider an approximate problem of (4.1). The existence of a weak solution of the last one will be proved by applying the result of section 3. Thereafter, to pass to the limit in the approximate problem, we will provide necessities a priori estimates on the approached solution.

**4.4.1 Approximate problem**

Let  $\underline{u}$  and  $\bar{u}$  respectively be the sub- and super-solution of the problem (4.1), we introduce for all  $u \in \mathcal{V}$  the following truncation function

$$\mathcal{T}(u) = u - (u - \bar{u})^+ + (\underline{u} - u)^+.$$

For any  $n \geq 0$ , we define the truncation function  $\psi_n \in \mathcal{C}_c^\infty(\mathbb{R})$  such as  $0 \leq \psi_n \leq 1$  and

$$\psi_n(s) = \begin{cases} 1 & \text{if } |s| \leq n, \\ 0 & \text{if } |s| \geq n + 1. \end{cases}$$

For almost all  $(t, x) \in Q_T$  and for all  $(r, \xi) \in \mathbb{R} \times \mathbb{R}^N$ , we approximate  $f$  by

$$f_n(t, x, u, \nabla u) = \psi_n(|u| + \|\nabla u\|) f(t, x, \mathcal{T}(u), \nabla \mathcal{T}(u)). \tag{4.22}$$

It is easy to verify that these functions  $f_n$  satisfies the properties  $(H_4)$ - $(H_6)$ . Moreover, from  $(H_5)$  and (4.22), we deduce that  $|f_n| \leq M_n$ , where  $M_n$  is a constante depending only on  $n$ . Now, we can define the approximate problem of (4.1) as follows

$$\begin{cases} \partial_t u_n - \operatorname{div}(A(t, x, \nabla u_n)) = f_n(t, x, u_n, \nabla u_n) & \text{in } Q_T, \\ u_n(0, x) = u_0(x) & \text{in } \Omega, \\ u_n(t, x) = 0 & \text{on } \Sigma_T. \end{cases} \tag{4.23}$$

From the result of Theorem 4.3.1, we obtain the existence of  $u_n$  a weak solution to the approximate problem (4.23). In the following lemma, we will prove that  $u_n$  is between  $\underline{u}$  and  $\bar{u}$  respectively the sub- and super-solution of (4.1). These estimate leads to obtain that  $u_n$  is belonging in  $L^\infty(Q_T)$ .

**Lemma 4.4.1**

Let  $u_n$  be the weak solution of the approximate problem (4.23), then

$$\underline{u} \leq u_n \leq \bar{u} \text{ a.e. in } Q_T. \quad (4.24)$$

**Proof.**

Let us prove that  $u_n \leq \bar{u}$  a.e. in  $Q_T$ . It is clearly that  $(u_n - \bar{u})^+ \in \mathcal{V} \cap L^\infty(\Omega)$ , then we can choose  $\varphi = (u_n - \bar{u})^+$  as a test function in the weak formulation of (4.23), one has

$$\int_0^T \langle \partial_t u_n, (u_n - \bar{u})^+ \rangle + \int_{Q_T} A(\cdot, \nabla u_n) \nabla (u_n - \bar{u})^+ = \int_{Q_T} f_n(\cdot, u_n, \nabla u_n) (u_n - \bar{u})^+. \quad (4.25)$$

Since  $\bar{u}$  is a super-solution of the problem (4.1), we then have

$$\int_0^T \langle \partial_t \bar{u}, (u_n - \bar{u})^+ \rangle + \int_{Q_T} A(\cdot, \nabla \bar{u}) \nabla (u_n - \bar{u})^+ \geq \int_{Q_T} f(\cdot, \bar{u}, \nabla \bar{u}) (u_n - \bar{u})^+. \quad (4.26)$$

By subtracting (4.26) from (4.25), we get

$$\begin{aligned} & \int_0^T \langle \partial_t (u_n - \bar{u}), (u_n - \bar{u})^+ \rangle + \int_{Q_T} (A(\cdot, \nabla u_n) - A(\cdot, \nabla \bar{u})) \nabla (u_n - \bar{u})^+ \\ & \leq \int_{Q_T} (f_n(\cdot, u_n, \nabla u_n) - f(\cdot, \bar{u}, \nabla \bar{u})) (u_n - \bar{u})^+. \end{aligned} \quad (4.27)$$

To deal with the first integral of (4.27) one may use Lemma 4.2.2, it comes that

$$\int_0^T \langle \partial_t (u_n - \bar{u}), (u_n - \bar{u})^+ \rangle = \int_\Omega \Pi((u_n - \bar{u})(T)) dx - \int_\Omega \Pi((u_n - \bar{u})(0)) dx,$$

where in this case  $\Pi(y) = \int_0^y s^+ ds$ . Since  $\bar{u}$  is a super-solution of (4.1), one may deduce that  $(u_n - \bar{u})(0) \leq 0$ , then  $\Pi((u_n - \bar{u})(0)) \leq 0$ . Therefore, one gets

$$\int_0^T \langle \partial_t (u_n - \bar{u}), (u_n - \bar{u})^+ \rangle \geq .0$$

For the right-hand side of (4.27), one may utilize (4.22) to obtain

$$\begin{aligned} & \int_{Q_T} (f_n(\cdot, u_n, \nabla u_n) - f(\cdot, \bar{u}, \nabla \bar{u}))(u_n - \bar{u})^+ \\ & \leq \int_{Q_T} (f(t, x, \mathcal{T}(u_n), \nabla \mathcal{T}(u_n)) - f(t, x, \bar{u}, \nabla \bar{u}))(u_n - \bar{u})^+ \\ & \leq \int_{\{u_n \geq \bar{u}\}} (f(t, x, \bar{u}, \nabla \bar{u}) - f(t, x, \bar{u}, \nabla \bar{u}))(u_n - \bar{u}) = 0. \end{aligned}$$

We therefore have

$$\int_{Q_T} (A(t, x, \nabla u_n) - A(t, x, \nabla \bar{u})) \nabla (u_n - \bar{u})^+ \leq 0.$$

which implies that,

$$\int_{\{u_n \geq \bar{u}\}} (A(t, x, \nabla u_n) - A(t, x, \nabla \bar{u})) \nabla (u_n - \bar{u}) \leq 0.$$

Using the property  $(H_3)$ , one gets  $\nabla(u_n - \bar{u}) = 0$  a.e. in the set  $\{(t, x) \in Q_T, u_n \geq \bar{u}\}$ . Consequently,  $u_n = \bar{u}$  a.e. in the set  $\{(t, x) \in Q_T, u_n \geq \bar{u}\}$  which implies that  $u_n \leq \bar{u}$  a.e. in  $Q_T$ .

By using similar reasoning of the first proof, we can obtain  $\underline{u} \leq u_n$  a.e. in  $Q_T$ .

**Remark 4.4.1**

*Note that the estimate (4.24) plays a crucial role in our work since it is helpful in several steps of the proof of a priori estimates. Moreover, from (4.24) one may deduce that*

$$\|u_n\|_\infty \leq \|\underline{u}\|_\infty + \|\bar{u}\|_\infty := \Lambda,$$

*which implies that  $(u_n)$  is bounded in  $L^\infty(Q_T)$ .*

**4.4.2 A priori estimates**

First of all, we give a technical lemma which is frequently used in what follows.

**Lemma 4.4.2**

*Let  $\theta(s) = se^{\eta s^2}$ ,  $s \in \mathbb{R}$  and let  $\Theta(s) = \int_0^s \theta(\tau) d\tau$ . Then*

$$\theta(0) = 0, \quad \Theta(s) \geq 0, \quad \theta'(s) > 0.$$

*When  $\eta \geq \frac{b^2}{4a^2}$  is fixed, the following relationships hold true*

$$a\theta'(s) - b|\theta(s)| \geq \frac{a}{2}, \quad \forall s \in \mathbb{R}. \tag{4.28}$$

**Lemma 4.4.3**

Let  $u_n$  be the sequence defined as above. Then there exists a constant  $C$  independent of  $n$  such that

$$\|u_n\|_{\mathcal{V}} \leq C,$$

$$\|f_n(t, x, u_n, \nabla u_n)\|_{L^1(Q_T)} \leq C,$$

$$\|\partial_t u_n\|_{\mathcal{V}^* + L^1(Q_T)} \leq C.$$

**Proof.**

Using the estimate (4.24), one may deduce that  $\theta(u_n) \in \mathcal{V} \cap L^\infty(Q_T)$ , then by tacking  $\theta(u_n)$  as a test function in the weak formulation of (4.23), we obtain

$$\int_0^T \langle \partial_t u_n, \theta(u_n) \rangle + \int_{Q_T} A(t, x, \nabla u_n) \nabla(u_n) \theta'(u_n) = \int_{Q_T} f_n(t, x, u_n, \nabla u_n) \theta(u_n). \quad (4.29)$$

For the first integral, we have

$$\int_0^T \langle \partial_t u_n, \theta(u_n) \rangle = \int_{\Omega} [\Theta(u_n(T)) - \Theta(u_0)].$$

Then, from  $(H_2)$  and (4.24) the inequality (4.29) becomes

$$\begin{aligned} \int_{\Omega} \Theta(u_n(T)) + d \int_{Q_T} |\nabla u_n|^{p(x)} \theta'(u_n) &\leq \int_{\Omega} \Theta(u_0) + \int_{Q_T} |f_n(t, x, u_n, \nabla u_n) \theta(u_n)| \\ &\leq \int_{\Omega} \Theta(u_0) + \int_{Q_T} c(|u_n|) \left( G(t, x) + |\nabla u_n|^{p(x)} \right) |\theta(u_n)| \\ &\leq \int_{\Omega} \Theta(u_0) + c(\Lambda) \int_{Q_T} \left( G(t, x) + |\nabla u_n|^{p(x)} \right) |\theta(u_n)|. \end{aligned}$$

We rewrite the above inequality as

$$\int_{\Omega} \Theta(u_n(T)) + \int_{Q_T} \left( d \theta'(u_n) - c(\Lambda) |\theta(u_n)| \right) |\nabla u_n|^{p(x)} \leq \int_{\Omega} \Theta(u_0) dx + \int_{Q_T} G(t, x) |\theta(u_n)|.$$

Choosing the constant  $\eta \geq \frac{(c(\Lambda))^2}{4d^2}$  in the Lemma 4.4.2, one obtains

$$d \theta'(u_n(t, x)) - c(\Lambda) |\theta(u_n(t, x))| \geq \frac{d}{2} \text{ a.e in } Q_T.$$

On the other hand  $\Theta(u_n(T)) \geq 0$ , therefore

$$\frac{d}{2} \int_{Q_T} |\nabla u_n|^{p(x)} \leq \int_{\Omega} \Theta(u_0) + \int_{Q_T} G(t, x) |\theta(u_n)|,$$

we may utilize estimate (4.24) to deduce that

$$\int_{Q_T} |\nabla u_n|^{p(x)} \leq C \tag{4.30}$$

where  $C$  is a constant depending only on  $\|\underline{u}\|_{\infty}$ ,  $\|\bar{u}\|_{\infty}$  and  $\|G\|_{L^1(Q_T)}$ . By employing the result of (4.6) in (4.30), we conclude that  $u_n$  is uniformly bounded in  $\mathcal{V}$ . To estimate the nonlinearity  $(f_n)$  in  $L^1(Q_T)$ , we use the growth condition (4.20), one gets

$$\begin{aligned} \int_{Q_T} |f_n(t, x, u_n, \nabla u_n)| &\leq c(|u_n|) \int_{Q_T} \left( G(t, x) + |\nabla u_n|^{p(x)} \right) \\ &\leq c(\Lambda) \int_{Q_T} \left( G(t, x) + |\nabla u_n|^{p(x)} \right). \end{aligned}$$

Applying the result of (4.30), we conclude that  $f_n$  is bounded in  $L^1(Q_T)$ . Consequently, from the equation satisfied by  $u_n$  it follows that  $(\partial_t u_n)$  is bounded in  $\mathcal{V}^* + L^1(Q_T)$ .

**Lemma 4.4.4**

*The sequence  $(u_n)$  converges strongly to some  $u$  in  $\mathcal{V}$ .*

**Proof.**

From the result of Lemma 4.4.3, we have  $(u_n)$  is bounded in  $\mathcal{V}$  and  $f_n(t, x, u_n, \nabla u_n)$  is bounded in  $L^1(Q_T)$ . Then, by applying the compactness result of Lemma 4.5.2, we can extract a subsequence of  $(u_n)$  still denoted by  $(u_n)$  such that

- $(u_n) \rightarrow u$  strongly in  $L^{p^-}(Q_T)$  and a.e. in  $Q_T$ ,
- $(\nabla u_n) \rightarrow \nabla u$  a.e. in  $Q_T$ .

Therefore,

$$A(t, x, \nabla u_n) \rightharpoonup A(t, x, \nabla u) \text{ weakly in } L^{p'(x)}(Q_T).$$

We shall prove that  $(u_n)$  converges strongly in  $\mathcal{V}$ . To do this, we use the difference between the equations satisfied by  $u_n$  and  $u_m$ , we have

$$\partial_t (u_n - u_m) - \operatorname{div}(A(\nabla u_n)) + \operatorname{div}(A(\nabla u_m)) = f_n(u_n, \nabla u_n) - f_m(u_m, \nabla u_m).$$

Tacking  $\theta(u_n - u_m) \in \mathcal{V} \cap L^\infty(Q_T)$  as a test function in the weak formulation of the latter equation, one obtains

$$\begin{aligned} \int_0^T \langle \partial_t(u_n - u_m), \theta(u_n - u_m) \rangle + \int_{Q_T} (A(\nabla u_n) - A(\nabla u_m)) \cdot \nabla(u_n - u_m) \theta'(u_n - u_m) \\ + \int_{Q_T} \left( f_n(u_n, \nabla u_n) - f_m(u_m, \nabla u_m) \right) \theta(u_n - u_m) = 0. \end{aligned}$$

Since  $u_n$  and  $u_m$  have the same initial condition, we have

$$\int_0^T \langle \partial_t(u_n - u_m), \theta(u_n - u_m) \rangle = \int_\Omega \Theta(u_n(T) - u_m(T)) \geq 0.$$

On the other hand, employing the growth condition (4.20), one has

$$\begin{aligned} \int_{Q_T} (A(\nabla u_n) - A(\nabla u_m)) \cdot \nabla(u_n - u_m) \theta'(u_n - u_m) \\ \leq c(\Lambda) \int_{Q_T} (G(t, x) + |\nabla u_n|^{p(x)} + |\nabla u_m|^{p(x)}) |\theta(u_n - u_m)|. \end{aligned}$$

Since  $\Theta$  is positive we get by using the coercivity condition  $(H_2)$

$$\begin{aligned} \int_{Q_T} (A(\nabla u_n) - A(\nabla u_m)) \cdot \nabla(u_n - u_m) \theta'(u_n - u_m) &\leq c(\Lambda) \int_{Q_T} G(t, x) |\theta(u_n - u_m)| \\ &+ \frac{c(\Lambda)}{d} \int_{Q_T} A(\nabla u_n) \cdot \nabla u_n |\theta(u_n - u_m)| + \frac{c(\Lambda)}{d} \int_{Q_T} A(\nabla u_m) \cdot \nabla u_m |\theta(u_n - u_m)| \\ &\leq c(\Lambda) \int_{Q_T} G(t, x) |\theta(u_n - u_m)| + \frac{c(\Lambda)}{d} \int_{Q_T} A(\nabla u_n) \cdot \nabla(u_n - u_m) |\theta(u_n - u_m)| \\ &+ \frac{c(\Lambda)}{d} \int_{Q_T} A(\nabla u_n) \cdot \nabla u_m |\theta(u_n - u_m)| + \frac{c(\Lambda)}{d} \int_{Q_T} A(\nabla u_m) \cdot \nabla u_n |\theta(u_n - u_m)| \\ &- \frac{c(\Lambda)}{d} \int_{Q_T} A(\nabla u_m) \cdot \nabla(u_n - u_m) |\theta(u_n - u_m)|. \end{aligned}$$

It follows that,

$$\begin{aligned} \frac{1}{d} \int_{Q_T} \left( d \theta'(u_n - u_m) - c(\Lambda) |\theta(u_n - u_m)| \right) (A(\nabla u_n) - A(\nabla u_m)) \cdot \nabla(u_n - u_m) \\ \leq c(\Lambda) \int_{Q_T} G(t, x) |\theta(u_n - u_m)| + \frac{c(\Lambda)}{d} \int_{Q_T} A(\nabla u_n) \cdot \nabla u_m |\theta(u_n - u_m)| \\ + \frac{c(\Lambda)}{d} \int_{Q_T} A(\nabla u_m) \cdot \nabla u_n |\theta(u_n - u_m)|. \end{aligned}$$

Choosing the constant  $\eta \geq \frac{c(\Lambda)^2}{4d^2}$  in the Lemma 4.4.2, one has

$$\begin{aligned} \frac{1}{2} \int_{Q_T} (A(\nabla u_n) - A(\nabla u_m)) \cdot \nabla (u_n - u_m) &\leq c(\Lambda) \int_{Q_T} G(t, x) |\theta(u_n - u_m)| \\ &+ \frac{c(\Lambda)}{d} \int_{Q_T} A(\nabla u_n) \cdot \nabla u_m |\theta(u_n - u_m)| + \frac{c(\Lambda)}{d} \int_{Q_T} A(\nabla u_m) \cdot \nabla u_n |\theta(u_n - u_m)|. \end{aligned} \quad (4.31)$$

Due to the fact that  $(\nabla u_n) \rightarrow \nabla u$  a.e. in  $Q_T$  and  $(A(t, x, \nabla u_n)) \rightharpoonup (A(t, x, \nabla u))$  weakly in  $L^{p'(x)}(Q_T)$ , we can use Fatou's Lemma to pass the limit when  $m$  tends to  $+\infty$  in (4.31), one obtains

$$\begin{aligned} \frac{1}{2} \int_{Q_T} (A(\nabla u_n) - A(\nabla u)) \cdot \nabla (u_n - u) &\leq c(\Lambda) \int_{Q_T} G(t, x) |\theta(u_n - u)| \\ &+ \frac{c(\Lambda)}{d} \int_{Q_T} A(\nabla u_n) \cdot \nabla u |\theta(u_n - u)| + \frac{c(\Lambda)}{d} \int_{Q_T} A(\nabla u) \cdot \nabla u_n |\theta(u_n - u)|. \end{aligned}$$

On the other hand, from (H<sub>3</sub>), (4.30), (4.24) and by applying Lebesgue theorem, we pass to the lim when  $n$  tends to  $+\infty$  to obtain

$$\lim_{n \rightarrow \infty} \int_{Q_T} (A(\nabla u_n) - A(\nabla u)) \cdot \nabla (u_n - u) \leq 0.$$

Consequently,

$$\nabla u_n \rightarrow \nabla u \text{ strongly in } L^{p(x)}(Q_T).$$

#### 4.4.3 Passing to the limit

In this stage, we will prove that the limit of the sequence  $u_n$  is a weak solution of the system (4.23) in the sense of the definition 4.2.1. Thanks to the result of Lemma 4.4.4, we obtain the existence of a subsequence, still denoted by  $u_n$  for simplicity, such that

$$\nabla u_n \rightarrow \nabla u \text{ strongly in } L^{p(x)}(Q_T) \text{ and a.e. in } Q_T$$

$$u_n \rightarrow u \text{ strongly in } L^{p^-}(Q_T) \text{ and a.e. in } Q_T$$

$$A(t, x, \nabla u_n) \rightharpoonup A(t, x, \nabla u) \text{ weakly in } L^{p'(x)}(Q_T)$$

$$f_n(t, x, u_n, \nabla u_n) \rightarrow f(t, x, u, \nabla u) \text{ a.e. in } Q_T.$$

Let us show that

$$f_n(t, x, u_n, \nabla u_n) \rightarrow f(t, x, u, \nabla u) \text{ strongly in } L^1(Q_T).$$

To do this, it suffices to prove that  $f_n(t, x, u_n, \nabla u_n)$  is equi-integrable in  $L^1(Q_T)$ , namely

$$\forall \varepsilon > 0, \exists \delta > 0, \forall E \subset Q_T, \text{ if } |E| < \delta \text{ then } \int_E |f_n(t, x, u_n, \nabla u_n)| dx dt \leq \varepsilon.$$

Let  $E$  be a measurable subset of  $Q_T$  and  $\varepsilon > 0$ , using the growth assumption (4.20) and (4.24), one has

$$\int_E |f_n(t, x, u_n, \nabla u_n)| \leq \int_E c(\Lambda) \left( G(t, x) + |\nabla u_n|^{p(x)} \right). \quad (4.32)$$

We have  $G \in L^1(Q_T)$  then  $G$  is equi-integrable in  $L^1(Q_T)$  and therefore there exists  $\delta_1 > 0$ , such that, if  $|E| \leq \delta_1$ , we have

$$c(\Lambda) \int_E G(t, x) \leq \frac{\varepsilon}{2}.$$

On the other hand, in view to the result of Lemma 4.4.4, it comes that  $(|\nabla u_n|^{p(x)})$  is equi-integrable in  $L^1(Q_T)$ , which implies the existence of  $\delta_2 > 0$ , such that, if  $|E| \leq \delta_2$ , we have

$$c(\Lambda) \int_E |\nabla u_n|^{p(x)} \leq \frac{\varepsilon}{2}.$$

By choosing  $\delta^* = \inf(\delta_1, \delta_2)$ , if  $|E| \leq \delta^*$ , it follows that

$$\int_E |f_n(t, x, u_n, \nabla u_n)| \leq \varepsilon.$$

this finishes the proof of theorem 4.4.1.

## 4.5 Appendix

In this appendix, we propose to prove some auxiliaries results used in the proof of the main result.

### Lemma 4.5.1

Assume that  $(H_1)$ - $(H_3)$  hold, then

i) for any  $v_0 \in L^2(\Omega)$  and  $g \in L^2(Q_T)$  the following problem

$$\begin{cases} \partial_t v - \operatorname{div}(A(t, x, \nabla v)) = g(t, x) & \text{in } Q_T \\ v(0, x) = v_0(x) & \text{in } \Omega \\ v(t, x) = 0 & \text{on } \Sigma_T \end{cases} \quad (4.33)$$

has a unique solution  $v \in \mathcal{V} \cap \mathcal{C}([0, T], L^2(\Omega))$  such that

$$\partial_t v \in \mathcal{V}^* + L^2(Q_T), \quad v(0, x) = v_0(x) \text{ in } L^2(\Omega)$$

$$\int_0^T \langle \partial_t v, \varphi \rangle + \int_{Q_T} A(t, x, \nabla v) \nabla \varphi = \int_{Q_T} g(t, x) \varphi, \quad (4.34)$$

with  $\varphi \in \mathcal{V} \cap L^2(Q_T)$ .

ii) if  $v$  is the solution of (4.33), then we have

$$\|v\|_{\mathcal{V}} + \sup_{0 \leq t \leq T} \|v(t)\|_{L^2(\Omega)} \leq C(\Omega, T) \left( \|v_0\|_{L^2(\Omega)} + \|g\|_{L^2(Q_T)} \right), \quad (4.35)$$

$$\|\partial_t v\|_{\mathcal{V}^* + L^2(Q_T)} \leq C(\Omega, T) \left( \|H\|_{p'(x)} + \|v_0\|_{L^2(\Omega)} + \|g\|_{L^2(Q_T)} \right). \quad (4.36)$$

**Proof.**

i) For the existence and uniqueness of the weak solution of the problem (4.33) we refer the reader for to see [123] and by a direct application of the Aubin-Simon theorem, we deduce that  $v$  belongs to  $\mathcal{C}([0, T], L^2(\Omega))$  which means that the initial condition makes a sens.

ii) By choosing  $\varphi = v\chi_{(0,t]}$  in (4.34) with  $t < T$ , one has

$$\frac{1}{2} \int_{\Omega} v^2(t) + \int_{Q_t} A(\tau, x, \nabla v) \nabla v = \frac{1}{2} \int_{\Omega} v_0^2 + \int_{Q_t} v g(\tau, x), \quad (4.37)$$

where  $Q_t = ]0, t[ \times \Omega$ . Employing the coercivity assumption  $(H_2)$  in (4.37), one has

$$\frac{1}{2} \int_{\Omega} v^2(t) + d \int_{Q_t} |\nabla v|^{p(x)} \leq \frac{1}{2} \int_{\Omega} v_0^2 + \int_{Q_t} v g(\tau, x). \quad (4.38)$$

As a consequence,

$$\int_{\Omega} v^2(t) \leq \int_{Q_t} g^2(\tau, x) + \int_{Q_t} v^2 + \int_{\Omega} v_0^2. \quad (4.39)$$

By applying Gronwall's lemma, it follows that

$$\int_{Q_T} v^2 \leq (\exp(T) - 1) \left( \|g\|_{L^2(Q_T)}^2 + \int_{\Omega} v_0^2 dx \right). \quad (4.40)$$

Substituting the above expression in (4.39), one obtains

$$\sup_{0 \leq t \leq T} \int_{\Omega} v^2(t) \leq \|g\|_{L^2(Q_T)}^2 + \exp(T) \left( \|g\|_{L^2(Q_T)} + \int_{\Omega} v_0^2 \right), \quad (4.41)$$

then we have,

$$\sup_{0 \leq t \leq T} \|v(t)\|_{L^2(\Omega)} \leq C(T, \Omega) \left( \|v_0\|_{L^2(\Omega)} + \|g\|_{L^2(Q_T)} \right), \quad (4.42)$$

by combining (4.37), (4.42) and  $(H_2)$ , we deduce that

$$\int_{Q_T} |\nabla v|^{p(x)} dx dt \leq C(T, \Omega) \left( \int_{Q_T} g^2 dx dt + \int_{\Omega} v_0^2 \right). \quad (4.43)$$

By applying the result of (4.6), one gets

$$\|v\|_{\mathcal{V}} \leq C(T, \Omega) \left( \|g\|_{L^2(Q_T)} + \|v_0\|_{L^2(\Omega)} \right), \quad (4.44)$$

which implies that  $v$  is uniformly bounded in  $\mathcal{V}$ . Due to the growth assumption  $(H_1)$ , we have

$$\begin{aligned} \int_{Q_T} |A(t, x, \nabla v)|^{p'(x)} &\leq C \left( \int_{Q_T} |H(t, x)|^{p'(x)} + \int_{Q_T} |\nabla v|^{p(x)} \right) \\ &\leq C(T, \Omega) \left( \int_{Q_T} |H(t, x)|^{p'(x)} + \int_{Q_T} g^2 + \int_{\Omega} v_0^2 \right). \end{aligned} \quad (4.45)$$

Hence,

$$\|A(t, x, \nabla v)\|_{p'(x)} \leq C(T, \Omega) \left( \|H\|_{p'(x)} + \|g\|_{L^2(Q_T)} + \|v_0\|_{L^2(\Omega)} \right). \quad (4.46)$$

To estimate  $\partial_t v$  in the norm of the space  $\mathcal{V}^* + L^2(Q_T)$ , we use the equation satisfied by  $v$ , one has

$$\begin{aligned} \|\partial_t v\|_{\mathcal{V}^* + L^2(Q_T)} &\leq C \left( \|A(t, x, \nabla v)\|_{p'(x)} + \|g\|_{L^2(Q_T)} \right) \\ &\leq C(T, \Omega) \left( \|H\|_{p'(x)} + \|g\|_{L^2(Q_T)} + \|v_0\|_{L^2(\Omega)} \right). \end{aligned} \quad (4.47)$$

**Lemma 4.5.2**

Assume that  $(H_1)$ - $(H_4)$  hold and let  $u_n \in \mathcal{V} \cap \mathcal{C}([0, T]; L^2(\Omega))$  be the weak solution of the problem

$$\begin{cases} \partial_t u_n - \operatorname{div}(A(t, x, \nabla u_n)) = f_n(t, x, u_n, \nabla u_n) & \text{in } Q_T \\ u_n(0, x) = u_0^n(x) & \text{in } \Omega \\ u_n(t, x) = 0 & \text{on } \Sigma_T \end{cases} \quad (4.48)$$

in the sense that

$$\begin{aligned} \partial_t u_n &\in \mathcal{V}^*, \quad u_n(0, x) = u_0^n(x) \text{ in } L^2(\Omega) \\ \int_0^T \langle \partial_t u_n, \varphi \rangle + \int_{Q_T} A(t, x, \nabla u_n) \nabla \varphi &= \int_{Q_T} f_n(t, x, u_n, \nabla u_n) \varphi, \end{aligned} \quad (4.49)$$

for all test function  $\varphi \in \mathcal{V}$ . If  $(u_0^n)$  is bounded in  $L^1(\Omega)$ ,  $(u_n)$  is bounded in  $\mathcal{V}$  and  $(f_n(t, x, u_n, \nabla u_n))$  is bounded in  $L^1(Q_T)$ . Then, we have (up to a subsequence)

- i)  $u_n \rightarrow u$  strongly in  $L^{p^-}(Q_T)$  and a.e. in  $Q_T$
- ii)  $\nabla u_n \rightarrow \nabla u$  a.e. in  $Q_T$ .

**Proof.**

i) For  $s$  fixed, we have the following embedding relationships

- $s > \frac{N}{2}$ , we have  $H_0^s(\Omega) \hookrightarrow L^\infty(\Omega)$ , and then  $L^1(\Omega) \hookrightarrow H^{-s}(\Omega)$
- $s - 1 > \frac{N}{2}$ , one has  $H_0^s(\Omega) \hookrightarrow W^{1, p(x)}(\Omega)$ , consequently,  $W^{-1, p'(x)}(\Omega) \hookrightarrow H^{-s}(\Omega)$ .

On the other hand, we have  $(u_n)$  is bounded in  $\mathcal{V}$  and  $(f_n(t, x, u_n, \nabla u_n))$  is bounded in  $L^1(Q_T)$ , and by employing the equation (4.48), it result that  $(\partial_t u_n)$  is bounded in  $L^1(0, T; H^{-s}(\Omega))$ . Furthermore, by using the embedding relationship (4.4), we get  $(u_n)$  is bounded in  $L^{p^-}(0, T; W_0^{1, p(x)}(\Omega))$ .

Moreover, we have

$$W_0^{1, p(x)}(\Omega) \xrightarrow{\text{compact}} L^{p(x)}(\Omega) \hookrightarrow H^{-s}(\Omega).$$

Thanks to the compactness result of Simon (see Corollary 4, page 85 of [124]), we deduce that (up to a subsequence)

$$u_n \rightarrow u \text{ strongly in } L^{p^-}(0, T; L^{p(x)}(\Omega)) \text{ and a.e. in } Q_T.$$

Therefore, the continuous embedding  $L^{p^-}(0, T; L^{p(x)}(\Omega)) \hookrightarrow L^{p^-}(Q_T)$  implies that  $u_n \rightarrow u$  strongly in  $L^{p^-}(Q_T)$  and a.e. in  $Q_T$ .

ii) In this stade, we aim to extend the compactness result of [110] to a more general class of quasilinear parabolic equation with variable exponent. Then, to prove the almost everywhere convergence of  $(\nabla u_n)$ , we propose to show that  $(\nabla u_n)$  is a Cauchy sequence in measure, namely

$$\forall \delta > 0, \forall \varepsilon > 0, \exists N_0 \text{ such that } \forall n, m \geq N_0$$

$$\text{meas} \{(t, x), |(\nabla u_n - \nabla u_m)(t, x)| \geq \delta\} \leq \varepsilon.$$

To do this, let  $\delta > 0$  and  $\varepsilon > 0$ . We remark that for  $k > 0$  and  $\eta > 0$  the following inequality holds

$$\text{meas} \{(t, x), |(\nabla u_n - \nabla u_m)(t, x)| \geq \delta\} \leq \text{meas}(\omega_1) + \text{meas}(\omega_2)$$

$$+ \text{meas}(\omega_3) + \text{meas}(\omega_4),$$

where,

$$\omega_1 = \{(t, x), |\nabla u_n| \geq k\}, \omega_2 = \{(t, x), |\nabla u_m| \geq k\}, \omega_3 = \{(t, x), |u_n - u_m| \geq \eta\},$$

$$\omega_4 = \{(t, x), |(\nabla u_n - \nabla u_m)| \geq \delta, |\nabla u_n| \leq k, |\nabla u_m| \leq k, |u_n - u_m| \leq \eta\}.$$

To bound  $\text{meas}(\omega_1)$  and  $\text{meas}(\omega_2)$ , we will use the boundness of  $u_n$  and  $u_m$  in  $\mathcal{V}$ . Let us remark that

$$k \text{meas}(\omega_1) \leq \int_{\omega_1} |\nabla u_n| \leq \int_{Q_T} |\nabla u_n|.$$

From assumption (4.2), the following continuous embedding  $\mathcal{V} \hookrightarrow L^1(0, T; W_0^{1,1}(\Omega))$  holds true, therefore

$$\text{meas}(\omega_1) \leq \frac{1}{k} \|\nabla u_n\|_{L^1(Q_T)} \leq \frac{C}{k} \|u_n\|_{\mathcal{V}} \leq \frac{C}{k}.$$

By the same manner, one has

$$\text{meas}(\omega_2) \leq \frac{C}{k}.$$

Then, we fix  $k$  large enough such that  $\text{meas}(\omega_1) \leq \varepsilon$  and  $\text{meas}(\omega_2) \leq \varepsilon$ . To bound  $\text{meas}(\omega_3)$ , we

will utilize the strong convergence of  $u_n$  in  $L^{p^-}(Q_T)$ . For all  $m, n \in \mathbb{N}$ , we have

$$\eta \operatorname{meas}(\omega_3) \leq \int_{\omega_3} |(u_n - u_m)| \leq \int_{Q_T} |(u_n - u_m)|.$$

Using Hölder's inequality, it follows that

$$\operatorname{meas}(\omega_3) \leq \frac{C}{\eta} \|u_n - u_m\|_{L^{p^-}(Q_T)}.$$

On the other hand, from *i*) it results that  $(u_n)$  is strongly convergent in  $L^{p^-}(Q_T)$  which implies that  $(u_n)$  is a Cauchy sequence in  $L^{p^-}(Q_T)$ . Then, for a given  $\eta$  there exists  $N_0$  such that for  $m, n \geq N_0$  one gets

$$\operatorname{meas}(\omega_3) \leq \varepsilon.$$

It remains to bound  $\operatorname{meas}(\omega_4)$  and to choose  $\eta$ . Due to the assumption  $(H_3)$ , one has  $[A(t, x, \xi_1) - A(t, x, \xi_2)](\xi_1 - \xi_2) > 0$  for  $\xi_1 - \xi_2 \neq 0$ . On the other hand, employing the fact that the set

$$\left\{ (\xi_1, \xi_2) \in \mathbb{R}^{2N} \text{ such that } |\xi_1| \leq k, |\xi_2| \leq k \text{ and } |\xi_1 - \xi_2| \geq \delta \right\},$$

is compact and the function  $\xi \mapsto A(t, x, \xi)$  is continuous for almost all  $(t, x)$  in  $Q_T$ , we deduce that  $[A(t, x, \xi_1) - A(t, x, \xi_2)](\xi_1 - \xi_2)$  reaches its minimum on this compact. Let us denote  $\gamma(t, x)$  this minimum, by applying the assumption  $(H_3)$ , one has  $\gamma(t, x) > 0$  a.e. in  $Q_T$ . Moreover, using  $\gamma(t, x) > 0$  a.e. in  $Q_T$ , we deduce the existence of  $\varepsilon' > 0$  such that, for all measurable set  $\omega \subset Q_T$

$$\int_{\omega} \gamma \leq \varepsilon' \quad \Rightarrow \quad \operatorname{meas}(\omega) \leq \varepsilon. \quad (4.50)$$

Then, to get  $\operatorname{meas}(\omega_4) \leq \varepsilon$ , it suffices to prove that  $\int_{\omega_4} \gamma \leq \varepsilon'$ . According to the properties of  $\gamma$  and  $A$ , one obtains

$$\int_{\omega_4} \gamma \leq \int_{\omega_4} [A(t, x, \nabla u_n) - A(t, x, \nabla u_m)] (\nabla u_n - \nabla u_m) \mathbf{1}_{\{|u_n - u_m| \leq \eta\}}.$$

It is clearly that  $\nabla T_{\eta}(u_n - u_m) = (\nabla u_n - \nabla u_m) \mathbf{1}_{\{|u_n - u_m| \leq \eta\}}$  and thanks to the monotony assumption  $(H_3)$ , one has

$$\int_{A_4} \gamma \leq \int_{Q_T} [A(t, x, \nabla u_n) - A(t, x, \nabla u_m)] \nabla T_{\eta}(u_n - u_m).$$

In accordance with (4.49), using the equation satisfied by  $(u_n - u_m)$  and choosing  $\varphi = T_\eta(u_n - u_m) \in \mathcal{V} \cap L^\infty(Q_T)$  as a test function, one obtains

$$\begin{aligned} & \int_0^T \langle (u_n - u_m)_t, T_\eta(u_n - u_m) \rangle + \int_{Q_T} [A(t, x, \nabla u_n) - A(t, x, \nabla u_m)] \nabla T_\eta(u_n - u_m) \\ &= \int_{Q_T} (f_n(t, x, u_n, \nabla u_n) - f_m(t, x, u_m, \nabla u_m)) T_\eta(u_n - u_m). \end{aligned}$$

For the first integral, we have

$$\int_0^T \langle (u_n - u_m)_t, T_\eta(u_n - u_m) \rangle = \int_\Omega S_\eta(u_n - u_m)(T) - \int_\Omega S_\eta(u_n - u_m)(0).$$

We remark that  $S_\eta(r) \geq 0$  and  $S_\eta(r) \leq \eta|r|$ , thus

$$\begin{aligned} & \int_{Q_T} [A(t, x, \nabla u_n) - A(t, x, \nabla u_m)] \nabla T_\eta(u_n - u_m) \leq \eta \int_\Omega |u_0^n - u_0^m| \\ &+ \eta \int_{Q_T} |f_n(t, x, u_n, \nabla u_n) - f_m(t, x, u_m, \nabla u_m)|. \end{aligned}$$

Since  $(u_0^n)$  is bounded in  $L^1(\Omega)$  and  $(f_n(t, x, u_n, \nabla u_n))$  is bounded in  $L^1(Q_T)$ , then the last inequality becomes

$$\int_{Q_T} [A(t, x, \nabla u_n) - A(t, x, \nabla u_m)] \nabla T_\eta(u_n - u_m) \leq \eta C.$$

Choosing  $\eta \leq \frac{\varepsilon'}{C}$ , one obtains  $\int_{\omega_4} \gamma \leq \varepsilon'$  and from the result of (4.50), it follows that  $\text{meas}(\omega_4) \leq \varepsilon$ .

As a consequence,  $\eta$  is fixed and due to boundness result of  $\text{meas}(\omega_3)$ , we deduce the existence of  $N_0 \in \mathbb{N}$  such that for all  $m, n \geq N_0$  we have

$$\text{meas}(\{ |(\nabla u_n - \nabla u_m)(x)| \geq \delta \}) \leq 4\varepsilon.$$

Hence  $(\nabla u_n)$  is a Cauchy sequence in measure, furthermore,  $(\nabla u_n)$  converges almost everywhere to  $\nabla u$  in  $Q_T$  (up to a subsequence).

# Weak solution for quasilinear parabolic systems with variable exponents and critical growth nonlinearities with respect to the gradient

## 5.1 Introduction

In recent years, there has been considerable attention in the study of various mathematical problems involving variable exponent conditions. These studies employ the new theory of Lebesgue and Sobolev spaces  $(L^{p(x)}(\Omega), W^{1,p(x)}(\Omega))$  instead of having the usual  $p$ -structure which employ the standard theory of  $L^p(\Omega)$  and  $W^{1,p}(\Omega)$  spaces [65, 137]. The interest in studying such problems is stimulated and motivated by their applications in elastic mechanics, dynamics fluid, nonlinear elasticity, electrorheological fluids, chemical reactions, heat transfer, population dynamics, epidemiological models, image restoration, and so forth [38, 48, 67, 89, 115, 123]. Special interest has been devoted to the study quasilinear boundary value problems. To enrich our presentation, we begin by recalling some interesting work with the constant case  $p(x) = p$ . A major and comprehensive introduction to quasilinear stationary problems still is the book by Drabek et al [50]. The authors presented a qualitative analysis of the existence, uniqueness and regularity properties of solutions included a general class of quasilinear partial differential equation.

In recent years, the exponent variable notion has given birth to a new type of partial differential

equation. Several researchers have been interested in this topic and various works have been established to answer the often questions about existence, uniqueness and asymptotic behavior of the solution to the considered systems. For instance, the excellent book by Rădulescu et al [113] presents the most suitable materials for the functional analysis of linear and nonlinear partial differential equations (PDEs) using spaces with variable exponents, in particular those of elliptical type. This book also makes it possible to introduce the readers to the most important variational methods in the case of PDEs described by non-homogeneous differential operators and containing one or more nonlinearities of power type with variable exponents as well as their applications to various processes from applied sciences. Shangerganesh et al.[123] studied a reaction-diffusion system with variable exponents modeling the spread of epidemic disease describing the spatial spread of the feline leukemia virus. The nonlinearities of their system depending on the solutions and not on their gradients. Using the Schauder fixed point Theorem, they showed the existence and uniqueness of a weak solution.

In this article, we consider a class of degenerate parabolic systems with variable exponents having critical growth nonlinearities with respect to gradient of the solutions. Our work is original in the sense that it constitutes a generalization of previous works on parabolic equations with variable exponent see for example [78, 123, 85] and their references, and also generalizes work on reaction-diffusion systems with Laplacian operator type with standard growth nonlinearities, see for example [11, 9, 12, 36, 37, 106].

We focus our interest in the existence of weak solutions of a class of quasilinear parabolic system modeled as follows

$$\begin{cases} \forall i = 1, \dots, M, \\ \partial_t u_i - \operatorname{div}(A_i(t, x, \nabla u_i)) = f_i(t, x, u, \nabla u) & \text{in } Q_T \\ u_i(0, x) = u_{0i}(x) & \text{in } \Omega \\ u_i(t, x) = 0 & \text{on } \Sigma_T \end{cases} \quad (5.1)$$

where  $u = (u_1, \dots, u_M)$ ,  $\nabla u = (\nabla u_1, \dots, \nabla u_M)$ ,  $M \geq 2$  and  $\Omega$  is an open bounded subset of  $\mathbb{R}^N$ , with smooth boundary  $\partial\Omega$ ,  $Q_T = (0, T) \times \Omega$ ,  $\Sigma_T = (0, T) \times \partial\Omega$ ,  $T > 0$ . The initial data  $u_0 = (u_{01}, \dots, u_{0M})$  is assumed to be a measurable function belonging to  $L^2(\Omega)^M$ . For all  $i = 1, \dots, M$ , the operator  $-\operatorname{div}(A_i(t, x, \nabla u_i))$  is of type Leray-Lions with variable exponents and  $A_i : Q_T \times \mathbb{R}^N \rightarrow \mathbb{R}^N$  is a Carathéodory function satisfying for almost every  $(t, x)$  in  $Q_T$  and, for every  $\xi_i, \xi_i^*$  in  $\mathbb{R}^N$  ( $\xi_i \neq \xi_i^*$ ) the following properties

$$|A_i(t, x, \xi_i)| \leq H_i(t, x) + |\xi_i|^{p_i(x)-1} \quad , \quad (5.2)$$

$$A_i(t, x, \xi_i) \xi_i \geq d_i |\xi_i|^{p_i(x)}, \quad (5.3)$$

$$\langle A_i(t, x, \xi_i) - A_i(t, x, \xi_i^*), \xi_i - \xi_i^* \rangle > 0, \quad (5.4)$$

where  $H_i \in L^{\frac{p_i(x)}{p_i(x)-1}}(Q_T)$  and  $d_i > 0$ .

For all  $i = 1, \dots, M$ , we assume that  $f_i$  satisfies the following assumptions

$$f_i : Q_T \times [0, +\infty)^M \times \mathbb{R}^M \times \mathbb{R}^{N \times M} \rightarrow \mathbb{R} \quad \text{are measurable,} \quad (5.5)$$

$$f_i : Q_T \times [0, +\infty)^M \times \mathbb{R}^M \times \mathbb{R}^{N \times M} \rightarrow \mathbb{R} \quad \text{are locally Lipschitz continuous.} \quad (5.6)$$

The result of this work include the case of  $p_i(x)$ -Laplacian operator modeled by the following system

$$\begin{cases} \forall i = 1, \dots, M, \\ \partial_t u_i - \operatorname{div}(|\nabla u_i|^{p_i(x)-2} \nabla u_i) = f_i(t, x, u, \nabla u) & \text{in } Q_T \\ u_i(0, x) = u_{0i}(x) & \text{in } \Omega \\ u_i(t, x) = 0 & \text{on } \Sigma_T. \end{cases} \quad (5.7)$$

On the other view, the obtained theoretical results remains applicable to the following mean curvature system

$$\begin{cases} \forall i = 1, \dots, M, \\ \partial_t u_i - \operatorname{div}\left(\left(1 + |\nabla u_i|^2\right)^{\frac{p_i(x)-2}{2}} \nabla u_i\right) = f_i(t, x, u, \nabla u) & \text{in } Q_T \\ u_i(0, x) = u_{0i}(x) & \text{in } \Omega \\ u_i(t, x) = 0 & \text{on } \Sigma_T. \end{cases}$$

We have organized this chapter as follows. In Section 2, we recall some elementary notations and properties of Lebesgue and Sobolev spaces with variable exponent and we introduce the notion of weak solution adapted to the system (5.1). Section 3 deals with auxiliary results which must be useful in the proof of the main result. In Section 4, we use Schauder fixed point Theorem to prove the existence of a weak periodic solution to the system (5.1) when the nonlinearities are bounded. Section 5 is devoted to proving the main result, we show the existence of a nonnegative weak approximate solution to the system (5.1),

then we establish necessary a priori estimates in order to pass to the limit in the approximate problem.

## 5.2 Notations and Preliminaries.

In this section, we recall some preliminary results of Lebesgue and Sobolev spaces with variable exponent, as well as some of their properties and basic facts. The readers can consult the details in the references [47, 79, 113, 57].

Let  $\mathcal{P}(\Omega)$  be the set of continuous functions  $p : \Omega \rightarrow ]1, \infty)^M$ , for a given  $p = (p_i)_{i=1, \dots, M}$  in  $\mathcal{P}(\Omega)$ , we denote, for  $i = 1, \dots, M$

$$p_i^+ = \sup_{x \in \Omega} p_i(x), \quad p_i^- = \inf_{x \in \Omega} p_i(x).$$

we define

$$p^+ = \sup_{1 \leq i \leq M} p_i^+, \quad p^- = \inf_{1 \leq i \leq M} p_i^-.$$

Throughout this chapter, we assume that for  $i = 1, 2, \dots, M$

$$1 < p^- \leq p_i(x) \leq p^+ < \infty. \tag{5.8}$$

The variable exponent Lebesgue space  $L^{p_i(x)}(\Omega)$  is defined such as

$$L^{p_i(x)}(\Omega) = \left\{ u : \Omega \rightarrow \mathbb{R} \text{ measurable such that } \rho_{p_i(x)}(u) < \infty \right\},$$

where  $\rho_{p_i(x)}$  is the convex modular

$$\rho_{p_i(x)}(u) = \int_{\Omega} |u(x)|^{p_i(x)} dx.$$

The space  $L^{p_i(\cdot)}(\Omega)$  is equipped by the so-called Luxemburg norm

$$\|u\|_{p_i(x)(\Omega)} = \inf \left\{ \alpha > 0, \rho_{p_i(x)}\left(\frac{u}{\alpha}\right) \leq 1 \right\}.$$

Related to the system case, we will introduce the space

$$L^{p(x)}(\Omega) = L^{p_1(x)}(\Omega) \times \dots \times L^{p_M(x)}(\Omega),$$

endowed with the following norme

$$\|u\|_{p(x)} = \sum_{i=1}^M \|u_i\|_{p_i(x)}.$$

Under the assumption (5.8), the space  $L^{p(x)}(\Omega)$  becomes a separable, uniformly convex Banach space, the dual space of  $L^{p(x)}(\Omega)$  is defined by  $L^{p'(x)}(\Omega)$  where  $p' = (p'_i)_{i=1, \dots, M}$  satisfying  $p'_i(x) = \frac{p_i(x)}{p_i(x)-1}$ . For any  $u \in L^{p(x)}(\Omega)$  and  $v \in L^{p'(x)}(\Omega)$ , we have the following Hölder inequality

$$\sum_{i=1}^M \int_{\Omega} |u_i v_i| dx \leq 2M \|u\|_{p(x)} \|v\|_{p'(x)}.$$

We can easily show the following Propositions using the known results for the case  $M = 1$ .

**Proposition 5.2.1**

1. if  $\|u\|_{p(x)} \geq 1$ , then  $\|u\|_{p(x)}^{p^-} \leq \|u\|_{p(x)} \leq \|u\|_{p(x)}^{p^+}$ ,
2. if  $\|u\|_{p(x)} < 1$ , then  $\|u\|_{p(x)}^{p^+} \leq \|u\|_{p(x)} \leq \|u\|_{p(x)}^{p^-}$ ,
3. if  $\Omega$  is bounded, the inclusion result between  $L^{p(x)}(\Omega)$  spaces still holds. Let  $p_1 = (p_{1,i})$ ,  $p_2 = (p_{2,i}) \in \mathcal{P}(\Omega)$ , such that  $p_1(x) \leq p_2(x)$  in the sense that

$$\forall i = 1, 2, \dots, M \quad \inf_{x \in \Omega} (p_{2,i}(x) - p_{1,i}(x)) \geq 0,$$

we have  $L^{p_2(x)}(\Omega) \hookrightarrow L^{p_1(x)}(\Omega)$  and the embedding is continuous. that is, the embedding  $L^{p_2(x)}(\Omega) \hookrightarrow L^{p_1(x)}(\Omega)$  is continuous.

4. Let  $q \in C(\bar{\Omega})$  such that  $1 \leq q(x) < p^*(x)$ , for all  $x \in \bar{\Omega}$ , then the embedding  $W_0^{1,p(x)}(\Omega) \hookrightarrow L^q(x)(\Omega)$  is continuous and compact, where

$$p^*(x) := \begin{cases} \frac{Np(x)}{N-p(x)}, & p(x) < N, \\ +\infty, & p(x) \geq N. \end{cases}$$

To generalize the variable exponent  $p : \bar{\Omega} \rightarrow ]1, \infty)^M$  to the case  $\bar{Q}_T = [0, T] \times \bar{\Omega}$ , we set  $p(t, x) := p(x)$  for all  $(t, x) \in \bar{Q}_T$ . Then, the generalized Lebesgue space is described as follows

$$L^{p(x)}(Q_T) = \left\{ u : Q_T \rightarrow \mathbb{R} \text{ measurable such that } \int_{Q_T} |u(t, x)|^{p(x)} dx dt < \infty \right\}.$$

The space  $(L^{p(x)}(Q_T), \|\cdot\|_{p(x)})$  is a separable, uniformly convex Banach space with

$$\|u\|_{p(x)} = \inf \left\{ \alpha > 0, \int_{Q_T} \left| \frac{u(t,x)}{\alpha} \right|^{p(x)} dx dt \leq 1 \right\}.$$

The variable exponent Sobolev space  $W^{1,p(x)}(\Omega)$  is introduced such as

$$W^{1,p(x)}(\Omega) = \left\{ u \in L^{p(x)}(\Omega), \quad |\nabla u| = (|\nabla u_i|)_{i=1,\dots,M} \in L^{p(x)}(\Omega) \right\},$$

we equipped with the norm

$$\|u\|_{1,p(x)} = \|u\|_{p(x)} + \|\nabla u\|_{p(x)}.$$

Due to this norm, the space  $W^{1,p(x)}(\Omega)$  is a separable and reflexive Banach space. We assume that  $p(x)$  satisfies the log-Hölder-continuity condition, i.e. there exists a constant  $C$  such that for all  $i = 1, \dots, M$

$$|p_i(x_1) - p_i(x_2)| \leq \frac{-C}{\log|x_1 - x_2|}, \quad \forall x_1, x_2 \in \Omega, \quad \text{with } |x_1 - x_2| < \frac{1}{2}. \quad (5.9)$$

As a consequence, the space of smooth functions is dense in the variable exponent Sobolev spaces and we define  $W_0^{1,p(x)}(\Omega)$  as the closure of  $\mathcal{C}_c^\infty(\Omega)$  in  $W^{1,p(x)}(\Omega)$ . Moreover, the spaces  $W_0^{1,p(x)}(\Omega)$  are reflexives and we denote by  $W^{-1,p'(x)}(\Omega)$  its dual space. In addition, the  $p(\cdot)$ -Poincaré inequality holds true and for all  $u \in W_0^{1,p(\cdot)}(\Omega)$ , we have

$$\|u\|_{p(x)} \leq C(\Omega, p(\cdot)) \|\nabla u\|_{p(x)},$$

where  $C(\Omega, p(\cdot))$  is a constant depends only on  $\Omega$  and  $p(\cdot)$ . Due to this result, one may deduce that  $\|\nabla u\|_{p(x)}$  becomes a norm in  $W_0^{1,p(x)}(\Omega)$ .

For  $0 < T < +\infty$  we introduce the time space

$$L^{p^-}(0, T; W_0^{1,p(x)}(\Omega)) = \left\{ u \in L^{p(x)}(Q_T) : \sum_{i=1}^M \int_0^T \|\nabla u_i\|_{p_i(x)}^{p^-} < \infty \right\},$$

endowed with the norm

$$\|u\|_{L^{p^-}(0, T; W_0^{1,p(x)}(\Omega))} = \left( \sum_{i=1}^M \int_0^T \|\nabla u_i\|_{p_i(x)}^{p^-} \right)^{\frac{1}{p^-}}.$$

Now, we introduce our functional framework which is already useful in the studies of parabolic system with variable exponent. We consider

$$\mathcal{V} = \left\{ v \in L^{p^-} \left( 0, T; W_0^{1,p(x)}(\Omega) \right) : |\nabla v| = (|\nabla v_i|)_{1 \leq i \leq M} \in L^{p(x)}(Q_T) \right\},$$

endowed with the standard norm

$$\|v\|_{\mathcal{V}} = \|v\|_{L^{p^-}(0,T;W_0^{1,p(x)}(\Omega))} + \|\nabla v\|_{p(x)}.$$

Thanks to the  $p(x)$ -Poincaré's inequality and the continuity of the embedding  $L^{p(x)}(Q_T) \hookrightarrow L^{p^-}(0, T; W_0^{1,p(x)}(\Omega))$  the standard norm  $\|\cdot\|_{\mathcal{V}}$  is equivalent to the following norm

$$\|u\|_{\mathcal{V}} = \|\nabla u\|_{L^{p(x)}(Q_T)}.$$

The space  $\mathcal{V}$  is a separable and reflexive Banach space and  $\mathcal{V}^*$  denoted its dual space. Some properties of the space  $\mathcal{V}$  are given in the following Lemma.

**Lemma 5.2.1**

[24] Let  $\mathcal{V}$  be the space defined as above. Then we have

i) the following continuous dense embedding

$$L^{p^+}(0, T; W_0^{1,p(\cdot)}(\Omega)) \hookrightarrow \mathcal{V} \hookrightarrow L^{p^-}(0, T; W_0^{1,p(\cdot)}(\Omega)). \quad (5.10)$$

In particular, since  $\mathcal{C}_c^\infty(Q_T)^M$  is dense in  $L^{p^+}(0, T; W_0^{1,p(\cdot)}(\Omega))$ , it is dense in  $\mathcal{V}$  and for the corresponding dual spaces we have

$$L^{(p^-)'}(0, T; (W_0^{1,p(\cdot)}(\Omega))^*) \hookrightarrow \mathcal{V}^* \hookrightarrow L^{(p^+)'}(0, T; (W_0^{1,p(\cdot)}(\Omega))^*). \quad (5.11)$$

ii) Moreover, the elements of  $\mathcal{V}^*$  are represented as follow: For all  $S \in \mathcal{V}^*$ , there exists  $\xi = (\xi_1, \dots, \xi_N) \in (L^{p'(\cdot)}(Q_T))^N$  such that:  $S = \operatorname{div}(\xi)$  and

$$\langle S, \varphi \rangle_{\mathcal{V}^*, \mathcal{V}} = \int_{Q_T} \xi \nabla \varphi \, dxdt,$$

for any  $\varphi \in \mathcal{V}$ . Furthermore, we have

$$\|S\|_{\mathcal{V}^*} = \max\{\|\xi_j\|_{L^{p(\cdot)}(Q_T)}, j = 1, \dots, N\}.$$

**Remark 5.2.1**

Related to the results of Proposition 5.2.1 and Lemma 5.2.1, we can deduce the useful relationship

$$\min \left\{ \|u\|_{\mathcal{V}^-}^{p^-}, \|u\|_{\mathcal{V}^+}^{p^+} \right\} \leq \int_{Q_T} |\nabla u_i|^{p_i(x)} dxdt \leq \max \left\{ \|u\|_{\mathcal{V}^-}^{p^-}, \|u\|_{\mathcal{V}^+}^{p^+} \right\}. \quad (5.12)$$

For the convenience of the readers, sometimes we work with  $f(t, x, u, \nabla u)$  instead of  $(f_i(t, x, u_1, \dots, u_M, \nabla u_1, \nabla u_2, \dots, \nabla u_M))$ .

We will also omit the space and time variable in the expressions of the functions operators and the integrals when there is no ambiguity. In several steps of the proof of the main result, we will denote by  $C$  any nonnegative constant independent on the index of the sequence.

It is necessary to precise in which sense we want to solve the system (5.1). For this reason, we propose to enunciate the notion of weak solution used to study system (5.1).

**Definition 5.2.1**

We say that  $u \in \mathcal{V} \cap \mathcal{C}(0, T; L^2(\Omega)^M)$  is a weak solution of the system (5.1), if it satisfies  $\partial_t u \in \mathcal{V}^* + L^1(Q_T)^M$ ,  $f(t, x, u, \nabla u) \in L^1(Q_T)^M$  and for  $i = 1, \dots, M$

$$u_i(0, x) = u_{0i}(x) \text{ in } L^2(\Omega)$$

$$\int_0^T \langle \partial_t u_i, \phi \rangle dt + \int_{Q_T} A_i(t, x, \nabla u_i) \nabla \phi = \int_{Q_T} f_i(t, x, u, \nabla u) \phi, \quad (5.13)$$

holds for every  $\phi \in \mathcal{V} \cap L^\infty(Q_T)^M$ .

**Remark 5.2.2**

In the previous definition  $\partial_t u \in \mathcal{V}^* + L^1(Q_T)^M$  is understood in the following sens

$$\int_0^T \langle \partial_t u, \phi \rangle dt := \langle \partial_t u, \phi \rangle_{\mathcal{V}^* + L^1(Q_T), \mathcal{V}} = \langle \alpha^{(1)}, \phi \rangle_{\mathcal{V}^* \times \mathcal{V}} + \int_{Q_T} \alpha^{(2)} \phi dxdt,$$

where  $\alpha^{(1)} \in \mathcal{V}^*$  and  $\alpha^{(2)} \in L^1(Q_T)^M$ .

In the following Lemma, we propose to show an interesting compactness result which will be used in several steps of our work.

**Lemma 5.2.2**

Let  $(v_n)$  be a bounded sequence in  $\mathcal{V}$  such that  $(\partial_t v_n)$  is bounded in  $\mathcal{V}^* + L^1(Q_T)^M$ . Then, up to a subsequence

$$v_n \rightarrow v \text{ strongly in } L^{p^-}(0, T; L^{p(x)}(\Omega)) \text{ and a.e. in } Q_T.$$

**Proof.**

For a suitable fixed  $s$ , the following embedding relationships hold

- $s > \frac{N}{2}$ , we have  $H_0^s(\Omega) \hookrightarrow L^\infty(\Omega)$ , and then  $L^1(\Omega) \hookrightarrow H^{-s}(\Omega)$ ,
- $s - 1 > \frac{N}{2}$ , one has  $H_0^s(\Omega)^M \hookrightarrow W^{1,p(x)}(\Omega)$ , consequently,  $W^{-1,p'(x)}(\Omega) \hookrightarrow H^{-s}(\Omega)^M$ .

In accordance with (5.11), it leads to  $(\partial_t v_n)$  is bounded in  $L^1(0, T; H^{-s}(\Omega)^M)$ . Since  $(v_n)$  is bounded in  $\mathcal{V}$ , it follows from the embedding relationship (5.10) that  $(v_n)$  is bounded in  $L^{p^-}(0, T; W_0^{1,p(x)}(\Omega))$ .

Moreover, we have

$$W_0^{1,p(x)}(\Omega) \xrightarrow{\text{compact}} L^{p(x)}(\Omega) \hookrightarrow H^{-s}(\Omega)^M.$$

Then, by applying the compactness result of Simon (see Corollary 4, page 85 of [124]) we obtain that  $(v_n)$  converges strongly to  $v$  in  $L^{p^-}(0, T; L^{p(x)}(\Omega))$  and a.e. in  $Q_T$  (up to a subsequence).

Before closing this section, we recall a classical embedding result which can be viewed such as a direct consequence of the Aubin-Simon Theorem [124].

**Lemma 5.2.3**

Assume that (5.8) and (5.9) hold true. If  $v$  belongs to  $\mathcal{V} \cap L^2(Q_T)^M$  with  $\partial_t v$  belonging in  $\mathcal{V}^* + L^2(Q_T)^M$ , then  $v \in \mathcal{C}([0, T], L^2(\Omega)^M)$ .

### 5.3 Auxilliary Results

In this section, we present the existence and uniqueness results of weak solutions for the system (5.1) when the nonlinearities  $f$  does not depend on the solution  $u$  and their gradient, namely  $f_i(t, x, r, \xi) = g_i(t, x)$ .

**Lemma 5.3.1**

i) Let  $v_0 \in L^2(\Omega)^M$ ,  $g \in L^2(Q_T)^M$  then the following system

$$\begin{cases} \forall i = 1, 2, \dots, M \\ \partial_t v_i - \operatorname{div}(A_i(t, x, \nabla v_i)) = g_i(t, x) & \text{in } Q_T \\ v_i(t, x) = 0 & \text{on } \Sigma_T \\ v_i(0, x) = v_{0i}(x) & \text{in } \Omega, \end{cases} \quad (5.14)$$

has a unique solution  $v \in \mathcal{V} \cap \mathcal{C}([0, T], L^2(\Omega)^M)$  such that

$$\partial_t v \in \mathcal{V}^* + L^2(Q_T)^M, \quad v(0, x) = v_0(x) \text{ in } L^2(\Omega)^M,$$

and for  $i = 1, \dots, M$

$$\int_0^T \langle \partial_t v_i, \phi_i \rangle + \int_{Q_T} A_i(t, x, \nabla v_i) \nabla \phi_i = \int_{Q_T} g_i(t, x) \phi_i, \quad (5.15)$$

with  $\phi = (\phi_1, \dots, \phi_M) \in \mathcal{V} \cap L^2(Q_T)^M$ .

ii) Let  $v$  be the solution of (5.14), then

$$\|v\|_{\mathcal{V}} + \sup_{0 \leq t \leq T} \|v(t)\|_{L^2(\Omega)^M} \leq C(\Omega, T) \left( \|v_0\|_{L^2(\Omega)^M} + \|g\|_{L^2(Q_T)^M} \right), \quad (5.16)$$

$$\|\partial_t v\|_{\mathcal{V}^* + L^2(Q_T)^M} \leq C(\Omega, T) \left( \|H\|_{p'(x)} + \|v_0\|_{L^2(\Omega)^M} + \|g\|_{L^2(Q_T)^M} \right). \quad (5.17)$$

**Proof.**

i) We refer the reader for to see [123] for the existence and uniqueness of the weak solution of the system (5.14). Due to the Lemma 5.2.3, we deduce that  $v$  belongs to  $\mathcal{C}([0, T], L^2(\Omega)^M)$  which means that the initial condition makes a sens.

ii) To prove the estimate (5.16), one may choose in (5.15)  $\phi_i = v_i \chi_{(0, t)}$  with  $t < T$ , we obtain

$$\frac{1}{2} \int_{\Omega} v_i^2(t) + \int_{Q_t} A_i(\tau, x, \nabla v_i) \nabla v_i = \frac{1}{2} \int_{\Omega} v_{0i}^2 + \int_{Q_t} v_i g_i(\tau, x), \quad (5.18)$$

where  $Q_t = ]0, t[ \times \Omega$ . By applying the coercivity assumption (5.3) in (5.18), one has

$$\frac{1}{2} \int_{\Omega} v_i^2(t) + d_i \int_{Q_t} |\nabla v_i|^{p_i(x)} \leq \frac{1}{2} \int_{\Omega} v_{0i}^2 + \int_{Q_t} v_i g_i(\tau, x). \quad (5.19)$$

Consequently,

$$\int_{\Omega} v_i^2(t) \leq \int_{Q_t} g_i^2(\tau, x) + \int_{Q_t} v_i^2 + \int_{\Omega} v_{0i}^2. \quad (5.20)$$

Using Gronwall's inequality we obtain

$$\int_{Q_T} v_i^2 \leq (\exp(T) - 1) \left( \|g_i\|_{L^2(Q_T)}^2 + \int_{\Omega} v_{0i}^2 dx \right). \quad (5.21)$$

Substituting the above expression in (5.20), we get

$$\sup_{0 \leq t \leq T} \int_{\Omega} v_i^2(t) \leq \|g_i\|_{L^2(Q_T)}^2 + \exp(T) \left( \|g_i\|_{L^2(Q_T)} + \int_{\Omega} v_{0i}^2 \right). \quad (5.22)$$

It comes that,

$$\sup_{0 \leq t \leq T} \|v_i(t)\|_{L^2(\Omega)} \leq C(T, \Omega) \left( \|v_{0i}\|_{L^2(\Omega)} + \|g_i\|_{L^2(Q_T)} \right). \quad (5.23)$$

Using (5.18) and (5.3), we deduce

$$\int_{Q_T} |\nabla v_i|^{p_i(x)} dx dt \leq C(T, \Omega) \left( \int_{Q_T} g_i^2 dx dt + \int_{\Omega} v_{0i}^2 \right). \quad (5.24)$$

Hence, from the result of (5.12) one obtains

$$\|v\|_{\mathcal{V}} \leq C(T, \Omega) \left( \|g\|_{L^2(Q_T)^M} + \|v_0\|_{L^2(\Omega)^M} \right), \quad (5.25)$$

which implies that  $v$  is uniformly bounded in  $\mathcal{V}$ . By arguing the results of (5.23) and (5.25) we obtain the estimate (5.16). It remains to estimate  $\partial_t v$  in the norm of the space  $\mathcal{V}^* + L^2(Q_T)^M$ .

Thanks to the growth assumption (5.2) we have

$$\begin{aligned} \int_{Q_T} |A_i(t, x, \nabla v_i)|^{p_i'(x)} &\leq C \left( \int_{Q_T} |H_i(t, x)|^{p_i'(x)} + \int_{Q_T} |\nabla v_i|^{p_i(x)} \right), \\ &\leq C(T, \Omega) \left( \int_{Q_T} |H_i(t, x)|^{p_i'(x)} + \int_{Q_T} g_i^2 dx dt + \int_{\Omega} v_{0i}^2 \right). \end{aligned} \quad (5.26)$$

Therefore,

$$\|A_i(t, x, \nabla v_i)\|_{p'_i(x)} \leq C(T, \Omega) \left( \|H_i\|_{p'_i(x)} + \|g_i\|_{L^2(Q_T)} + \|v_{0i}\|_{L^2(\Omega)} \right). \quad (5.27)$$

Hence, employing the equation satisfied by  $v_i$  with the help of (5.27), one gets

$$\begin{aligned} \|\partial_t v\|_{\mathcal{V}' + L^2(Q_T)^M} &\leq C \left( \|A(t, x, \nabla v)\|_{p'(x)} + \|g\|_{L^2(Q_T)^M} \right) \\ &\leq C(T, \Omega) \left( \|H\|_{p'(x)} + \|g\|_{L^2(Q_T)^M} + \|v_0\|_{L^2(\Omega)^M} \right). \end{aligned} \quad (5.28)$$

## 5.4 An existence result for bounded nonlinearities

We are concerned to study the existence of a weak solution to system (5.1) with bounded nonlinearities.

### Theorem 5.4.1

Assume that (5.2)-(5.6) and (5.8) hold. If there exist a nonnegative function  $\Lambda = (\Lambda_i)_{i=1,2,\dots,M} \in L^\infty(Q_T)^M$  such that for almost everywhere  $(t, x) \in Q_T$ ,

$$|f_i(t, x, r, \xi)| \leq \Lambda_i(t, x) \quad \text{for all } (r, \xi) \in \mathbb{R}^M \times \mathbb{R}^{N \times M}, \quad (5.29)$$

then for every  $u_0 \in L^2(\Omega)^M$ , the system (5.1) has a weak solution.

### Proof.

To prove the result of Theorem 5.4.1, we propose to use Schauder fixed point Theorem [98]. We start by introducing the following mapping

$$\mathcal{F} : \mathcal{V} \rightarrow \mathcal{V}$$

$$v \longmapsto u,$$

where  $u$  is the unique weak solution to the following

$$\begin{cases} \forall i = 1, \dots, M, \\ \partial_t u_i - \operatorname{div}(A_i(t, x, \nabla u_i)) = f_i(t, x, v, \nabla v) & \text{in } Q_T \\ u_i(0, x) = u_{0i}(x) & \text{in } \Omega \\ u_i(t, x) = 0 & \text{on } \Sigma_T. \end{cases} \quad (5.30)$$

In view of the assumption (5.29), the function  $f_i(t, x, v, \nabla v)$  belongs to  $L^2(Q_T)$  and since  $u_0 \in L^2(Q_T)^M$ ,

we deduce from Lemma 5.3.1 the existence of  $u \in \mathcal{V} \cap \mathcal{C}(0, T; L^2(\Omega)^M)$  unique weak solution to the system (5.30) satisfying

$$\begin{aligned} \partial_t u &\in \mathcal{V}^* + L^2(Q_T)^M, \quad u(0, x) = u_0(x) \text{ in } L^2(\Omega)^M, \\ \int_0^T \langle \partial_t u_i, \phi \rangle + \int_{Q_T} A_i(t, x, \nabla u_i) \nabla \phi_i &= \int_{Q_T} f_i(t, x, v, \nabla v) \phi_i, \\ \forall \phi &= (\phi_1, \dots, \phi_M) \in \mathcal{V} \cap L^2(Q_T)^M. \end{aligned} \quad (5.31)$$

which implies that the application  $\mathcal{F}$  is clearly well defined. To apply Schauder fixed point Theorem, we require to check the continuity and the compactness of the application  $\mathcal{F}$ . To check the continuity of  $\mathcal{F}$ , we take  $v^n = (v_1^n, \dots, v_M^n)$  a sequence in  $\mathcal{V}$  such that  $(v^n)$  converges strongly to  $v = (v_1, \dots, v_M)$  in  $\mathcal{V}$ . We put

$$\begin{aligned} u^n &= (u_1^n, \dots, u_M^n) = \mathcal{F}(v^n), \\ u &= (u_1, \dots, u_M) = \mathcal{F}(v). \end{aligned}$$

Hence, we shall prove that  $(u^n)$  converges strongly to  $u$  in  $\mathcal{V}$ . Let us recall that  $u$  satisfies the weak formulation (5.31) and  $(u^n)$  satisfies

$$\begin{aligned} \partial_t u^n &\in \mathcal{V}^* + L^2(Q_T)^M, \quad u^n(0, x) = u_0(x) \text{ in } L^2(\Omega)^M, \\ \int_0^T \langle \partial_t u_i^n, \phi \rangle + \int_{Q_T} A_i(t, x, \nabla u_i^n) \nabla \phi_i &= \int_{Q_T} f_i(t, x, v^n, \nabla v^n) \phi_i, \\ \forall \phi &= (\phi_1, \dots, \phi_M) \in \mathcal{V} \cap L^2(Q_T)^M. \end{aligned} \quad (5.32)$$

Due to the results of Lemma 4.5.1, one has

$$\begin{aligned} \|u^n\|_{\mathcal{V}} &\leq C(\Omega, T) \left( \|u_0\|_{L^2(\Omega)^M} + \|f(t, x, v^n, \nabla v^n)\|_{L^2(Q_T)^M} \right), \\ \|\partial_t u^n\|_{\mathcal{V}^* + L^2(Q_T)^M} &\leq C(\Omega, T) \left( \|H\|_{p'(x)} + \|u_0\|_{L^2(\Omega)^M} + \|f(t, x, v^n, \nabla v^n)\|_{L^2(Q_T)^M} \right). \end{aligned}$$

Therefore, by applying the assumption (5.29), we deduce that  $(u^n)$  is bounded in  $\mathcal{V}$  and  $(\partial_t u^n)$  is bounded in  $\mathcal{V}^* + L^2(Q_T)^M$ . Hence, one may deduce the existence of a subsequence still denoted by  $(u^n)$  for

simplicity such that

$$\begin{aligned} u^n &\rightharpoonup u \text{ weakly in } \mathcal{V}, \\ \partial_t u^n &\rightharpoonup \partial_t u \text{ weakly in } \mathcal{V}^*, \\ u^n &\rightarrow u \text{ strongly in } L^{p^-}(0, T; L^{p(x)}(\Omega)) \text{ and a.e. in } Q_T. \end{aligned}$$

The later convergence is obtained by using the compactness result of Lemma 5.2.2. Furthermore, employing the continuous embedding  $L^{p^-}(0, T; L^{p(x)}(\Omega)) \hookrightarrow L^{p^-}(Q_T)$ , one obtains that  $(u^n)$  converges strongly to  $u$  in  $L^{p^-}(Q_T)$  and a.e. in  $Q_T$ . To prove the strong convergence of  $(u^n)$  in  $\mathcal{V}$ , we subtract the weak formulations (5.31) and (5.32). Thereafter, we take  $(u_i^n - u_i)$  as a test function, one gets for  $i = 1, \dots, M$

$$\begin{aligned} \int_0^T \langle \partial_t(u_i^n - u_i), (u_i^n - u_i) \rangle + \int_{Q_T} (A_i(t, x, \nabla u_i^n) - A_i(t, x, \nabla u_i))(\nabla u_i^n - \nabla u_i) \\ = \int_{Q_T} (f_i(t, x, v^n, \nabla v^n) - f_i(t, x, v, \nabla v))(u_i^n - u_i). \end{aligned} \quad (5.33)$$

Let us remark that

$$\int_0^T \langle \partial_t(u_i^n - u_i), (u_i^n - u_i) \rangle = \frac{1}{2} \int_{\Omega} |(u_i^n - u_i)(T)|^2 \geq 0.$$

In addition, by applying Hölder's inequality in the right-hand side of (5.33), one obtains

$$\begin{aligned} \int_{Q_T} (A_i(t, x, \nabla u_i^n) - A_i(t, x, \nabla u_i))(\nabla u_i^n - \nabla u_i) \\ \leq \|f_i(t, x, v^n, \nabla v^n) - f_i(t, x, v, \nabla v)\|_{L^{(p^-)'}(Q_T)} \|u_i^n - u_i\|_{L^{p^-}(Q_T)}. \end{aligned} \quad (5.34)$$

From the strong convergence of  $(v^n)$  in  $\mathcal{V}$ , it follows that for  $i = 1, \dots, M$

$$f_i(t, x, v^n, \nabla v^n) \rightarrow f_i(t, x, v, \nabla v) \text{ a.e in } Q_T.$$

On the other hand, using hypothesis (5.29) and dominated convergence Theorem, one has

$$f_i(t, x, v^n, \nabla v^n) \rightarrow f_i(t, x, v, \nabla v) \text{ strongly in } L^{(p^-)'}(Q_T).$$

Now, we can pass to the limit in (5.34) to obtain

$$\lim_{n \rightarrow \infty} \int_{Q_T} (A_i(t, x, \nabla u_i^n) - A_i(t, x, \nabla u_i))(\nabla u_i^n - \nabla u_i) \leq 0.$$

Therefore, one may apply the result of the Lemma 5 in [27] to get

$$\nabla u^n \rightarrow \nabla u \text{ strongly in } L^{p(x)}(Q_T)^M$$

Which means that  $(u^n)$  converges strongly to  $u$  in  $\mathcal{V}$ . In accordance with the previous convergence results, one may pass to the limit in the weak formulation (5.32) to get

$$\begin{aligned} \partial_t u &\in \mathcal{V}^* + L^2(Q_T)^M, \quad u(0, x) = u_0(x) \text{ in } L^2(\Omega)^M, \\ \int_0^T \langle \partial_t u_i, \phi \rangle + \int_{Q_T} A_i(t, x, \nabla u_i) \nabla \phi_i &= \int_{Q_T} f_i(t, x, v, \nabla v) \phi_i, \\ \forall \phi &= (\phi_1, \dots, \phi_M) \in \mathcal{V} \cap L^2(Q_T)^M. \end{aligned} \tag{5.35}$$

Which implies that the limit  $u$  verifies  $\mathcal{F}(v) = u$ . Furthermore, the uniqueness of the weak solution to the system (5.35) gives us the continuity of  $\mathcal{F}$ .

To show the compactness of  $\mathcal{F}$ , we consider  $v^n = (v_1^n, \dots, v_M^n)$  a bounded sequence in  $\mathcal{V}$ , we shall prove that  $u^n = \mathcal{F}(v^n)$  is relatively compact in  $\mathcal{V}$ . Following the same reasoning as of the continuity step, it comes that

- $u^n$  is bounded in  $\mathcal{V}$ ,
- $\partial_t u^n$  is bounded in  $\mathcal{V}^* + L^2(Q_T)^M$ ,
- $\left( f_i(t, x, v^n, \nabla v^n) \right)_n$  is bounded in  $L^2(Q_T)$ .

Due to the compactness result of Lemma 5.2.2, we can extract a subsequence still denoted by  $(u^n)$  for simplicity such that

$$u^n \rightarrow u \text{ strongly in } L^{p^-}(0, T; L^{p(x)}(\Omega)) \text{ and a.e. in } Q_T.$$

Following the same reasoning as in [135, 139], we can prove that  $\nabla u^n \rightarrow \nabla u$  a.e. in  $Q_T$ . Furthermore, we have

$$A_i(t, x, \nabla u_i^n) \rightharpoonup A_i(t, x, \nabla u_i) \text{ weakly in } L^{p'_i(x)}(Q_T).$$

We shall prove that  $(u^n)$  converges strongly in  $\mathcal{V}$ . To do this, we subtract the equation (5.32) with different index  $m$  and  $n$ , we get for all  $i = 1, 2, \dots, M$ .

$$\partial_t (u_i^n - u_i^m) - \operatorname{div}(A_i(\nabla u_i^n)) + \operatorname{div}(A_i(\nabla u_i^m)) = f_i(v^n, \nabla v^n) - f_i(v^m, \nabla v^m). \tag{5.36}$$

We choose  $(u_i^n - u_i^m)$  as a test function in the weak formulation of (5.36), we obtain

$$\begin{aligned} \int_0^T \langle \partial_t(u_i^n - u_i^m), (u_i^n - u_i^m) \rangle + \int_{Q_T} (A_i(\nabla u_i^n) - A_i(\nabla u_i^m)) \cdot \nabla(u_i^n - u_i^m) \\ = \int_{Q_T} \left( f_i(v^n, \nabla v^n) - f_i(v^m, \nabla v^m) \right) (u_i^n - u_i^m). \end{aligned} \quad (5.37)$$

Concerning the first integral, we have

$$\int_0^T \langle \partial_t(u_i^n - u_i^m), (u_i^n - u_i^m) \rangle = \frac{1}{2} \int_{\Omega} |(u_i^n - u_i^m)(T)|^2 \geq 0.$$

On the other hand, applying Hölder's inequality in the right-hand side of (5.37) and using the assumption (5.29), one gets

$$\int_{Q_T} (A_i(\nabla u_i^n) - A_i(\nabla u_i^m)) \cdot \nabla(u_i^n - u_i^m) \leq C \|\Lambda_i\|_{L^\infty(Q_T)} \|u_i^n - u_i^m\|_{L^{p^-}(0,T;L^{p(x)}(\Omega))} \quad (5.38)$$

By applying the strong convergence of  $(u^n)$  in  $L^{p^-}(0,T;L^{p(x)}(\Omega))$ , we can pass to the limit in (5.38) as  $m, n$  tends to  $+\infty$ , we get

$$\lim_{n,m \rightarrow \infty} \int_{Q_T} (A_i(\nabla u_i^n) - A_i(\nabla u_i^m)) \cdot \nabla(u_i^n - u_i^m) \leq 0.$$

Hence, we can use the Lemma 5 of [27] to obtain

$$\nabla u^n \rightarrow \nabla u \text{ strongly in } L^{p(x)}(Q_T)^M,$$

which implies that  $(u^n)$  converges strongly in  $\mathcal{V}$ , as consequence  $\mathcal{F}$  is compact.

It remains to prove the existence of a radius  $R$  such that the mapping  $\mathcal{F}$  send the ball  $\mathcal{B}(0,R)$  of  $\mathcal{V}$  to itself. To deal with this, we take  $v \in \mathcal{V}$  such that  $u = \mathcal{F}(v)$ , as it demonstrates in (5.16) we will have

$$\|v\|_{\mathcal{V}} \leq C(\Omega, T) \left( \|u_0\|_{L^2(\Omega)^M} + \|f(v, \nabla v)\|_{L^2(Q_T)^M} \right).$$

Thanks to assumption (5.29), it comes that by choosing

$$R \geq C(\Omega, T) \left( \|u_0\|_{L^2(\Omega)^M} + \|\Lambda\|_{L^2(Q_T)^M} \right).$$

One has

$$\mathcal{F} \left( \mathcal{B}(0, R) \right) \hookrightarrow \mathcal{B}(0, R).$$

Consequently, a direct application of Schauder fixed point Theorem implies the existence of a weak solution to the system (5.1).

## 5.5 An existence result for subquadratic growth

The goal of this section is to establish an existence result of a nonnegative weak solution to (5.1) under two fairly general conditions namely:

- The nonlinearities  $(f_i)_{1 \leq i \leq M}$  are nonnegative and have a critical growth with respect to the gradient namely

$$|f_i(t, x, r_1, \dots, r_M, \xi_1, \dots, \xi_M)| \leq C_i \left( \sum_{j=1}^M |r_j| \right) \left[ B_i(t, x) + |\xi_i|^{p_i(x)} \right], \quad (5.39)$$

where  $C_i : [0, +\infty) \rightarrow [0, +\infty)$  is a non-decreasing function and  $B_i$  is a nonnegative function belonging to  $L^1(Q_T)$ .

- The existence of a weak super-solution defined as follows:

### Definition 5.5.1

A weak super-solution of system (5.1) is a function  $w = (w_1, \dots, w_M) \in \mathcal{V} \cap L^\infty(Q_T)^M$ ,  $\partial_t w \in \mathcal{V}^* + L^1(Q_T)^M$  and for  $i = 1, \dots, M$

$$w_i(0, x) \geq u_{0i}(x) \text{ in } L^2(\Omega)$$

,

$$\int_0^T \langle \partial_t w_i, \phi \rangle dt + \int_{Q_T} A_i(t, x, \nabla w_i) \nabla \phi \geq \int_{Q_T} f_i(t, x, w, \nabla w) \phi, \quad (5.40)$$

for every nonnegative test function  $\phi \in \mathcal{V} \cap L^\infty(Q_T)^M$ .

### Theorem 5.5.1

Assume that  $A_i$  satisfies (5.2)-(5.4) and the nonlinearities  $(f_i)_{1 \leq i \leq M}$  satisfies (5.5), (5.6) and (5.39). Moreover, we assume the existence of  $w$  a nonnegative super-solution to (5.1). Then, for any nonnegative  $u_0 \in L^2(Q_T)^M$ , the system (5.1) has a weak solution  $u$  such that  $0 \leq u \leq w$  a.e. in  $Q_T$ .

### Exemples 5.5.1

We propose to give an example of the construction of a weak super-solution to a particular case of (5.1), which permit us to assure the validity of the proposed assumptions in Theorem 5.5.1. Let us consider the

$p_i(x)$ -Laplacian system (5.7) such that the nonlinearities  $(f_i)_{1 \leq i \leq M}$  are nonnegative and satisfies

$$|f_i(t, x, r_1, \dots, r_M, \xi_1, \dots, \xi_M)| \leq K_i(t, x) + L_i(t, x)|\xi_i|^{p_i(x)}, \quad (5.41)$$

where  $K_i$  and  $L_i$  are a nonnegative functions belonging to  $L^\infty(Q_T)$  and satisfying for all  $i = 1, \dots, M$

$$0 \leq K_i(t, x) \leq k_i, \quad 0 \leq L_i(t, x) \leq l_i \quad \text{a.e in } Q_T, \quad (5.42)$$

with  $k_i, l_i > 0$  are a constants. It is clear that the assumption (5.41) can be viewed as a particular case of (5.39), let us assume that  $u_0$  is a nonnegative function that belongs to  $L^\infty(Q_T)^M$ . To build a nonnegative weak super-solution to (5.7), we consider the following system

$$\begin{cases} \forall i = 1, \dots, M, \\ \partial_t w_i - \operatorname{div} (|\nabla w_i|^{p_i(x)-2} \nabla w_i) = k_i + l_i |\nabla w_i|^{p_i(x)} & \text{in } Q_T \\ w_i(0, x) = u_{0i}(x) & \text{in } \Omega \\ w_i(t, x) = 0 & \text{on } \Sigma_T. \end{cases} \quad (5.43)$$

According to the result of [85], one may deduce the existence of  $(w_i)_{1 \leq i \leq M} \in \mathcal{V} \cap L^\infty(Q_T)^M$  a weak solution to (5.43). Furthermore, using (5.41)-(5.42) and following the same reasoning as of the proof below of Lemma 5.5.1 (positivity part), we can conclude that  $(w_i)_{1 \leq i \leq M}$  is a nonnegative weak super-solution to (5.7).

To prove Theorem 5.5.1, we will proceed by steps. In the first step, we will truncate the problem and show that the approximate system has a weak solution  $u^n$ . The second step is devoted to prove that  $0 \leq u^n \leq w$ , this means that the approximate solution  $u^n$  mains nonnegative and bounded by  $w$ . Thereafter, we will provide some a priori estimates on the approximate solution in order to pass to the limit and rigorously demonstrate the existence of a global weak solution of our system.

### 5.5.1 Construction of the approximate problem

Let  $n \in \mathbb{N}$ , we consider the truncation function  $\psi_n \in \mathcal{C}_c^\infty(\mathbb{R})$  such that

$$0 \leq \psi_n \leq 1,$$

and

$$\psi_n(s) = \begin{cases} 1 & \text{if } |s| \leq n, \\ 0 & \text{if } |s| \geq n+10 \end{cases}$$

For almost everywhere  $(t, x) \in Q_T$  and for all  $(r, \xi) \in \mathbb{R}^M \times \mathbb{R}^{M \times N}$ , we approximate  $f_i$  by

$$f_i^n(t, x, r, \xi) = \psi_n \left( \sum_{j=1}^M (|r_j| + \|\xi_j\|) \right) f_i(t, x, T(r), T(\xi)) \quad (5.44)$$

Where  $T(r) = r - (r - w)^+$  and  $w$  is the super-solution defined in (5.40). We mention that these functions enjoy the same properties as  $f_i$ , moreover they are measurable with respect to  $(t, x)$ , locally Lipschitzian with respect to  $(r, \xi)$  and  $|f_i^n| \leq \Lambda_i^n$ , where  $\Lambda_i^n$  is a constant depending only on  $n$  (these estimates can be derived from (5.6)).

Thus, we can state the following approximate system

$$\begin{cases} \partial_t u_i^n - \operatorname{div}(A_i(t, x, \nabla u_i^n)) = f_i^n(t, x, u^n, \nabla u^n) & \text{in } Q_T \\ u_i^n(0, x) = u_{0i}(x) & \text{in } \Omega \\ u_i^n(t, x) = 0 & \text{on } \Sigma_T. \end{cases} \quad (5.45)$$

Thanks to the result of Theorem 5.4.1, the approximate system (5.45) has a weak solution  $u^n = (u_1^n, \dots, u_M^n)$ .

In the following, we establish necessary estimates in order to pass to the limit in (5.45).

**Lemma 5.5.1**

*Let  $u^n$  be the weak solution of (5.45), then*

$$0 \leq u^n \leq w \quad (5.46)$$

**Proof.**

*Let  $\varepsilon > 0$ , we can build a sequence of convex functions  $j_\varepsilon(s)$  such as*

- $j'_\varepsilon(s)$  is bounded for all  $s \in \mathbb{R}$ ,
- $j'_\varepsilon(s) \rightarrow \operatorname{sign}^-(s)$  when  $\varepsilon \rightarrow 0$ ,
- $j_\varepsilon(s) \rightarrow (s)^-$  when  $\varepsilon \rightarrow 0$ ,

where  $\text{sign}^-$  presents the following sign function

$$\text{sign}^-(r) = \begin{cases} -1 & \text{if } r < 0 \\ 0 & \text{if } r \geq 0 \end{cases}$$

A typical construction of the function  $j_\varepsilon(s)$  can be given as follows

$$j_\varepsilon(s) = \begin{cases} -\frac{1}{\varepsilon} + \frac{1}{\varepsilon} \exp(-\varepsilon s - \varepsilon^2 \ln(|\frac{s-\varepsilon}{\varepsilon}|)) & \text{if } s < 0 \\ 0 & \text{if } s \geq 0. \end{cases}$$

To prove the non-negativity of  $u^n$ , we multiply both sides of the first equation in (5.45) by  $j'_\varepsilon(u_i^n)$  and we integrate over  $Q_t$  with  $0 \leq t \leq T$ , one has

$$\int_0^t \langle \partial_t u_i^n, j'_\varepsilon(u_i^n) \rangle + \int_{Q_t} A_i(\cdot, \nabla u_i^n) \nabla j'_\varepsilon(u_i^n) = \int_{Q_t} f_i^n(t, x, u^n, \nabla u^n) j'_\varepsilon(u_i^n).$$

Using (5.3), we have

$$\int_{\Omega} [j_\varepsilon(u_i^n)(t) - j_\varepsilon(u_i^n)(0)] + d_i \int_{Q_t} |\nabla u_i^n|^{p_i(x)} j'_\varepsilon(u_i^n) \leq \int_{Q_t} f_i^n(t, x, u^n, \nabla u^n) j'_\varepsilon(u_i^n).$$

Since  $\int_{\Omega} j_\varepsilon(u_i^n)(0) dx = 0$  and  $d_i \int_{Q_t} |\nabla u_i^n|^{p_i(x)} j'_\varepsilon(u_i^n) \geq 0$ , we have

$$\begin{aligned} \int_{\Omega} j_\varepsilon(u_i^n)(t) &\leq \int_{Q_t} f_i^n(t, x, u^n, \nabla u^n) j'_\varepsilon(u_i^n) \\ &\leq \int_{[u_i^n < 0]} f_i^n(t, x, u^n, \nabla u^n) j'_\varepsilon(u_i^n) + \int_{[u_i^n \geq 0]} f_i^n(t, x, u^n, \nabla u^n) j'_\varepsilon(u_i^n). \end{aligned}$$

We remark that  $j'_\varepsilon(u_i^n) = 0$  on the set where  $u_i^n \geq 0$ , therefore

$$\int_{\Omega} j_\varepsilon(u_i^n)(t) \leq \int_{[u_i^n < 0]} f_i^n(t, x, u^n, \nabla u^n) j'_\varepsilon(u_i^n),$$

letting  $\varepsilon \rightarrow 0$ , we obtain

$$\int_{\Omega} (u_i^n)^-(t) \leq - \int_{[u_i^n \leq 0]} f_i^n(t, x, u^n, \nabla u^n)$$

Using the positivity of  $f_i^n$  we deduce that  $(u_i^n)^-(t, x) = 0$  on  $\Omega$ , which means that  $u_i^n \geq 0$  a.e. on  $Q_T$ .

We have  $w \in \mathcal{V} \cap L^\infty(Q_T)$ , then we can choose  $v^n = u^n - (u^n - w)^+$  as a test function in the weak

formulation of (5.45), we obtain

$$\int_0^T \langle \partial_t u_i^n, v_i^n \rangle + \int_{Q_T} A_i(t, x, \nabla u_i^n) \nabla v_i^n = \int_{Q_T} f_i^n(t, x, u^n, \nabla u^n) v_i^n \quad (5.47)$$

Hence, we obtain

$$\int_0^T \langle \partial_t u_i^n, (u_i^n - w_i)^+ \rangle + \int_{Q_T} A_i(\cdot, \nabla u_i^n) \nabla (u_i^n - w_i)^+ = \int_{Q_T} f_i^n(\cdot, u^n, \nabla u^n) (u_i^n - w_i)^+. \quad (5.48)$$

Since  $w$  is a super-solution of the system (5.1), one has

$$\int_0^T \langle \partial_t w_i, (u_i^n - w_i)^+ \rangle + \int_{Q_T} A_i(\cdot, \nabla w_i) \nabla (u_i^n - w_i)^+ \geq \int_{Q_T} f_i(\cdot, w, \nabla w) (u_i^n - w_i)^+. \quad (5.49)$$

By subtracting (5.49) from (5.48), we get

$$\int_{Q_T} (A_i(\cdot, \nabla u_i^n) - A_i(\cdot, \nabla w_i)) \nabla (u_i^n - w_i)^+ \leq \int_{Q_T} (f_i^n(\cdot, u^n, \nabla u^n) - f_i(\cdot, w, \nabla w)) (u_i^n - w_i)^+.$$

To deal with the right-hand side, we use the properties (5.44) one obtains

$$\begin{aligned} & \int_{Q_T} (f_i^n(t, x, u^n, \nabla u^n) - f_i(t, x, w, \nabla w)) (u_i^n - w_i)^+ \\ & \leq \int_{Q_T} (f_i(t, x, T(u^n), \nabla T(u^n)) - f_i(t, x, w, \nabla w)) (u_i^n - w_i)^+ \\ & \leq \int_{u_i^n > w_i} (f_i(t, x, w, \nabla w) - f_i(t, x, w, \nabla w)) (u_i^n - w_i) = 0. \end{aligned}$$

We therefore have

$$\int_{Q_T} (A_i(t, x, \nabla u_i^n) - A_i(t, x, \nabla w_i)) \nabla (u_i^n - w_i)^+ \leq 0,$$

which implies,

$$\int_{u_i^n \geq w_i} (A_i(t, x, \nabla u_i^n) - A_i(t, x, \nabla w_i)) \nabla (u_i^n - w_i) \leq 0.$$

Thanks to the monotony properties (5.4), one has  $\nabla(u_i^n - w_i) = 0$  a.e. in  $\{(t, x) \in Q_T, u_i^n \geq w_i\}$  for all  $i = 1, \dots, M$ . Then,  $u_i^n - w_i = 0$  a.e. in  $\{(t, x) \in Q_T, u_i^n \geq w_i\}$  which means that  $u^n \leq w$  a.e. in  $Q_T$ .

**Remark 5.5.1**

As we can see, the super-solution of (5.1) belongs to  $L^\infty(Q_T)^M$ , consequently the initial data  $u_0$  is belonging in  $L^\infty(\Omega)^M$  and due to the result of Lemma 5.5.1 it follows that  $u^n$  belongs to  $L^\infty(Q_T)^M$ .

### 5.5.2 A priori estimates

We start by recalling a technical Lemma which has already used to estimate typical growth nonlinearities with respect to the gradient.

#### Lemma 5.5.2

Let  $\theta(s) = se^{\eta s^2}$ ,  $s \in \mathbb{R}$  and let  $\Theta(s) = \int_0^s \theta(\tau) d\tau$ . Then

$$\theta(0) = 0, \quad \Theta(s) \geq 0, \quad \theta'(s) > 0.$$

When  $\eta \geq \frac{b^2}{4a^2}$  is fixed, the following relationships hold true

$$a\theta'(s) - b|\theta(s)| \geq \frac{a}{2}, \quad \forall s \in \mathbb{R}. \quad (5.50)$$

#### Lemma 5.5.3

Let  $(u^n)$  be a solution of (5.45) and  $w$  the super-solution to (5.1). Then there exists a constant  $C$  such that

$$\|u^n\|_{\mathcal{V}} \leq C$$

$$\|f^n(t, x, u^n, \nabla u^n)\|_{L^1(Q_T)^M} \leq C.$$

#### Proof.

From the estimate (5.46), it follows that  $\theta(u_i^n) \in \mathcal{V} \cap L^\infty(Q_T)$ , then by choosing  $\theta(u_i^n)$  as a test function in the weak formulation of (5.45), we have

$$\int_0^T \langle \partial_t u_i^n, \theta(u_i^n) \rangle + \int_{Q_T} A_i(t, x, \nabla u_i^n) \nabla(u_i^n) \theta'(u_i^n) = \int_{Q_T} f_i^n(t, x, u^n, \nabla u^n) \theta(u_i^n). \quad (5.51)$$

For the first integral, we have

$$\int_0^T \langle \partial_t u_i^n, \theta(u_i^n) \rangle = \int_{\Omega} [\Theta(u_n(T)) - \Theta(u_{i0})].$$

From (5.3) and (5.46) the inequality (5.51) becomes

$$\begin{aligned} \int_{\Omega} \Theta(u_i^n(T)) + d_i \int_{Q_T} |\nabla u_i^n|^{p_i(x)} \theta'(u_i^n) &\leq \int_{\Omega} \Theta(u_{0i}) + \int_{Q_T} f_i^n(t, x, u^n, \nabla u^n) \theta(u_i^n) \\ &\leq \int_{\Omega} \Theta(u_{0i}) + \int_{Q_T} C_i (\|w\|_{\infty}) \left( B_i(x, t) + |\nabla u_i^n|^{p_i(x)} \right) \theta(u_i^n). \end{aligned}$$

We rewrite the above inequality as

$$\begin{aligned} \int_{\Omega} \Theta(u_i^n(T)) + \int_{Q_T} \left( d_i \theta'(u_i^n) - C_i(\|w\|_{\infty}) |\theta(u_i^n)| \right) |\nabla u_i^n|^{p(x)} \\ \leq \int_{\Omega} \Theta(u_{0i}) dx + \int_{Q_T} |B_i(x,t)| \theta(u_i^n). \end{aligned}$$

By choosing the constant  $\eta \geq \max_{i \in \{1, \dots, M\}} \left\{ \frac{C_i(\|w\|_{\infty})^2}{4d_i^2} \right\}$ , we obtain from Lemma 5.5.2

$$d_i \theta'(u_i^n(t,x)) - C_i(\|w\|_{\infty}) |\theta(u_i^n(t,x))| \geq \frac{d_i}{2} \text{ a.e in } Q_T.$$

On the other hand  $\Theta(u_i^n(T)) \geq 0$ , then

$$\frac{d_i}{2} \int_{Q_T} |\nabla u_i^n|^{p_i(x)} \leq \int_{\Omega} \Theta(u_{0i}) + \int_{Q_T} |B_i(x,t)| \theta(u_i^n)$$

We may utilize estimate (5.46) to deduce that

$$\int_{Q_T} |\nabla u_i^n|^{p_i(x)} \leq C \left( \|B_i\|_{L^1(Q_T)}, \|w_i(0)\|_{L^\infty(\Omega)}, \|w_i\|_{L^\infty(Q_T)} \right) \quad (5.52)$$

Employing the result of (5.12), we conclude that  $(u^n)$  is uniformly bounded in  $\mathcal{V}$ . To estimate the nonlinearities, we use the growth condition (5.39) combined with (5.12), one gets

$$\int_{Q_T} |f_i^n(t,x,u^n, \nabla u^n)| \leq C_i(\|w\|_{L^\infty(Q_T)}) \int_{Q_T} \left( B_i(x,t) + |\nabla u_i^n|^{p_i(x)} \right).$$

By applying (5.52), we deduce that  $(f^n)$  is bounded in  $L^1(Q_T)^M$ . Consequently, from the equation satisfies by  $(u^n)$  it follows that  $(\partial_t u^n)$  is bounded in  $\mathcal{V}^* + L^1(Q_T)^M$ .

**Lemma 5.5.4**

The sequence  $(u^n)$  converges strongly to some  $u$  in  $\mathcal{V}$ .

**Proof.**

From the previous estimates, we have  $(u^n)$  is bounded in  $\mathcal{V}$  and  $(\partial_t u^n)$  is bounded in  $\mathcal{V}^* + L^1(Q_T)^M$ .

Thanks to the compactness result of Lemma 5.2.2, we can extract a subsequence of  $(u^n)$  still denoted by  $(u^n)$  such that

- $(u^n) \rightarrow u$  strongly in  $L^{p^-}(0, T; L^{p(x)}(\Omega))$  and a.e. in  $Q_T$ ,
- $(u^n) \rightharpoonup u$  weakly in  $\mathcal{V}$

Since  $(u^n)$  belongs to  $L^\infty(Q_T)$ , we can use the same reasoning as in [135, 139] to obtain  $\nabla u^n \rightarrow \nabla u$  a.e. in  $Q_T$ . As a consequence, we have

$$A_i(t, x, \nabla u_i^n) \rightharpoonup A_i(t, x, \nabla u_i) \text{ weakly in } L^{p_i(x)}(Q_T)$$

We shall show that  $(u^n)$  converges strongly in  $\mathcal{V}$ . To do this, we use the difference between the equations satisfied by  $(u^n)$  and  $(u^m)$ , respectively. We have for all  $i = 1, 2, \dots, M$ .

$$\partial_t (u_i^n - u_i^m) - \operatorname{div}(A_i(\nabla u_i^n)) + \operatorname{div}(A_i(\nabla u_i^m)) = f_i^n(u^n, \nabla u^n) - f_i^m(u^m, \nabla u^m).$$

By choosing  $\theta(u_i^n - u_i^m)$  as a test function in the weak formulation of the latter equation, we obtain

$$\begin{aligned} \int_0^T \langle \partial_t (u_i^n - u_i^m), \theta(u_i^n - u_i^m) \rangle + \int_{Q_T} (A_i(\nabla u_i^n) - A_i(\nabla u_i^m)) \cdot \nabla (u_i^n - u_i^m) \theta'(u_i^n - u_i^m) \\ = \int_{Q_T} \left( f_i^n(u^n, \nabla u^n) - f_i^m(u^m, \nabla u^m) \right) \theta(u_i^n - u_i^m). \end{aligned}$$

Using the growth condition (5.39), we obtain

$$\begin{aligned} \int_{\Omega} \Theta(u_i^n(T) - u_i^m(T)) + \int_{Q_T} (A_i(\nabla u_i^n) - A_i(\nabla u_i^m)) \cdot \nabla (u_i^n - u_i^m) \theta'(u_i^n - u_i^m) \\ \leq C_i(\|w\|_\infty) \int_{Q_T} (B_i(t, x) + |\nabla u_i^n|^{p_i(x)} + |\nabla u_i^m|^{p_i(x)}) |\theta(u_i^n - u_i^m)|. \end{aligned}$$

Since  $\Theta$  is positive we get by using the coercivity condition (5.4)

$$\begin{aligned}
 & \int_{Q_T} (A_i(\nabla u_i^n) - A_i(\nabla u_i^m)) \cdot \nabla (u_i^n - u_i^m) \theta'(u_i^n - u_i^m) \\
 & \leq C(\|w\|_\infty) \int_{Q_T} B_i(t, x) |\theta(u_i^n - u_i^m)| \\
 & \quad + \frac{C(\|w\|_\infty)}{d_i} \int_{Q_T} A_i(\nabla u_i^n) \cdot \nabla u_i^n |\theta(u_i^n - u_i^m)| \\
 & \quad + \frac{C(\|w\|_\infty)}{d_i} \int_{Q_T} A_i(\nabla u_i^m) \cdot \nabla u_i^m |\theta(u_i^n - u_i^m)| \\
 & \leq C(\|w\|_\infty) \int_{Q_T} B_i(t, x) |\theta(u_i^n - u_i^m)| \\
 & \quad + \frac{C(\|w\|_\infty)}{d_i} \int_{Q_T} A_i(\nabla u_i^n) \cdot \nabla (u_i^n - u_i^m) |\theta(u_i^n - u_i^m)| \\
 & \quad + \frac{C(\|w\|_\infty)}{d_i} \int_{Q_T} A_i(\nabla u_i^n) \cdot \nabla u_i^m |\theta(u_i^n - u_i^m)| \\
 & \quad + \frac{C(\|w\|_\infty)}{d_i} \int_{Q_T} A_i(\nabla u_i^m) \cdot \nabla u_i^n |\theta(u_i^n - u_i^m)| \\
 & \quad - \frac{C(\|w\|_\infty)}{d_i} \int_{Q_T} A_i(\nabla u_i^m) \cdot \nabla (u_i^n - u_i^m) |\theta(u_i^n - u_i^m)|.
 \end{aligned}$$

It follows that,

$$\begin{aligned}
 & \frac{1}{d_i} \int_{Q_T} \left( d_i \theta'(u_i^n - u_i^m) - C(\|w\|_\infty) |\theta(u_i^n - u_i^m)| \right) (A_i(\nabla u_i^n) - A_i(\nabla u_i^m)) \cdot \nabla (u_i^n - u_i^m) \\
 & \leq C(\|w\|_\infty) \int_{Q_T} B_i(t, x) |\theta(u_i^n - u_i^m)| \\
 & \quad + \frac{C(\|w\|_\infty)}{d_i} \int_{Q_T} A_i(\nabla u_i^n) \cdot \nabla u_i^m |\theta(u_i^n - u_i^m)| \\
 & \quad + \frac{C(\|w\|_\infty)}{d_i} \int_{Q_T} A_i(\nabla u_i^m) \cdot \nabla u_i^n |\theta(u_i^n - u_i^m)|.
 \end{aligned}$$

We choose the constant  $\eta \geq \max_{i \in \{1, \dots, M\}} \left\{ \frac{C(\|w\|_\infty)^2}{4d_i^2} \right\}$  in the Lemma 5.5.2, one has

$$\begin{aligned}
 & \frac{1}{2} \int_{Q_T} (A_i(\nabla u_i^n) - A_i(\nabla u_i^m)) \cdot \nabla (u_i^n - u_i^m) \leq C(\|w\|_\infty) \int_{Q_T} B_i(t, x) |\theta(u_i^n - u_i^m)| \\
 & \quad + \frac{C(\|w\|_\infty)}{d_i} \int_{Q_T} A_i(\nabla u_i^n) \cdot \nabla u_i^m |\theta(u_i^n - u_i^m)| \tag{5.53} \\
 & \quad + \frac{C(\|w\|_\infty)}{d_i} \int_{Q_T} A_i(\nabla u_i^m) \cdot \nabla u_i^n |\theta(u_i^n - u_i^m)|.
 \end{aligned}$$

Using the almost everywhere convergence of  $(\nabla u_i^n)$  in  $Q_T$ , the weak convergence of  $A_i(\nabla u_i^n)$  in  $L^{p_i(x)}(Q_T)$

and with the help of Fatou's Lemma we can pass to the limit when  $m$  tends to  $+\infty$  in (5.53) to obtain

$$\begin{aligned} \frac{1}{2} \int_{Q_T} (A_i(\nabla u_i^n) - A_i(\nabla u_i)) \cdot \nabla (u_i^n - u_i) &\leq C(\|w\|_\infty) \int_{Q_T} B_i(t, x) |\theta(u_i^n - u_i)| \\ &+ \frac{C(\|w\|_\infty)}{d_i} \int_{Q_T} A_i(\nabla u_i^n) \cdot \nabla u_i |\theta(u_i^n - u_i)| \\ &+ \frac{C(\|w\|_\infty)}{d_i} \int_{Q_T} A_i(\nabla u_i) \cdot \nabla u_i^n |\theta(u_i^n - u_i)| \end{aligned}$$

On the other hand, from (5.2), (5.52), (5.46) and by applying Lebesgue Theorem, we pass to the limit when  $n$  tends to  $+\infty$  to obtain

$$\lim_{n \rightarrow \infty} \int_{Q_T} (A_i(\nabla u_i^n) - A_i(\nabla u_i)) \cdot \nabla (u_i^n - u_i) \leq 0$$

Hence, we can deduce as in the Lemma 5 of [27], that

$$\nabla u^n \rightarrow \nabla u \text{ strongly in } L^{p(x)}(Q_T)^M.$$

### 5.5.3 Passing to the limit

The goal of this subsection is to prove that the limit of the sequence  $u^n$  is a weak solution of the system (5.1) in the sense of the definition 5.2.1. According to Lemma 5.5.4 we conclude the existence of a subsequence, still denoted by  $(u^n)$  for simplicity, such that

$$\begin{aligned} \nabla u^n &\rightarrow \nabla u \text{ strongly in } L^{p(x)}(Q_T)^M \text{ and a.e. in } Q_T \\ u^n &\rightarrow u \text{ strongly in } L^{p^-}(0, T; L^{p(x)}(\Omega)) \text{ and a.e. in } Q_T \\ A_i(t, x, \nabla u_i^n) &\rightarrow A_i(t, x, \nabla u_i) \text{ strongly in } L^{p_i'(x)}(Q_T) \text{ and a.e. in } Q_T \\ f_i^n(t, x, u^n, \nabla u^n) &\rightarrow f_i(t, x, u, \nabla u) \text{ a.e. in } Q_T. \end{aligned}$$

It remains to prove that

$$f_i^n(t, x, u^n, \nabla u^n) \rightarrow f_i(t, x, u, \nabla u) \text{ strongly in } L^1(Q_T).$$

To do this, it suffices to prove that  $f_i^n(t, x, u^n, \nabla u^n)$  is equi-integrable in  $L^1(Q_T)$  namely

$$\forall \varepsilon > 0, \exists \delta > 0, \forall E \subset Q_T, \text{ if } |E| < \delta \text{ then } \int_E |f_i^n(t, x, u^n, \nabla u^n)| dx dt \leq \varepsilon.$$

Let  $E$  be a measurable subset of  $Q_T$  and  $\varepsilon > 0$ , using the growth assumption (5.39) and (5.46), we have for all  $i = 1, 2, \dots, M$

$$\int_E |f_i^n(t, x, u^n, \nabla u^n)| \leq \int_E C_i(\|w\|_\infty) \left( B_i(t, x) + |\nabla u_i^n|^{p_i(x)} \right). \quad (5.54)$$

Since  $B_i \in L^1(Q_T)$  then  $B_i$  is equi-integrable in  $L^1(Q_T)$  and therefore there exists  $\delta_1 > 0$ , such that, if  $|E| \leq \delta_1$ , we have

$$C_i(\|w\|_\infty) \int_E B_i(t, x) \leq \frac{\varepsilon}{2}.$$

On the other hand, we deduce from Lemma 5.5.4 that  $\left( |\nabla u_i^n|^{p_i(x)} \right)$  is equi-integrable in  $L^1(Q_T)$ , which implies the existence of  $\delta_2 > 0$ , such that, if  $|E| \leq \delta_2$ , we have

$$C_i(\|w\|_\infty) \int_E |\nabla u_i^n|^{p_i(x)} \leq \frac{\varepsilon}{2}.$$

Finally, by choosing  $\delta^* = \inf(\delta_1, \delta_2)$ , if  $|E| \leq \delta^*$ , we obtain

$$\int_E |f_i^n(t, x, u_n, \nabla u_n)| \leq \varepsilon,$$

this finishes the proof of Theorem 5.5.1.

**Part 3: Spherical Harmonics:**  
**Application to Image**  
**Processing**

# Spherical Harmonics

## 6.0.4 Introduction

In mathematics, spherical harmonics are particular harmonic functions defined as the eigenfunctions of the angular part of the Laplacian in three dimensions. Spherical harmonics are a set of functions used to represent functions on the surface of the sphere  $S^2$ . They are a higher-dimensional analogy of Fourier series, which form a complete basis for the set of periodic functions of a single variable (functions on the circle  $S^1$ ). They are particularly useful for solving rotational invariant problems and representing solutions to partial differential equations in which the Laplacian appears. they are also particularly important for representing physical quantities

Spherical harmonic decomposition can be applied to non-spherical domains using spherical parametrization. This is used in particular for 3D shapes described by triangular meshes. Common methods for computing spherical harmonics representation of spherical functions, often samples these functions on a regular 2D or 3D grid surrounding the sphere. Then, an algorithm is applied on this regular grid to evaluate the coefficients of the spherical harmonics. In this chapter, we will study in details the spherical harmonic decomposition. We will present the basics of the spherical coordinate system as well as spherical harmonics. Then we will show how the spherical functions are decomposed on the spherical harmonic basis.

## 6.1 Spherical harmonics on $S^1$

In this section, we discuss spherical harmonics in the circle  $S^1$ . Then on the sphere  $S^2$ . Spherical harmonics are not only important for theoretical reasons, they have interesting practical applications in computer

graphics and computer vision.

Fourier series was invented by Joseph Fourier (1768-1830) in order to solve heat equation[80]. Using them, every square-integrable periodic function  $f$  (of period  $2\pi$ ) can be uniquely expressed as the sum of a power series of the form

$$f(\theta) = a_0 + \sum_{k=1}^{\infty} (a_k \cos k\theta + b_k \sin k\theta),$$

where the Fourier coefficients,  $a_k$  and  $b_k$  of  $f$  are given by the expression

$$a_0 = \frac{1}{2\pi} \int_{-\pi}^{\pi} f(\theta) d\theta, a_k = \frac{1}{\pi} \int_{-\pi}^{\pi} f(\theta) \cos k\theta d\theta, b_k = \frac{1}{\pi} \int_{-\pi}^{\pi} f(\theta) \sin k\theta d\theta,$$

for  $k \geq 1$ .

These remarkable series has many theoretical and practical applications in physics, signal processing, engineering, etc. Fourier series can be described in a more conceptual way if we introduce the following inner product on square-integrable functions

$$\langle f, g \rangle = \int_{-\pi}^{\pi} f(\theta) g(\theta) d\theta.$$

This can also be noted by

$$\langle f, g \rangle = \int_{S^1} f(\theta) g(\theta) d\theta$$

where  $S^1$  represents the unit circle. Any periodic function (of period  $2\pi$ ) can be represented as functions on the circle. Using this inner product, the space  $L^2(S^1)$  is a complete normed vector space, which is, a Hilbert space. Also, if we define the subspaces,  $\mathcal{H}_k(S^1)$ , of  $L^2(S^1)$ , in order that  $\mathcal{H}_0(S^1)(= \mathbb{R})$  is the set of constant functions and  $\mathcal{H}_k(S^1)$  is the space of 2-dimension generated by the functions  $\cos k\theta$  and  $\sin k\theta$ , which gives a Hilbert sum decomposition

$$L^2(S^1) = \bigoplus_{k=1}^{\infty} \mathcal{H}_k(S^1),$$

in pairwise orthogonal subspaces, where  $\cup_{k=1}^{\infty} \mathcal{H}_k(S^1)$  is dense in  $L^2(S^1)$ . The functions  $\cos k\theta$  et  $\sin k\theta$  are also orthogonal in  $\mathcal{H}_k(S^1)$ .

Now the spaces,  $\mathcal{H}_k(S^1)$ , appear naturally when we look for homogeneous solutions of Laplace equation,  $\Delta f = 0$ , in  $\mathbb{R}^2$ . In short, a homogeneous function in  $\mathbb{R}^2$  is a function which can be expressed in polar

coordinates  $(r, \theta)$ , such that

$$f(r, \theta) = r^k g(\theta),$$

where  $f : \mathbb{R}^2 \rightarrow \mathbb{R}$  is a function which is at least of the class  $C^2$ . In polar coordinates  $(r, \theta)$ , where  $(x, y) = (r \cos \theta, r \sin \theta)$  and  $r > 0$ , the Laplacian is given by

$$\Delta f = \frac{1}{r} \frac{\partial}{\partial r} \left( r \frac{\partial f}{\partial r} \right) + \frac{1}{r^2} \frac{\partial^2 f}{\partial \theta^2}.$$

If  $f$  is restrict to the unit circle,  $S^1$ , the Laplacian on  $S^1$  is given by

$$\Delta_{S^1} f = \frac{\partial^2 f}{\partial \theta^2}.$$

To prove that the space  $\mathcal{H}^k(S^1)$  is the eigenspace of  $\Delta_{S^1}$  for the eigenvalue  $-k^2$ , we look for the harmonic functions  $f$  on  $\mathbb{R}^2$ , solutions of the Laplace equation,

$$\Delta f = 0.$$

Back to literature, the above equation can be solved by separation of variables. Which means that we can write  $f(r, \theta) = F(r)g(\theta)$ , where  $F(r)$  and  $g(\theta)$  are independent functions. To this end, assume that  $F(r) = r^k$ , for  $k \geq 0$ , which means that  $f$  is a homogeneous function of degree  $k$ .

$$f(tx, ty) = t^k f(x, y) \quad \text{pour tout } t > 0.$$

The Laplacian in polar coordinates, is given by

$$\begin{aligned} \Delta f &= \frac{1}{r} \frac{\partial}{\partial r} \left( r \frac{\partial r^k g(\theta)}{\partial r} \right) + \frac{1}{r^2} \frac{\partial^2 r^k g(\theta)}{\partial \theta^2} \\ &= \frac{1}{r} \frac{\partial}{\partial r} (kr^k g) + r^{k-2} \frac{\partial^2 g}{\partial \theta^2} \\ &= r^{k-2} k^2 g + r^{k-2} \frac{\partial^2 g}{\partial \theta^2} \\ &= r^{k-2} (k^2 g + \Delta_{S^1} g). \end{aligned}$$

Thus, we conclude that

$$\Delta f = 0 \quad \text{if and only if} \quad \Delta_{S^1} g = -k^2 g$$

where  $g$  is an eigenfunction of  $\Delta_{S^1}$  for the eigenvalue  $-k^2$ . Since the above equation is equivalent to the following second order differential equation

$$\frac{\partial^2 g}{\partial \theta^2} + k^2 g = 0.$$

Whose general solution is given by the following expression

$$g(\theta) = a_n \cos k\theta + b_n \sin k\theta.$$

In brief, the integers,  $0, -1, -4, -9, \dots, -k^2, \dots$  are the eigenvalues of  $\Delta_{S^1}$  and the functions  $\cos k\theta$  and  $\sin k\theta$  are eigenfunctions for the eigenvalue  $-k^2$ , with  $k \geq 0$ . Therefore, the dimension of the subspace corresponding to the eigenvalue  $-k^2$  is equal to 1 when  $k = 0$  and equal to 2 when  $k \geq 1$ .

Indeed, we can show that  $\Delta_{S^1}$  has no other eigenvalues and that the dimensions claimed for the eigenspaces are correct. Note that if we go back to the homogeneous harmonic functions,  $f(r, \theta) = r^k g(\theta)$ , we observe that this space is generated by the functions

$$u_k = r^k \cos k\theta, \quad v_k = r^k \sin k\theta.$$

Since  $(x + iy)^k = r^k (\cos k\theta + i \sin k\theta)$ ,  $\Re(x + iy)^k$  and  $\Im(x + iy)^k$  are homogeneous polynomials, then  $u_k$  and  $v_k$  are homogeneous polynomials called harmonic polynomials. As an example, here is a basic list for harmonic polynomials (with two dimensions) of degree  $k = 0, 1, 2, 3, 4$

$k = 0$	1
$k = 1$	$x, y$
$k = 2$	$x^2 - y^2, xy$
$k = 3$	$x^3 - 3xy^2, 3x^2y - y^3$
$k = 4$	$x^4 - 6x^2y^2 + y^4, x^3y - xy^3$

In summary, the Laplacian eigenfunctions on  $S^1$  are the restrictions of the harmonic polynomials on  $\mathbb{R}^2$  into  $S^1$  and we get a Hilbert decomposition sum,  $L^2(S^1) = \bigoplus_{k=0}^{\infty} \mathcal{H}_k(S^1)$ . This study can be generalized to the sphere  $S^n \subseteq \mathbb{R}^{n+1}$  for every  $n \geq 1$ .

## 6.2 Spherical harmonics on $S^2$

The contents of this section is classical and can be found in many references, Andrews et all [16](chapter 9), Sansone [119](chapter 3), Hochstadt [73] (chapter 6) and Lebedev [39]. We recommend Lebedev [39] as it is particularly clear.

As in the previous section, our goal is to find the homogeneous solutions of the Laplace equation,  $\Delta f = 0$ , but this time in  $\mathbb{R}^3$ , and show that they correspond to  $\mathcal{H}_k(S^2)$  spaces, Laplacian eigenfunctions,  $\Delta_{S^2}$ , on the sphere,

$$S^2 = \{(x, y, z) \in \mathbb{R}^3 \mid x^2 + y^2 + z^2 = 1\}.$$

Next, the space  $\mathcal{H}_k(S^2)$  will give us a Hilbert sum decomposition of the Hilbert space,  $L^2(S^2)$ , of square integrable functions on  $S^2$ . This is a generalization of the Fourier series to the sphere. The functions defined in the spaces  $\mathcal{H}_k(S^2)$  are called spherical harmonics.

The expression of the Laplacian in  $\mathbb{R}^3$  is given by

$$\Delta f = \frac{\partial^2 f}{\partial x^2} + \frac{\partial^2 f}{\partial y^2} + \frac{\partial^2 f}{\partial z^2}.$$

By using spherical coordinates

$$x = r \sin \theta \cos \varphi,$$

$$y = r \sin \theta \sin \varphi,$$

$$z = r \cos \theta,$$

where  $0 \leq \theta < \pi$ ,  $0 \leq \varphi < 2\pi$  and  $r > 0$  ( $\varphi$  is the azimuthal angle originating at the x-axis and  $\theta$  is the polar angle from the z-axis), we derive the Laplacian in spherical coordinates, we have

$$\begin{aligned} \frac{\partial}{\partial r} &= \sin \theta \cos \varphi \frac{\partial}{\partial x} + \sin \theta \sin \varphi \frac{\partial}{\partial y} + \cos \theta \frac{\partial}{\partial z} = \hat{r}, \\ \frac{\partial}{\partial \theta} &= r \left( \cos \theta \cos \varphi \frac{\partial}{\partial x} + \cos \theta \sin \varphi \frac{\partial}{\partial y} - \sin \theta \frac{\partial}{\partial z} \right) = r \hat{\theta}, \\ \frac{\partial}{\partial \varphi} &= r \left( -\sin \theta \sin \varphi \frac{\partial}{\partial x} + \sin \theta \cos \varphi \frac{\partial}{\partial y} \right) = r \hat{\varphi}. \end{aligned}$$

These base vectors are orthogonal, which gives

$$\hat{r} \cdot \hat{r} = \hat{\theta} \cdot \hat{\theta} = \hat{\varphi} \cdot \hat{\varphi} = 1,$$

and

$$\hat{r} \cdot \hat{\theta} = \hat{\theta} \cdot \hat{\varphi} = \hat{\varphi} \cdot \hat{r} = 0.$$

Then the matrix  $(g_{ij})$  is defined by

$$(g_{ij}) = \begin{pmatrix} 1 & 0 & 0 \\ 0 & r^2 & 0 \\ 0 & 0 & r^2 \sin^2 \theta \end{pmatrix},$$

where  $|g| = r^4 \sin^2 \theta$ . The inverse of  $(g_{ij})$  is defined by

$$(g^{ij}) = \begin{pmatrix} 1 & 0 & 0 \\ 0 & r^{-2} & 0 \\ 0 & 0 & r^{-2} \sin^{-2} \theta \end{pmatrix}.$$

Then the Laplacian in spherical coordinates is given by

$$\Delta f = \frac{1}{r^2} \frac{\partial}{\partial r} \left( r^2 \frac{\partial f}{\partial r} \right) + \frac{1}{r^2 \sin \theta} \frac{\partial}{\partial \theta} \left( \sin \theta \frac{\partial f}{\partial \theta} \right) + \frac{1}{r^2 \sin^2 \theta} \frac{\partial^2 f}{\partial \varphi^2}.$$

As  $(\theta, \varphi)$  are the coordinates in the sphere  $S^2$  via

$$x = r \sin \theta \cos \varphi,$$

$$y = r \sin \theta \sin \varphi,$$

$$z = r \cos \theta.$$

We see that in these coordinates, the matrix,  $(\tilde{g}_{ij})$ , over  $S^2$  is given by

$$(\tilde{g}_{ij}) = \begin{pmatrix} 1 & 0 \\ 0 & \sin^2 \theta \end{pmatrix},$$

as  $|\tilde{g}| = \sin^2 \theta$ , and the inverse of  $(\tilde{g}_{ij})$  and

$$(\tilde{g}^{ij}) = \begin{pmatrix} 1 & 0 \\ 0 & \sin^{-2} \theta \end{pmatrix},$$

which immediately gives

$$\Delta_{S^2} f = \frac{1}{\sin \theta} \frac{\partial}{\partial \theta} \left( \sin \theta \frac{\partial f}{\partial \theta} \right) + \frac{1}{\sin^2 \theta} \frac{\partial^2 f}{\partial \phi^2},$$

we have therefore verified that

$$\Delta f = \frac{1}{r^2} \frac{\partial}{\partial r} \left( r^2 \frac{\partial f}{\partial r} \right) + \frac{1}{r^2} \Delta_{S^2} f.$$

$\Delta_{S^2}$  is the Laplacian on the sphere,  $S^2$  Ref.[82](chapter 8). Now as in the previous section, we are looking for the homogeneous harmonic functions  $f(r, \theta, \phi) = r^k g(\theta, \phi)$  on  $\mathbb{R}^3$  that represent solutions of the Laplace equation

$$\Delta f = 0.$$

We obtain

$$\begin{aligned} \Delta f &= \frac{1}{r^2} \frac{\partial}{\partial r} \left( r^2 \frac{\partial r^k g(\theta)}{\partial r} \right) + \frac{1}{r^2} \Delta_{S^2} f \\ &= \frac{1}{r} \frac{\partial}{\partial r} (k r^{k+1} g) + r^{k-2} \Delta_{S^2} g \\ &= r^{k-2} k(k+1) g + r^{k-2} \Delta_{S^2} g \\ &= r^{k-2} (k(k+1) g + \Delta_{S^2} g). \end{aligned}$$

Thus,

$$\Delta f = 0 \quad \text{if and only if} \quad \Delta_{S^2} g = -k(k+1)g.$$

That means that  $g$  is an eigenfunction of  $\Delta_{S^2}$  for the eigenvalue  $-k(k+1)$ . Therefore, we can look for solutions of the above equation using the variable separation method. Let  $g(\theta, \varphi) = \Theta(\theta)\Phi(\varphi)$ , then we get

$$\frac{\Phi}{\sin \theta} \frac{\partial}{\partial \theta} \left( \sin \theta \frac{\partial \Theta}{\partial \theta} \right) + \frac{\Theta}{\sin^2 \theta} \frac{\partial^2 \Phi}{\partial \varphi^2} = -k(k+1)\Theta\Phi.$$

By dividing by  $\Theta\Phi$  and multiplying by  $\sin^2 \theta$  we get

$$\frac{\sin \theta}{\Theta} \frac{\partial}{\partial \theta} \left( \sin \theta \frac{\partial \Theta}{\partial \theta} \right) + k(k+1) \sin^2 \theta = -\frac{1}{\Phi} \frac{\partial^2 \Phi}{\partial \varphi^2}.$$

Since  $\Theta$  and  $\Phi$  are independent functions, the above result is possible only if both sides are equal to a constant,  $\mu$ . This leads to two equations

$$\frac{\partial^2 \Phi}{\partial \varphi^2} + \mu \Phi = 0,$$

$$\frac{\sin \theta}{\Theta} \frac{\partial}{\partial \theta} \left( \sin \theta \frac{\partial \Theta}{\partial \theta} \right) + k(k+1) \sin^2 \theta - \mu = 0.$$

However, we want  $\Phi$  to be periodic in  $\varphi$  since we are considering functions on  $S^2$ , to this end we must have  $\mu = m^2$ , where  $m$  is a positive integer. Therefore the space of solutions of the following equation

$$\frac{\partial^2 \Phi}{\partial \varphi^2} + m^2 \Phi = 0,$$

is two-dimensional and generated by the following two functions

$$\Phi(\varphi) = \cos m\varphi, \quad \Phi(\varphi) = \sin m\varphi.$$

But we still have to solve the equation

$$\sin \theta \frac{\partial}{\partial \theta} \left( \sin \theta \frac{\partial \Theta}{\partial \theta} \right) + (k(k+1) \sin^2 \theta - m^2) \Theta = 0.$$

Which is equivalent to a variant of Legendre's equation as follows

$$\sin^2 \theta \Theta'' + \sin \theta \cos \theta \Theta' + (k(k+1) \sin^2 \theta - m^2) \Theta = 0.$$

Using the variable change  $t = \cos \theta$ , and by considering the function,  $u$ , given by  $u(\cos \theta) = \Theta(\theta)$  (remember that  $0 \leq \theta \leq \pi$ ), we get the following second order differential equation, sometimes called the general Legendre equation

$$(1-t^2)u'' - 2tu' + \left(k(k+1) - \frac{m^2}{1-t^2}\right)u = 0.$$

To solving this equation we have to make substitution [82]( chapter 7, Section 7.12), let

$$u(t) = (1-t^2)^{\frac{m}{2}} v(t),$$

Then, we get

$$(1 - t^2)v'' - 2(m + 1)tv' + (k(k + 1) - m(m + 1))v = 0.$$

When  $m = 0$  we obtain the Legendre equation

$$(1 - t^2)v'' - 2tv' + k(k + 1)v = 0.$$

This equation has two fundamental solutions,  $P_k(t)$  and  $Q_k(t)$ , called the Legendre functions of the first and second types.  $P_k(t)$  are polynomials and  $Q_k(t)$  are given by power series of which diverge for  $t = 1$ , that's why we only keep the Legendre polynomials,  $P_k(t)$ . Legendre polynomials are defined by Rodriguez formula

$$P_n(t) = \frac{1}{2^n n!} \frac{d^n}{dt^n} (t^2 - 1)^n.$$

As they can be defined in various ways, this version of Legendre polynomials, they are normalized so that  $P_n(1) = 1$ . They also verifies the following recurrence relation:

$$P_0 = 1,$$

$$P_1 = t,$$

$$(n + 1)P_{n+1} = (2n + 1)tP_n - nP_{n-1} \quad n \geq 1.$$

For example, the first six Legendre polynomials are given by [82] (chapter 4, section 4.3)

$$\begin{aligned} &1 \\ &t \\ &\frac{1}{2}(3t^2 - 1) \\ &\frac{1}{2}(5t^3 - 3t) \\ &\frac{1}{8}(35t^4 - 30t^2 + 3) \\ &\frac{1}{8}(63t^5 - 70t^3 + 15t). \end{aligned}$$

Now back to our differential equation

$$(1 - t^2)v'' - 2(m + 1)tv' + (k(k + 1) - m(m + 1))v = 0. \tag{6.1}$$

Observe that if we drift with respect to  $t$ , we obtain the equation

$$(1 - t^2)v''' - 2(m + 2)tv'' + (k(k + 1) - m(m + 1)(m + 2))v' = 0.$$

This shows that, if  $v$  is a solution of our equation (6.1) for given  $k$  and  $m$ , then  $v'$  is a solution of the same equation for  $k$  and  $m + 1$ . Thus, if  $P_k(t)$  allows to solve (6.1) for given  $k$  and  $m = 0$ , then  $P'_k(t)$  allows to solve (6.1) for the same  $k$  and  $m = 1$ ,  $P''_k(t)$  solves (6.1) for the same  $k$  and  $m = 2$ , then in general,  $\frac{d^m}{dt^m}(P_k(t))$  solves (6.1) for  $k$  and  $m$ . Hence, our original equation

$$(1 - t^2)u'' - 2tu' + (k(k + 1) - \frac{m^2}{1 - t^2})u = 0. \quad (6.2)$$

has the solution of the form

$$u(t) = (1 - t^2)^{\frac{m}{2}} \frac{d^m}{dt^m}(P_k(t)).$$

The function  $u(t)$  is generally denoted by  $P_k^m(t)$  and called the associated Legendre function, [82](chapter 7, Section 7.12). The index  $k$  is often called the band index. Indeed,  $P_k^m(t) \equiv 0$  if  $m > k$  and  $P_k^0(t) = P_k(t)$ , the Legendre polynomial of degree  $k$ . An associated Legendre function is not a polynomial in general and because of the factor  $(1 - t^2)^{\frac{m}{2}}$ , it is defined only in the closed interval  $[-1, 1]$ .

Some authors add the factor  $(-1)^m$  to the expression of the associated Legendre function  $P_k^m(t)$ , as in [82](chapter 7, Section 7.12). In the literature of quantum mechanics this seems to be common practice where it is called the phase factor Condon Shortley

The associated Legendre functions satisfy various recurrence relations which allows there computations. For example, for  $m \geq 0$  fixed, we have [82](chapter 7, Section 7.12) the following recurrence

$$(k - m + 1)P_{k+1}^m(t) = (2k + 1)tP_k^m(t) - (k + m)P_{k-1}^m(t) \quad k \geq 1,$$

for  $k \geq 2$  we have

$$P_k^{m+2}(t) = \frac{2(m + 1)t}{(t^2 - 1)^{\frac{1}{2}}} P_k^{m+1}(t) - (k - m)(k + m + 1)P_k^m(t), \quad 0 \leq m \leq k - 2,$$

which can also be used to compute  $P_k^m$  starting from

$$P_k^0(t) = P_k(t),$$

$$P_k^1(t) = \frac{kt}{(t^2 - 1)^{\frac{1}{2}}} P_k(t) - \frac{k}{(t^2 - 1)^{\frac{1}{2}}} P_{k-1}(t).$$

Note that the recurrence relation for fixed  $m$  gives the following equation for  $k = m$  (Since  $P_{m-1}^m = 0$ ):

$$P_{m+1}^m(t) = (2m + 1)tP_m^m.$$

It is also easy to see that

$$P_m^m(t) = \frac{(2m)!}{2^m m!} (1 - t^2)^{\frac{m}{2}}.$$

Observe that

$$\frac{(2m)!}{2^m m!} = (2m - 1)(2m - 3) \dots 5.3.1,$$

this expression sometimes denoted  $(2m - 1)!!$  and called the double factorial.

Some papers in computer graphics adopt the definition of Legendre functions associated with the scale factor  $(-1)^m$  added, for example, [68]. The above equation allows us to "lift"  $P_m^m$  to the highest band  $m + 1$ . The graphical computer community [68] uses the following three steps to compute  $P_k^m(t)$  where  $0 \leq m \leq k$ :

1 Compute

$$P_m^m(t) = \frac{(2m)!}{2^m m!} (1 - t^2)^{\frac{m}{2}}.$$

If  $m = k$ , stop. Otherwise, do step 2

2 Compute

$$P_{m+1}^m(t) = (2m + 1)tP_m^m(t).$$

If  $k = m + 1$  Stop. Otherwise, do step 3:

3 From  $i = m + 1$ , Compute

$$(i - m + 1)P_{i+1}^m(t) = (2i + 1)tP_i^m(t) - (i + m)P_{i+m}^m(t),$$

until  $i+1=k$ .

we recall that the equation (6.2) was obtained from the following equation

$$\sin^2 \theta \Theta'' + \sin \theta \cos \theta \Theta' + (k(k + 1) \sin^2 \theta - m^2) \Theta = 0.$$

Using  $u(\cos \theta) = \Theta(\theta)$ , we get

$$\Theta(\theta) = P_k^m(\cos \theta),$$

which is a solution for the above equation. By bringing everything together, as  $f(r, \theta, \varphi) = r^k \Theta(\theta)\Phi(\varphi)$ , we proved that the homogeneous functions

$$f(r, \theta, \varphi) = r^k \cos(m\varphi)P_k^m(\cos \theta), \quad f(r, \theta, \varphi) = r^k \sin(m\varphi)P_k^m(\cos \theta),$$

are solutions of the Laplacian  $\Delta$ , in  $\mathbb{R}^3$ , and that the functions

$$\cos(m\varphi)P_k^m(\cos \theta), \quad \sin(m\varphi)P_k^m(\cos \theta),$$

are Laplacian  $\Delta_{S^2}$  eigenfunctions on the sphere  $S^2$  for the eigenvalue  $-k(k+1)$ . For fixed  $k$ , as  $0 \leq m \leq k$ , we obtain  $2k+1$  linearly independent functions.

The notation of the above functions varies a bit mainly due to the choice normalization factors used in various fields (such as physics, quantum mechanics, magnetism, seismology, geodesy, spectral analysis, etc.). In this study we will adopt the notation  $Y_l^m$ , where  $l$  is a positive integer, but  $m$  is allowed to be negative, with  $-l \leq m \leq l$ . Then, we set

$$Y_l^m(\theta, \varphi) = \begin{cases} N_l^0 P_l(\cos \theta) & \text{si } m = 0, \\ \sqrt{2} N_l^m \cos m\varphi P_l^m(\cos \varphi) & \text{si } m > 0, \\ \sqrt{2} N_l^m \sin(-m\varphi) P_l^m(\cos \varphi) & \text{si } m < 0, \end{cases} \quad (6.3)$$

for  $l = 0, 1, 2, \dots$ , And where the endpoint  $N_l^m$  are normalization functions. In physics and computer graphics,  $N_l^m$  are chosen to be

$$N_l^m = \sqrt{\frac{(2l+1)(l-|m|)!}{4\pi(l+|m|)!}}.$$

$Y_l^m$  are called the real spherical harmonics of degree  $l$  and order  $m$ ,  $l$  is called the index of the band 6.2.

The functions,  $Y_l^m$ , have very nice properties, in order to explain them we have to recall the structure of Hilbert space with the space,  $L^2(S^2)$ , of square integrable functions on the sphere  $S^2$ .

Recall that, the inner product on  $L^2(S^2)$  is given by

$$\langle f, g \rangle = \int_{S^2} f g \Omega_2 = \int_0^{2\pi} \int_0^\pi f(\theta, \varphi) g(\theta, \varphi) \sin \theta d\theta d\varphi,$$

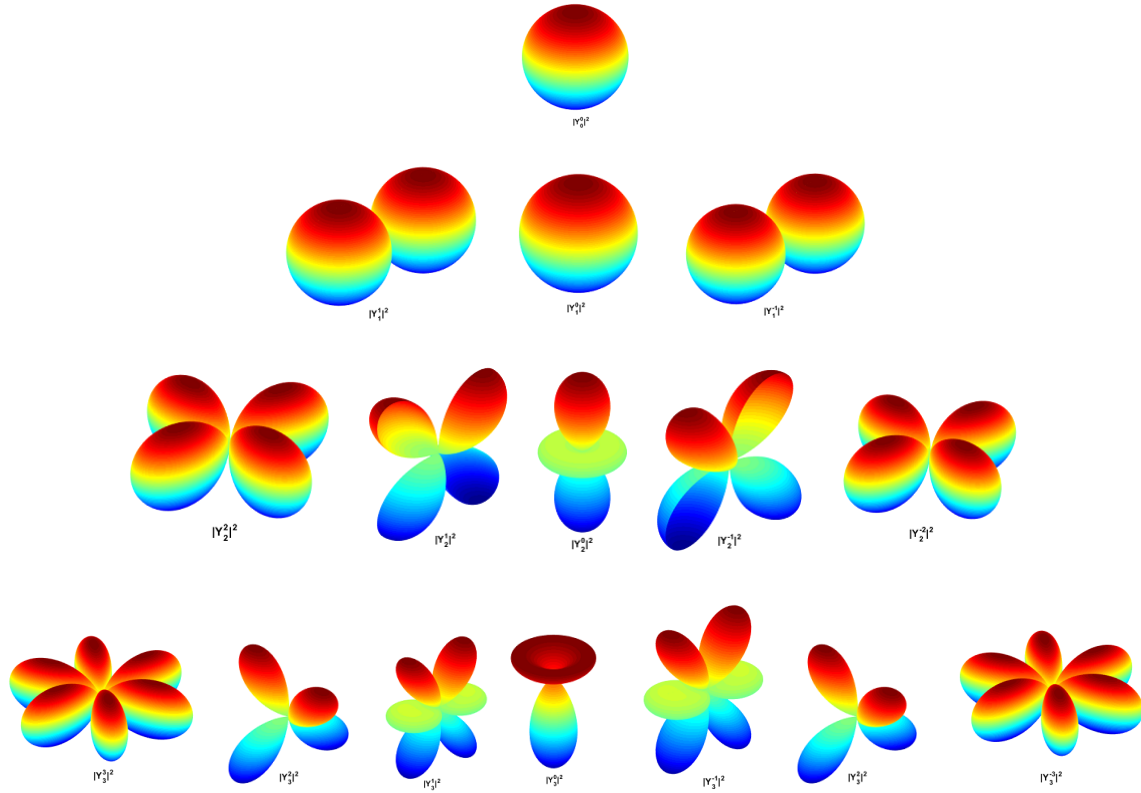


Figure 6.1: 3D representation of the modulus of the  $Y_l^m$  first terms.

where  $f, g \in L^2(S^2)$  and  $\Omega_2$  is the volume form on  $S^2$  (induced by the metric in  $\mathbb{R}^3$ ), with this inner product,  $L^2(S^2)$  is a full normalized vector space using the norm  $\|f\| = \sqrt{\langle f, f \rangle}$  associate with the inner product such that  $L^2(S^2)$  is a Hilbert space. We can also show that the Laplacian  $\Delta_{S^2}$  on the sphere is an self-adjoint linear operator with respect to this inner product. Since the functions  $Y_{l_1}^{m_1}$  and  $Y_{l_2}^{m_2}$  where  $l_1 \neq l_2$  are eigenfunctions corresponding to distinct eigenvalues  $(-l_1(l_1 + 1))$  and  $(-l_2(l_2 + 1))$ , they are orthogonal such that

$$\langle Y_{l_1}^{m_1}, Y_{l_2}^{m_2} \rangle = 0 \quad \text{si } l_1 \neq l_2.$$

It is also easy to show that for the fixed  $l$

$$\langle Y_{l_1}^{m_1}, Y_{l_2}^{m_2} \rangle = \delta_{m_1, m_2},$$

Where  $Y_l^m$  with  $-l \leq m \leq l$  form an orthonormal basis. We denote by  $\mathcal{H}_l(S^2)$  the space of dimension  $(2l + 1)$  generated by these functions. It turns out that  $Y_l^m$  form a basis of the eigenspace  $E_l$  of  $\Delta_{S^2}$  associated with the eigenvalue  $-l(l + 1)$  then  $E_l = \mathcal{H}_l(S^2)$  and  $\Delta_{S^2}$  has no other eigenvalue, besides the

space  $L^2(S^2)$  is an orthogonal sum of Hilbert eigenspace  $\mathcal{H}_l(S^2)$  which means  $\mathcal{H}_l(S^2)$  is

- 1) Mutually orthogonal.
- 2) Closed.
- 3) The space  $L^2(S^2)$  is a Hilbert sum  $\bigoplus_{l=0}^{infy} \mathcal{H}_l(S^2)$  that is to say for any function  $f \in L^2(S^2)$  there exists a unique sequence of spherical harmonics  $f_j \in \mathcal{H}_l(S^2)$  such as

$$f = \sum_{l=0}^{\infty} f_l,$$

see figure6.2 and the sequence  $\sum_{l=0}^{\infty} f_j$  converges to  $f$  (for  $L^2(S^2)$  norm ). Observing that each  $f_l$  is a unique linear combination,  $f_l = \sum_{m_l} a_{m_l, l} Y_l^{m_l}$ .

Therefore, 3) shows the Fourier series decomposition on the sphere  $S^2$  which generalizes the Fourier decomposition on the circle  $S^1$ . Furthermore, Fourier coefficients  $a_{m_l, l}$  can be computed using the fact that  $Y_l^m$  form an orthonormal Hilbert basis

$$a_{m_l, l} = \langle f, Y_l^m \rangle.$$

We also have the homogeneous harmonic functions  $H_l^m(r, \theta, \varphi)$  in  $\mathbb{R}^3$  given by

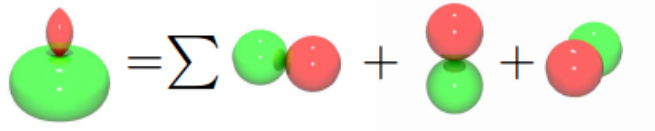


Figure 6.2: Development of a spherical function in spherical harmonics

$$H_l^m(r, \theta, \varphi) = r^l Y_l^m(\theta, \varphi).$$

Starting computing explicitly the expression of  $H_l^m$  for small values of  $l$  and  $m$ , we find that it is always possible to explain these functions in terms of Cartesian coordinates  $x, y, z$  as homogeneous polynomials. The Laplacian  $\Delta_{S^2}$  eigenfunctions and the spherical harmonics are the restrictions of the homogeneous harmonic polynomials in  $\mathbb{R}^3$  (this remarkable fact holds in general). Here is a list of the bases of homogeneous harmonic polynomials of degree  $k$  in  $\mathbb{R}$  up to  $k = 4$

$$k = 0 \quad 1$$

$$k = 1 \quad x, y, z$$

$$k = 2 \quad x^2 - y^2, x^2 - z^2, xy, xz, yz$$

$$k = 3 \quad x^3 - 3xy^2, 3x^2y - y^3, x^3 - 3xz^2, 3x^2z, -z^3, y^3 - 3yz^2, 3y^2z - z^3, xyz$$

$$k = 4 \quad x^4 - 6x^2y^2 + y^4, x^4 - 6x^2z^2 + z^4, y^4 - 6y^2z^2 + z^4, x^3y - xy^3, x^3z - xz^3, y^3z - yz^3, 3y^2z - yz^3, 3x^2yz - yz^3, 3xy^2z - xz^3, 3xyz^2 - x^3y.$$

		Spherical	Cartesian
$l = 0$	$y_0^0(\theta, \phi) =$	$\sqrt{\frac{1}{4\pi}}$	$\sqrt{\frac{1}{4\pi}}$ ,
$l = 1$	$y_1^{-1}(\theta, \phi) =$	$\sqrt{\frac{3}{4\pi}} \sin \phi \sin \theta$	$\sqrt{\frac{3}{4\pi}} x,$
	$y_1^0(\theta, \phi) =$	$\sqrt{\frac{3}{4\pi}} \cos \theta$	$\sqrt{\frac{3}{4\pi}} z,$
	$y_1^1(\theta, \phi) =$	$\sqrt{\frac{3}{4\pi}} \cos \phi \sin \theta$	$\sqrt{\frac{3}{4\pi}} y,$
$l = 2$	$y_2^{-2}(\theta, \phi) =$	$\sqrt{\frac{15}{4\pi}} \sin \phi \cos \phi \sin^2 \theta$	$\sqrt{\frac{15}{4\pi}} xy,$
	$y_2^{-1}(\theta, \phi) =$	$\sqrt{\frac{15}{4\pi}} \sin \phi \sin \theta \cos \theta$	$\sqrt{\frac{15}{4\pi}} yz,$
	$y_2^0(\theta, \phi) =$	$\sqrt{\frac{5}{16\pi}} (3 \cos^2 \theta - 1)$	$\sqrt{\frac{5}{16\pi}} (3z^2 - 1),$
	$y_2^1(\theta, \phi) =$	$\sqrt{\frac{15}{4\pi}} \cos \phi \sin \theta \cos \theta$	$\sqrt{\frac{15}{8\pi}} xz,$
	$y_2^2(\theta, \phi) =$	$\sqrt{\frac{15}{16\pi}} (\cos^2 \phi - \sin^2 \phi) \sin^2 \theta$	$\sqrt{\frac{15}{32\pi}} (x^2 - y^2).$

Figure 6.3: Analytical representation of the real part of the first spherical harmonics

## 6.3 Numerical implementation

This section is reserved for the numerical implementation in Matlab programming language to compute and visualize the spherical harmonics for a fixed degree  $L$  and a discretization of longitude  $\theta$  and colatitude  $\phi$  angles.

### 6.3.1 Computation of the spherical harmonics

To compute spherical harmonics we use the predefined function **Legendre** in Matlab as follows

```
Pl=legendre(L,cos(theta),'norm');
```

This instruction evaluates at the point  $\cos(\theta)$ , the normalized Legendre functions  $NP$  defined by

$$NP(L,M;X) = (-1)^M \sqrt{\frac{(L+1/2)(L-M)!}{(L+M)!}} P(L,M;X),$$

where  $P(L,M;X)$  denotes the usual Legendre function.

It should be noted that the **Legendre** function returns an object containing a superposition of  $(L+1)$  ordered matrices according to the value of the coefficient  $M$ . To extract from this latter the matrix which corresponds to the polynomial  $P(L,M;X)$  we use the following Matlab **squeeze** function

```
Plm=squeeze(Pl(M+1, :, :));
```

Finally, we evaluate the expression of the harmonics for the orders  $M$  from 0 up to  $L$  by the following instructions

```
Yp=[];
for M=0:1:L
Ylm=(-1)^M.*squeeze(Plm(M+1, :, :)).*exp(1i*M*phi);
Yp=[Yp;Ylm];
end
```

Harmonics of negative order are deduced from positive orders by the following formula

```
Yn=[];
for i=1:nyp-1
Yn=[Yn; (-1)^(L-i-1)*conj(Yp(nlt-i*nl+1:nlt-(i-1)*nl, :))];
end
```

### 6.3.2 Visualization of the spherical harmonics

To visualize the geometric shape of spherical harmonics, we first sampled the angles  $\theta$  and  $\phi$  according to a regular grid using the following instructions

```
te=linspace(0,2*pi,200);
p=linspace(0,pi,200);
[theta,phi]=meshgrid(te,p);
```

then we called the function *spherical\_harmonics* implemented previously to compute the spherical harmonics

```
Yl= spherical_harmonics(L, theta , phi );
```

finally to visualize a spherical harmonic  $Y_l^m$  we draw the map

$$[0, \pi] \times [0, 2\pi[ \longrightarrow \mathbb{R}^3$$
$$(\theta, \phi) \longrightarrow |Y_l^m(\theta, \phi)| \cdot (\cos(\phi) \sin(\theta), \sin(\phi) \sin(\theta), \cos(\theta)),$$

using the following instructions

```
xr=rr .* cos(phi) .* sin(theta);  
yr=rr .* sin(phi) .* sin(theta);  
zr=rr .* cos(theta);
```

```
f=figure;  
axis off;  
surf(xr, yr, zr);  
colormap jet;  
shading interp  
axis equal off;
```

# Application to Image Decomposition, Reconstruction and Fingerprints Identification.

## 7.0.3 Introduction

In the field of image processing and image analysis, particularly in medical imaging, the primary task is to represent the original image in a standard description. The process begins with an initial representation of the original object in a chosen coordinate system. The choice of the coordinate system in which the image is represented is based on the symmetry of the original image. The spherical coordinate system is one of the choices used to represent any object, the main topic of this chapter is to apply the tools of spherical harmonics to represent and reconstruct an image. Spherical harmonics use the orthogonality relations of its parameters to represent and process images. The image is first represented on the unit sphere it undergoes a distortion which is maximum at the level of the north and south poles, the smoothing is approximated by leaving  $0.15\pi$  empty of space at each pole. Sampling is performed for the parameters  $\theta$  and  $\phi$  and the image is represented by spherical harmonics whose coefficients are computed. The least significant values of the spherical harmonics coefficients are truncated which induces compression in the reconstructed image while keeping the memory allocation in view.

## 7.1 Spherical representation

Let  $I$  be an image of size  $N \times M$  see figure 7.1.

$$I : [0, N] \times [0, M] \longrightarrow \mathbb{R}$$

$$(i, j) \longrightarrow I(i, j),$$



Figure 7.1: The given image  $I$

In order to represent and visualize the image on the sphere we apply the transformation

$$T : [0, \pi] \times [0, 2\pi[ \longrightarrow \mathbb{R}^3$$

$$(\theta, \varphi) \longrightarrow (\sin \theta \cos \varphi, \sin \theta \sin \varphi, \cos \theta).$$

By discretizing the angles  $\theta$  and  $\varphi$  according to a regular grid such that  $\theta$  is discretized over the interval  $[0, \pi]$  and  $\varphi$  is discretized over the interval  $[0, M]$ , we get

$$I' : [0, N] \times [0, M] \longrightarrow \mathbb{R}^3 \longrightarrow \mathbb{R}$$

$$(\theta_i, \varphi_j) \longrightarrow (\sin \theta_i \cos \varphi_j, \sin \theta_i \sin \varphi_j, \cos \theta_i) \longrightarrow I'(\theta_i, \varphi_j) = T \circ I.$$

Where  $I'$  is the representation of the image  $I$  on the sphere we have therefore obtained a textured sphere see figure 7.1 The image is now represented on the sphere it is therefore decomposed on the basis of spherical harmonics as follows

$$I(\theta_i, \varphi_j) = \sum_{l=0}^{l_{max}} \sum_{m=-l}^l c_{lm} Y_l^m(\theta_i, \varphi_j). \quad (7.1)$$

## 7.2 Reconstruction

To reconstruct an image using spherical harmonics, we must first represent it on the sphere in order to be decomposed into HS (already done) then compute its coefficients and finally obtain the expression which allows the image to be reconstructed

### 7.2.1 Coefficients computation

The coefficients of the spherical harmonics are necessary for the reconstruction of the image. Once calculated, they can be used dynamically to reconstruct several versions of the original image with different degree of precision depending on the value of the degree of spherical harmonics.

The coefficients are computed by multiplying the two sides of the equality by the conjugate of the spherical harmonic. After integration over the whole domain we obtain the following expression

$$I(\theta, \varphi)Y_l^{m'}(\theta, \varphi) = \sum_{l=0}^{l_{max}} \sum_{m=-l}^l c_{lm}Y_l^m(\theta, \varphi)Y_l^{m'}(\theta, \varphi), \quad (7.2)$$

$$\int_0^{2\pi} \int_0^\pi I(\theta, \varphi)Y_l^{m'}(\theta, \varphi)d\Omega = \int_0^{2\pi} \int_0^\pi \sum_{l=0}^{l_{max}} \sum_{m=-l}^l c_{lm}Y_l^m(\theta, \varphi)Y_l^{m'}(\theta, \varphi)d\Omega,$$

where  $d\Omega = \sin(\theta)d\theta d\varphi$

$$\int_0^{2\pi} \int_0^\pi I(\theta, \varphi)Y_l^{m'}(\theta, \varphi)d\Omega = \sum_{l=0}^{l_{max}} \sum_{m=-l}^l c_{lm} \int_0^{2\pi} \int_0^\pi Y_l^m(\theta, \varphi)Y_l^{m'}(\theta, \varphi)d\Omega,$$



Figure 7.2: Image I': sphere representation of the given image I

$$c_{l',m'} = \sum_{l=0}^{\infty} \sum_{m=-l}^l c_{lm} \delta_{ll'} \delta_{mm'} = \int_0^{2\pi} \int_0^{\pi} I(\theta, \varphi) Y_{l'}^{m'}(\theta, \varphi) d\Omega,$$

we approximate the integral by a sum using one of the methods: Trapeze, Simpson, Monte-Carlo ...

A simple discretization leads to the following expression

$$\sum_{l=0}^{l_{max}} \sum_{m=-l}^l c_{lm} \delta_{ll'} \delta_{mm'} \approx \sum_{i=0}^N \sum_{j=0}^M I(\theta_i, \varphi_j) Y_{l'}^{m'}(\theta_i, \varphi_j) \sin(\theta_i) \Delta(\theta_i) \Delta(\varphi_j).$$

In the next step, the coefficients are replaced in the equation (7.1) and by choosing the harmonic set to a certain degree  $l$ , the image is reconstructed. The result for a part of the image  $I$  reconstructed for different degrees  $l$  see figure 7.2.1



Figure 7.3: Representation of one part of the image  $I$  by different degrees

## 7.3 Numerical simulations

### 7.3.1 Representation of an image on the sphere

The program below establishes a correspondence between the pixels of a given image, in this case the image "eight.tif" and the points of the sphere. the result of running this program is shown in figure ref Fig: sphere.

```
%% Original image to be constructed
I=imread('eight.tif');
```



Figure 7.4: Representation of the image I on the sphere

```
I=im2double(I(:,:,1));  
  
theta = linspace(0, pi, size(I,1));  
phi    = linspace(0, 2*pi, size(I,2));  
[phigrid , thetagrid ]=meshgrid(phi , theta );  
  
X=cos(phigrid).*sin(thetagrid);  
Y=sin(phigrid).*sin(thetagrid);  
Z=cos(thetagrid);  
  
surface(X,Y,Z,I, 'EdgeColor', 'none', 'FaceColor', 'texturemap');  
r=0:1/255:1; v=0:1/255:1; b=0:1/255:1;  
map=[r' v' b'];  
colormap(map); grid on,
```

### 7.3.2 Reconstruction

This MATLAB code allows us to reconstruct an image from a calculation of the coefficients given by the integral formula

$$c_l^m = \int_0^{2\pi} \int_0^\pi I(\theta, \varphi) Y_l^m(\theta, \varphi) d\Omega.$$

The instruction

```
Ct=[];
for i= 0:Lmax
Ct=[Ct;[ i*ones(2*i+1,1) (-i:i) ' ]];
end
```

allows to position the coefficients according to a connectivity table in the form

```
0 0
1 -1
1 0
1 1
2 -2
2 -1
2 0
2 1
2 2
. .
. .
. .
```

where the first column corresponds to the values of degree  $L$  and the second column corresponds to the order  $M$ . This table allows to relate the spherical harmonic with its respective coefficient using the row index of the connectivity table. For example: the spherical harmonic ( $L = 1, M = 1$ ) is stored in row of index 4 therefore  $c_1^1$  is stored in the fourth row of the vector of coefficients  $CLM$ . Then we compute the integral using the predefined method **trapeze**

```
ind1=find((Ct(:,1))==0)&(Ct(:,2))==0);
```

$\text{CLM}(\text{ind1}) = \text{trapz}(\text{phi}, \text{trapz}(\text{theta}, \text{I}.*\text{conj}(\text{FLM}).*\text{sin}(\text{theta grid})));$

Finally, we move on to reconstruction by performing the following operation:

$$I(\theta_i, \varphi_j) = \sum_{l=0}^{l_{\max}} \sum_{m=-l}^l c_{lm} Y_l^m(\theta_i, \varphi_j),$$

by multiplying the spherical harmonic by its coefficient  $c_l^m$  obtained as previously by the connectivity table.

## 7.4 Fingerprints identification by a shape descriptor based on spherical harmonics

A fingerprint is the pattern formed by the lines of the skin of the fingers, palms of the hands, toes or the soles of the feet. This pattern is formed during the foetal period.

There exist two types of imprints: the direct imprint (which leaves a visible mark) and the latent imprint (dirt, sweat or other residue deposited on an object). They are unique and immutable, they do absolutely not change over time (except by accident as a burn for example).

The probability of finding two similar fingerprints is  $10^{-24}$ . Twins, for example, coming from the same cell, will have very close but not alike fingerprints. Fingerprints are classified according to a very old system called the Henry system. In this system, the classification is based on the general topography

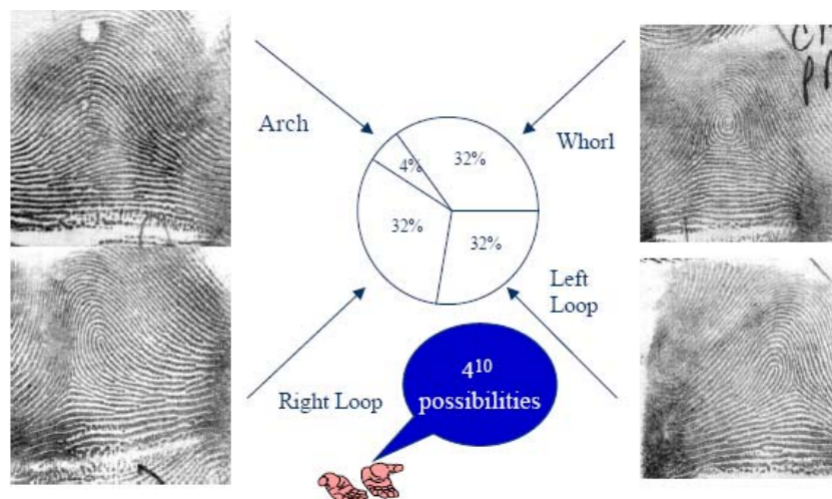


Figure 7.5: Henry Classification

of the fingerprint, it allows to define families such as loops, arches and whorls. They are composed of

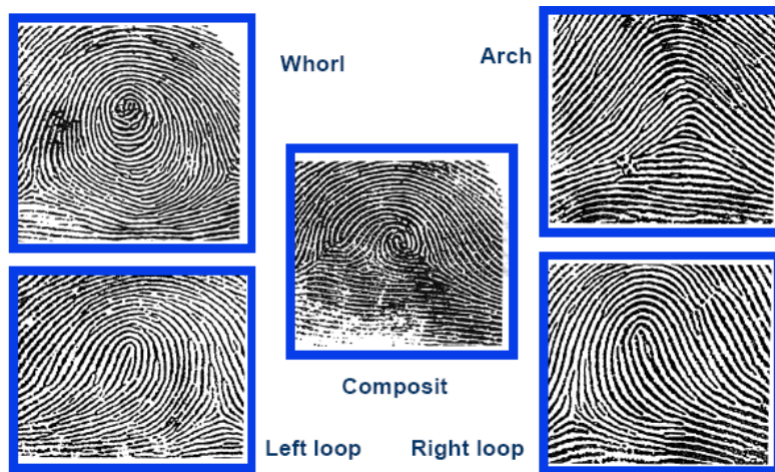


Figure 7.6: Arches, loops and whorls

endings in ridges, that is the point where the ridge ends, and bifurcations, which is, the point where the ridge divides in two.

The core is the interior point, usually located in the middle of the fingerprint. It is often used as a landmark to locate other minutiae. Other terms are also encountered: the lake, the island, the delta, the valley ...

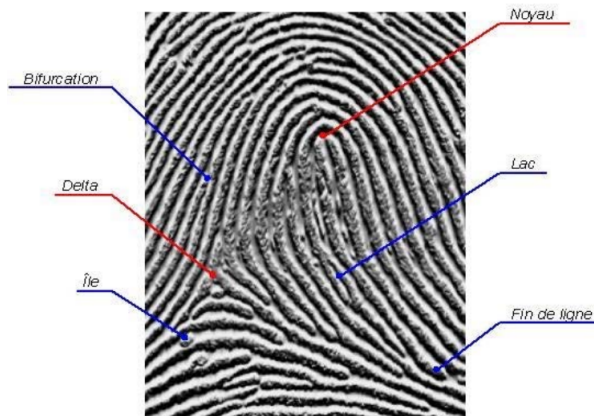


Figure 7.7: The components of a fingerprint

These fingerprints can be scanned. A complete fingerprints contains on average a hundred characteristic points but the controls are performed only from 14 points.

Statistically, it is impossible to find 2 individuals with 14 identical characteristic points, even in a population of several million people.

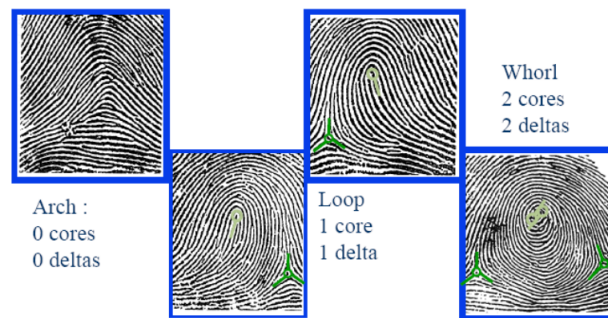


Figure 7.8: Cores and deltas

In this chapter we will first look at the functionality of fingerprint extraction, which constitutes an important component in fingerprint identification algorithms.

Next, we will introduce a shape descriptor based on spherical harmonics. Finally, numerical simulations carried out on fingerprint databases confirm that this shape descriptor is very efficient, which means, it allows to identify and even classify fingerprints.

### Extraction of the characteristic points (minutiae)

The minutiae-based methods have been used in many systems to identify fingerprints. Based mainly on a comparison model between the extracted points, these methods rely heavily on the precision of the extraction of minutiae and the detection of landmarks like kernel and delta. Wrong or missing minutiae

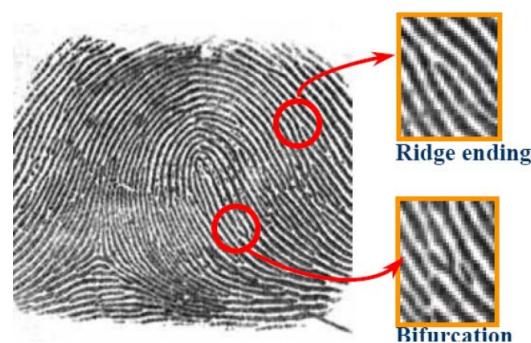


Figure 7.9: Events on an edge (minutiae)

can introduce errors in the identification of fingerprints.

Fortunately, the contextual information provided by the peak flows and the orientation of the neigh-

borhood of detected minutiae can help eliminate wrong minutiae.

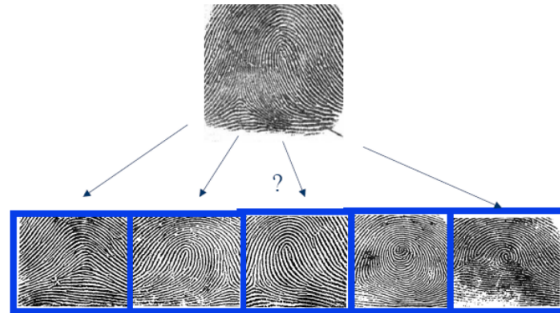


Figure 7.10: Automatic classification (pattern recognition)

### Recognition of a fingerprint

An essential component of fingerprint automatic recognition systems is the comparison module which uses fingerprint identification algorithms in order to compare a test fingerprint to another model fingerprint for identification / verification (see figure 7.4). Currently, the efficiency of fingerprint identification algorithms is a significant problem due to environmental noise. The accuracy of these algorithms depends on the image quality, the image enhancement methods, and the functionality of the extraction algorithms. Noisy characteristics introduced by environmental factors such as dust, scarring, and dryness of the skin, are highly desired to be removed or reduced to a minimum. Even very robust recognition algorithms will suffer when inaccurate extraction, for example, a high noise, poor image quality, or unwanted image enhancement effects occur. Even without having environmental noise, the deformations applied to a fingerprint do not guarantee identification due to the variability of the deformations, rotation, translation, noise effect and homothety. The deformations detected in translation, rotation, nonlinear distortion ... are obviously due to the difference in the physical location of the finger on the scanner. Figure 7.4, shows different deformations of the same finger and the notable variability in the fields mentioned. One aspect that might be more difficult to see is the nonlinear distortion, which is due to both the elasticity of the skin from the angular variability and the force of the applied pressure.

### Extraction of minutiae

Since the vast majority of fingerprint identification algorithms rely on identifying minutiae, information on minutiae is considered to be very important characteristics [17]. The two main methods of extracting

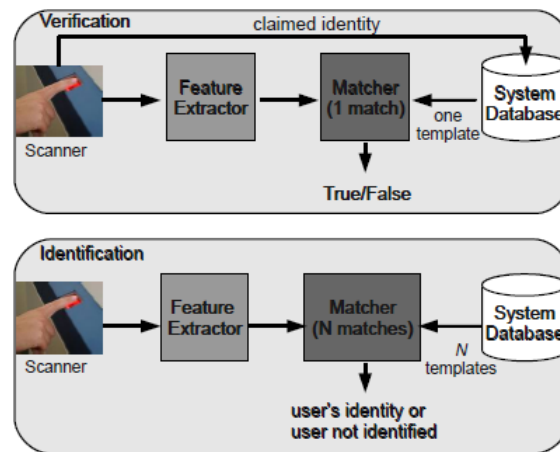


Figure 7.11: Basic model for fingerprint verification and identification process



Figure 7.12: Eight prints of the same fingerprint from the FVC2002 database (Maio et al. 2002) with differences in operations, translation, rotation and image quality.)

characteristic minutiae either require converting a gray-scale image to a binary image, or working directly on a raw image where gray-scale is enhanced. In the binary image-based method, binarization of the gray-scale image is the first step. This requires that each gray-scale pixel intensity value is transformed to a binary intensity of black (0) or white (1). The simplest approach is to apply a global threshold to each pixel and use the application.

$$I(x,y) = \begin{cases} 1 & \text{si } I(x,y) \geq t, \\ 0 & \text{sinon.} \end{cases} \quad (7.3)$$

This method is generally not sufficient as the prints may have different levels of contrast throughout the image. However, the same procedure can be applied locally at adaptive starting points. Once produced, the binary image naturally undergoes a thinning operation, where the structures are reduced to a thickness of 1 pixel, called a skeleton, in order to facilitate the detection of the characteristic points. The resulting thinned binary image analyzed at each pixel  $p$  in order to find the location of the minutiae.

$$cn(p) = \frac{1}{2} \sum_{i=1 \dots 8} |val(p_{(i \bmod 8)}) - val(p_{i-1})|. \quad (7.4)$$

Where  $val \in \{0, 1\}$  (which means, the pixel intensity value of a binary image). the location of the pixels of the minutiae can now be identified, such as for example the peak endings will have a  $cn = 1$  and the bifurcations will have a  $cn = 3$ .

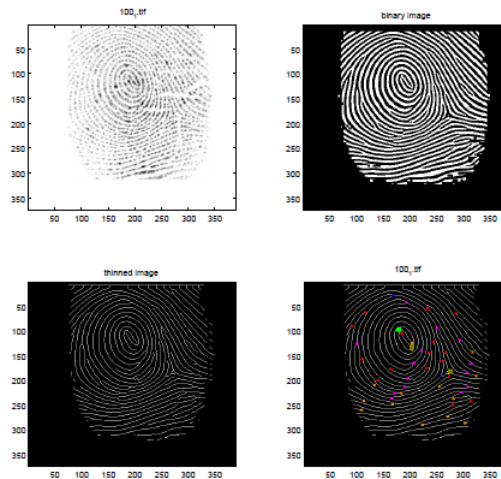


Figure 7.13: Top left: Original grayscale image. top right: the binary image. on the bottom left: the image to be thinned. on the bottom right: the image with thinned out with the core (green), delta (gold), bifurcations (blue for  $\theta \in [0^\circ - 180^\circ]$  and purple for  $\theta \in [180^\circ - 360^\circ]$ ). crest endings (orange for  $\theta \in [0^\circ - 180^\circ]$  and red for  $\theta \in [180^\circ - 360^\circ]$ ).

#### 7.4.1 Shape descriptor based on Spherical Harmonics

The oversize expansion of databases incorporating images and the extreme need to use them as decision support has brought new challenges such as image storage and retrieval. Thus, the high demand for better retrieval quality has caused a large amount of research activity around the world to improve the underlying image-based content retrieval technologies. Thus, several effective methods, based solely on

digital content, have succeeded in introducing a radical and efficient change in the field of image recovery. The digitized image is considered as a set of directly interpreted meaningless pixels. The technologies to improve based on the recovery of the images consists in analyzing these digital data in order to draw invariant or stable information which should allow the measurement of the similarity between the images. The criteria widely used in these approaches are color, texture and shape.

Shape descriptors have interesting properties and contain a lot of information about the identity of objects contained in an image. This type of descriptor is suitable for representing part of the image rather than the whole image. In fact, several works propose to use descriptors for recognition of images. In this context, some authors are inspired by the famous transformation into spherical harmonics in their design of descriptors. Spherical harmonics are effectively kept as robust 3D model descriptor.

In this part, we are inspired by spherical harmonics as they have the properties of being complete and orthogonal on the unit sphere and separable in spherical coordinates, with a complex exponential for the angular part as we saw in the first chapter. We will apply this transformation to obtain a shape descriptor which has a respectful robustness to noise. The main motivation for our work is to speed up and improve the image search process. We are therefore going to introduce a fast and robust shape descriptor which processes the shape which is based globally on these spherical harmonics and which just requires a simple preprocessing step.

## Spherical Harmonics

According to the previous chapter, spherical harmonics are defined as follows

$$Y_l^m(\theta, \phi) = N_l^m P_l^m(\cos \theta) e^{jm\phi}, \quad -l \leq m \leq l \quad \text{and} \quad l \geq 0,$$

where  $N_l^m$  is the normalization function

$$N_l^m = \sqrt{\frac{2l + l(l - m)!}{4\pi(l + m)!}}.$$

$P_l^m$  denote the associated Legendre polynomial, and  $\theta$  and  $\phi$  denote the ordinary spherical coordinates.

The spherical harmonics  $Y_l^m(\theta, \phi)$  are orthogonal and normalized functions because they satisfy the equality

$$\int_0^\pi \int_0^{2\pi} Y_l^m(\theta, \phi) Y_{l'}^{m'}(\theta, \phi)^* \sin(\theta) d\theta d\phi = \delta_{ll'} \delta_{mm'}.$$

The spherical harmonics are related by the following relation

$$Y_l^{-m}(\theta, \phi) = (-1)^m Y_l^m(\theta, \phi)^*.$$

### Spherical representation

Let  $M(x, y)$  be a point of  $\mathbb{R}^2$  which will be represented on the sphere  $S^2$  by the point  $M'(X, Y, Z)$  or

$$X = x, \tag{7.5}$$

$$Y = y, \tag{7.6}$$

$$Z = \sqrt{1 - X^2 - Y^2}. \tag{7.7}$$

We write, subsequently, the expression of X, Y and Z in spherical coordinates  $(\theta, \phi)$

$$X = \sin \theta \cos \phi, \tag{7.8}$$

$$Y = \sin \theta \sin \phi, \tag{7.9}$$

$$Z = \cos \theta. \tag{7.10}$$

This transformation will allow us to represent the image on the sphere in order to get a spherical function that can be decomposed into spherical harmonics.

Let I be a fingerprint, such that I can be decomposed in the bases of the spherical harmonics as follows

$$I(\theta, \phi) = \sum_{l=0}^{l_{max}} \sum_{m=-l}^l a_{lm} Y_l^m(\theta, \phi),$$

where  $a_{lm}$  is the spherical harmonic coefficient of degree l and order m,  $I(\theta, \phi)$  an image function defined on the unit sphere in spherical coordinates and  $Y_l^m(\theta, \phi)$  represents the spherical harmonic function

### Generation of a new region-based shape descriptor

In this part, we use the spherical harmonic functions to design an efficient region-based shape descriptor, called a shape descriptor based on spherical harmonics. The components of the characteristic vectors are obtained from a sphere according to the transformation into spherical harmonics. We present below some formulas to compute these harmonic coefficients and a vector extraction algorithm is detailed at the end

of this section.

The coefficients of harmonics  $C_l^m$  based on TSH are obtained by the following integration formula

$$C_l^m = \int_0^\pi \int_0^{2\pi} Y_l^m(\theta, \phi) I(\theta, \phi) \sin(\theta) d\theta d\phi.$$

Numerically, this formula can be calculated as the sum over all the pixels located in the unit sphere

$$C_l^m = \frac{\pi}{N} \sum_{\theta} \sum_{\phi} I(\theta, \phi) Y_l^{m*}(\theta, \phi), \quad 0 \leq \theta \leq \pi \quad \text{and} \quad 0 \leq \phi \leq 2\pi.$$

The term  $\frac{\pi}{N}$  represents the weighting coefficients of the uniform sample points used in Monte Carlo integration, where  $\pi$  represents the area of the unit disk and  $N$  is the number of stratified samples. We just take all the pixels in the sphere as samples. NB: One can use other method to calculate the coefficient numerically like the trapez method, simpson, ...

These coefficients  $C_l^m$  have complex values. In addition, the rotation of the  $I$  function results in a phase shift of these SHs. If we want an invariance of rotation, then it is necessary to combine the  $C_l^m$  so as to eliminate the dependence on  $\phi$ . The simplest solution is to take their magnitudes  $\|C_l^m\|$ .

The steps involved to extract the harmonic representation of a 3D shape are illustrated in figure 7.4.1. Our DHS descriptor is rotational invariant. In order to provide the invariance of DHS with respect to geometric transformations, some pre-steps are applied before computation of DHS.

Pretreatment:

We first proceed through pre-treatment phases which consists of

1. Represent the image on the sphere (the sphere which contains the form).
2. Resized the textured sphere to a standard scale.
3. Convert the coordinates of the pixels so that they belong to the unity sphere.
4. Decomposition of the image function (imprint) into spherical harmonics.

In order to ensure the invariance by rotation, the modulus of the corresponding coefficient  $\|C_l^m\|$  is calculated for each  $l$  and  $m$  and stored in the characteristic vector. By exploiting the symmetry relation of spherical harmonics, we can considerably reduce the size of the characteristic vector, because we only retain the  $\|C_l^m\|$  coefficients with  $0 \leq m \leq l$ , but all the terms  $\|C_l^0\|$  (with  $m = 0$ ) must be divided by 2.

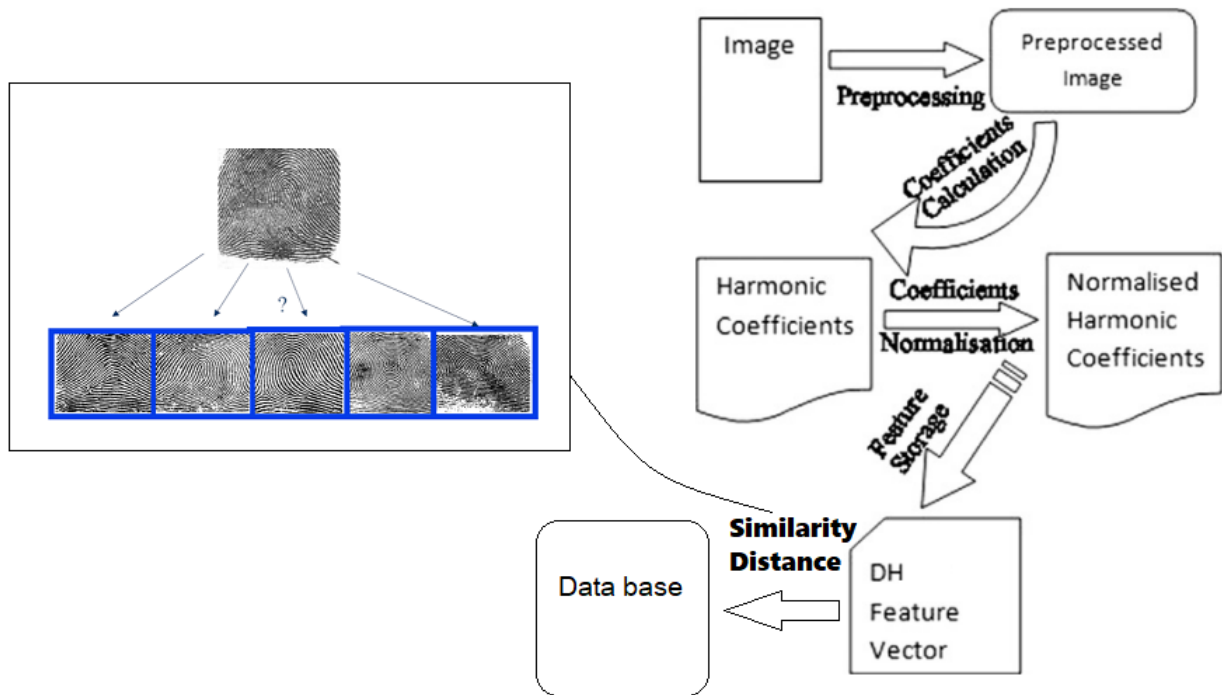


Figure 7.14: Extraction algorithm of the harmonic descriptor.

Once these steps are completed, we ensure the invariance, as well as the efficiency of our spherical harmonics descriptor.

### Coefficients Normalization

Finally, we apply the normalization of the surface by dividing the coefficients Modules  $\|C_l^m\|$  by the first coefficient  $\|C_0^0\|$ .

### Characteristic vector

The characteristic vector  $V$  take the form of a triangular matrix

$$V = \{\mathcal{V}_k / k = 1, 2, \dots, l\}.$$

where

$$\mathcal{V}_k = \frac{1}{\|C_0^0\|} \left\{ \frac{\|C_k^0\|}{2}, \|C_k^1\|, \dots, \|C_k^k\| \right\}.$$

Up to degree  $l$ , the size of the characteristic vector DFSH is equal to  $[(l+1)(l-2)/2 - 1]$ . For example, for  $L = 10$ , the dimension is equal to 65.

The measure of the dissimilarity between the two fingerprints is computed according to the norm  $L^1$ .

$$Distance(R, I) = \frac{1}{D} \sum_{k=1}^D | Discr(R)_k - Discr(I)_k |.$$

With  $Discr(I)_k$  is the  $k$ -th coefficient of the descriptor vector of our image  $I$ ,  $Discr(R)_k$  is the  $k$ -th coefficient of the descriptor vector of the image  $R$  that we want to compare to  $I$ , and  $D$  represents the characteristic vector dimension. Other types of distance measurement are also possible.

### 7.4.2 Matlab Code

#### Database

Before getting into the details of the fingerprint identification program code. We will first of all build a database composed of images of 4 people's fingerprints, each fingerprint undergoes 4 different deformations, as translation, rotation, homothety and noise effects. This database will be used to test the effectiveness of our shape descriptor established in the previous section.



Figure 7.15: Illustration of the database made up of 4 people fingerprints

### 7.4.3 Construction of the database

This MATLAB code makes it possible to calculate and store the descriptor vector associated with each image of the database. The latter include the images of the footprints of 4 people.

```
clear all; close all; clc;  
  
degre=10;  
for i=1:4  
empreintes(i).image=sprintf('personne%d.tif',i);  
empreintes(i).descripteur=get_descripteur(empreintes(i).image,degre);  
end  
save empreintes
```

or the **get\_descripteur** subroutine is used to calculate the shape descriptor vector.

### 7.4.4 Calculation of the descriptor vector

The function implemented below is used to calculate the descriptor vector defined by the expression

$$V = \{\mathcal{V}_k/k = 1, 2, \dots, l\},$$

where

$$\mathcal{V}_k = \frac{1}{\|C_0^0\|} \left\{ \frac{\|C_k^0\|}{2}, \|C_k^1\|, \dots, \|C_k^k\| \right\},$$

the code is as follows

```
function [ V ] = get_descripteur( image ,Lmax )  
  
I3=im2double(imread(image));  
I=I3(:,: ,1);  
  
theta = linspace(0, pi, size(I,1));  
phi = linspace(0, 2*pi, size(I,2));
```

```
[ phigrd , thetagrid ]=meshgrid ( phi , theta );

Ct=[];
for i=0:Lmax
Ct=[Ct;[ i*ones (2*i+1,1) (-i:i) ']];
end

% Initialisation of the SH decomposition coefficients
CLM=zeros ( size ( Ct , 1 ) , 1 );

%% Computation of normalized Legendre
% function in the case where L=0

PLM=legendre ( 0 , cos ( thetagrid ) , 'norm' );
FLM=sqrt ( 1/2/ pi ) * PLM;

%% Compute the coefficients corresponding to CT(1,:)= [ 0 0 ]

ind1=find ( ( Ct (: , 1) == 0 ) & ( Ct (: , 2) == 0 ) );

CLM(ind1)=trapz ( phi , trapz ( theta , I.*conj ( FLM ).* sin ( thetagrid ) ) );

%% Computation of normalized
%Legendre function in the case where L~=0

for L=1:Lmax
PL=legendre ( L , cos ( thetagrid ) , 'norm' ); %legendre
%fucntions for positive m
for M=0:L
```

```

PLM=squeeze (PL(M+1 ,: ,:));
FLM=((-1)^M)*sqrt (1/2/ pi)*PLM.*exp(1i*M*phigrd);

ind1=find (( Ct (: ,1)==L)&(Ct (: ,2)==M));

if (M~=0)
ind2=find (( Ct (: ,1)==L)&(Ct (: ,2)==-M));
CLM(ind2)=((-1)^M)*conj (CLM(ind1));
end
end
end

%% Reconstruction of the image
%using the previously computed coefficients CLM
PLM=legendre (0 ,cos (thetagrid) , 'norm' );
FLM=sqrt (1/2/ pi)*PLM;
IR=CLM(1)*FLM;

for L=1:Lmax
PL=legendre (L ,cos (thetagrid) , 'norm' );%legendre
% fucntions for positive m
for M=0:L
PLM=squeeze (PL(M+1 ,: ,:));
FLM=((-1)^M)*sqrt (1/2/ pi)*PLM.*exp(1i*M*phigrd);
ind=find (( Ct (: ,1)==L)&(Ct (: ,2)==M));
IR=IR+CLM(ind)*FLM;

if (M~=0)
ind2=find (( Ct (: ,1)==L)&(Ct (: ,2)==-M));
IR=IR+CLM(ind2)*((-1)^M)*conj (FLM);
end

```

```
end
end
%% computing image descriptor
a0=abs(CLM(1));

for L=1:Lmax
for M=0:L
indice=find((Ct(:,1)==L)&(Ct(:,2)==M));
if (M==0)
V(L,M+1)=abs(CLM(indice))/(2*a0);
else
V(L,M+1)=abs(CLM(indice))/(a0);
end
end
end
end
```

This program allows to identify and recognize the shape by giving it a fingerprint, and compares it with all the elements in the database in order to indicate the corresponding person.

### Fingerprint search

```
function [name] = search_empreintes( image )

load empreintes;
L=size(empreintes(1).descripteur,1);
V=get_descriptor(image,L);

for i=1:size(empreintes,2)
Coef=empreintes(i).descripteur;
dist(i)=sum(abs(Coef(:)-V(:)));
```

```
end  
[ val , ind ]=min( dist );  
name=sprintf( 'l' image identifiee est %s ' , empreintes ( ind ). image );  
end
```

We applied our program on the database illustrated in the figure 7.4.2 the preliminary results show that our descriptor is efficient. Indeed, it allows to identify all the images of the database above. In practice, to prove the robustness of our descriptor, the tests must be carried out on databases comprising at least hundreds of images and this in large applications. However, the latter require efficient material resources. This may be the subject of future work.

#### 7.4.5 Conclusion

In this part of the thesis, we have made a contribution to the field of 2D and 3D object representation using spherical harmonics. These representations have been used in two types of applications the first application is related to the decomposition and reconstruction of images and the other constitutes in fingerprints identification.

Both applications are in the field of image processing, the function representing the object is given by the pixels of the image in spherical coordinates. Given a 2D object, we focused on the computation of the coefficients of spherical harmonics performed directly on a sample of the object. In the case of the function describing the pixels of the image on the sphere we have approached two applications the first consists in using the calculated coefficients to reconstruct the image and the second this manifests in the fact of using these coefficients to generate a shape descriptor that allowed us to identify fingerprints. Subsequently, we are interested in applying this method on 3D objects.

In particular, objects of gender zero are homeomorphic to a sphere. They can therefore be parameterized on a sphere by applying a spherical parameterization algorithm. Otherwise, non-zero gender objects are first segmented into a set of zero gender sub-objects. The calculations of spherical harmonics are thus applied locally to these sub-objects. Finally, the local representations in spherical harmonics are merged within the framework of implicit surfaces for a recomposition of the object.

# Bibliography

- [1] Abkarian, M., Faivre, M., Viallat, A. (2007). Swinging of red blood cells under shear flow. *Physical review letters*, 98(18), 188302.
- [2] Abkarian, M., Viallat, A. (2008). Vesicles and red blood cells in shear flow. *Soft Matter*, 4(4), 653-657.
- [3] Abraham, J., Kwan, P., Gao, J. (2011). Fingerprint matching using a hybrid shape and orientation descriptor. *State of the art in Biometrics*, 25-56.
- [4] Abreu, D., Levant, M., Steinberg, V., Seifert, U. (2014). Fluid vesicles in flow. *Advances in colloid and interface science*, 208, 129-141.
- [5] Adalsteinsson, D., Sethian, J. A. (2003). Transport and diffusion of material quantities on propagating interfaces via level set methods. *Journal of Computational Physics*, 185(1), 271-288.
- [6] Ainseba, B. E., Bendahmane, M., Noussair, A. (2008). A reaction–diffusion system modeling predator–prey with prey-taxis. *Nonlinear Analysis: Real World Applications*, 9(5), 2086-2105.
- [7] Akagi, G., Matsuura, K. (2011). Well-posedness and large-time behaviors of solutions for a parabolic equation involving  $p(x)$ -Laplacian. In *The eighth international conference on dynamical systems and differential equations, a supplement volume of discrete and continuous dynamical systems* (pp. 22-31).
- [8] Alaa, N. (1996). Solutions faibles d'équations paraboliques quasilinéaires avec données initiales mesures. In *Annales mathématiques Blaise Pascal* (Vol. 3, No. 2, pp. 1-15).

- [9] Alaa, N., Lefraich, H. (2013). Computational simulation of a new system modelling ions electromigration through biological membranes. *Theoretical Biology and Medical Modelling*, 10(1), 51.
- [10] Alaa, N., Mounir, I. (2001). Global existence for reaction-diffusion systems with mass control and critical growth with respect to the gradient. *Journal of mathematical analysis and applications*, 253(2), 532-557.
- [11] Alaa, N. E., Pierre, M. (1993). Weak solutions of some quasilinear elliptic equations with data measures. *SIAM journal on mathematical analysis*, 24(1), 23-35.
- [12] Alaa, N. E., Zirhem, M. (2018). Bio-inspired reaction diffusion system applied to image restoration. *International Journal of Bio-Inspired Computation*, 12(2), 128-137.
- [13] Alexandrov, A. D. (1962). A characteristic property of spheres. *Annali di Matematica Pura ed Applicata*, 58(1), 303-315.
- [14] Aliziane, T., Langlais, M. (2006). Degenerate diffusive SEIR model with logistic population control. *Acta Mathematica Universitatis Comenianae. New Series*, 75(2), 185-198.
- [15] Ambrosio, L., Buttazzo, G. (1993). An optimal design problem with perimeter penalization. *Calculus of variations and partial differential equations*, 1(1), 55-69.
- [16] Andrews, G. E., Askey, R., Roy, R. (1999). *Special functions* (Vol. 71). Cambridge university press.
- [17] Antonny, B. (2011). Mechanisms of membrane curvature sensing. *Annual review of biochemistry*, 80, 101-123.
- [18] Antontsev, S. N., Shmarev, S. I. (2005). A model porous medium equation with variable exponent of nonlinearity: existence, uniqueness and localization properties of solutions. *Nonlinear Analysis: Theory, Methods and Applications*, 60(3), 515-545.
- [19] Au, T. K. K., Wan, T. Y. H. (2003). Analysis on an ODE arisen from studying the shape of a red blood cell. *Journal of mathematical analysis and applications*, 282(1), 279-295.
- [20] Axler, S., Bourdon, P., Wade, R. (2013). *Harmonic function theory* (Vol. 137). Springer Science and Business Media.

- [21] Bagchi, P., Kalluri, R. M. (2009). Dynamics of nonspherical capsules in shear flow. *Physical Review E*, 80(1), 016307.
- [22] Baumgart, T., Capraro, B. R., Zhu, C., Das, S. L. (2011). Thermodynamics and mechanics of membrane curvature generation and sensing by proteins and lipids. *Annual review of physical chemistry*, 62, 483-506.
- [23] Bendahmane, M., Saad, M. (2011). Mathematical analysis and pattern formation for a partial immune system modeling the spread of an epidemic disease. *Acta applicandae mathematicae*, 115(1), 17-42.
- [24] Bendahmane, M., Wittbold, P., Zimmermann, A. (2010). Renormalized solutions for a nonlinear parabolic equation with variable exponents and  $L^1$ -data. *Journal of Differential Equations*, 249(6), 1483-1515.
- [25] Biben, T., Farutin, A., Misbah, C. (2011). Three-dimensional vesicles under shear flow: Numerical study of dynamics and phase diagram. *Physical Review E*, 83(3), 031921.
- [26] Boccardo, L., Murat, F. (1992). Almost everywhere convergence of the gradients of solutions to elliptic and parabolic equations. *Nonlinear Analysis: Theory, Methods & Applications*, 19(6), 581-597.
- [27] Boccardo, L., Murat, F., Puel, J. P. (1988). Existence of bounded solutions for non linear elliptic unilateral problems. *Annali di Matematica Pura ed Applicata*, 152(1), 183-196.
- [28] Bull, B. (1973). Red Cell Biconcavity and Deformability A macromodel based on flow chamber observations. In *Red Cell Shape* (pp. 115-124). Springer, Berlin, Heidelberg.
- [29] Byun, S. S., Lee, K. A., Oh, J., Park, J. (2019). Regularity results of the thin obstacle problem for the  $p(x)$ -Laplacian. *Journal of Functional Analysis*, 276(2), 496-519.
- [30] Dieudonn, J. (1980). *Special functions and linear representations of Lie groups* (Vol. 42). American Mathematical Soc..
- [31] Canham, P. B. (1970). The minimum energy of bending as a possible explanation of the biconcave shape of the human red blood cell. *Journal of theoretical biology*, 26(1), 61-81.
- [32] Cantat, I. (2012). *Le globule rouge*, <http://images.math.cnrs.fr/Le-globule-rouge>.

- [33] C ea, J. (1986). Conception optimale ou identification de formes, calcul rapide de la d riv e directionnelle de la fonction co t. *ESAIM: Mathematical Modelling and Numerical Analysis*, 20(3), 371-402.
- [34] Chambolle, A. (2003). A density result in two-dimensional linearized elasticity, and applications. *Archive for rational mechanics and analysis*, 167(3), 211-233.
- [35] Charkaoui, A., Alaa, N. E. (2020). Weak Periodic Solution for Semilinear Parabolic Problem with Singular Nonlinearities and  $L^1$  Data. *Mediterranean Journal of Mathematics*, 17(4), 1-17.
- [36] Charkaoui, A., Kouadri, G., Selt, O., Alaa, N. E. (2019). Existence results of weak periodic solution for some quasilinear parabolic problem with  $L^1$  data. *Annals of the University of Craiova- Mathematics and Computer Science Series*, 46(1), 66-77.
- [37] Charkaoui, A., Kouadri, G., Alaa, N. Some Results on The Existence of Weak Periodic Solutions For Quasilinear Parabolic Systems With  $L^1$  Data. *Boletim da Sociedade Paranaense de Matem tica*.
- [38] Chen, Y., Levine, S., Rao, M. (2006). Variable exponent, linear growth functionals in image restoration. *SIAM journal on Applied Mathematics*, 66(4), 1383-1406.
- [39] Chenais, D. (1975). On the existence of a solution in a domain identification problem. *Journal of Mathematical Analysis and Applications*, 52(2), 189-219.
- [40] Cherkaev, A., Kohn, R. (Eds.). (1997). *Topics in the mathematical modelling of composite materials*. Boston: Birkh user.
- [41] Choksi, R., Veneroni, M. (2013). Global minimizers for the doubly-constrained Helfrich energy: the axisymmetric case. *Calculus of Variations and Partial Differential Equations*, 48(3-4), 337-366.
- [42] Cordasco, D., Bagchi, P. (2014). Intermittency and synchronized motion of red blood cell dynamics in shear flow. *Journal of fluid mechanics*, 759, 472.
- [43] Danker, G., Biben, T., Podgorski, T., Verdier, C., Misbah, C. (2007). Dynamics and rheology of a dilute suspension of vesicles: Higher-order theory. *Physical Review E*, 76(4), 041905.
- [44] Danker, G., Misbah, C. (2007). Rheology of a dilute suspension of vesicles. *Physical review letters*, 98(8), 088104.

- [45] Danker, G., Verdier, C., Misbah, C. (2008). Rheology and dynamics of vesicle suspension in comparison with droplet emulsion. *Journal of non-newtonian fluid mechanics*, 152(1-3), 156-167.
- [46] Deuling, H. J., Helfrich, W. (1976). Red blood cell shapes as explained on the basis of curvature elasticity. *Biophysical journal*, 16(8), 861-868.
- [47] Diening, L., Harjulehto, P., Hästö, P., Ruzicka, M. (2011). *Lebesgue and Sobolev spaces with variable exponents*. Springer.
- [48] Diening, L., Hästö, P., Nekvinda, A. (2004). Open problems in variable exponent Lebesgue and Sobolev spaces. *FSDONA04 proceedings*, 38-58.
- [49] Divet, F., Danker, G., Misbah, C. (2005). Fluctuations and instability of a biological membrane induced by interaction with macromolecules. *Physical Review E*, 72(4), 041901.
- [50] Drábek, P., Kufner, A., Nicolosi, F. (2011). *Quasilinear elliptic equations with degenerations and singularities (Vol. 5)*. Walter de Gruyter.
- [51] Du, Q., Liu, C., Wang, X. (2006). Simulating the deformation of vesicle membranes under elastic bending energy in three dimensions. *Journal of computational physics*, 212(2), 757-777.
- [52] Dupire, J., Abkarian, M., Viallat, A. (2010). Chaotic dynamics of red blood cells in a sinusoidal flow. *Physical review letters*, 104(16), 168101.
- [53] Dupire, J., Socol, M., Viallat, A. (2012). Full dynamics of a red blood cell in shear flow. *Proceedings of the National Academy of Sciences*, 109(51), 20808-20813.
- [54] Elaassri, A., Uahabi, K. L., Charkaoui, A., Alaa, N. E., Mesbahi, S. (2019). Existence of weak periodic solution for quasilinear parabolic problem with nonlinear boundary conditions. *Annals of the University of Craiova-Mathematics and Computer Science Series*, 46(1), 1-13.
- [55] Ennahnahi, N., Oumsis, M., Bouhouch, A., Meknassi, M. (2010). Fast shape description based on a set of moments defined on the unit disc and inspired by three-dimensional spherical harmonics. *IET image processing*, 4(2), 120-131.
- [56] Evans, E., Fung, Y. C. (1972). Improved measurements of the erythrocyte geometry. *Microvascular research*, 4(4), 335-347.

- [57] Fan, X., Zhao, D. (2001). On the spaces  $L^{p(x)}(\Omega)$  and  $W^{m,p(x)}(\Omega)$ . Journal of mathematical analysis and applications, 263(2), 424-446.
- [58] Faraudo, J. (2002). Diffusion equation on curved surfaces. I. Theory and application to biological membranes. The Journal of chemical physics, 116(13), 5831-5841.
- [59] Farsad, K., De Camilli, P. (2003). Mechanisms of membrane deformation. Current opinion in cell biology, 15(4), 372-381.
- [60] Farutin, A., Biben, T., Misbah, C. (2010). Analytical progress in the theory of vesicles under linear flow. Physical Review E, 81(6), 061904.
- [61] Farutin, A., Misbah, C. (2012). Squaring, parity breaking, and S tumbling of vesicles under shear flow. Physical review letters, 109(24), 248106.
- [62] Farutin, A., Misbah, C. (2012). Rheology of vesicle suspensions under combined steady and oscillating shear flows. Journal of fluid mechanics, 700, 362.
- [63] Finken, R., Kessler, S., Seifert, U. (2011). Micro-capsules in shear flow. Journal of physics: Condensed matter, 23(18), 184113.
- [64] Fu, Y. Q. (2002). The existence of solutions for elliptic systems with nonuniform growth. Studia Mathematica, 151, 227-246.
- [65] Fu, Y., Pan, N. (2010). Existence of solutions for nonlinear parabolic problem with  $p(x)$ -growth. Journal of Mathematical Analysis and Applications, 362(2), 313-326.
- [66] Fung, Y. C. B., Tong, P. (1968). Theory of the sphering of red blood cells. Biophysical journal, 8(2), 175-198.
- [67] Giacomoni, J., Radulescu, V., Warnault, G. (2018). Quasilinear parabolic problem with variable exponent: qualitative analysis and stabilization. Commun. Contemp. Math, 20(8), 38.
- [68] Green, R. (2003). Spherical harmonic lighting: The gritty details. In Archives of the Game Developers Conference (Vol. 56, p. 4).
- [69] Guedda, M., Abaidi, M., Benlahsen, M., Misbah, C. (2012). Dynamic modes of quasispherical vesicles: Exact analytical solutions. Physical Review E, 86(5), 051915.

- [70] Guedda, M., Benlahsen, M., Misbah, C. (2014). Rheological properties of a vesicle suspension. *Physical Review E*, 90(5), 052302.
- [71] Hadamard, J. (1908). *Mémoire sur le problème d'analyse relatif à l'équilibre des plaques élastiques encastrées* (Vol. 33). Imprimerie nationale.
- [72] Helfrich, W. (1973). Elastic properties of lipid bilayers: theory and possible experiments. *Zeitschrift für Naturforschung C*, 28(11-12), 693-703.
- [73] Hochstadt, H. (2012). *The functions of mathematical physics*. Courier Corporation.
- [74] Kaoui, B., Biroş, G., Misbah, C. (2009). Why do red blood cells have asymmetric shapes even in a symmetric flow?. *Physical review letters*, 103(18), 188101.
- [75] Kessler, S., Finken, R., Seifert, U. (2009). Elastic capsules in shear flow: Analytical solutions for constant and time-dependent shear rates. *The European Physical Journal E*, 29(4), 399-413.
- [76] Kessler, S., Finken, R., Seifert, U. (2007). Swinging and tumbling of elastic capsules in shear flow. *arXiv preprint arXiv:0709.2610*.
- [77] Keller, S. R., Skalak, R. (1982). Motion of a tank-treading ellipsoidal particle in a shear flow. *Journal of Fluid Mechanics*, 120, 27-47
- [78] Khalfi, H., Fahim, H. and Alaa N., (2019). Mathematical analysis of a modified Weikert system for image enhancement *Annals of the University of Craiova, Mathematics and Computer Science Series*, 46 1, 90—98.
- [79] Kováčik, O., Rákosník, J. (1991). On spaces  $L^{p(x)}$  and  $W^{k,p(x)}$ . *Czechoslovak mathematical journal*, 41(4), 592-618.
- [80] Laadhari, A., Misbah, C., Saramito, P. (2010). On the equilibrium equation for a generalized biological membrane energy by using a shape optimization approach. *Physica D: Nonlinear Phenomena*, 239(16), 1567-1572.
- [81] Ladyzhenskaya, O., Solonnikov, V., Uraltseva, N. (1968). *Linear and quasilinear parabolic equations of second order*. Translation of Mathematical Monographs, AMS, Rhode Island.
- [82] Lebedev, N. N.(1972). *Special functions and their applications*, Revised edition, translated from the Russian and edited by Richard A. Silverman.

- [83] Leung, C. S., Sum, J., So, H. C., Constantinides, A. G., Chan, F. K. (2014). Lagrange programming neural networks for time-of-arrival-based source localization. *Neural Computing and Applications*, 24(1), 109-116.
- [84] Li, Z., Gao, W. (2015). Existence of renormalized solutions to a nonlinear parabolic equation in  $L^1$  setting with nonstandard growth condition and gradient term. *Mathematical Methods in the Applied Sciences*, 38(14), 3043-3062.
- [85] Li, Z., Yan, B., Gao, W. (2015). Existence of solutions to a parabolic  $p(x)$ -Laplace equation with convection term via  $L^\infty$  estimates. *Electronic Journal of Differential Equations*, 2015(46), 1-21.
- [86] Liang, J., Leung, C. S., So, H. C. (2015). Lagrange programming neural network approach for target localization in distributed MIMO radar. *IEEE Transactions on Signal Processing*, 64(6), 1574-1585.
- [87] Lions, J. L. (1969). *Quelques méthodes de résolution des problèmes aux limites non linéaires*.
- [88] Michalet, X., Jülicher, F., Fourcade, B., Seifert, U., Bensimon, D. (1994). *La physique des liposomes*.
- [89] Mihăilescu, M., Pucci, P., Rădulescu, V. (2008). Eigenvalue problems for anisotropic quasilinear elliptic equations with variable exponent. *Journal of Mathematical Analysis and Applications*, 340(1), 687-698.
- [90] Mikucki, M., Zhou, Y. C. (2017). Curvature-driven molecular flow on membrane surface. *SIAM journal on applied mathematics*, 77(5), 1587-1605.
- [91] Misbah, C. (2006). Vacillating breathing and tumbling of vesicles under shear flow. *Physical review letters*, 96(2), 028104.
- [92] Mitsui, T. (2008). Nonchaotic stagnant motion in a marginal quasiperiodic gradient system. *Physical Review E*, 78(2), 026206.
- [93] Montiel, S., Ros, A. (2005). *Curves and Surfaces*, volume 69 of. *Graduate Studies in Mathematics*.
- [94] Montiel, S., & Ros, A. (2009). *Curves and surfaces (Vol. 69)*. American Mathematical Soc.
- [95] Murat, F., Simon, J. (1975). Etude de problèmes d'optimal design. In *IFIP Technical Conference on Optimization Techniques* (pp. 54-62). Springer, Berlin, Heidelberg.

- [96] Murat, F., Simon, J. (1976). Sur le contrôle par un domaine géométrique. Publication du Laboratoire d'Analyse Numérique de l'Université Paris, 6, 189.
- [97] Nait-Ouhra, A., Farutin, A., Ez-Zahraouy, H., Benyoussef, A., Misbah, C. (2019). Rheology of a confined vesicle suspension. *Physical Review Fluids*, 4(10), 103602.
- [98] Nirenberg, L. (1974). *Topics in nonlinear functional analysis (Vol. 6)*. American Mathematical Soc.
- [99] Noguchi, H. (2010). Dynamics of fluid vesicles in oscillatory shear flow. *Journal of the Physical Society of Japan*, 79(2), 024801.
- [100] Noguchi, H. (2010). Dynamic modes of red blood cells in oscillatory shear flow. *Physical Review E*, 81(6), 061920.
- [101] Noguchi, H. (2009). Swinging and synchronized rotations of red blood cells in simple shear flow. *Physical Review E*, 80(2), 021902.
- [102] Noguchi, H., Gompper, G. (2007). Swinging and tumbling of fluid vesicles in shear flow. *Physical review letters*, 98(12), 128103.
- [103] Omori, T., Ishikawa, T., Barthès-Biesel, D., Salsac, A. V., Imai, Y., Yamaguchi, T. (2012). Tension of red blood cell membrane in simple shear flow. *Physical Review E*, 86(5), 056321.
- [104] Osher, S., Sethian, J. A. (1988). Fronts propagating with curvature-dependent speed: algorithms based on Hamilton-Jacobi formulations. *Journal of computational physics*, 79(1), 12-49.
- [105] Ouaro, S., Ouedraogo, A. (2017). Nonlinear parabolic problems with variable exponent and L1-data. *Electronic Journal of Differential Equations*, 32(2017), 1-32.
- [106] Pao, C. V. (1982). On nonlinear reaction-diffusion systems. *Journal of Mathematical Analysis and Applications*, 87(1), 165-198.
- [107] Papageorgiou, N. S., Rădulescu, V. D., Repovš, D. D. (2019). *Nonlinear analysis-theory and methods*. Springer.
- [108] Parton, D. L., Klingelhoefer, J. W., Sansom, M. S. (2011). Aggregation of model membrane proteins, modulated by hydrophobic mismatch, membrane curvature, and protein class. *Biophysical journal*, 101(3), 691-699.

- [109] Pomeau, Y., Manneville, P. (1980). Intermittent transition to turbulence in dissipative dynamical systems. *Communications in Mathematical Physics*, 74(2), 189-197.
- [110] Prignet, A. (1997). Existence and uniqueness of “entropy” solutions of parabolic problems with L data. *Nonlinear analysis, theory, methods & applications*, 28(12), 1943-1954.
- [111] Qamar, A., Din, I., Khan, M. A. (2012). Analysis of Spherical Harmonics and Singular Value Decomposition as Compression Tools in Image Processing.
- [112] Radulescu, V. D. (2019). Isotropic and anisotropic double-phase problems: old and new. *Opuscula Mathematica*, 39.
- [113] Radulescu, V. D., Repovš, D. D. (2015). Partial differential equations with variable exponents: variational methods and qualitative analysis (Vol. 9). CRC press.
- [114] Różycki, B., Lipowsky, R. (2015). Spontaneous curvature of bilayer membranes from molecular simulations: Asymmetric lipid densities and asymmetric adsorption. *The Journal of chemical physics*, 142(5), 02B601\_1.
- [115] Růžička, M. (2000). *Electrorheological fluids: modeling and mathematical theory*. Springer Science & Business Media.
- [116] Růžička, M. (1999). Flow of shear dependent electrorheological fluids. *Comptes Rendus de l'Académie des Sciences-Series I-Mathematics*, 329(5), 393-398.
- [117] Sadollah, A., Sayyaadi, H., Yadav, A. (2018). A dynamic metaheuristic optimization model inspired by biological nervous systems: Neural network algorithm. *Applied Soft Computing*, 71, 747-782.
- [118] Salac, D., Miksis, M. (2011). A level set projection model of lipid vesicles in general flows. *Journal of Computational Physics*, 230(22), 8192-8215.
- [119] Sansone, G. (1991). *Orthogonal Functions*, rev. English ed, 158.
- [120] Seifert, U. (1997). Configurations of fluid membranes and vesicles. *Advances in physics*, 46(1), 13-137.
- [121] Seifert, U., Berndl, K., Lipowsky, R. (1991). Shape transformations of vesicles: Phase diagram for spontaneous-curvature and bilayer-coupling models. *Physical review A*, 44(2), 1182.

- [122] Segal, S. S. (2005). Regulation of blood flow in the microcirculation. *Microcirculation*, 12(1), 33-45.
- [123] Shangerganesh, L., Balachandran, K. (2014). Solvability of reaction–diffusion model with variable exponents. *Mathematical Methods in the Applied Sciences*, 37(10), 1436-1448.
- [124] Simon, J. (1986). Compact sets in the space  $L^p(0, T; B)$ . *Annali di Matematica pura ed applicata*, 146(1), 65-96.
- [125] Skotheim, J. M., Secomb, T. W. (2007). Red blood cells and other nonspherical capsules in shear flow: oscillatory dynamics and the tank-treading-to-tumbling transition. *Physical review letters*, 98(7), 078301.
- [126] Stein, E. M., Weiss, G. (2016). *Introduction to Fourier Analysis on Euclidean Spaces (PMS-32)*, Volume 32. Princeton university press.
- [127] Sui, Y., Low, H. T., Chew, Y. T., Roy, P. (2008). Tank-treading, swinging, and tumbling of liquid-filled elastic capsules in shear flow. *Physical Review E*, 77(1), 016310.
- [128] Šverák, V. (1993). On optimal shape design. *Journal de mathématiques pures et appliquées*, 72(6), 537-551.
- [129] Villarrubia, G., De Paz, J. F., Chamoso, P., De la Prieta, F. (2018). Artificial neural networks used in optimization problems. *Neurocomputing*, 272, 10-16.
- [130] Vlahovska, P. M., Barthes-Biesel, D., Misbah, C. (2013). Flow dynamics of red blood cells and their biomimetic counterparts. *Comptes Rendus Physique*, 14(6), 451-458.
- [131] Vlahovska, P. M., Gracia, R. S. (2007). Dynamics of a viscous vesicle in linear flows. *Physical Review E*, 75(1), 016313.
- [132] Vlahovska, P. M., Young, Y. N., Danker, G., Misbah, C. (2011). Dynamics of a non-spherical microcapsule with incompressible interface in shear flow. *Journal of fluid mechanics*, 678, 221.
- [133] Walter, J., Salsac, A. V., Barthes-Biesel, D. (2011). Ellipsoidal capsules in simple shear flow: prolate versus oblate initial shapes. *Journal of Fluid Mechanics*, 676, 318.
- [134] Willmore, T. J. (1996). *Riemannian geometry*. Oxford University Press.

- [135] Xu, X. (1996). On the Cauchy problem for a singular parabolic equation. *Pacific Journal of Mathematics*, 174(1), 277-294.
- [136] Zhang, S., Constantinides, A. G. (1992). Lagrange programming neural networks. *IEEE Transactions on Circuits and Systems II: Analog and Digital Signal Processing*, 39(7), 441-452.
- [137] Zhang, C., Zhou, S. (2010). Renormalized and entropy solutions for nonlinear parabolic equations with variable exponents and  $L^1$  data. *Journal of Differential Equations*, 248(6), 1376-1400.
- [138] Zhao, M., Bagchi, P. (2011). Dynamics of microcapsules in oscillating shear flow. *Physics of Fluids*, 23(11), 111901.
- [139] Zhou, S. (2000). A priori  $L^\infty$ -estimate and existence of solutions for some nonlinear parabolic equations. *Nonlinear Analysis: Theory, Methods and Applications*, 42(5), 887-904.
- [140] Zhong-Can, O. Y., Helfrich, W. (1989). Bending energy of vesicle membranes: General expressions for the first, second, and third variation of the shape energy and applications to spheres and cylinders. *Physical Review A*, 39(10), 5280.

# Conclusion and Perspectives

The aim of this thesis was to study several biological and physical problems in order to translate observations by applying mathematical tools, techniques and theories, or vice versa, to translate mathematical results obtained into predictions or operations in the real world.

The first problem we chose to study in this thesis is a first step towards understanding the blood rheology. This work, concern the mathematical and numerical modeling of red blood cells, biological membranes in the presence of diffusive molecules and the dynamical behavior of vesicles. Despite there simplicity, these models remains difficult to solve theoretically and even numerically and constitutes very rich models to exploit. This is why several computation tools must be set up to overcome these difficulties.

Initially, a special attention was paid to modeling the equilibrium shape of red blood cells. According to this model, the shape of the red blood cell is the solution of an optimization problem under constraint: minimization Canham Helfrich energy for a fixed volume and area. After formalizing the problem mathematically, we derive the optimality condition leading to a nonlinear ordinary differential equation verified by the red blood cell shapes. We treat the two-dimensional and three-dimensional axis-symmetric cases. The qualitative analyzes of the obtained shapes by simulations seem to validate the Canham-Helfrich-Evans model. An interesting perspective would be to study the stability of these shapes, by looking at the second derivative of Canham-Helfrich energy and by studying the sign of the latter. Thus, shapes not observed in nature may be unstable which would explain the impossibility of observing them. If some unobserved shapes are stable, then it will be necessary to highlight such shapes in nature, in order to see if the model can surpass the experiment, which would complete the validation of this latter.

Then we introduced a molecule concentration of the bilayer membrane. The bending energy and energy of molecules distributions consist of the total energy of the interacting protein-membrane system. The transport of molecules on membrane surfaces follows the gradient flow of this total energy.

We derived a drift-diffusion equation for the gradient flow, where the difference between the local membrane curvature and the molecule concentration dependent local spontaneous curvature appears as a drift potential, a feature that models the biophysics of molecular localization on membrane surfaces. The numerical simulations, corresponding to the diffusive molecules using level set method shows the effect of the diffusion on the surface membrane.

Finally, we have developed an effective tool to model the dynamics of a vesicle in an oscillatory shear flow. The analytical results showed, first, that we find certain classic results and secondly, have enabled us to predict, the dynamics of vesicles in flow. These latest results are original, they open up promising avenues for the study of blood rheology. It would be interesting to consider other types of dynamic such as the case where the vesicle is near a substrate. The Experimental results have shown that, during the movement of the chariot caterpillar, vesicles slide and roll. In addition, the deformability of the vesicles generates a lifting force, originally purely viscous, which makes them nonstick from the substrate. Numerical simulations are used to determine a dependence law between the lift force and the distance to the substrate. At the same time, it would be interesting to study the passage of the vesicles in a bifurcation. These two dynamics poses problems of the vesicle/substrate contact process in numerical point of view. In order to see the effect of the presence of vesicles on the rheological blood behavior, it is important to increase the concentration of vesicles in the dynamics. The difficulty of this problem lies in avoiding the inter-penetration between different particles.

The second part of this thesis deals with the study of variational problems involving variable growth conditions. Since, a great attention has been paid in the recent years, to study mathematical models of electro-rheological fluids. These models include parabolic or elliptic equations which are nonlinear with respect to gradient of the solution and with variable exponents of nonlinearity. Besides, another important application is the image processing where the anisotropy and nonlinearity of the diffusion operator and convection terms are used to underline the borders of the distorted image and to eliminate noises. In this part we prove the existence of a weak solution for a nonlinear parabolic equation having a nonstandard growth condition with respect to the gradient and the variable exponent using Schaeffer's fixed point theorem and the sub- and super- solution method under appropriate assumptions. We also prove the existence of a global weak solution for a class of degenerate parabolic systems with variable exponents and nonlinearities critical growth with respect to the gradient. In this work we establish two interesting existence results for this class of degenerate parabolic system with variable exponents. The first result concerns the case where the non-linearities are bounded. In this case, we prove the existence of solutions

using the Schauder fixed point theorem in appropriate spaces. The second relates to the case where the nonlinearities have a critical growth with respect to the gradient of the solution, the existence of a weak solution is obtained via the existence of a weak super-solution. It would be interesting to study this kind of problems, since there are only a few works about parabolic equations with variable exponents of nonlinearity, knowing that they have many applications in various fields.

The third and the last part of this thesis is related to the field of image processing, especially to reconstruction and recognition of digital images. In this work we propose to use an orthogonal spherical expansion to convert the 2D image into a 3D object (which consists a representation of the image on the sphere  $S^2$ ). The conversion technique is efficient. Once the 3D image is obtained and decomposed using spherical harmonics, the original image can be reconstructed from the characteristic coefficients. The algorithm is implemented and computer simulations results shows the efficiency and accuracy of the proposed reconstruction algorithm. In this field, another result is obtained, in which we build a strong and efficient shape descriptor for fingerprints identification based on spherical harmonics, where the components of the characteristic vector of the fingerprints is obtained from a sphere according to the transformation into spherical harmonics. Numerical simulations show that our based spherical harmonics descriptor is efficient. It allows the identification of all the images in a database composed of 16 image, these images are composed of 4 people's fingerprints, each fingerprint undergoes 4 different deformations, as translation, rotation, homothety and noise effects. In practice, to prove the robustness of our descriptor, the tests must be carried out on databases comprising at least hundreds of images. However, the latter require efficient material resources. This may be a perspective for future work.

## Abstract

The aim of the present PhD thesis is to study some ordinary differential equations and partial differential equations arising in modeling the deformation of biological membranes, electro-rheological fluids and image processing. This thesis is divided into three independent parts. The first part focuses on the dynamics and deformation of red blood cells and vesicles. We have analytically obtained the biconcave shape of red blood cells by using the energy of Canham and Helfrich, and analyzed a mathematical model for the diffusion of several species on a biological membrane. We have also examined the motion and dynamics of a deformable vesicle under an oscillatory shear flow, and obtained an analytical expression of the effective viscosity of a suspension of vesicles.

In the second part, we focus on the study of a family of partial differential equations and systems of partial differential equations involving the operators of type- $p(x)$  Laplacian. Here, we have demonstrated the existence of a weak solution for a nonlinear parabolic equation having a nonstandard growth condition with respect to the gradient (presence of variable exponent). We have also shown the existence of a weak global solution for a class of degenerate parabolic systems with variable exponents and critical growth nonlinearities with respect to the gradient.

In the third part, we present applications in the image processing. Our contribution concerns the representation of 2D and 3D objects using spherical harmonics.

**Keywords:** Red blood cells, vesicles, rheology, membrane morphology, simple and oscillatory shear flows, ordinary differential equation, partial differential equations, electro and magneto rheological fluids, image processing.

## Résumé

Le but de cette thèse de doctorat est d'étudier des équations différentielles et équations aux dérivées partielles apparaissant dans la modélisation de la déformation des membranes biologiques, des fluides électro-rhéologique et dans le traitement d'images. Cette thèse est divisée en trois parties indépendantes. La première partie porte sur de la dynamique et la déformation des globules rouges et des vésicules. Nous avons obtenu analytiquement la forme biconcave des globules rouges en utilisant l'énergie de Canham et Helfrich, et nous avons analysé un modèle mathématique pour la diffusion de plusieurs espèces sur une membrane biologique. Nous avons aussi examiné le mouvement et la dynamique d'une vésicule déformable sous un écoulement oscillatoire, et nous avons obtenu une expression analytique de la viscosité effective d'une suspension de vésicules.

Dans la deuxième partie, nous étudions une famille d'équations aux dérivées partielles et systèmes d'équations aux dérivées partielles avec des opérateurs de type  $p(x)$ -Laplacien. Nous avons obtenu l'existence d'une solution faible pour une équation parabolique non-linéaire avec une condition de croissance non standard par rapport au gradient (présence d'exposant variable). Nous avons également montré l'existence d'une solution globale faible pour une classe de systèmes paraboliques dégénérés avec exposants variables et des non-linéarités à croissance critique par rapport au gradient.

Dans la troisième partie, nous présentons des applications en traitement d'image. Notre contribution concerne la représentation d'objets 2D et 3D à l'aide des harmoniques sphériques.

**Mots clé:** Globules rouges, vésicules, rhéologie, morphologie de la membrane, écoulement de cisaillement simple et oscillatoire, équations différentielles ordinaires et équations aux dérivées partielles, fluides électro et magnéto rhéologiques, traitement d'image.